3D Multimodal X-ray microscopy of biological specimens

Dissertation

zur Erlangung des Doktorgrades
an der Fakultät für Mathematik, Informatik und Naturwissenschaften
Fachbereich Physik
der Universität Hamburg

vorgelegt von

Karolina Maria Stachnik

aus Kraków

Hamburg
2019

Gutachter/in der Dissertation:	Dr. Alke Meents Prof. Dr. Henry N. Chapman
Gutachter/in der Disputation:	Prof. Dr. Daniela Pfannkuche Dr. Alke Meents Prof. Dr. Henry N. Chapman Prof. Dr. Christian G. Schroer Prof. Dr. Michael A. Rübhausen
Vorsitzender des Prüfungsausschusses:	Prof. Dr. Daniela Pfannkuche
Datum der Disputation:	23. September 2019
Vorsitzender des Fach-Promotionsausschusses Physik:	Prof. Dr. Michael Potthoff
Leiter des Fachbereichs Physik:	Prof. Dr. Wolfgang Hansen
Dekan der Fakultät für Mathematik, Informatik und Naturwissenschaften:	Prof. Dr. Heinrich Graener

Abstract

Studies of biological systems typically require the application of several complementary methods able to yield statistically-relevant results at a unique level of sensitivity. Long penetration depth of X-rays makes them particularly suitable for non-destructive volumetric investigations of whole cells and tissue sections, providing structural and elemental specificity at nanoscale spatial resolutions.

X-ray ptychography is a promising imaging technique for sub-100-nm structural studies of weakly-scattering extended biological specimens. It provides quantitative phase-contrast maps revealing the morphology of an investigated object. In addition, its scanning nature allows for a simultaneous acquisition of nanoscale X-ray fluorescence, yielding the element distributions at an unmatched sensitivity.

Thus, the goal of this PhD project has been to combine X-ray fluorescence and ptychography to enable a robust correlation of elemental distributions with respect to the cellular morphology. Exploiting a highly intense and coherent X-ray beam at beamline P11 of the low-emittance synchrotron light source PETRA III in Hamburg, Germany, a versatile multimodal scanning X-ray microscope was developed in the framework of this PhD project. This thesis describes the consecutive stages of the microscope's development and highlights its application in structural determination of biological samples.

In the first stage of this PhD project, a 2D long-range scanning unit was developed, enabling seamless, serial measurements of many targets at nanometer precision. With this setup, the PhD work allowed to optimise the correlative imaging method at higher incident photon energies for mapping of first-row transition metals up to iron, while using a nano-focussed beam. In this way, it addressed limitations of the so-far presented demonstrations, restrained to light-element mapping in the context of organelles of single cells. The correlative imaging method was then used to quantify the iron distributions in a population of macrophages treated with *Mycobacterium-tuberculosis*-targeting iron-oxide nanocontainers in the context of their sub-cellular structure obtained by ptychography. In the second application, the calcium content in a human bone matrix was mapped in close proximity to osteocyte lacunae (perilacunar matrix). A concurrently acquired ptychographic image was then used to remove the mass-thickness effect from the raw calcium map.

In the second stage of this work, the concept of concurrent ptychography and X-ray fluorescence was extended to 3D correlative imaging in the framework of computed tomography. For this purpose, an upgraded 3D scanning X-ray microscope was built, commissioned, and used in volumetric imaging of two specimens, using ptychographic X-ray computed tomography. The final performance of the 3D microscope reached far beyond the throughputs of the available ptychographic tomography setups which, until now, have hindered application of the method by a broader biomedical community. A tomogram of the nano-porous glass demonstrated the fastest on-the-fly ptychographic tomography, to date, at an isotropic spatial resolution of 52 nm. In the second application, ptychographic tomography of a chiton's radular tooth provided a quantitative insight into one of the nature's hardest biominerals, at a Nyquist-sampling limited spatial resolution of 65 nm.

The work has been concluded with a prospect for future operation and opportunities of the correlative method of simultaneous ptychographic and X-ray fluorescence imaging at upcoming diffraction-limited synchrotron light sources.

Zusammenfassung

Untersuchungen biologischer Systeme erfordern in der Regel die Anwendung mehrerer komplementärer Methoden, mit denen statistisch relevante Ergebnisse mit einer einzigartigen Empfindlichkeit erzielt werden können.

Aufgrund ihrer großen Eindringtiefe ist Röntgenstrahlung besonders gut zur zerstörungsfreien Untersuchung ganzer Zellen und von Gewebeschnitte in 3D geeignet und ermöglicht es dabei, räumliche Auflösungen im Nanometerbereich bei gleichzeitiger Elementspezifität zu erzielen.

Die Röntgenptychographie ist ein bildgebendes Verfahren, welches besonders für Strukturuntersuchungen von schwach streuenden biologischen Proben geeignet ist. Mit der Methode werden quantitative Phasenkontrastbilder erhalten, mit denen sich die Morphologie der Proben im Sub-100-nm-Bereich untersuchen lässt. Darüber hinaus ermöglicht das angewandte Scanverfahren der Probe eine simultane Erfassung der Röntgenfluoreszenz im Nanometerbereich, wodurch die Elementverteilungen mit einer bisher unerreichten Empfindlichkeit erhalten werden.

Ziel dieses Promotionsprojekts war es, ein kombiniertes Messverfahren für simultane Röntgenfluoreszenz und Ptychographie zu entwickeln, um eine Korrelation der Elementverteilungen in Bezug auf die zelluläre Morphologie zu ermöglichen. Unter Ausnutzung eines hochintensiven und kohärenten Röntgenstrahls an der Strahlführung P11 der Synchrotronstrahlungsquelle PETRA III in Hamburg wurde dazu ein vielseitiges multimodales Röntgenrastermikroskop entwickelt. Diese Dissertation beschreibt die Entwicklungsstadien des Mikroskops und seine anschließende Anwendung zur Strukturuntersuchung biologischer Proben.

Im ersten Teil des Promotionsprojekts wurde zunächst eine 2D-Scaneinheit mit einem großen Verfahrbereich entwickelt, welche die seriellen Messungen von vielen Objekten mit Nanometergenauigkeit ermöglicht. Durch die Verwendung höherer Photonenenergien konnte dabei die Elementverteilung von 3d-Übergangsmetallen bis zu Eisen korrelativ untersucht werden. Mit der entwickelten Bildgebungsmethode wurde anschließend die Eisenverteilung in Makrophagen, die mit Eisenoxid-Nanokapsel gegen eine *Mycobacterium-Tuberculosis*-Infektion behandelt wurden, quantitativ untersucht. Das Verfahren ermöglichte es, die genaue Verteilung der Eisenpartikeln innerhalb der subzellulären Struktur zu bestimmen. In einer zweiten Anwendung wurde die Kalziumverteilung innerhalb Perilacunarmatrix eines menschlichen Knochens bestimmt. Durch die simultane Aufnahme eines ptychographischen Bildes, konnte dabei die um den Massendickeneffekt korrigierte, reale Kalziumverteilung bestimmt werden.

Im zweiten Teil der Arbeit wurde die Methode der simultanen Ptychographie und Röntgenfluoreszenz auf die Bildgebung in 3D erweitert. Dazu wurde ein neuartiges 3D-Röntgenmikroskop entwickelt, welches es erlaubt, ptychographische Tomographie Untersuchungen viel schneller als bisher durchführen zu können. Die Effizienz dieses neuen Mikroskops wurde anhand der Strukturbestimmung von 2 Proben in 3D demonstriert. In dem ersten Experiment konnte mit der Methode der On-the-fly-scanning Ptychographie mit bisher unerreichter Geschwindigkeit ein Tomogramm von nanoporösen Glases mit einer isotropen Auflösung von 52 nm aufgezeichnet werden. In einem weiteren Experiment konnten Struktur und Dichte eines Radulazahns einer Käferschnecke, einem der härtesten Biomineralien der Natur, mit einer isotropen Auflösung von 65 nm in 3D bestimmt werden.

Die Arbeit schließt mit einem Ausblick auf die zukünftigen Anwendungsmöglichkeiten des Mikroskops und der Methode der simultanen Ptychographie- und Röntgenfluoreszenzmikroskopie an künftigen neuen beugungsbegrenzten Röntgenstrahlungsquellen.

Eidesstattliche Versicherung / Declaration on oath

Hiermit versichere ich an Eides statt, die vorliegende Dissertationsschrift selbst verfasst und keine anderen als die angegebenen Hilfsmittel und Quellen benutzt zu haben. Die eingereichte schriftliche Fassung entspricht der auf dem elektronischen Speichermedium. Die Dissertation wurde in der vorgelegten oder einer ähnlichen Form nicht schon einmal in einem früheren Promotionsverfahren angenommen oder als ungenügend beurteilt.

I hereby declare that this thesis is my own work and effort and that it has not been submitted anywhere for any award. Where other sources of information have been used, they have been acknowledged. The submitted dissertation text corresponds to the version provided on the digital medium.

Hamburg, den 19.07.2019 .....

Unterschrift der Doktorandin
PhD candidate's signature

The most beautiful experience we can have is the mysterious. It is the fundamental emotion that stands at the cradle of true art and true science.

Albert Einstein

To my Family

Contents

Introduction

Vision is undoubtedly one of the human's most powerful senses. It opens us to a world of shapes and colours. It allows the human mind to identify and assign structures and functions of surrounding objects. Finally, thanks to a certain anatomic arrangement, it renders a three dimensional view of the world around. Evolution has optimised the human vision for detecting ubiquitous sunlight, hence termed the visible light. In such a light most of the solid objects appear opaque, holding tight the mystery of their interiors. While a magnifying glass may help us investigate visually small objects, yet to unravel the mystery of the smallest is again limited by the light.

Another great power of humanity is curiosity. To reach, to discover, to understand. Indefatigably pursuing the unknown. To answer the fundamental questions. To disentangle mysteries of the universe and the surrounding nature.

Over the past century our curiosity has brought us far beyond the capabilities of our senses. Seeing beyond their limits has namely required another type of light and adequate *eyes* to process the new type of information. Using the invisible has made us see more than ever before.

X-ray radiation, discovered at the turn of 19^{th} and 20^{th} century, allowed for establishing a broad spectrum of methods for pursuing answers to fundamental questions of nature. Its high penetration power and wavelengths much shorter than those of the visible light, have made X-rays an ideal probe for non-invasive imaging of optically thick objects, at micro- and nano length scales, down to atomic structure determination of crystalline specimens. These and other applications have though become vastly feasible only in the second half of the 20^{th} century, with the development of synchrotron radiation sources. Synchrotrons descended from the high-energy physics where they were utilised as particle accelerators. Later on, they were converted into storage rings, in which beams of light and charged particles, typically electrons, circulate at relativistic speeds. When forced to follow a curved trajectory, the electrons emit a beam of highly collimated X-ray radiation, many orders of magnitude more brilliant than the so-far known conventional X-ray sources. Synchrotron storage rings have therefore enabled a foundation of large scientific facilitates, where research together with cutting-edge technology has allowed for conducting many interdisciplinary projects, utilising a rich portfolio of X-ray techniques.

Amongst them, X-ray microscopy methods can be distinguished which, combined with computed tomography, enable volumetric investigations of whole specimens. Comprising both full-field and scanning techniques, X-ray microscopy can exploit both absorption and phase contrasts to form an image. Phase contrast is particularly suitable in biological applications, as it falls off less quickly than the absorption contrast with increasing photon energy. Performing imaging experiments at higher photon energies decreases namely the radiation dose absorbed by the specimen, alleviating radiation damage. Moreover, a growing brilliance and coherent properties of X-ray beams at the third-generation synchrotron light sources allowed coherent diffraction X-ray microscopy to emerge in the

early 2000s. Its scanning variant, so-called ptychography [1, 2], has become especially successful and robust. Ptychography provides quantitative optical density contrast at dose-limited spatial resolutions beyond the fabrication limits of X-ray optics. Since it derives from the coherent diffraction imaging, it uses an iterative phase retrieval algorithm [3, 4, 5] to reconstruct complex object and probe functions from a redundant set of far-field diffraction patterns. The redundancy is achieved by keeping a known relative spatial overlap [6] between illuminated areas. Thanks to its sensitivity, the technique is suitable for imaging of both radiation-resistant high-Z-element-rich specimens and soft biological tissue allowing for a vast range of applications. Moreover, ptychography can exploit both chemical [7, 8, 9, 10] and magnetic [11, 12] contrast mechanisms. Finally, combined with computed tomography, it can be extended to non-destructive 3D studies of extended specimens, yielding volumetric electron-density distributions.

Despite these advances in the field of X-ray microscopy, X-rays do not hold the monopoly for imaging in biological applications. In the recent years, the pioneering works on superresolution techniques [13] have allowed to overcome the diffraction-limit barrier in visible-light fluorescence imaging of certain pre-selected molecules in living cells. On the other hand, cryo-electron tomography has become a typical method of choice in cell biology, yielding 3D representations of cellular ultrastructure, at unprecedented spatial resolutions even down to individual protein complexes [14, 15]. Nevertheless, both microscopy branches have their limitations. The superresolution visible-light imaging requires namely fluorescent labels bound to a group of cell constituents, selected *a priori*. The cryo-electron tomography is in turn restrained to either less than 1-µm-thick non-eukaryotic cells or thin tissue sections, due to short penetration depth of electrons interacting with the biological matter. These limitations do not hold for correlative X-ray microscopy methods, which offer complementary contrast mechanisms for investigations of unlabelled, whole cells and large tissue sections. In particular, combined scanning techniques, such as simultaneous ptychography and nanoscale X-ray fluorescence, allow for outstanding, artefact-free mapping of elements at native concentrations with respect to the cellular electron-density volumes at sub-100-nm spatial resolutions.

The aim of this PhD thesis is to develop multimodal scanning X-ray microscopy for structure determination of biological specimens at the low-emittance synchrotron light source PETRA III, and demonstrate its capability of imaging of a statistically-relevant population of samples. The dissertation consists of six chapters.

Chapter 1 provides a theoretical background for the properties of X-ray radiation in the context of the imaging methods utilised in this thesis. It introduces first X-rays as electromagnetic waves, the formalism of their free-space propagation based on the scalar diffraction theory, and the coherence of an X-ray wave field. Subsequently, it discusses interactions of X-rays with matter and is concluded with a section about the complex index of refraction in the X-ray regime.

Chapter 2 summarises ways of generating X-ray radiation, with a focus on historical evolution of the synchrotron storage rings. Further sections familiarise the reader with the characteristics of the contemporary third-generation synchrotron light sources, and provide description of highly brilliant and collimated X-ray beams produced by undulator insertion devices.

Chapter 3 introduces the concepts of two X-ray microscopy methods utilised in this thesis. First sections present the historical background of ptychographic imaging, its generic experimental realisation and iterative phase retrieval algorithms, with a generalisation to partially coherent illuminations. Further, extension of the method to ptychographic X-ray computed tomography is discussed. The second part of the chapter is dedicated to energy-dispersive X-ray fluorescence (XRF), giving an overview of XRF

detection, spectra evaluation methods, and quantitative XRF analysis.

The following three chapters summarise the experimental work relevant to this thesis, performed at beamline P11, at PETRA III synchrotron light source at DESY, Hamburg, Germany.

Chapter 4 describes the evolution of the bio-imaging experiments at beamline P11, based on scanning X-ray microscopy, conducted in the framework of this PhD project. Deriving from the description of the beamline, the design case for a bio-imaging end-station is presented. First, experiments aiming to establish simultaneous ptychography and X-ray fluorescence in 2D are presented. The respective sections outline advances in instrumentation and preliminary results obtained in the commissioning phase and provide a detailed description of the final 2D scanner used in the application phase for experiments with biological specimens. Subsequently, the experience gained with the 2D setup was used to develop a new 3D scanning microscope. The final section presents chronological optimisations of the 3D microscope together with a preliminary tomographic measurement of a tuberculosis-infected macrophage.

Chapter 5 reports the application of simultaneous ptychographic and X-ray fluorescence 2D mapping in quantitative imaging of two vital biological systems. In the first application, the correlative methods were used to visualise and quantify uptake iron-oxide nanocontainers in a population of macrophages, using their ptychographic phase images and the corresponding iron maps. The second application concerned mapping of the local degree of mineralisation in human cortical bone matrix, by means of the ptychography-enhanced calcium distribution.

In Chapter 6, two successful demonstrations of on-the-fly ptychographic X-ray computed tomography of a nano-porous glass test structure and a piece of chiton's radular tooth are shown. Two different operation modes of the 3D scanning microscope are discussed. Quantitative contrast of the obtained tomograms is outlined.

The dissertation is concluded with a summary and outlook, which renders prospects for the multimodal imaging method and the versatile 3D X-ray microscope at future diffraction-limited synchrotrons and compact X-ray sources.

A set of 8 appendices complements the main text with additional results relevant to this thesis.

Chapter 1

X-ray radiation characteristics

The discovery of a new type of radiation by Wilhelm Röntgen in 1895 deeply impacted the scientific community. The following years resulted in a number of experimental works that contributed to the description of characteristics of X-ray radiation. The weak interaction of X-rays with matter, reflected in their high penetration power, and their elemental specificity have allowed for many scientific, but also medical and industrial applications until now. X-rays offer therefore manifold contrast mechanisms allowing to non-invasively study structure and function of various specimens.

The aim of this chapter is to summarise the properties of X-ray radiation most relevant to the imaging methods utilised in this thesis. In the first section 1.1, the formalism of representing X-rays as electromagnetic waves is presented. From the Maxwell's equations (1.1.1), the Helmholtz wave equation is derived (1.1.2). Further, the free-space propagation of an X-ray wave field is discussed using the Fresnel-Kirchhoff integral approach (1.1.3.1) and the angular spectrum (1.1.3.2). Finally, the coherence of an X-ray field is introduced (1.1.4), being particularly important for this thesis. The second section 1.2 provides a theoretical background for interactions of X-rays with matter. Three most important processes are discussed: elastic and inelastic scattering, and photoelectric absorption. The chapter is concluded with a subsection about the complex index of refraction (1.2.4), which combines both the atomic and the wave natures of X-ray interactions with matter.

1.1 X-rays as electromagnetic waves

Electromagnetic radiation, in the classical description, consists of electromagnetic waves which are alternating and synchronised oscillations of electric and magnetic fields, propagating at the speed of light in a given medium. In homogenous and isotropic media, the undulations of the two fields are perpendicular to each other and normal to the propagation direction. An electromagnetic wave is therefore a transverse wave characterised by its wavelength or the frequency of oscillations, inversely proportional to each other. Charged particles that are subject to acceleration are common sources of electromagnetic waves. In this way the source particles pass energy, momentum, and angular momentum that are carried away by the emitted electromagnetic waves and may be deposited in matter with which they interact. General classification of electromagnetic waves distinguishes the following radiation groups in order of increasing frequency: radio waves, microwaves, infrared radiation, visible light, ultraviolet radiation, X-rays, and gamma rays. The interaction of electromagnetic radiation with chemical compounds depends on the radiation power and its frequency. Radiation types of visible and lower frequencies

comprise a group of non-ionising radiation. They do not carry enough energy to either ionise atoms or molecules, or break chemical bonds. Their interaction with matter results essentially in heating effects. On the contrary, the higher frequency ultraviolet, X-ray, and gamma radiations are energetic enough to ionise the atomic matter and break chemical bonds. They are referred to as ionising radiation that is capable of causing chemical reactions and damaging living organisms, which reaches beyond the heating effects.

In a quantum mechanical description, a portion of monochromatic electromagnetic radiation is quantised into photons, uncharged elementary particles with zero rest mass. Photons are carriers of electromagnetic interactions. Each of them carries a quantised energy E that depends on the photon frequency ν and is given by Planck's equation:

$$E = h\nu \tag{1.1.1}$$

where $h = 6.626\,070\,15 \times 10^{-34}\,\mathrm{J\,s}$ is Planck's constant. The intensity of a radiation beam is defined by a number of photons that pass through a given area in a unit time. Since the square of the electric field is proportional to the intensity, it implies that the magnitude of the field is quantised as well.

X-rays are ionising electromagnetic radiation with wavelengths in the Ångstrom range ($1\,\text{Å} = 10^{-10}\,\mathrm{m}$) spanning 3 orders of magnitude of photon energies between 100 eV to 100 keV. Far enough from the source, a well-collimated X-ray beam can be approximated by a plane wave. The electric vector of such a wave is in general characterised by its polarisation vector $\hat{\boldsymbol{\varepsilon}}$ and its wavevector $\mathbf{k}$, so that:

$$\mathbf{E}(\mathbf{r}, t) = \hat{\boldsymbol{\varepsilon}} E_0 \mathrm{e}^{\mathrm{i}(\mathbf{k}\cdot\mathbf{r} - \omega t)} \tag{1.1.2}$$

which in the case of propagation along the z axis can be simplified to:

$$\mathrm{E}(z, t) = \hat{\boldsymbol{\varepsilon}} E_0 \mathrm{e}^{\mathrm{i}(k_z z - \omega t)} \tag{1.1.3}$$

where E_0 denotes the electric field amplitude and $\omega = 2\pi\nu$ is the angular frequency of the wave.

1.1.1 Wave equation

Let us consider propagation of an electromagnetic wave in a dielectric medium characterised by its electrical permittivity ϵ and magnetic permeability μ. The medium is further assumed to be **linear**, **isotropic** (its properties are independent of the wave polarisation direction), **homogenous** (the electrical permittivity is constant within the propagation region), **nondispersive** (the electrical permittivity does not depend on wavelength over the bandwidth occupied by the propagating wave), and **nonmagnetic** (its magnetic permeability is invariant and equal to the vacuum permeability μ_0). Our goal is to obtain the wave equations that describe the spatial and temporal evolution of the electromagnetic wave in free space. In the absence of free charge, the analysis starts with the Maxwell's equations expressed in SI units that read as follows:

$$\nabla \times \mathbf{E}(\mathbf{r}, t) = -\mu_0 \frac{\partial \mathbf{H}(\mathbf{r}, t)}{\partial t} \tag{1.1.4a}$$

$$\nabla \times \mathbf{H}(\mathbf{r}, t) = \epsilon \frac{\partial \mathbf{E}(\mathbf{r}, t)}{\partial t} \tag{1.1.4b}$$

$$\nabla \cdot \epsilon \mathbf{E}(\mathbf{r}, t) = \mathbf{0} \tag{1.1.4c}$$

$$\nabla \cdot \mu_0 \mathbf{H}(\mathbf{r}, t) = \mathbf{0} \tag{1.1.4d}$$

Here $\mathbf{H}$ and $\mathbf{E}$ are vectors of the magnetic and the electric fields, respectively, both being functions of position $\mathbf{r}$ and time t. ∇ denotes the Nabla operator, being a vector differential operator defined in the Cartesian coordinate system as $\nabla = \left(\frac{\partial}{\partial x}, \frac{\partial}{\partial y}, \frac{\partial}{\partial z}\right)$, while $\mathbf{0}$ is a zero-length vector. These equations are also known as: the Faraday's Law of induction (Eq. 1.1.4a), the free-space form of the Ampere's Law with Maxwell's modification (Eq. 1.1.4b), the free-space of the Gauss' Law (Eq. 1.1.4c), and the magnetic equivalent of the Gauss' Law (Eq. 1.1.4d), asserting non-existance of magnetic monopoles. Taking the curl operator ($\nabla\times$) of the Eq. (1.1.4a), we exploit the following vector identity:

$$\nabla \times (\nabla \times \mathbf{E}) = \nabla(\nabla \cdot \mathbf{E}) - \nabla^2\mathbf{E} \tag{1.1.5}$$

to obtain

$$\nabla(\nabla \cdot \mathbf{E}(\mathbf{r}, t)) - \nabla^2\mathbf{E}(\mathbf{r}, t) + \mu_0\nabla \times \frac{\partial \mathbf{H}(\mathbf{r}, t)}{\partial t} = \mathbf{0} \tag{1.1.6}$$

According to the free-space form of the Gauss' law (Eq. 1.1.4c), the first term of the equation above vanishes. Plugging in Eq. (1.1.4b) under all aforementioned medium characteristics assumptions, we arrive at:

$$\left(\nabla^2 - \mu_0\epsilon\frac{\partial^2}{\partial t^2}\right)\mathbf{E}(\mathbf{r}, t) = \mathbf{0} \tag{1.1.7}$$

The wave equation for the magnetic field can be obtained in a similar manner:

$$\left(\nabla^2 - \mu_0\epsilon\frac{\partial^2}{\partial t^2}\right)\mathbf{H}(\mathbf{r}, t) = \mathbf{0} \tag{1.1.8}$$

Both equations (1.1.7) and (1.1.8) have a form of the d'Alambert wave equation. Defining the refractive index n of the medium as:

$$n = \sqrt{\frac{\epsilon}{\epsilon_0}} \tag{1.1.9}$$

where ϵ_0 is the electric permittivity of vacuum, and the velocity of propagation in vacuum c, given by:

$$c = \frac{1}{\sqrt{\mu_0\epsilon_0}} \tag{1.1.10}$$

we can rewrite Eqs. (1.1.7) and (1.1.8), as follows:

$$\left(\nabla^2 - \frac{n^2}{c^2}\frac{\partial^2}{\partial t^2}\right)\mathbf{E}(\mathbf{r}, t) = \mathbf{0} \tag{1.1.11a}$$

$$\left(\nabla^2 - \frac{n^2}{c^2}\frac{\partial^2}{\partial t^2}\right)\mathbf{H}(\mathbf{r}, t) = \mathbf{0} \tag{1.1.11b}$$

Given the above equations, one concludes that in a dielectric medium, which is linear, isotropic, homogenous, nondispersive, and nonmagnetic, all components of the electric field $\mathbf{E}$ and the magnetic field $\mathbf{H}$ can be decoupled from one another and obey an identical scalar wave equation:

$$\left(\nabla^2 - \frac{n^2}{c^2}\frac{\partial^2}{\partial t^2}\right)\Psi(\mathbf{r}, t) = 0 \tag{1.1.12}$$

where $\Psi(\mathbf{r}, t)$ represents any of the scalar field components being a function of both position and time. This changes in the case of propagation through the medium with

inhomogeneous position-dependent permittivity $\epsilon(\mathbf{r})$. It gives rise to a new refractive-index-dependent term in the wave equation that introduces coupling between various components of the electric field **E**. Similarly, boundary conditions imposed on a wave propagating in a homogenous medium cause coupling between both the electric and the magnetic fields and between their scalar components. Yet, the error resulting from application of the scalar theory here will be negligible, provided that the boundary conditions affect a small part of the area, which a wave is passing. More specifically, as far as diffraction of light by an aperture is concerned, the modification of **E** and **H** fields takes place only at the aperture edges, where the light interacts with the material which the edges consist of. The effect extends further only a few wavelengths into the aperture itself. Therefore, the coupling effects of the boundary conditions of the **E** and **H** fields will be small, provided that the aperture area is considerably larger than the wavelength.

1.1.2 Helmholtz equation

Let us represent a particular wave field by the complex scalar function $\Psi(\mathbf{r}, t)$. Using the Fourier integral, this wave field function may be expressed as a superposition of monochromatic fields, as follows:

$$\Psi(\mathbf{r}, t) = \frac{1}{\sqrt{2\pi}} \int_0^\infty \psi(\mathbf{r}, \omega) \mathrm{e}^{-\mathrm{i}\omega t} \mathrm{d}\omega \tag{1.1.13}$$

Each monochromatic component $\psi(\mathbf{r}, \omega)\mathrm{e}^{-\mathrm{i}\omega t}$ in this decomposition is expressed by a multiplication of a stationary monochromatic wave field function $\psi(\mathbf{r}, \omega)$ and the complex time-dependent factor $\mathrm{e}^{-\mathrm{i}\omega t}$. Subsequently, a time-independent differential equation is sought that describes evolution of the spatial wave field function $\psi(\mathbf{r}, \omega)$, being associated with a particular monochromatic component of the spectral decomposition in Eq. (1.1.13). It is obtained by substituting the spectral wave field representation in Eq. (1.1.13) into the d'Alambert wave equation (1.1.12) which results in:

$$\frac{1}{\sqrt{2\pi}} \int_0^\infty \left[\left(\nabla^2 + \omega^2 \frac{n^2}{c^2} \right) \psi(\mathbf{r}, \omega) \right] \mathrm{d}\omega = 0 \tag{1.1.14}$$

The expression inside the square brackets must then vanish, yielding the time-independent equation, that governs the spatial component $\psi(\mathbf{r}, \omega)$ of a monochromatic wave field:

$$\left(\nabla^2 + n^2 k^2 \right) \psi(\mathbf{r}, \omega) = 0 \tag{1.1.15}$$

where k is termed the wave number and is given by:

$$k = \frac{\omega}{c} = 2\pi \frac{\nu}{c} = \frac{2\pi}{\lambda} \tag{1.1.16}$$

Eq. (1.1.15) is referred to as the Helmholtz equation and is a central equation in the scalar diffraction theory. The scalar diffraction aims at constructing solutions to the Helmholtz equation, given the boundary values and the boundary conditions for the wave field $\psi(\mathbf{r}, \omega)$. Only in special situations the Helmholtz equation can be solved exactly. In other cases numerical methods or series expansions are required.

1.1.3 Free-space propagation

One of the boundary-value problems for the Helmholtz equation (1.1.15) is the free-space diffraction. The problem assumes a division of the three dimensional space into the lower

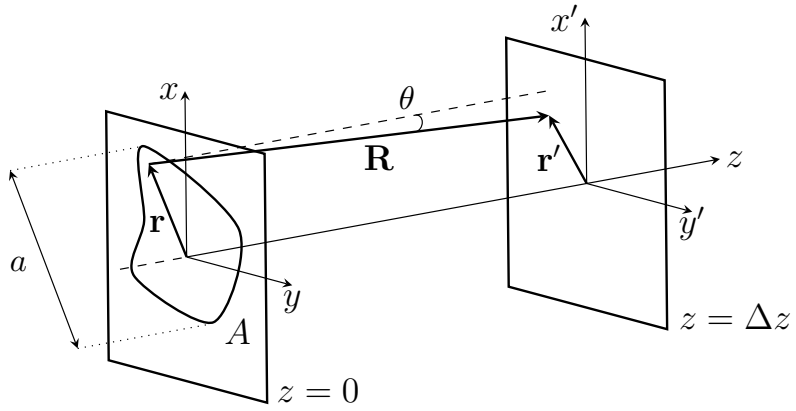

Fig. 1.1.1: Free-space diffraction of a monochromatic wave field on an aperture A and spatial evolution of the field between two planes.

and the upper halves along the z direction. All the radiation sources are to be located in the lower half space $z < 0$ and the stationary monochromatic wave field $\psi_0(\mathbf{r}, \omega)$ is known in the plane $z = 0$. The upper half space $z > 0$ is considered to be in turn free of any matter and wave field sources. One seeks therefore the solution for the wave field $\psi_z(\mathbf{r}', \omega)$ anywhere in the upper half space. The most practical approach to this problem is to consider solutions on planes $z = \Delta z > 0$. Any wave field on such plane is a propagated version of the boundary field $\psi_0(\mathbf{r}, \omega)$. The propagation direction is therefore chosen along the z direction and defines the optical axis.

A general solution to the free-space diffraction is based on the Helmholtz-Kirchhoff or the Rayleigh-Sommerfeld diffraction integrals [16]. They provide the solution of the homogenous wave equation at an arbitrary point in the upper half space in terms of values of the wave field and, for the Helmholtz-Kirchhoff integral, its first derivative on an arbitrary closed smooth surface surrounding that point. It allows to derive diffraction formulae, that relate the wave field at $z > 0$ with the field at $z = 0$.

In this section, we will consider free-space propagation of the wave field diffracted on an opaque aperture using two approaches: the Fresnel-Kirchhoff integral and the angular spectrum method.

1.1.3.1 Fresnel-Kirchhoff integral approach

Let us consider diffraction of a monochromatic wave field of a wavelength λ on an aperture A in an infinite opaque screen, as shown in Fig. 1.1.1. The wave field $\psi_0(\mathbf{r}, \omega)$ impinges on the screen at $z = 0$ from the left and solution for the propagated wave field $\psi_{\Delta z}(\mathbf{r}', \omega)$ is sought in the plane $z = \Delta z$. A general solution provided by the Helmholtz-Kirchhoff formalism can be approximated by an assumption that the observation plane is many optical wavelengths away from the aperture. Then the propagation of the wave field between the two planes can be described by the Fresnel-Kirchhoff diffraction formula, as follows:

$$\psi_{\Delta z}(\mathbf{r}', \omega) = \frac{1}{\mathrm{i}\lambda} \iint_A \psi_0(\mathbf{r}, \omega) \frac{\mathrm{e}^{\mathrm{i}\mathbf{k}\cdot\mathbf{R}}}{R} \cos(\theta) \mathrm{d}^2\mathbf{r} \tag{1.1.17}$$

where $R = \sqrt{\Delta z^2 + |\mathbf{r}' - \mathbf{r}|^2}$ is the distance between a point in the aperture and an observation point, and θ is an angle between the distance vector $\mathbf{R}$ and the z-direction unit vector $\hat{\mathbf{e}}_\mathbf{z}$. Substituting the cosine term with its exact form $\cos\theta = \Delta z/R$, the

diffraction integral can be further rewritten:

$$\psi_{\Delta z}(\mathbf{r}', \omega) = \frac{\Delta z}{\mathrm{i}\lambda} \iint\limits_{A} \psi_0(\mathbf{r}, \omega) \frac{\mathrm{e}^{\mathrm{i}\mathbf{k}\cdot\mathbf{R}}}{R^2} \mathrm{d}^2\mathbf{r} \tag{1.1.18}$$

The above formula holds for all propagation problems that fulfil the approximations of the scalar diffraction theory with an additional condition of the observation distance being much greater than the wave field wavelength, $R \gg \lambda$. Additional assumptions can be applied to the observation distance R, which further simplify the diffraction integral to operator-like expressions valid for certain propagation regimes.

Fresnel approximation

Let us assume that the propagation distance Δz is much greater than the maximal linear extent a of the aperture and that the observation plane is limited to a finite area in the proximity of the optical axis. It is therefore valid to say that $\dfrac{|\mathbf{r}' - \mathbf{r}|}{\Delta z} < 1$. Given this, the expression for the observation distance R can be rewritten as:

$$R = \Delta z \sqrt{1 + \left(\frac{|\mathbf{r}' - \mathbf{r}|}{\Delta z} \right)^2} \tag{1.1.19}$$

and further expanded around $\eta \equiv \dfrac{|\mathbf{r}' - \mathbf{r}|}{\Delta z} = 0$ in its Taylor series:

$$\sqrt{1 + \eta^2} = 1 + \frac{1}{2}\eta^2 - \frac{1}{8}\eta^4 + \dots \tag{1.1.20}$$

Retaining only the first two terms of the expansion, we obtain:

$$R \approx \Delta z \left[1 + \frac{1}{2} \left(\frac{|\mathbf{r}' - \mathbf{r}|}{\Delta z} \right)^2 \right] \tag{1.1.21}$$

which is referred to as the Fresnel approximation. All propagation cases, for which all aforementioned assumptions are fulfilled, are said to be in the Fresnel or near-field regime of diffraction. Applying the Fresnel approximation to the diffraction formula in Eq. (1.1.18), we apply only its first term to the R^2 in the denominator, for dropping the quadratic term does not introduce significant errors. Doing so in the case of $\mathrm{e}^{\mathrm{i}\mathbf{k}\cdot\mathbf{R}}$ would make all errors be multiplied by a very large wave number k, causing the value of the exponent change considerably. For this reason, in this case both terms of the Fresnel approximation must be retained. Thus, the resulting expression for the propagated field reads:

$$\psi_{\Delta z}(\mathbf{r}', \omega) = \frac{\mathrm{e}^{\mathrm{i}k\Delta z}}{\mathrm{i}\lambda\Delta z} \iint \psi_0(\mathbf{r}, \omega) \mathrm{e}^{\frac{\mathrm{i}k}{2\Delta z}(\mathbf{r}' - \mathbf{r})^2} \mathrm{d}^2\mathbf{r} \tag{1.1.22}$$

which can further be expressed in a form of the convolution[1.1] between the initial wave field $\psi_0(\mathbf{r}, \omega)$ and the Fresnel operator $\mathcal{N}$, as follows:

$$\psi_{\Delta z}(\mathbf{r}', \omega) = \psi_0(\mathbf{r}, \omega) \otimes \mathcal{N}_{\Delta z}(\mathbf{r}) \tag{1.1.23}$$

[1.1] The convolution of f and g is denoted by a symbol $\otimes$ and defined as: $(f \otimes g)(r') = \int f(r) g(r' - r) \mathrm{d}r$.

where the Fresnel operator $\mathcal{N}$ is given by:

$$\mathcal{N}_{\Delta z}(\mathbf{r}) = \frac{\mathrm{e}^{\mathrm{i}k\Delta z}}{\mathrm{i}\lambda\Delta z}\mathrm{e}^{\frac{\mathrm{i}k}{2\Delta z}\mathbf{r}^2} \tag{1.1.24}$$

The accuracy of the Fresnel approximation is determined by errors introduced by dropping all higher terms than quadratic in the expansion in Eq. (1.1.20). If the maximum phase change caused by dropping the $\eta^4/8$ term is much less than 1 rad, the Fresnel approximation is considered to be accurate. The final condition then is given by:

$$\Delta z \gg \frac{\pi}{4\lambda}(\mathbf{r}' - \mathbf{r})^4_{\max} \tag{1.1.25}$$

The physical interpretation of the Fresnel approximation is a replacement of the spherical secondary wavelets of the Fresnel-Kirchhoff formula in Eq. (1.1.18) by the paraboloidal wave fronts.

Fraunhofer approximation

Calculations of the free-space wave field propagation can be greatly simplified by applying another even stronger approximation to the diffraction formula. To formulate it, let us consider the quadratic term in the exponent of the Fresnel integral in Eq. (1.1.22), that can be explicitly expanded, as follows:

$$\psi_{\Delta z}(\mathbf{r}', \omega) = \frac{\mathrm{e}^{\mathrm{i}k\Delta z}}{\mathrm{i}\lambda\Delta z}\iint \psi_0(\mathbf{r}, \omega)\mathrm{e}^{\frac{\mathrm{i}k}{2\Delta z}\mathbf{r}'^2}\mathrm{e}^{\frac{\mathrm{i}k}{\Delta z}\mathbf{r}'\mathbf{r}}\mathrm{e}^{\frac{\mathrm{i}k}{2\Delta z}\mathbf{r}^2}\mathrm{d}^2\mathbf{r} \tag{1.1.26}$$

The last factor $\mathrm{e}^{\frac{\mathrm{i}k}{2\Delta z}\mathbf{r}^2}$ can be approximated to unity, provided that:

$$\Delta z \gg \frac{k}{2}\mathbf{r}^2_{\max} \tag{1.1.27}$$

This assumption is called the Fraunhofer approximation and is justified for a finite aperture size and much larger propagation distances. The diffraction integral then reads:

$$\psi_{\Delta z}(\mathbf{r}', \omega) = \frac{\mathrm{e}^{\mathrm{i}k\Delta z}}{\mathrm{i}\lambda\Delta z}\mathrm{e}^{\frac{\mathrm{i}k}{2\Delta z}\mathbf{r}'^2}\iint \psi_0(\mathbf{r}, \omega)\mathrm{e}^{\frac{\mathrm{i}k}{\Delta z}\mathbf{r}'\mathbf{r}}\mathrm{d}^2\mathbf{r} \tag{1.1.28}$$

Redefining the coordinates to $\mathbf{q}' = \dfrac{k}{\Delta z}\mathbf{r}'$, one obtains:

$$\psi_{\Delta z}(\mathbf{q}', \omega) = \frac{\mathrm{e}^{\mathrm{i}k\Delta z}}{\mathrm{i}\lambda\Delta z}\mathrm{e}^{\frac{\mathrm{i}k}{2\Delta z}\mathbf{r}'^2}\iint \psi_0(\mathbf{r}, \omega)\mathrm{e}^{\mathrm{i}\mathbf{q}'\mathbf{r}}\mathrm{d}^2\mathbf{r} \tag{1.1.29}$$

which can finally be expressed as a product of the Fraunhofer operator $\mathcal{P}$ and the Fourier transform $\mathcal{F}$ of the initial wave field $\psi_0(\mathbf{r}, \omega)$, as follows:

$$\psi_{\Delta z}(\mathbf{q}', \omega) = \mathcal{P}_{\Delta z}\left(\frac{\Delta z}{k}\mathbf{q}'\right)\mathcal{F}[\psi_0(\mathbf{r}, \omega)](\mathbf{q}') \tag{1.1.30}$$

where the Fraunhofer operator is given by:

$$\mathcal{P}_{\Delta z}(\mathbf{r}') = \frac{\mathrm{e}^{\mathrm{i}k\Delta z}}{\mathrm{i}\lambda\Delta z}\mathrm{e}^{\frac{\mathrm{i}k}{2\Delta z}\mathbf{r}'^2} \tag{1.1.31}$$

Unlike in the Fresnel approximation, the Fraunhofer diffraction formula loses its convolutional form, meaning that the secondary wavelets with parabolic surfaces do not shift

laterally in the observation plane, given the particular point in the aperture plane. Upon the Fourier shift theorem, any lateral translation of the initial wave field translates in the linear phase ramp (a tilt of the quadratic surface) of the wave field in the observation plane. The region where the assumptions for the Fraunhofer approximations apply is said to be in the Fraunhofer or far-field regime of propagation.

A useful dimensionless quantity that permits to identify the regime of a given diffraction problem is called the Fresnel number N_F and defined as:

$$N_F = \frac{a^2}{\lambda \Delta z} \tag{1.1.32}$$

where a is the maximal linear extent of the aperture. As it can also be seen from the condition in Eq. (1.1.27), the Fresnel number in the far-field regime must reach values much less than one, unlike in the near-field where it approaches unity.

1.1.3.2 Angular spectrum approach

An alternative method exists to describe the free-space propagation of a monochromatic and coherent wave field. It derives from a general solution to the Helmholtz equation by considering a Fourier spectral decomposition of the propagated wave field. If Fourier formalism is used to analyse the distribution of such a disturbance across any plane, the plane waves travelling in different directions from that plane can be identified as various spatial Fourier components. The complex wave field amplitude across any other parallel plane can then be found by summing the contributions of these plane waves accounting for the phase shifts caused by respective propagation. Therefore, the wave field at an arbitrary plane $z > 0$ can be expressed as a two-dimensional Fourier integral, as follows:

$$\psi_z(\mathbf{r}, \omega) = \frac{1}{2\pi} \iint_{-\infty}^{+\infty} \tilde{\psi}_z(k_x, k_y, \omega) \mathrm{e}^{\mathrm{i}(k_x x + k_y y)} \, \mathrm{d}k_x \mathrm{d}k_y \tag{1.1.33}$$

where $\tilde{\psi}_z(k_x, k_y, \omega)$ is the Fourier transform of $\psi_z(\mathbf{r}, \omega)$ with respect to $\mathbf{r} = (x, y)$, and k_x, k_y are the Fourier-space spatial frequencies, conjugate to the position coordinates x, y. The function $\tilde{\psi}_z(k_x, k_y, \omega)$ is explicitly given by:

$$\tilde{\psi}_z(k_x, k_y, \omega) = \frac{1}{2\pi} \iint_{-\infty}^{+\infty} \psi_z(\mathbf{r}, \omega) \mathrm{e}^{-\mathrm{i}(k_x x + k_y y)} \, \mathrm{d}x \mathrm{d}y \tag{1.1.34}$$

and is referred to as the angular spectrum of the disturbance $\psi_z(\mathbf{r}, \omega)$ [17].

Given such representation, let us consider again the free-space propagation between two planes $z = 0$ and $z = \Delta z$, as shown in Fig. 1.1.1. The wave field $\psi_z(\mathbf{r}, \omega)$ must satisfy the Helmholtz equation. Direct substitution to Eq. (1.1.15) yields the following differential equation:

$$\left[\frac{\partial^2}{\partial z^2} + (k^2 - k_x^2 - k_y^2) \right] \tilde{\psi}_z(k_x, k_y, \omega) \Big|_{z=\Delta z} = 0 \tag{1.1.35}$$

that has the solution which takes into account the boundary condition at the plane $z = 0$:

$$\tilde{\psi}_z(k_x, k_y, \omega) \Big|_{z=\Delta z} = \tilde{\psi}_0(k_x, k_y, \omega) \mathrm{e}^{\mathrm{i}\Delta z \sqrt{k^2 - k_x^2 - k_y^2}} \tag{1.1.36}$$

The obtained solution for $\tilde{\psi}_z(k_x, k_y, \omega)\Big|_{z=\Delta z}$ can be inserted into Eq. (1.1.33), which yields the final formula:

$$\psi_{\Delta z}(\mathbf{r}, \omega) = \frac{1}{2\pi} \iint_{-\infty}^{+\infty} \tilde{\psi}_0(k_x, k_y, \omega) \mathrm{e}^{\mathrm{i}\Delta z\sqrt{k^2-k_x^2-k_y^2}} \mathrm{e}^{\mathrm{i}(k_x x + k_y y)} \, \mathrm{d}k_x \mathrm{d}k_y \tag{1.1.37}$$

The above equation is known as the angular spectrum representation of the propagated wave field. It describes the spatial evolution of the wave field propagating in free space over a distance $\Delta z \geq 0$, in terms of the initial boundary value $\psi_0(\mathbf{r}, \omega)$. Moreover, the angular spectrum method allows to express the process of free-space diffraction in an operator form, formally written as:

$$\psi_{\Delta z}(\mathbf{r}, \omega) = \mathcal{AS}_{\Delta z} \left[\psi_0(\mathbf{r}, \omega)\right] \tag{1.1.38}$$

where $\mathcal{AS}_{\Delta z}$ denotes the angular-spectrum diffraction operator that acts on the initial wave field and is a function of the propagation distance Δz. Eq. (1.1.37) lets isolate the operations acting on the unpropagated wave field, yielding the operator formula given by:

$$\mathcal{AS}_{\Delta z} = \mathcal{F}^{-1} \mathrm{e}^{\mathrm{i}\Delta z\sqrt{k^2-k_x^2-k_y^2}} \mathcal{F} \tag{1.1.39}$$

As a result, the free-space propagation operator applies on the initial wave field a two-dimensional spatial filter with the following transfer function:

$$T(k_x, k_y) = \mathrm{e}^{\mathrm{i}\Delta z k_z} \tag{1.1.40}$$

where $k_z = \sqrt{k^2 - k_x^2 - k_y^2}$, provided that $k_z \geq 0$, because only forward-propagating wave fields with respect to the optical axis are considered. In the case when $k^2 \geq k_x^2 + k_y^2$, k_z is real and the wave field is a propagating one. Yet, there exists a possibility for $k^2 \leq k_x^2 + k_y^2$ which implies that k_z may be a purely imaginary complex number. In such a case, the wave field is exponentially dumped in the optical axis direction and referred to as an evanescent wave.

The form of the angular-spectrum diffraction operator (1.1.39) allows for a straightforward numerical implementation exploiting efficient numerical routines for calculating Fourier transforms.

Fresnel approximation

Application of the angular-spectrum method to the plane-to-plane free-space propagation of a coherent scalar wave field yields rigorous solution to a given boundary-value problem of the Helmholtz equation. An often used approximation of this formalism considers the free-space propagating wave field to be paraxial. It means that an angle between all non-negligible field components and the optical axis is small, and hence is also referred to as the small-angle approximation. Here, we will also see how in this particular case the angular spectrum method converges with the Fresnel diffraction theory introduced in section 1.1.3.1.

Let us consider therefore once again the diffraction geometry, as shown in Fig. 1.1.1. Since the wave field is paraxial, the wave vector component k_z will be significantly greater than the two remaining k_x and k_y. Therefore, we can expand the exponent of the transfer function in Eq. (1.1.40) using binomial approximation, as follows:

$$\Delta z\sqrt{k^2 - k_x^2 - k_y^2} \approx \Delta z \left[k - \frac{k_x^2 + k_y^2}{2k}\right] \tag{1.1.41}$$

provided that $\frac{k_x^2+k_y^2}{k^2} < 1$. Inserting into the angular-spectrum diffraction operator in Eq. (1.1.39), we obtain the diffraction operator associated to Fresnel diffraction:

$$\mathcal{AS}_{\Delta z} \approx \mathrm{e}^{\mathrm{i}k\Delta z}\mathcal{F}^{-1}\mathrm{e}^{-\mathrm{i}\Delta z\frac{k_x^2+k_y^2}{2k}}\mathcal{F} \tag{1.1.42}$$

Substituting the newly-obtained approximated operator into the propagation formula in Eq. (1.1.38), an operator form of the Fresnel diffraction integral can be derived:

$$\psi_{\Delta z}(\mathbf{r},\omega) = \mathrm{e}^{\mathrm{i}k\Delta z}\mathcal{F}^{-1}\left[\mathrm{e}^{-\mathrm{i}\Delta z\frac{k_x^2+k_y^2}{2k}}\mathcal{F}\left[\psi_0(\mathbf{r},\omega)\right]\right] \tag{1.1.43}$$

Utilising the convolution theorem, that relates a convolution of two functions with the multiplication of their Fourier transforms in the following form:

$$f(\mathbf{r}) \otimes g(\mathbf{r}) = 2\pi\mathcal{F}^{-1}\left\{\mathcal{F}[f(\mathbf{r})] \times \mathcal{F}[g(\mathbf{r})]\right\} \tag{1.1.44}$$

the operator-form Fresnel diffraction integral in Eq. (1.1.43) can be rewritten, as follows:

$$\begin{aligned}\psi_{\Delta z}(\mathbf{r},\omega) &= \mathcal{F}^{-1}\left\{\mathrm{e}^{\mathrm{i}k\Delta z}\mathrm{e}^{-\mathrm{i}\Delta z\frac{k_x^2+k_y^2}{2k}}\mathcal{F}\left[\psi_0(\mathbf{r},\omega)\right]\right\} \\ &= 2\pi\mathcal{F}^{-1}\left\{\mathcal{F}\left[\mathcal{F}^{-1}\left[\frac{\mathrm{e}^{\mathrm{i}k\Delta z}}{2\pi}\mathrm{e}^{-\mathrm{i}\Delta z\frac{k_x^2+k_y^2}{2k}}\right]\right] \times \mathcal{F}\left[\psi_0(\mathbf{r},\omega)\right]\right\}\end{aligned} \tag{1.1.45}$$

It can be shown, that $\mathcal{F}\left[\mathcal{F}^{-1}\left[\frac{\mathrm{e}^{\mathrm{i}k\Delta z}}{2\pi}\mathrm{e}^{-\mathrm{i}\Delta z\frac{k_x^2+k_y^2}{2k}}\right]\right]$ is equivalent to the near-field propagator $\mathcal{N}_{\Delta z}(\mathbf{r})$ introduced in section 1.1.3.1. Therefore, the expression in Eq. (1.1.45) can further be generalised as a convolution of the unpropagated wave field $\psi_0(\mathbf{r},\omega)$ and the Fresnel operator $\mathcal{N}_{\Delta z}(\mathbf{r})$:

$$\psi_{\Delta z}(\mathbf{r},\omega) = \psi_0(\mathbf{r},\omega) \otimes \mathcal{N}_{\Delta z}(\mathbf{r}) \tag{1.1.46}$$

At this point, the angular spectrum method merges with the analysis presented using the Fresnel-Kirchhoff integral in section 1.1.3.1. Also there, further approximations concerning derivation of the Fraunhofer diffraction integral are discussed.

1.1.4 Coherence

The wave-field propagation formalism presented so far was based on the assumption of fully coherent scalar electromagnetic waves. In general, the term coherence refers to the correlation between physical quantities of a single wave or between several wave fields. More specifically, coherence is an ideal wave property enabling temporally and spatially invariant (i.e. stationary) interference. Interference, understood as an addition of the input wave fields, depends on their relative phase offset and can be constructive, resulting in a signal of a greater amplitude than either of the added components, or destructive in the opposite case. The degree of coherence can be measured by the interference visibility that quantifies the contrast of the interference fringes with respect to the relative phase offset between the interfering wave fields. A degree of correlation between the wave fields at different points in space is referred to as spatial coherence. It can be measured with Young's double slit experiment [18], in which an increase of the slits separation results in a diminishing contrast of the interference fringes. Alternatively, the correlation between the wave fields can be measured at the different moments in time, which is referred to as

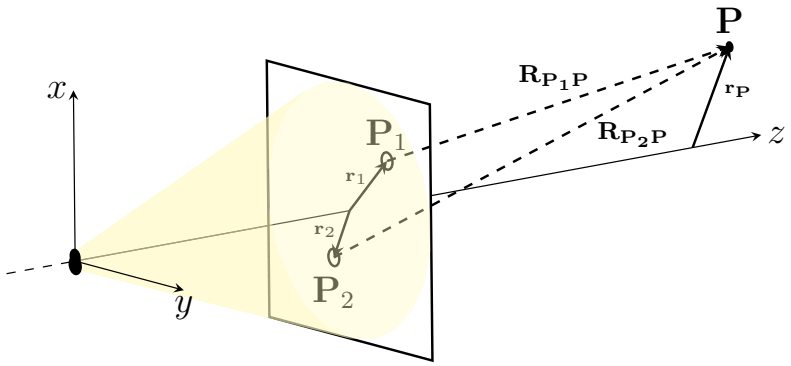

Fig. 1.1.2: Diffraction of statistically stationary quasi-monochromatic radiation on two pinholes P_1 and P_2 in the opaque planar screen. The resulting interference pattern is detected at the observation point P downstream of the screen.

temporal coherence. A representative experiment here uses the Michelson-Morley interferometer [18, 19] that splits the input wave field, introduces a time delay to one of the counterparts and makes them interfere. The fall-off of the interference fringes contrast corresponds to the temporal coherence of the incident wave field.

In reality, an X-ray field is an example of a stochastic process and is therefore denoted to be partially coherent. An important class of the partially coherent disturbances are the so-called quasi-monochromatic wave fields. They are characterised by a very narrow finite spectral range making their behaviour, in general, quite different from that of the monochromatic radiation. In this section we will introduce excerpts of the more general theory of partially coherent fields that allows to represent the degree of wave field coherence in terms of its mutual coherence function. We will further use this formalism to represent a partially coherent wavefront as a superposition of coherent modes. The presented considerations are based on the respective literature [17, 18].

Let us consider diffraction from two pinholes in a planar opaque screen, as shown in Fig. 1.1.2. The screen is illuminated by a source of statistically stationary quasi-monochromatic radiation of a mean wavelength $\tilde{\lambda}$. Two small pinholes P_1 and P_2 are located at the position vectors $\mathbf{r}_1$ and $\mathbf{r}_2$ on the screen. The resulting two exit wave fields propagate in the vacuum-filled half space downstream of the screen and interfere with each other. The corresponding interference pattern is probed at the point P located at the position vector $\mathbf{r}_P$. Let us further name the quasi-monochromatic wave field $\Psi(\mathbf{r}, t)$ impinging on the screen. It can be expressed as a superposition of monochromatic fields $\psi_z(\mathbf{r}, \omega)\mathrm{e}^{-\mathrm{i}\omega t}$ by means of Fourier decomposition. Provided that all non-zero components have an angular frequency ω confined to the interval $\tilde{\omega} - \frac{1}{2}\Delta\omega \leq \omega \leq \tilde{\omega} + \frac{1}{2}\Delta\omega$, we can describe the complex quasi-monochromatic wave field using the Fourier integral, as follows:

$$\Psi(\mathbf{r}, t) = \frac{1}{\sqrt{2\pi}} \int_{\tilde{\omega}-\frac{1}{2}\Delta\omega}^{\tilde{\omega}+\frac{1}{2}\Delta\omega} \psi_z(\mathbf{r}, \omega)\mathrm{e}^{-\mathrm{i}\omega t}\, \mathrm{d}\omega \tag{1.1.47}$$

If we choose $\delta\omega$ to denote the difference between the angular frequency of a given monochromatic component and the mean angular frequency $\tilde{\omega}$, i.e. $\omega = \tilde{\omega} + \delta\omega$, we can rewrite the

above integral to the following form:

$$\Psi(\mathbf{r},t) = \mathrm{e}^{-\mathrm{i}\tilde{\omega}t} \underbrace{\int_{-\frac{1}{2}\Delta\omega}^{\frac{1}{2}\Delta\omega} \frac{1}{\sqrt{2\pi}} \psi_z(\mathbf{r},\tilde{\omega}+\delta\omega)\mathrm{e}^{-\mathrm{i}\,\delta\omega\,t}\,\mathrm{d}\delta\omega}_{A(\mathbf{r},t)} \tag{1.1.48}$$

The complex wave field $\Psi(\mathbf{r},t)$ is therefore a multiplication of the harmonic time factor $\mathrm{e}^{-\mathrm{i}\tilde{\omega}t}$ and a slowly varying complex envelope $A(\mathbf{r},t)$, as $\delta\omega \ll \tilde{\omega}$. Hence, the exit fields diffracted by the two pinholes are expected to slowly vary in both relative phase and time. As a result, the resulting interference pattern will also be time-dependent, with its time average being given by the intensity distribution measured at the observation point P. The complex wave field at this point is a superposition of the two wave fields emerging from each of the pinholes:

$$\Psi(\mathbf{r},t) = \kappa_1 \underbrace{\Psi\left(\mathbf{r}_1, t - \frac{R_{P_1P}}{c}\right)}_{\Psi_1} + \kappa_2 \underbrace{\Psi\left(\mathbf{r}_2, t - \frac{R_{P_2P}}{c}\right)}_{\Psi_2} \tag{1.1.49}$$

where $\Psi_i(\mathbf{r}_i,t) = A(\mathbf{r}_i,t_i)\mathrm{e}^{-\mathrm{i}\tilde{\omega}t}$, for $i = 1,2$, correspond to the time-dependent complex wave fields at the exit plane of both pinholes. The time retardations stem in turn from the finite speed of light c. Furthermore, κ_1, κ_2 are purely imaginary complex coefficients depending on the propagation geometry and the pinholes' dimensions.

The time-averaged intensity at the observation point P is expressed by the following formula:

$$\begin{aligned}\langle I(\mathbf{r}_P)\rangle &= \langle|\Psi(\mathbf{r}_P,t)|^2\rangle \\ &= \langle|\kappa_1\Psi_1|^2\rangle + \langle|\kappa_2\Psi_2|^2\rangle + 2|\kappa_1\kappa_2^*|\,\Re\left\{\langle\Psi_1\Psi_2^*\rangle\right\}\end{aligned} \tag{1.1.50}$$

where $|\kappa_1\kappa_2^*| \in \mathbb{R}$ and $|\kappa_1\kappa_2^*| > 0$, while time averaging is denoted by angular brackets. As previously assumed, the incident wave field is statistically stationary, which means that its statistical properties do not depend on the origin of time. Therefore, the time averages in the above formula remain invariant under the following time transformation $t \to t + \dfrac{R_{P_2P}}{c}$, so that the last additive time-averaged component in Eq. (1.1.50) reads:

$$\langle\Psi_1\Psi_2^*\rangle = \left\langle \Psi\left(\mathbf{r}_1, t + \underbrace{\frac{R_{P_2P} - R_{P_1P}}{c}}_{\tau}\right)\Psi\left(\mathbf{r}_2,t\right)\right\rangle \tag{1.1.51}$$

Defining the time τ as the difference between the propagation times of light from the two pinholes to the observation point, we can further simplify Eq. (1.1.50):

$$\langle I(\mathbf{r}_P)\rangle = \langle I_1(\mathbf{r}_1)\rangle + \langle I_2(\mathbf{r}_2)\rangle + 2|\kappa_1\kappa_2^*|\,\Re\left\{\Gamma(\mathbf{r}_1,\mathbf{r}_2,\tau)\right\} \tag{1.1.52}$$

whose last additive term stands for the interference between the two wave fields, where:

$$\Gamma(\mathbf{r}_1,\mathbf{r}_2,\tau) = \langle\Psi(\mathbf{r}_1,t+\tau)\Psi^*(\mathbf{r}_2,t)\rangle \tag{1.1.53}$$

is the mutual coherence function of the wave field at the locations of the two pinholes. It provides a measure of the correlation between the exit wave fields of each of the two pinholes. Lack of correlation between them results in no interference fringes visible at

the observation point P. Their occurrence is conditioned by some degree of correlation between the radiation exiting both pinholes. The normalised mutual coherence function defines a complex degree of coherence, as follows:

$$\gamma(\mathbf{r}_1, \mathbf{r}_2, \tau) = \frac{\Gamma(\mathbf{r}_1, \mathbf{r}_2, \tau)}{\sqrt{\Gamma(\mathbf{r}_1, \mathbf{r}_1, 0)\Gamma(\mathbf{r}_2, \mathbf{r}_2, 0)}} \tag{1.1.54}$$

where $|\gamma| \leq 1$. Perfect correlation between the exit wave fields at the pinholes yields $|\gamma| = 1$ and a maximal visibility of the interference fringes, denoting perfect coherence. Zero correlation results in turn in $|\gamma| = 0$ and no interference pattern is measured in the detection plane, indicating incoherence of the incoming wave field.

Until now we have mainly considered the coherence properties in the space-time domain. In fact, the mutual coherence function can be transformed into the space-frequency domain that provides a convenient framework to represent a partially coherent wave field with a set of coherent modes. With this in mind, let us again consider a stationary wave field $\Psi(\mathbf{r}, t)$ incident on the opaque screen containing two pinholes, as in Fig. 1.1.2. Let us further specify a finite closed domain D in free space enclosing the two pinholes, such that $\mathbf{r}_1 \in D$ and $\mathbf{r}_2 \in D$. The mutual coherence function of the wave field has the following Fourier frequency transform:

$$W(\mathbf{r}_1, \mathbf{r}_2, \omega) = \frac{1}{2\pi} \int_{-\infty}^{+\infty} \Gamma(\mathbf{r}_1, \mathbf{r}_2, \tau) \mathrm{e}^{\mathrm{i}\omega\tau} \, \mathrm{d}\tau \tag{1.1.55}$$

referred to as the cross-spectral density function, being continuous in the angular frequency domain. It can be shown [17] that W obeys the following two Helmholtz equations:

$$(\nabla_i^2 + k^2) W(\mathbf{r}_1, \mathbf{r}_2, \omega) = 0 \tag{1.1.56}$$

for $i = 1, 2$ denoting the Laplacian operator ∇^2 acting with respect to the position vectors $\mathbf{r}_1$ and $\mathbf{r}_2$, respectively, and for $k = \omega/c$ being the wave number. In the space-frequency formulation of the coherence theory, the cross-spectral density is introduced as a generally infinite and convergent series in the following form:

$$W(\mathbf{r}_1, \mathbf{r}_2, \omega) = \sum_n \alpha_n(\omega) \phi_n^*(\mathbf{r}_1, \omega) \phi_n(\mathbf{r}_2, \omega) \tag{1.1.57}$$

where the functions $\phi_n(\mathbf{r}, \omega)$ are the eigenfunctions and α_n are the corresponding eigenvalues of the integral equation:

$$\int_D W(\mathbf{r}_1, \mathbf{r}_2, \omega) \phi_n(\mathbf{r}_1, \omega) \, \mathrm{d}^3 r_1 = \alpha_n(\omega) \phi_n(\mathbf{r}_2, \omega) \tag{1.1.58}$$

whose eigenvalues are real and positive $\alpha_n(\omega) > 0$, while the eigenfunctions form an orthonormal basis, that is:

$$\int_D \phi_n^*(\mathbf{r}, \omega) \phi_m(\mathbf{r}, \omega) \, \mathrm{d}^3 r = \delta_{nm} \tag{1.1.59}$$

where δ_{nm} is the Kronecker symbol, being unity if $n = m$ and zero for all remaining cases. The series in Eq. (1.1.57) can be rewritten in the following form:

$$W(\mathbf{r}_1, \mathbf{r}_2, \omega) = \sum_n \alpha_n(\omega) W_n(\mathbf{r}_1, \mathbf{r}_2, \omega) \tag{1.1.60}$$

where $W_n(\mathbf{r}_1, \mathbf{r}_2, \omega) = \phi_n^*(\mathbf{r}_1, \omega)\phi_n(\mathbf{r}_2, \omega)$, which represents the cross-spectral density function of a field that is completely coherent in the space-frequency domain. Substituting such a representation into Eq. (1.1.56), we can show that every W_n satisfies the same two Helmholtz equations as the cross-spectral density W, as follows:

$$(\nabla_i^2 + k^2)W_n(\mathbf{r}_1, \mathbf{r}_2, \omega) = 0, \qquad i = 1, 2 \tag{1.1.61}$$

$W_n(\mathbf{r}_1, \mathbf{r}_2, \omega)$ may therefore be regarded as a mode of the wave field. The equation (1.1.60) constitutes the cross-spectral density of the field as a superposition of mutually orthonormal modes, that are fully coherent in the space-frequency domain. Therefore, the expansion in Eq. (1.1.57) is often called the coherent-mode representation of the cross-spectral density.

In the case when $\mathbf{r}_1 = \mathbf{r}_2 \equiv \mathbf{r}$, the cross-spectral density function simplifies to the spectral density of the wave field $S(\mathbf{r}, \omega) \equiv W(\mathbf{r}, \mathbf{r}, \omega)$. Substituting into Eq. (1.1.60) yields an analogous series:

$$S(\mathbf{r}, \omega) = \sum_n \alpha_n(\omega) S_n(\mathbf{r}, \omega) \tag{1.1.62}$$

where $S_n(\mathbf{r}, \omega) = |\phi_n(\mathbf{r}, \omega)|^2$, which combined with the orthonormality of the basis $\{\phi_i\}$ ensures, that

$$\int_D S_n(\mathbf{r}, \omega)\ \mathrm{d}^3 r = 1 \tag{1.1.63}$$

Using this property while integrating Eq. (1.1.62) throughout the domain D, we obtain the following:

$$\int_D S(\mathbf{r}, \omega)\ \mathrm{d}^3 r = \sum_n \alpha_n(\omega) \tag{1.1.64}$$

The equation (1.1.62) provides the n-th mode contribution to the spectral density, given by $\alpha_n(\omega)|\phi_n(\mathbf{r}, \omega)|^2$. Furthermore, the formula in Eq. (1.1.64) shows that the contribution of this mode to the spectral density integral within the domain D, measuring the total energy in D, is exactly $\alpha_n(\omega)$.

In conclusion, there exists a formalism that allows to express a partially coherent quasi-monochromatic wave field as a weighted superposition of the mutually orthogonal, coherent modes in the space-frequency domain. In this thesis, it provides the theoretical context to experimental and algorithmic approaches allowing for relaxation of the coherence conditions in X-ray imaging techniques utilising primarily highly coherent radiation.

In its general form, the mutual coherence function $\Gamma(\mathbf{r}_1, \mathbf{r}_2, \tau)$ contains information about both the spatial and temporal coherence. In the case of $\tau = 0$, the mutual coherence function $\Gamma(\mathbf{r}_1, \mathbf{r}_2, 0)$ describes the spatial coherence properties of a given partially coherent wave field. It provides a measure of the time-averaged fringe visibility originating from the interference of the statistically stationary wave fields coming from two distinct points in space with no relative offset in time. Alike, when probing the wave field correlation at the same point $\mathbf{r}_1 = \mathbf{r}_2 \equiv \mathbf{r}$ in different moments in time, the mutual coherence function $\Gamma(\mathbf{r}, \mathbf{r}, \tau)$ represents the temporal coherence properties of the disturbance. Although the mutual coherence function cannot be cleanly decomposed to represent spatial and temporal coherence separately, below we introduce the concept of coherence lengths as measures of the degree of both coherence types.

1.1.4.1 Longitudinal coherence length

Let us consider a quasi-monochromatic wave field of a finite narrow bandwidth $\Delta\lambda$, at a wavelength $\lambda \gg \Delta\lambda$. Let us further select its components, two waves of slightly different

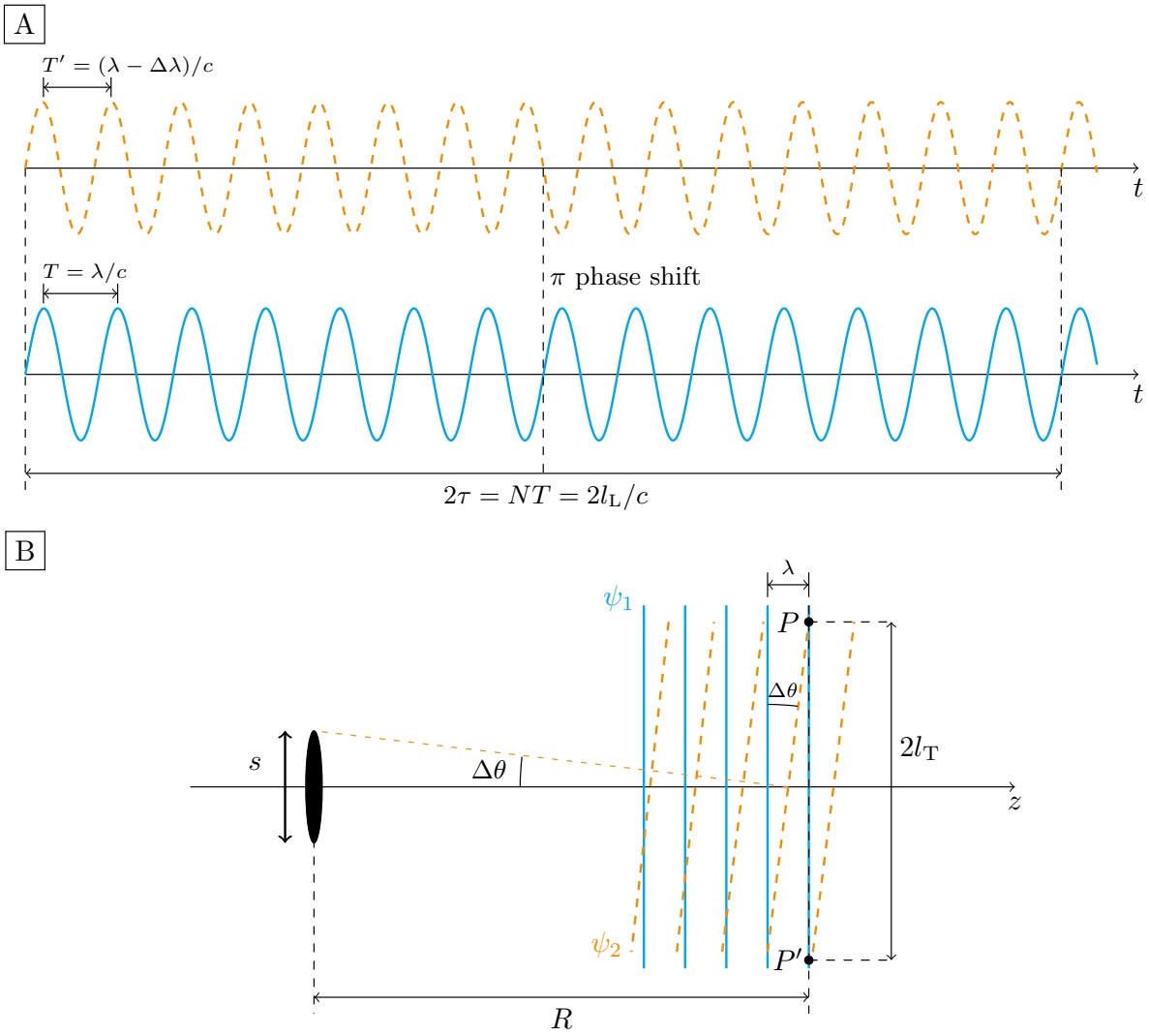

Fig. 1.1.3: The coherence lengths of a wave field. (A) shows time evolution of two waves of slightly different wavelengths at a given point in space. The coherence time τ is needed for the two waves to get out of phase. The corresponding spatial distance is obtained by comparing the numbers of oscillations of the two waves and is referred to as the longitudinal coherence length l_L. (B) shows two wave fields ψ_1 and ψ_2 emanating from two distinct points in the source of a lateral dimension s. At the observation plane at $z = R$, the respective wavefronts coincide being in phase at the points P and P' and out of phase in the middle. The half of the distance PP' denotes the transverse coherence length l_T.

wavelengths, propagating in the same direction, as shown in Fig. 1.1.3A, and consider their time evolution at a given point in space. The wavefronts are in phase at $t = 0$, yet, due to different wavelengths they will get out of phase after the time τ, to be back in phase at $t = 2\tau$. Let this total time be N periods $T = \lambda/c$ or alternatively:

$$2\tau = NT = (N + 1)(T + \Delta T) \tag{1.1.65}$$

It can be shown that $N = (T - \Delta T)/T$ which can be approximated to $N \approx T/\Delta T$, as $T \gg \Delta T$. As a consequence, the time τ necessary for the two waves to get out of phase reads:

$$\tau \approx \frac{1}{2}\frac{T^2}{\Delta T} \tag{1.1.66}$$

which is referred to as the coherence time. The corresponding distance in space is called the longitudinal coherence length l_{L}, defined as:

$$l_{\mathrm{L}} = c\tau \approx \frac{1}{2}\frac{\lambda^2}{\Delta\lambda} \tag{1.1.67}$$

The longitudinal coherence length provides therefore information about the degree of coherence along the propagation direction of the wave field. In general, the constant coefficient in Eq. (1.1.67) depends on the power spectral density of the radiation source [20] and equals to $\frac{1}{\pi}$ for a Lorentzian spectrum or $\frac{\sqrt{2\ln 2}}{\pi}$ for a Gaussian spectrum.

1.1.4.2 Transverse coherence length

Let us consider now another case shown in Fig. 1.1.3B, namely two wave fields ψ_1 and ψ_2 of the same wavelength λ propagating along slightly different directions separated by an angle $\Delta\theta$. The waves have emerged form two different points of the same source at the distance R upstream of the observation plane. The observation plane was chosen to be perpendicular to the wavefront of the wave ψ_1. The point P denotes where the wavefronts coincide. Further along the observation plane, the wavefronts will gradually get out of phase to eventually coincide again at the point P'. The half of that distance defines the transverse coherence length l_{T}. From the propagation geometry in Fig. 1.1.3B, we derive that $2l_{\mathrm{T}}\Delta\theta = \lambda$, which transforms to $l_{\mathrm{T}} = \frac{\lambda}{2\Delta\theta}$, provided that $\Delta\theta$ is small. Given a lateral size of the source of s, the angle between the two waves equals $\Delta\theta = \frac{s}{2R}$ and it yields:

$$l_{\mathrm{T}} = \frac{R\lambda}{s} \tag{1.1.68}$$

The presented derivation considers a one-dimensional case. Analogously, the transverse coherence length in the other lateral dimension can be found, accounting for a possible difference between the horizontal and the vertical sizes of the source. Multiplication of the both coherence lengths defines the so-called coherence area, that becomes larger with increasing propagation distance R.

1.2 Interaction of X-rays with matter

X-rays as any other radiation type interact with matter they encounter. This interaction is strong enough for the matter to alter the passing radiation and, in the same time, sufficiently weak to let the X-rays penetrate far enough to probe the whole sample's

volume. Additionally, their wavelength permits resolving the corresponding distances down to the atomic scale. These two unique characteristics make X-ray radiation a robust and powerful probe for various states of matter.

X-ray radiation wavelengths are on the order of 1 Å which correspond to the typical size of an atom. Therefore, X-rays intrinsically interact with the combined electric fields of the electron orbitals that shield the atomic nucleus. To interact with the nucleus of an atom, more energetic gamma rays, of even shorter wavelength, are necessary to penetrate deeper beyond the electron orbitals. In turn, the X-ray energy spectrum matches or exceeds the binding energies of the atomic core electrons (e.g. 13.6 eV for the electron in a hydrogen atom). Therefore, the probability for interaction between the inner-shell electrons is greater than with loosely-bound valence electrons. In general, an X-ray photon interacting with matter can be elastically or inelastically scattered, absorbed – triggering emission of electrons or lower-energy photons – or transmitted. The fundamental quantity that describes the efficiency of a given interaction event is the so-called differential cross-section. It is an energy- or angular-dependent function proportional to the interaction probability. It will be used to characterise the aforementioned interaction scenarios in this section.

1.2.1 Elastic scattering

An incoming X-ray wave field can interact with an electron in such a way that both the particle energy and the incident and the scattered wave frequencies remain unchanged. Such an interaction is termed elastic and can occur on a single and free electron, which is called Thomson scattering, and on a bound electron in an atom, referred to as the Rayleigh scattering. The differential cross-section $\frac{\mathrm{d}\sigma}{\mathrm{d}\Omega}$ of an elastic scattering is defined by the normalised experimental parameters, such as the flux of the incident beam and the number of scattered photons detected at a distance R away from the scatterer within a solid angle $\Delta\Omega$. The incoming and the scattered wave intensities can be expressed in terms of the moduli of their corresponding electric fields. It can therefore be shown [21], that the differential cross-section of a scattering event is given by:

$$\frac{\mathrm{d}\sigma}{\mathrm{d}\Omega} = R^2 \left| \frac{E_{\mathrm{out}}}{E_{\mathrm{in}}} \right|^2 \tag{1.2.1}$$

where E_{in} and E_{out} are the amplitudes of the incoming and the scattered waves, respectively.

Thomson scattering on a free electron

Let us consider the classical description of the scattering event on an isolated, free electron. Here, the electric field $\mathbf{E_{in}}$ of the incoming X-rays exerts a force on the electron making it accelerate sinusoidally and radiate the scattered wave at the same frequency. As the incident and the scattered wavelengths are the same, the scattering is referred to as elastic. We seek the solution for the electric field of the reradiated scattered wave at an observation point P at the distance R from the oscillating charge, as shown in Fig. 1.2.1. Provided that the distance R is much greater than the spatial extent of the electronic charge distribution and the wavelength of the incident radiation, the dipole approximation can be applied. The time-dependent electron acceleration $\mathbf{a}$, resulting from the force exerted by the incoming electric field, is given by:

$$e\mathbf{E_{in}} = m_e\mathbf{a} \tag{1.2.2}$$

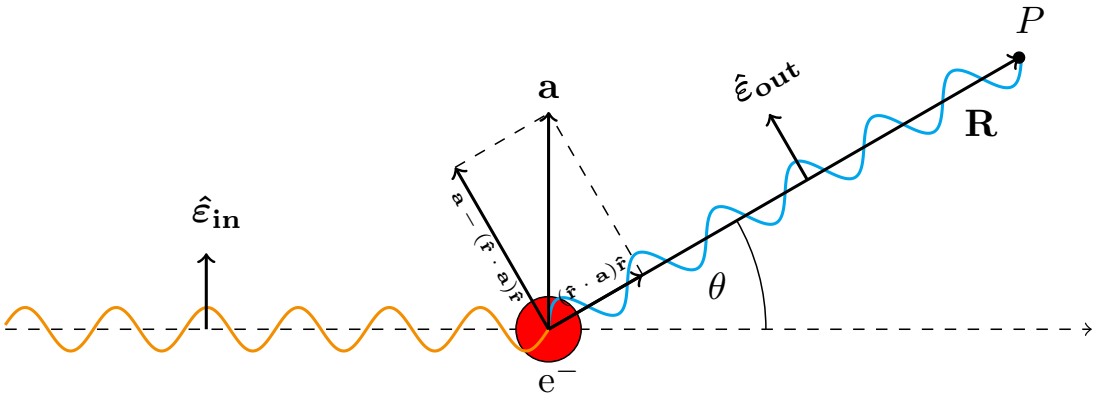

Fig. 1.2.1: Geometry of a scattering process of a polarised X-ray wave field from a free electron (e^-).

where e is the electron charge and m_e is the electron rest-mass. Finding the scattered electric field $\mathbf{E_{out}}$ involves solving the Maxwell's equations introducing the so-called retarded vector potential. The detailed derivation can be found in the relevant literature [21, 22]. One of its results is a general formula for the radiation from an accelerated electron, whose electric field vector at the distance R reads:

$$\mathbf{E_{out}}(\mathbf{R},t) = \frac{1}{4\pi\epsilon_o}\frac{e}{c^2R^3}\left[(\mathbf{R}\cdot\mathbf{a})\mathbf{R} - R^2\mathbf{a}\right] \tag{1.2.3}$$

where ϵ_0 is the electric permittivity of vacuum. The electric field vector of the incident field $\mathbf{E_{in}}$ can be expressed using the generic complex representation in Eq. (1.1.2) and, at the observation point P, takes the following form:

$$\mathbf{E_{in}}(\mathbf{R},t') = \hat{\boldsymbol{\varepsilon}}_{\mathbf{in}} E_{\text{in}} \mathrm{e}^{\mathrm{i}\mathbf{k}\cdot\mathbf{R}} \mathrm{e}^{-\mathrm{i}\omega(t-R/c)} \tag{1.2.4}$$

where $\hat{\boldsymbol{\varepsilon}}_{\mathbf{in}}$ denotes the incident wave field polarisation vector and the time $t' = t - R/c$ stands for the delay caused by the finite speed of light c. Inserting Eqs. (1.2.2) and (1.2.4) into Eq. (1.2.3), we obtain:

$$\mathbf{E_{out}} = -\underbrace{\frac{1}{4\pi\epsilon_o}\frac{e^2}{m_e c^2}}_{r_0}\underbrace{\left[\hat{\boldsymbol{\varepsilon}}_{\mathbf{in}} - (\hat{\mathbf{r}}\cdot\hat{\boldsymbol{\varepsilon}}_{\mathbf{in}})\hat{\mathbf{r}}\right]}_{(\hat{\boldsymbol{\varepsilon}}_{\mathbf{in}}\cdot\hat{\boldsymbol{\varepsilon}}_{\mathbf{out}})\hat{\boldsymbol{\varepsilon}}_{\mathbf{out}}} E_{\text{in}}\frac{\mathrm{e}^{\mathrm{i}\mathbf{k}\cdot\mathbf{R}}}{R}\,\mathrm{e}^{-\mathrm{i}\omega(t-R/c)} \tag{1.2.5}$$

where $\mathbf{R} = R\hat{\mathbf{r}}$. The multiplicative constants in front let us isolate an expression for the fundamental length scale of the scattering problem r_0, $r_0 = 2.82 \times 10^{-5}$ Å, which is referred to as the Thomson scattering length or the electron classical radius. It quantifies the ability of the electron to scatter X-ray radiation and can also be obtained by equating the electron rest-mass energy $m_e c^2$ to the electrostatic energy at the radius r_0. The negative sign in Eq. (1.2.5) indicates a phase shift of π rad between the incident and the scattered waves.

The ratio between the amplitudes of the incoming and the scattered waves is given by:

$$\left|\frac{E_{\text{out}}}{E_{\text{in}}}\right| = \frac{r_0}{R}|\hat{\boldsymbol{\varepsilon}}_{\mathbf{in}}\cdot\hat{\boldsymbol{\varepsilon}}_{\mathbf{out}}| \tag{1.2.6}$$

Here, the polarisation factor $\hat{\boldsymbol{\varepsilon}}_{\mathbf{in}}\cdot\hat{\boldsymbol{\varepsilon}}_{\mathbf{out}}$ specifies an angular distribution of the scattered radiation with respect to the polarisation of the incident wave. Assuming a horizontally-polarised incident X-ray beam, the polarisation factor takes the following forms:

$$|\hat{\boldsymbol{\varepsilon}}_{\mathbf{in}}\cdot\hat{\boldsymbol{\varepsilon}}_{\mathbf{out}}| = \begin{cases} 1, & \text{vertical scattering plane} \\ \cos\theta, & \text{horizontal scattering plane} \end{cases} \tag{1.2.7}$$

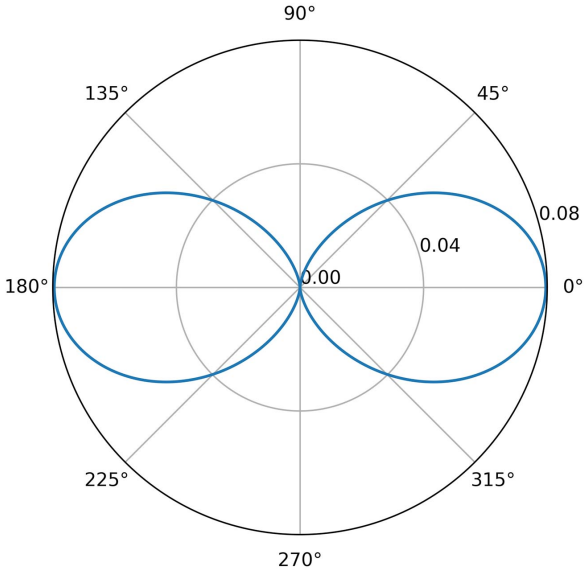

Fig. 1.2.2: Angular distribution of the differential cross-section for the Thomson scattering on an unbound electron in the plane of dipole oscillations. The maximum values are observed in the forward- and the backward-scattering directions ($\theta = 0°$ and $\theta = 180°$), while transversally, at $\theta = 90°$ and $\theta = 270°$, the elastic scattering signal vanishes. The cross-section values are given in barns.

whereas for an unpolarised source of the incoming radiation it equals $|\hat{\boldsymbol{\varepsilon}}_{\mathbf{in}} \cdot \hat{\boldsymbol{\varepsilon}}_{\mathbf{out}}| = \sqrt{\frac{1}{2}(1 + \cos^2\theta)}$ [21]. The azimuthal angle θ spans between the propagation direction of the incident wave and the observation direction. In accordance with these considerations, the ratio in Eq. (1.2.6) can be substituted into the formula in Eq. (1.2.1), yielding the differential cross-section for the Thomson scattering, as follows:

$$\left.\frac{\mathrm{d}\sigma}{\mathrm{d}\Omega}\right|_{\mathrm{Th}} = r_0^2 |\hat{\boldsymbol{\varepsilon}}_{\mathbf{in}} \cdot \hat{\boldsymbol{\varepsilon}}_{\mathbf{out}}|^2 = r_0^2 \cos^2\theta \tag{1.2.8}$$

Fig. 1.2.2 shows the angular distribution of the Thomson scattering differential cross-section in the plane of electron oscillations. The scattered signal vanishes perpendicularly to the incident wave ($\theta = 90°$) in the polarisation plane, which is a preferential position for e.g. X-ray fluorescence measurements due to the lowest elastic scattering background. As indicated in Eq. (1.2.7), in the scattering plane perpendicular to the electron oscillations, the differential cross-section is independent of the angle θ, and hence the three-dimensional angular distribution takes a well-known dounought-shape form. The total cross-section for Thomson scattering $\sigma_{\mathrm{Th}}^{\mathrm{tot}}$ can be obtained by integrating Eq. (1.2.8) over both polar angles, yielding:

$$\sigma_{\mathrm{Th}}^{\mathrm{tot}} = \frac{8\pi}{3} r_0^2 \tag{1.2.9}$$

which is an energy-independent constant.

Thomson scattering on a bound electron

The aforementioned formalism for the scattering on a free electron can further be generalised to describe the X-ray wave scattering on an electron bound in an atom. In the classical picture, the response of a bound electron to the incident X-ray field can be modelled as a single damped harmonic oscillator [21], with a resonant frequency ω_s and

a damping constant Γ. The expression for the scattered electric field $\mathbf{E_{out}}$ in Eq. (1.2.5) will then get an additional frequency-dependent factor, as follows:

$$\mathbf{E_{out}} = -r_0(\hat{\boldsymbol{\varepsilon}}_{\mathbf{in}} \cdot \hat{\boldsymbol{\varepsilon}}_{\mathbf{out}})\hat{\boldsymbol{\varepsilon}}_{\mathbf{out}} \, \frac{\omega^2}{\omega^2 - \omega_s^2 + \mathrm{i}\omega\Gamma} \, E_{\mathrm{in}} \frac{\mathrm{e}^{\mathrm{i}\mathbf{k}\cdot\mathbf{R}}}{R} \, \mathrm{e}^{-\mathrm{i}\omega(t-R/c)} \tag{1.2.10}$$

The corresponding ratio of the incident and the scattered electric field amplitudes is given by:

$$\left|\frac{E_{\mathrm{out}}}{E_{\mathrm{in}}}\right| = \frac{r_0}{R} \underbrace{\frac{\omega^2}{\omega^2 - \omega_s^2 + \mathrm{i}\omega\Gamma}}_{f_s} |\hat{\boldsymbol{\varepsilon}}_{\mathbf{in}} \cdot \hat{\boldsymbol{\varepsilon}}_{\mathbf{out}}| \tag{1.2.11}$$

and lets us isolate the atomic scattering length f_s which directly determines the amplitude of the scattered wave. If $\omega \gg \omega_s$, it approaches unity indicating that the electron can be treated as free and the above expression takes the form of the Thomson scattering on a free electron. Provided that $\Gamma \ll \omega_s$, the expression for f_s can be rearranged and approximated to take the following form:

$$f_s(\omega) \cong 1 + f_s'(\omega) - \mathrm{i}f_s''(\omega) \tag{1.2.12}$$

where

$$f_s'(\omega) = \frac{\omega_s^2(\omega^2 - \omega_s^2)^2}{(\omega^2 - \omega_s^2)^2 + (\omega\Gamma)^2} \tag{1.2.13}$$

and

$$f_s''(\omega) = \frac{\omega_s^2\omega\Gamma}{(\omega^2 - \omega_s^2)^2 + (\omega\Gamma)^2} \tag{1.2.14}$$

are the dispersion correction for the single oscillator model.

In contrast to a constant total cross-section for the scattering on a free electron, a general formula for the total cross-section for X-ray scattering on a bound electron is a function of energy and is expressed, as follows:

$$\sigma^{\mathrm{tot}} = \frac{8\pi}{3} \, \frac{\omega^4}{(\omega^2 - \omega_s^2)^2 + (\omega\Gamma)^2} \, r_0^2 \tag{1.2.15}$$

As mentioned previously, for frequencies much greater than the resonance frequency, the above expression reduces to the total cross-section for Thomson scattering on a free electron. The opposite asymptotic case for $\omega \ll \omega_s$ and $\Gamma \to 0$ yields the total cross-section for scattering of the lower-energetic electromagnetic radiation, given by:

$$\sigma_{\mathrm{Ray}}^{\mathrm{tot}} = \frac{8\pi}{3} \, \left(\frac{\omega}{\omega_s}\right)^4 \, r_0^2 \tag{1.2.16}$$

which is energy-dependent. Such scattering of X-rays by atomic electrons is also often referred to as the Rayleigh scattering.

Coherent scattering from atoms and molecules

The elastic scattering from an atom involves a collective response of all its Z electrons. It leaves the atom neither excited nor ionised and hence is also referred to as the coherent scattering. The classical description assumes a continuous electron distribution $\rho(\mathbf{r})$ around the nucleus of an atom and expresses the scattered radiation field as a superposition of contributions from different volume elements $\mathrm{d}\mathbf{r}$ of this distribution. The electric field of the outgoing scattered wave is therefore given by:

$$\mathbf{E_{out}} = -r_0(\hat{\boldsymbol{\varepsilon}}_{\mathbf{in}} \cdot \hat{\boldsymbol{\varepsilon}}_{\mathbf{out}})\hat{\boldsymbol{\varepsilon}}_{\mathbf{out}} \, E_{\mathrm{in}} \frac{\mathrm{e}^{\mathrm{i}\mathbf{k}\cdot\mathbf{R}}}{R} \, \mathrm{e}^{-\mathrm{i}\omega(t-R/c)} \int \rho(\mathbf{r}) \mathrm{e}^{\mathrm{i}\mathbf{q}\cdot\mathbf{r}} \, \mathrm{d}\mathbf{r} \tag{1.2.17}$$

where $\mathbf{q} = \mathbf{k}_\mathrm{f} - \mathbf{k}_\mathrm{i}$ is the so-called scattering vector denoting the momentum transfer defined by the difference between the final and the initial wave vectors. Its inner product with the position vector $\mathbf{r}$ is a phase difference between the scattering contributions at the position $\mathbf{r}$ and at the atom origin. A total contribution of all volume elements to the scattered wave field is given by the following integral:

$$f^0(\mathbf{q}) = \int \rho(\mathbf{r}) \mathrm{e}^{\mathrm{i}\mathbf{q}\cdot\mathbf{r}} \, \mathrm{d}\mathbf{r} \tag{1.2.18}$$

where $f^0(\mathbf{q})$ is termed the atomic form factor, being essentially an energy-independent Fourier transform of the distribution of electrons in the atom. In the case of forward coherent scattering, all scattering volume elements radiate in phase and $f^0(\mathbf{q} = \mathbf{0})$ equals the number of electrons in the atom, Z. With an increasing momentum transfer, the scatterers get out of phase reaching the opposite asymptotic limit of $f^0(\mathbf{q} \to \infty) = 0$. Tabulated values of $f^0(\mathbf{q})$ can be found in [23].

In the more general quantum mechanical description, it is necessary to take the discretisation of the energy levels of the atomic electrons into account. This results in two energy-dependent corrections to the atomic form factor, yielding the following expression for the atomic scattering factor $F(\mathbf{q}, \omega)$:

$$F(\mathbf{q}, \omega) = f^0(\mathbf{q}) + f'(\omega) - \mathrm{i}f''(\omega) \tag{1.2.19}$$

where f' and f'' are called the dispersion corrections to f^0. For the X-ray photon energies much less than the binding energy of the core shell electrons, the incoming wave field will see these electrons as bound, hence reducing their response to an external field. The overall scattering strength will therefore be reduced by an amount denoted f'. In the case of the X-ray energies being much greater than the electron binding energies, the electrons may be treated as free and f' equals 0. For the intermediate energy range, f' exhibits a resonant trend at the corresponding absorption edge energies. f'' relates in turn to the phase retardation of the scattered wave field. Similarly to the model of a forced harmonic oscillator, the imaginary part f'' represents the dissipation in the system and relates to the absorption.

The differential cross-section for the coherent scattering from an atom is defined for the linearly polarised radiation by:

$$\left.\frac{\mathrm{d}\sigma}{\mathrm{d}\Omega}\right|_\mathrm{coh} = r_0^2 \, |F(\mathbf{q}, \omega)|^2 \, \cos^2\theta \tag{1.2.20}$$

in the plane of the dipole oscillations. As an example, Fig. 1.2.3A shows differential cross-sections for coherent scattering from an atom of carbon ($Z = 6$), calcium ($Z = 20$), and iron ($Z = 26$) as functions of the scattering angle θ at an incident photon energy of 7.4 keV. The scattering power increases with the increasing atomic number Z, with absolute most of the radiation being forward-scattered. Fig. 1.2.3B shows in turn angular distributions of coherent scattering from a carbon atom at three different incident photon energies. With an increasing incident photon energy, coherent scattering dramatically narrows down to the forward direction $\theta = 0°$, while retaining the peak scattering magnitude.

As the next level in complexity, we will consider coherent scattering from molecules. The overall response to the incoming wave field is defined by a sum of respective contributions from atoms, that a molecule consists of. Given a molecule with $j = 1, \ldots, N$ atoms, the expression for its molecular scattering factor, $F^\mathrm{mol}(\mathbf{q})$, takes the following form:

$$F^\mathrm{mol}(\mathbf{q}) = \sum_{j=1}^{N} F_j(\mathbf{q}, \omega) \mathrm{e}^{\mathrm{i}\mathbf{q}\cdot\mathbf{r}_j} \tag{1.2.21}$$

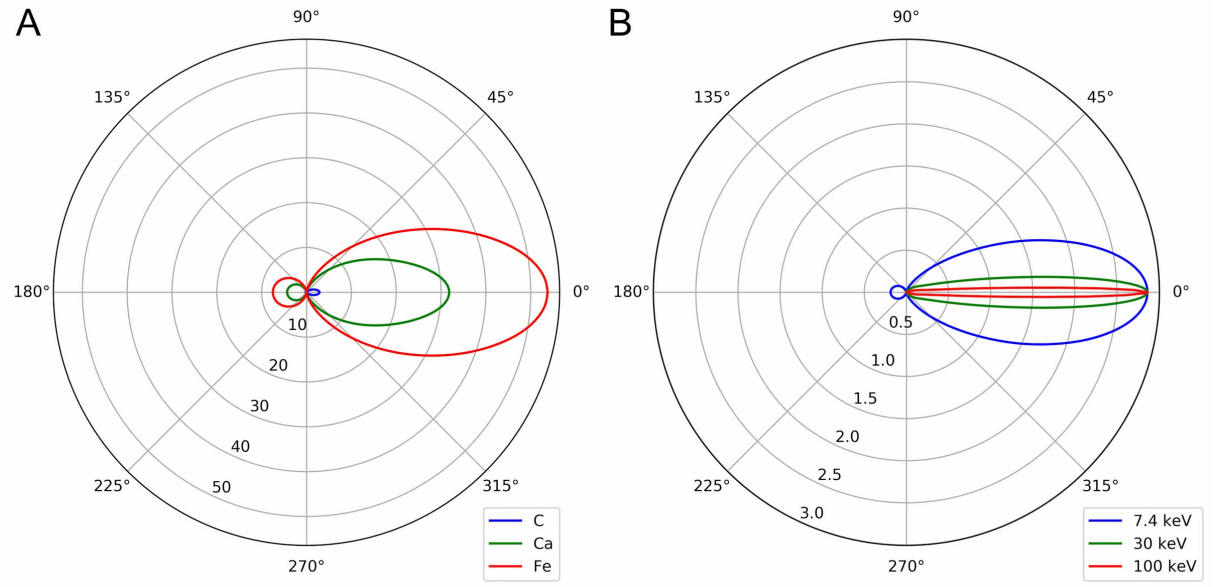

Fig. 1.2.3: Angular distribution of the differential cross-section for the coherent scattering from an atom in the plane of dipole oscillations. (A) shows the corresponding distributions for an atom of carbon (C), calcium (Ca), and iron (Fe) at an incident photon energy of 7.4 keV. (B) shows how the differential cross-section for coherent scattering from a carbon atom changes with increasing incident photon energy. The cross-section values are given in barns.

where $F_j(\mathbf{q}, \omega)$ is the atomic scattering factor of the jth atom in the molecule. Experimentally, it is possible to measure only $|F^{\mathrm{mol}}(\mathbf{q})|^2$, meaning that the phase information is inevitably lost. This is referred to as the phase problem. Additionally, the signal generated by a single molecule in standard synchrotron experiments is currently insufficient to be measured. Hence, bulk – crystalline or non-crystalline – samples, consisting of many molecules, are required. In this thesis, samples in a non-crystalline form were studied using spatially coherent and monochromatic X-ray radiation (section 1.1.4). An imaging method able to solve the phase problem from a set of appropriately-sampled coherent diffraction patterns was utilised to obtain complex-valued optical density distributions of the investigated specimens, by means of sophisticated phase retrieval algorithms (section 3.1).

1.2.2 Inelastic scattering

According to the wave-particle duality, in quantum mechanics an X-ray wave field impinging on matter can be considered as a beam of energy quanta, called photons. Let us consider a collision of a photon with a free electron, which is initially at rest. In a quantum-mechanical description, kinetic energy of the photon may partially be transferred to the electron, resulting in the scattered photon with lower energy than that of the incident one. Such a scattering process is inelastic and is referred to as the Compton effect. A sketch of the collision is shown in Fig. 1.2.4. As a consequence of the energy loss, the scattered photon features a longer wavelength λ' than the wavelength λ of the incident photon. The ratio between them can be derived from the principle of conservation of total energy and momentum, resulting in the following expression:

$$\frac{\lambda'}{\lambda} = 1 + \frac{E_\gamma}{m_e c^2}(1 - \cos\theta) \tag{1.2.22}$$

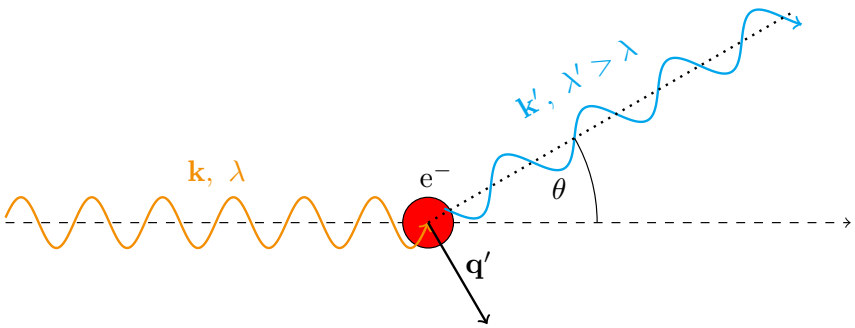

Fig. 1.2.4: Compton scattering. An incident photon of a wavelength λ is scattered by a free electron (e^-), initially at rest. Consequently, a fraction of the photon kinetic energy is transferred to the kinetic energy of the electron, resulting in the lower-energy photon of a wavelength λ', $\lambda' > \lambda$, scattered at an angle θ.

where $E_\gamma = hc/\lambda$ is the energy of the incident photon, m_e is the electron rest-mass, and c is the speed of light in vacuum. The Compton-scattered photons exhibit a continuous energy spectrum while the fractional energy loss increases with the increasing incident energy and scattering angle.

In relativistic quantum mechanics, a scattering event from a free electron is described by the Klein-Nishina (KN) formula [24]. The generalised differential cross-section is given by the following expression:

$$\left.\frac{\mathrm{d}\sigma}{\mathrm{d}\Omega}\right|_{\mathrm{KN}} = r_0^2 P(E_\gamma,\theta)^2 \left[P(E_\gamma,\theta) + P(E_\gamma,\theta)^{-1} - \sin^2\theta\right] \tag{1.2.23}$$

where $P(E_\gamma,\theta) = \lambda/\lambda'$ is the ratio of the initial and scattered photon energies, as in Eq. (1.2.22). At low incident photon energies, $E_\gamma \ll m_e c^2$, the ratio $P(E_\gamma,\theta) \to 1$ and the KN formula reduces to the Thomson differential cross-section (Eq. (1.2.8)). At high incident photon energies, the KN formula yields in turn the Compton scattering.

The inelastic scattering from an atom causes ejection of an electron from the atom, leaving the latter in an ionised state. The modified differential cross-section for the incoherent scattering from an atom takes the subsequent form:

$$\left.\frac{\mathrm{d}\sigma}{\mathrm{d}\Omega}\right|_{\mathrm{inc}} = \left.\frac{\mathrm{d}\sigma}{\mathrm{d}\Omega}\right|_{\mathrm{KN}} S(\mathbf{q},Z) \tag{1.2.24}$$

where $S(\mathbf{q},Z)$ is referred to as the incoherent scattering function, expressed in terms of the respective atomic form factor, yet, generalised to include excited states. In contrast to the atomic form factor, the incoherent scattering function equals 0 for forward scattering, $S(\mathbf{q}=\mathbf{0},Z) = 0$, whereas approaches the atomic number Z at high momentum transfers, $S(\mathbf{q}\to\infty,Z) = Z$. Corresponding values of the incoherent scattering function for all elements are typically tabulated as momentum-transfer functions [23]. Fig. 1.2.5A shows calculated angular distributions of differential cross-sections for incoherent scattering from carbon ($Z = 6$), calcium ($Z = 20$), and iron ($Z = 26$) atoms at an incident photon energy of 7.4 keV. The magnitude of the distributions clearly increases with the atomic number Z and is most prominent at back-scattering angles. On the other hand, Fig. 1.2.5B shows incoherent-scattering differential cross-sections for a carbon atom at different incident photon energies. It becomes apparent that with an increasing incident energy, more and more photons are scattered forwards.

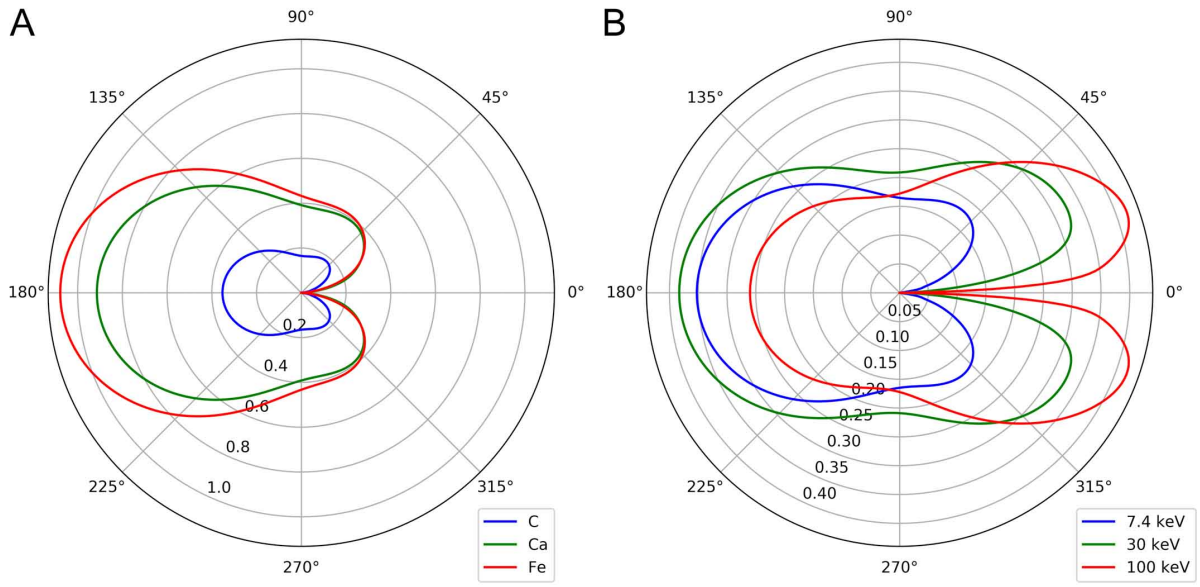

Fig. 1.2.5: Angular distributions of the differential cross-section for the incoherent (Compton) scattering on a bound electron in the plane of dipole oscillations. (A) shows the corresponding distributions for an atom of carbon (C), calcium (Ca), and iron (Fe) at an incident photon energy of 7.4 keV. (B) shows changes in incoherent differential cross-section distributions for a carbon atom at three distinct increasing incident photon energies: 7.4, 30, and 100 keV. The cross-section values are given in barns.

1.2.3 Photoelectric absorption

An alternative process of interaction of X-rays with matter, apart from scattering, is the so-called photoelectric absorption. It allowed to popularise X-rays in medical diagnostics in the form of X-ray projectional radiography, being currently replaced by alternative, less-irradiating imaging techniques. In the photoelectric absorption, an incident X-ray photon is fully absorbed by an atom and its energy is transferred to an electron, which is ejected from the atom. The interaction leaves the atom ionised. A measure of absorption is given by the linear absorption coefficient μ, which can in principle be determined in a transmission experiment, in which the ratio between intensities of the incident and the outgoing beams are measured. The intensity of X-ray beam traversing through the specimen of a thickness Δz falls off exponentially, according to the Lambert-Beer law [21]. Therefore, the transmitted intensity, $I_{\mathrm{out}}(z)$, is given by the following expression:

$$I_{\mathrm{out}}(z) = I_{\mathrm{in}} \mathrm{e}^{-\mu \Delta z} \tag{1.2.25}$$

where I_{in} is the intensity of the incident X-ray beam. The linear absorption coefficient μ is an element-specific quantity and a function of the X-ray energy. It exhibits a strong dependence on the atomic number of the element, varying approximately as Z^4. Furthermore, it decreases with an increasing incident photon energy, being inversely proportional to its third power, E^{-3}. Additionally, the linear absorption coefficient is related to the absorption cross-section per atom, σ_{ab}, through the following formula:

$$\mu = \frac{\rho_{\mathrm{m}} N_{\mathrm{A}}}{A} \sigma_{\mathrm{ab}} \tag{1.2.26}$$

where ρ_{m} and A are the mass density and the molar mass of the atom, respectively, while N_{A} is the Avogadro constant. As photoelectric absorption cannot be explained in terms

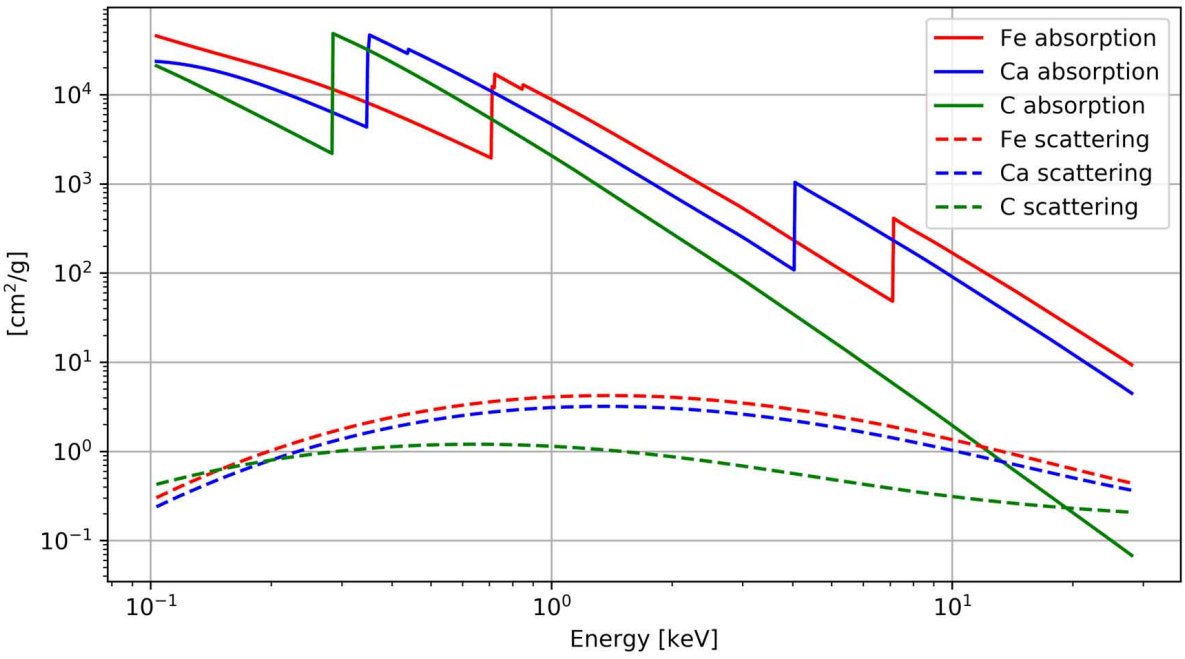

Fig. 1.2.6: Absorption and scattering cross-sections as functions of the incident photon energy for an atom of carbon (C), calcium (Ca), and iron (Fe). The sharp, discountinuous jumps in the absorption cross-sections correspond to the respective absorption edges. The scattering cross-sections represent a sum of coherent and incoherent scattering contributions. Data retrieved from [25].

of classical physics, the quantum-mechanical formalism must be invoked to consider the photon-electron interaction in the context of the first-order perturbation theory. Through the Fermi's Golden Rule [21], which determines the transition probability of such a system, it is possible to obtain the exact absorption cross-section values.

It is though more common to quantify photoelectric absorption in terms of the mass absorption coefficient, defined as μ/ρ_m. At a fixed photon energy, μ/ρ_m is constant for a given element, independently of the form of matter. Therefore, the mass absorption coefficient of a chemical compound or a mixture is approximately a weighted average of the coefficients for the constituent elements, as follows:

$$\left.\frac{\mu}{\rho_\mathrm{m}}\right|_\mathrm{mix} = \sum_j w_j \left(\frac{\mu}{\rho_\mathrm{m}}\right)_j \tag{1.2.27}$$

where w_j is the weight fraction of the jth element. Energy-dependent mass absorption coefficients of first 92 elements are tabulated in [25]. Fig. 1.2.6 shows absorption (solid lines) and total scattering (dashed lines) cross-sections as functions of the incident photon energy for an atom of carbon (green), calcium (blue), and iron (red). The total scattering cross-sections represent sums of coherent and incoherent scattering processes. The absorption cross-section lines feature discontinuous and sharp jumps at the element-specific energies. These sharp increases are called absorption edges and are a direct consequence of discrete binding energies of atomic electrons. As an example, the K-shell electrons in Fe have a binding energy of 7.112 keV. If the incident photon energy exceeds that value, photoelectric absorption may result in recoil of a K electron and annihilation of the photon. Yet, in case the photon energy decreases below the threshold of 7.112 keV, this particular absorption process becomes energetically impossible making the absorption cross-section fall sharply by a certain amount (K absorption edge). In the lower photon energy range

(< 1 keV), there are other discontinuities, as in the case of Ca and Fe in Fig. 1.2.6. These are the L absorption edges indicating energy thresholds required for the removal of L-shell electrons. The apparent 3-level structure of the L edges stems from the degeneracy of the L-shell electron energies. It is caused by: (1) screening of the nuclear charge by the inner K-shell electrons, resulting in lower energy of the 2s electrons than the 2p electrons, and (2) spin-orbit coupling (splitting of the 2p level). As demonstrated in Fig. 1.2.6, the photoelectric absorption usually dominates over other processes (coherent and incoherent scattering), which also contribute to an overall attenuation of the X-ray beam. The scattering processes prevail for the lightest elements (see the plots for a carbon atom) at higher photon energies.

As mentioned before, when an atom absorbs an incident X-ray photon, the photon energy is transferred to one of the core-shell electrons, as illustrated in Fig. 1.2.7A. As a result, the electron is expelled to the continuum, leaving the atom in an excited state. The ionised atom will relax back into its ground state, by filling the inner-shell vacancy with an outer-shell electron. Since the inner-shell electrons are more strongly bound to the nucleus, the resulting energy difference will then be emitted in one of the two forms: (1) fluorescence radiation (Fig. 1.2.7B) or (2) an Auger electron (Fig. 1.2.7C).

In the first process, as shown in Fig. 1.2.7B, the energy excess is emitted as X-ray fluorescence photons. It is discrete and monochromatic characteristic radiation which can be used to identify the atom it was emitted from. First to observe this was Henry Moseley, who discovered a systematic relation between the energy of the most intense characteristic line, currently known as K_α, and the atomic number Z of a given element. He reflected this in the following empirical law [21]:

$$E_{K_\alpha}\ [\text{keV}] \approx 1.017 \times 10^{-2}(Z-1)^2 \tag{1.2.28}$$

It can be explained by the fact, that the differences between the binding energies of the respective atomic orbitals are strictly dependent on the atomic number Z. Additionally, the possible transitions of electronic states within an atom are defined by the selection rules for electric dipole radiation [26]. Considering the timescale of such transitions, relaxation of an outer-shell electron to the inner-shell hole remaining after the recoil photoelectron

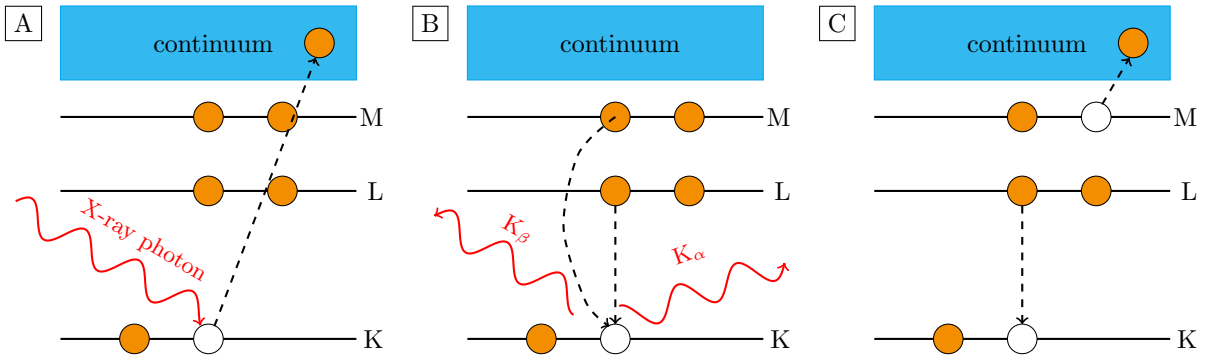

Fig. 1.2.7: The photoelectric absorption (A) results in ejection of a photoelectron into the continuum and leaves the atom ionised. The atom may relax back into its ground state following two phenomena: (B) emission of a characteristic fluorescent X-ray radiation or (C) ejection of an outer-shell Auger electron.

occurs of the order of 10 to 100 fs. From the Heisenberg's uncertainty principle, the natural width of the resulting characteristic X-ray lines is therefore of the order of 0.01 eV, with more precise values depending on the considered element and transition. Summarising, the energy values of fluorescent lines are tabulated for the entire table of elements and can be found in, e.g. the X-ray Data Booklet [27].

The second, competitive relaxation process subsequent to the photoelectric absorption is shown in Fig. 1.2.7C. It is non-radiative and involves transferring the energy excess into another, loosely-bound electron, whose binding energy is less than the transferred energy. Consequently, the electron is ejected from the atom. The Auger process dominates over the fluorescence emission for the low-Z elements. The quantity that measures probability of relaxation occurring through the fluorescence emission rather than through the Auger process is called the fluorescence yield. It is particularly low for all biologically-relevant structural elements (C, N, O), for which the Auger process prevails, and increases with the atomic number Z.

1.2.4 Complex index of refraction

Interaction of X-rays with matter on the atomic level, as discussed so far, has its consequences in macroscopically observed phenomena. At the beginning of this chapter, X-rays were introduced as electromagnetic waves with all their properties. It is hence expected that X-ray radiation is refracted, while passing though sharp interfaces between optically different media. In section 1.1.1, as a result of the Maxwell's equations, the refractive index n of a medium, through which an X-ray wave field propagates, was macroscopically defined by means of its electric permittivity in Eq. (1.1.9). It is therefore a medium-specific quantity, which by definition is unity for vacuum. Additionally, the refractive index is generally a function of the electromagnetic wave frequency ω, causing normal dispersion in the low-frequency optical-spectrum range ($|n| > 1$), exhibiting resonant behaviour at energies of atomic and molecular transitions, and falling below unity in the X-ray regime ($|n| < 1$). It is possible to determine the relation between the refractive index of a material and its scattering properties [21]. For a homogenous medium, the refractive index is related to the atomic scattering factor of individual atoms constituting the material [28]. Given the expression for the forward atomic scattering factor, as in Eq. (1.2.19) for $\mathbf{q} = \mathbf{0}$, the refractive index becomes a complex-valued quantity, given by the following formula:

$$n(\omega) = 1 - \frac{r_0}{2\pi}\rho_{at}\lambda^2 \left[f^0(\mathbf{0}) + f'(\omega) - \mathrm{i}f''(\omega)\right] \tag{1.2.29}$$

where ρ_{at} is the atomic density, $\rho_{at} = \dfrac{N_\mathrm{A}}{A}\rho_\mathrm{m}$, and λ is the X-rays wavelength. It is also customary to isolate the respective real and imaginary parts, according to the following convention:

$$n = 1 - \delta_\omega + \mathrm{i}\beta_\omega \tag{1.2.30}$$

where δ_ω is the refractive index decrement, informing how much the real part of the refractive index differs from unity:

$$\delta_\omega = \frac{r_0}{2\pi}\rho_{at}\lambda^2 \left[Z + f'(\omega)\right] \tag{1.2.31}$$

In the X-ray regime, δ varies from typically 10^{-5} for solids to around 10^{-8} for air. The imaginary part of the complex refractive index, β_ω, is called the absorption index and

expressed by:

$$\beta_\omega = \frac{r_0}{2\pi}\rho_{at}\lambda^2 f''(\omega) \tag{1.2.32}$$

Given such definition of the refractive index, it is possible to derive the consequences of interaction of the X-ray wave field $\psi_0(\mathbf{r})$ incident on a specimen of a thickness Δz and refractive index n. The resulting exit wave $\psi_{\Delta z}(\mathbf{r})$ can be represented by a general solution to the Helmholtz equation (1.1.15), as follows:

$$\psi_{\Delta z}(\mathbf{r}) = \psi_0(\mathbf{r})\mathrm{e}^{\mathrm{i}nk\Delta z} = \psi_0(\mathbf{r})\mathrm{e}^{\mathrm{i}k\Delta z}\mathrm{e}^{-\mathrm{i}k\int_0^{\Delta z}\delta_\omega(\mathbf{r},z)\,\mathrm{d}z}\mathrm{e}^{-k\int_0^{\Delta z}\beta_\omega(\mathbf{r},z)\,\mathrm{d}z} \tag{1.2.33}$$

The two last exponent factors define the so-called object transmission function, $O(\mathbf{r})$, which for a sample composed of a single material takes the following form:

$$O(\mathbf{r}) = \underbrace{\mathrm{e}^{-\mathrm{i}\delta_\omega k\Delta z}}_{\text{phase shift}}\,\underbrace{\mathrm{e}^{-\beta_\omega k\Delta z}}_{\text{attenuation}} \tag{1.2.34}$$

The interaction of the X-ray beam traversing through the specimen results in two phenomena: (1) the phase shift $\phi(\mathbf{r})$ of the outgoing wave field, given in general by:

$$\phi(\mathbf{r}) = -\frac{2\pi}{\lambda}\int_0^{\Delta z}\delta_\omega(\mathbf{r})\,\mathrm{d}z \tag{1.2.35}$$

and (2) the attenuation of the X-ray beam. Given the Lambert-Beer law, as in Eq. (1.2.25), the explicit relation between the absorption index and the linear absorption coefficient can be derived:

$$\beta_\omega = \frac{\mu_\omega}{2k} \tag{1.2.36}$$

which by combining with Eq. (1.2.26) allows to derive the relationship between the absorption cross-section σ_{ab} and the dispersion correction f'' of the atomic scattering factor.

Chapter 2

X-ray generation

In natural conditions, X-ray radiation is generated by naturally occurring radioisotopes and astrophysical objects, such as black holes or neutron stars. In order to produce X-rays in laboratory conditions, one of the three most prominent effects can be used: (1) Bremsstrahlung, (2) emission of characteristic X-ray fluorescence line, and (3) dipole radiation. Bremsstrahlung is a result of deceleration of moving charged particles, usually electrons, and is characterised by a continuous energy spectrum. By means of spectral filtering it can be tuned to deliver the requested photon energy, yet, it is considerably weaker than characteristic line radiation, spectrally narrow X-rays at fixed photon energy corresponding to a given atomic electron transition. Both of these phenomena are exploited in X-ray tubes, which have been utilised practically since the discovery of X-rays. In an X-ray tube, a beam of electrons is produced by a glowing filament and is subsequently accelerated by means of high voltage towards a water-cooled metal anode. The resulting spectrum of generated X-rays consists of a continuous Bremsstrahlung component caused by decelerating electrons which finally stop in the metal. Additionally, it also features superimposed sharp and much stronger characteristic lines. The electrons colliding with atoms of the target anode may eject an inner-shell atomic electron, resulting in a vacancy. This vacancy is subsequently filled by an outer-shell electron, as the atom relaxes back to its ground state. The energy difference is released in a form of fluorescent radiation, characteristic to the anode atoms. Such a concept has allowed for a number of table-top laboratory implementations. Nevertheless, it could not be used as an X-ray source for the imaging methods utilised in this thesis, that require X-ray radiation of several orders of magnitude more photon density and of a high degree of spatial coherence. These requirements are fulfilled by synchrotron storage rings, which exploit the fact that acceleration of relativistic electrons makes them emit a strongly confined and intense dipole radiation that enables production of a partially coherent radiation. The following sections will introduce the concept of a synchrotron storage ring together with its most important parameters and provide necessary information about an insertion device, called undulator, that yields highly intense X-ray beams in contemporary synchrotrons.

2.1 Synchrotron radiation sources

The concept of a synchrotron was coined in the 1940s in the field of particle acceleration, as a cyclic particle accelerator descending from cyclotrons. It involved using magnetic fields to bend the beam of charged particles, so that it keeps traveling along a closed circular trajectory in ultrahigh vacuum while being accelerated to relativistic speeds. Unlike cyclotrons, synchrotrons provided a fixed-length path of the particles, realised by

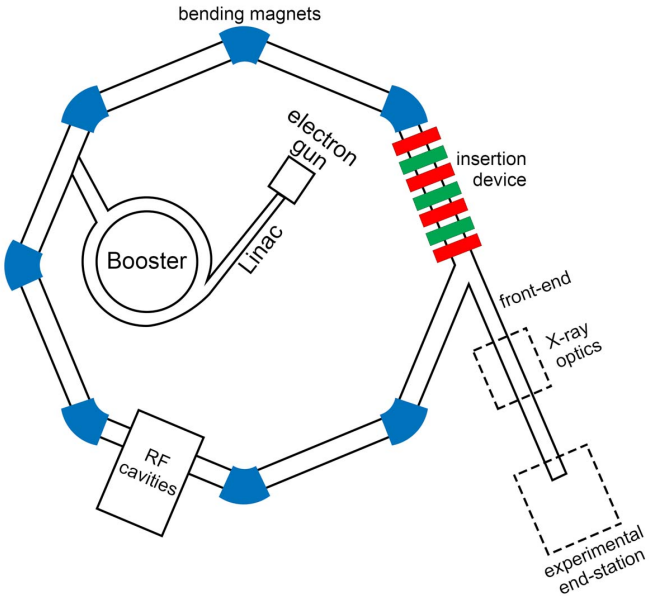

Figure 2.1.1: Schematic layout of a contemporary 3rd-generation synchrotron storage ring.

varying the magnetic field strength in time, as the particles gained energy. A typical synchrotron would consist of a series of straight sections separated with dipole bending magnets to deflect and, eventually, close the particle beam path. Beam focussing and chromatic-abberation correction would be achieved using quadrupole and sextupole magnets, while radio-frequency cavities would be responsible for a direct acceleration of the particle beam. Construction of first synchrotrons allowed to observe the electromagnetic radiation emitted by radially accelerated charged particles, as they travelled along curved paths. Termed synchrotron radiation, it was first considered unwanted, as it led to an energy loss of the accelerated particle beam. Later on, it became apparent, that synchrotrons could serve as robust and highly intense X-ray sources. They could be used as storage rings for electron or positron beams, circulating at a constant and relativistic energy. Moreover, production of synchrotron radiation, occurring at every curved section of such a storage ring, would permit to simultaneously perform many independent experiments.

Fig. 2.1.1 shows a schematic layout of a contemporary synchrotron storage ring using an electron beam. The particles are generated in an electron gun and pre-accelerated in a linear accelerator (Linac) to an energy of hundreds of MeV. The electrons subsequently enter a booster pre-accelerator, which further increases the particle beam energy to the final energy of several GeV used in the main storage ring. The electrons are periodically injected into the main ring, to maintain a constant beam current, that would otherwise decay upon collisions of the electrons with residual gas particles. Most of the modern facilities have implemented a so-called *top-up* operation, meaning that small portions of electrons are quasi-continuously injected into the storage ring, as soon as its beam current decreases by a small fraction, typically 1 mA ($\leq 1\%$). Such an operation mode ensures no injection-related downtimes, fairly steady X-ray beam intensity delivered to experimental end-stations, and a constant heat load on X-ray optics components. Having reached the main storage ring, the electrons keep circulating, while producing synchrotron radiation at every bending magnet (in blue) or at insertion devices, like wigglers or undulators (in green-red), installed in the straight sections. This results in an energy loss, which is com-

pensated by radio-frequency (RF) resonant cavities, which utilise an alternating electric field to accelerate the passing electrons. The inherent working principle of the cavities structures the electron beam into *bunches*, promoting only these particles which arrive in phase with the electric field. Along the direction of synchrotron radiation, produced tangentially to the storage ring, beamlines are built. They typically span a distance of several tens of meters, and consist of a front-end section, an X-ray optics hutch, and an experimental end-station.

According to the evolution of synchrotron light sources, four generations can be distinguished. 1^{st} generation covers the time of synchrotrons as particle accelerators. 2^{nd} generation denotes first synchrotron storage rings, producing synchrotron radiation with bending magnets, characterised by a broad spectral bandwidth. Installing insertion devices (wigglers, undulators) in the straight sections of the storage rings allowed for a dramatic intensity increase of produced radiation and its significantly narrower bandwidth. This has been a key characteristic of 3^{rd} generation of synchrotron light sources, using only undulators as insertion devices and designed for a sole purpose of generation of synchrotron radiation. Since then, the synchrotron facilities have not been shared with high-energy particle physics experiments. Finally, 4^{th}-generation synchrotron storage rings, coming currently to operation, are supposed to deliver ultimately bright X-ray beams by exploiting the physical limit of electron beam focussing set by diffraction. Intensity of generated synchrotron radiation depends namely on the parameters of the electron beam, i.e. its lateral size s and divergence θ. Their product is known as the emittance of the electron beam ε, given for both lateral directions by:

$$\varepsilon_i = s_i\, \theta_i, \qquad i = \mathrm{h}, \mathrm{v} \tag{2.1.1}$$

Following the Liouville's theorem [21], the electron-beam emittance in a given transverse direction is conserved along the orbit of a storage ring, while its components periodically oscillate, as a response to external magnetic fields. Additionally, magnetic deflection required to keep the electron beam on a horizontal circular trajectory, introduces a strong electron dispersion in the horizontal direction, which effectively worsens horizontal beam parameters. Hence, the horizontal electron-beam emittance of synchrotrons is inherently greater than the vertical (around 100 times), which directly translates into photon beam quality, especially the corresponding source size. The resulting photon-beam emittance is a convolution of the electron-beam emittance and the emittance of the photon beam generated by a single electron passing through the source [26]. Minimising the emittance yields therefore a nearly perfect X-ray source, able to produce almost parallel X-ray beams. The fundamental limit to this is set by the Heisenberg's uncertainty principle between the photon beam source and the transverse photon momentum. It results in the so-called diffraction-limited emittance:

$$\varepsilon_{\min} = \frac{\lambda}{4\pi} \tag{2.1.2}$$

The majority of currently operational 3^{rd}-generation synchrotron light sources is diffraction-limited only in low soft X-ray energy range. Reaching the diffraction limit in the hard X-ray regime is the aim of currently upcoming 4^{th}-generation storage rings. Additionally, they implement so-called multi-bend achromat devices [29] into their magnet lattice to significantly compensate for the horizontal electron beam dispersion. This allows to largely reduce the asymmetry between the horizontal and vertical electron-beam emittances, and hence achieve the diffraction limit in the both directions.

The electron- and the resulting photon-beam parameters depend on the design specifications of a particular storage ring, and hence differ between the facilities. A single

quantity, referred to as brilliance, combines several key aspects, like the source area, beam collimation and spectral distribution, permitting comparison of X-ray beams between different sources. It is defined as the number of photons emitted per second, i.e. the photon flux F, produced per unit source area, per unit solid angle at 0.1% of the fixed relative fractional energy bandwidth BW, as given by:

$$\mathcal{B} = \frac{F}{(s_\mathrm{h} s_\mathrm{v})\ (\theta_\mathrm{h}\theta_\mathrm{v})\ (0.1\%\ \mathrm{BW})} \qquad \left[\frac{\mathrm{photons\,s^{-1}}}{\mathrm{mm^2\ mrad^2\ (0.1\%\ BW)}}\right] \tag{2.1.3}$$

The brilliance is a function of the photon energy and for a typical 3$^{\mathrm{rd}}$-generation synchrotron light source is of the order of 10^{21} photons s^{-1}mm^{-2}mrad^{-2} (0.1% BW)$^{-1}$ [21, 26].

Bending magnets and insertion devices exploit differently the same phenomenon, that leads to production of electromagnetic radiation. Therefore, generation of synchrotron radiation can first be explained by considering a relativistic electron moving in a constant magnetic field. The electron experiences the magnetic-field-induced Lorentz force perpendicular to its motion, which makes it accelerate along a circular orbit and emit electromagnetic radiation. Due to the relativistic Doppler effect, the radiation becomes compressed into tightly collimated cones, in contrast to a characteristic doughnut-like distribution of a non-relativistic radiating dipole. The natural opening angle of such a cone equals γ^{-1}, being typically a fraction of milliradian, where the Lorentz factor $\gamma = E_e/m_e c^2$ is the electron energy in units of its rest-mass energy. The emitted radiation features a broad and continuous energy spectrum, which falls off rapidly for photon frequencies higher than $\gamma^3\omega_0$, where ω_0 is the angular frequency of the electron in the storage ring (typically in the range of MHz). Moreover, it is linearly polarised in the orbit plane of the electron, while circularly polarised for an off-axis observer. In a synchrotron storage ring, this type of radiation can readily be obtained from a bending magnet. An electron bunch, passing a bending magnet, emits tangentially the fan of radiation, whose horizontal angular divergence depends on the magnet length, yet is ultimately limited by the angular acceptance of the beamline slits. The total power radiated from a bending magnet is proportional to the square power of the electron beam energy E_e and of the magnetic field B, the magnet length L, and the electron beam current I, i.e. $P \propto E_e^2 B^2 L I$. Finally, due to the intrinsic bunch structure of the electron beam, synchrotron radiation is produced as pulses, whose duration is determined by the length of an electron bunch.

2.2 Undulator radiation

Synchrotron radiation can be generated much more efficiently by forcing the electrons to oscillate along a straight path, rather than to orbit a single, purely circular arc. This concept is utilised by a device referred to as the undulator, that can be installed in straight sections of a typical storage ring. Fig. 2.2.1A shows schematically the basic principle of undulator operation. The insertion device consists of two arrays of magnets (in red-green), between which the electron beam passes (in blue). The magnets produce spatially alternating magnetic fields, that cause the electrons to follow an oscillatory path, i.e. *to undulate*. Every oscillation results in generation of synchrotron radiation. Provided a small enough spatial period of the undulator, λ_u, which ensures small angular oscillations on a scale of the natural opening angle, γ^{-1}, amplitudes of the waves radiated at the subsequent oscillations can be coherently added to yield the resulting summed intensity. An undulator features therefore a quasi-monochromatic spectrum with harmonics, determined by its finite number of periods N.

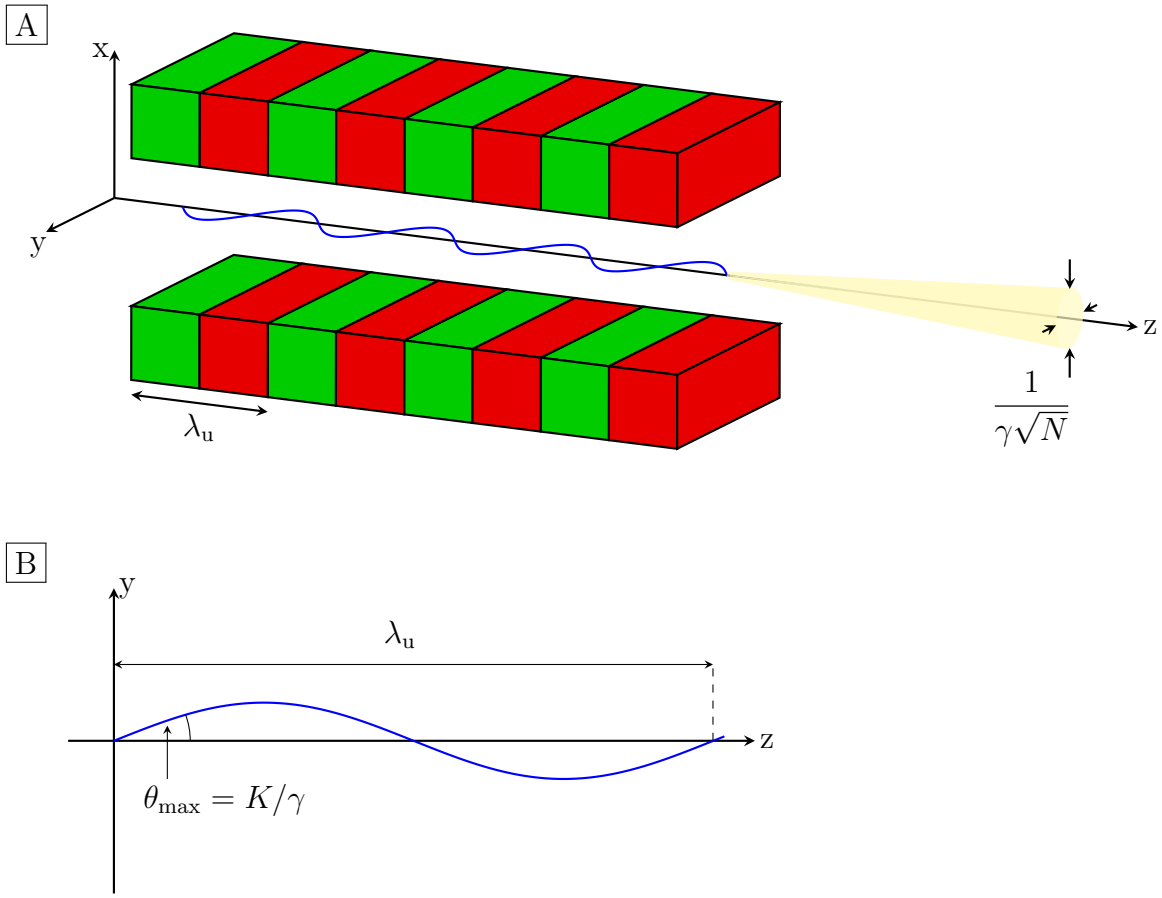

Figure 2.2.1: Undulator radiation. (A) shows a schematic diagram of an undulator. It is an insertion device installed in straight sections of a typical synchrotron storage ring. An undulator consists of two sets of magnets generating a spatially alternating magnetic field. The electron beam (denoted in blue) passes through the gap between the magnetic sets, whose magnetic fields make it oscillate. At each oscillation the electrons emit synchrotron radiation, whose amplitudes add coherently, provided a small enough undulator period λ_u. The intrinsic angular divergence of undulator radiation is proportional to $1/\gamma\sqrt{N}$, where N is the number of undulator periods. (B) denotes a maximum angular deviation θ_{max} of the electron beam from the undulator axis. The deflection parameter K determines how much that angle differs from the natural opening angle of the bending magnet radiation and is a characteristic measure of a given undulator.

A maximum angular deviation $\theta_{\max}$ from the undulator axis is defined by a dimensionless parameter K, namely $\theta_{\max} = K/\gamma$, as shown in Fig. 2.2.1B. The parameter K allows to characterise the amplitude of the electron oscillations, and is defined in terms of the maximum magnetic field B_0 in the undulator, as follows:

$$K = \frac{eB_0}{2\pi m_e c}\lambda_{\mathrm{u}} \tag{2.2.1}$$

For an undulator, K is close to unity, as the maximum angular deviation $\theta_{\max}$ is less or equals γ^{-1}. Due to the coherent addition of signal amplitudes emitted from consecutive oscillations, the fundamental wavelength in the undulator spectrum is directly related to the spatial undulator period, as given by the following expression:

$$\lambda_1(\theta) = \frac{\lambda_{\mathrm{u}}}{2\gamma^2}\left[1 + \frac{K^2}{2} + (\gamma\theta)^2\right] \tag{2.2.2}$$

where θ is an angle between the undulator axis and the observation direction. The key feature of an undulator is a tunable gap between the two magnet arrays, allowing to modify the magnetic field strength and hence the parameter K. It becomes therefore apparent, that by modifying the undulator gap, the value of a given harmonic wavelength can be adjusted, being one of the most powerful characteristics of synchrotron radiation at 3$^{\mathrm{rd}}$-generation storage rings. The higher harmonics λ_n are regularly separated, like $n\lambda_n = \lambda_1$. Moreover, the finite number of undulator periods N produces a finite number of radiation pulses of a given duration. This results in a finite spectral width of the undulator harmonics, inversely proportional to N. The resulting monochromaticity of odd harmonics is expressed by:

$$\frac{\Delta\lambda}{\lambda_n} \approx \frac{1}{nN} \tag{2.2.3}$$

Radiation produced by an undulator features a substantially reduced angular divergence in comparison with the bending magnet radiation. The finite bandwidth of undulator harmonics, as in Eq. (2.2.3), sets namely the limit for an off-axis angle θ in Eq. (2.2.2) [21]. In such a way, the intrinsic angular divergence of the undulator fundamental wavelength and its odd harmonics radiation is given by:

$$\theta_{\mathrm{FWHM}} \approx \frac{1}{\gamma}\sqrt{\frac{1 + K^2/2}{nN}} \tag{2.2.4}$$

with a major contribution from the number of periods N. In practice though, the final photon beam divergence is a convolution of the above with the finite angular divergence of the electron beam, leading to a somewhat larger values, especially in the horizontal direction.

Letting the electron beam oscillate, emitting a train of intense and highly collimated X-ray pulses, results in a dramatic increase of radiation intensity. The on-axis peak photon flux F_n in the central cone of the nth undulator harmonic satisfies the following proportionality [26]:

$$F_n \propto \gamma^2 N^2 \frac{\Delta\lambda}{\lambda_n} I\ f_n(K) \tag{2.2.5}$$

where I is the electron beam current. The undulator flux is therefore also proportional to the number of electrons in a bunch. The tuning functions $f_n(K)$ determine relative intensities of the undulator harmonics at a given parameter K and their explicit formula is based on Bessel functions. They ascend with increasing K to reach a maximum, after

Tab. 2.1: Parameters of an U32 undulator utilised at the PETRA III synchrotron storage ring, Hamburg, Germany [31].

Parameter	**Value**
Minimum gap [mm]	9.5
Undulator period λ_u [mm]	31.4
Undulator length [m]	2
Number of periods N	63
Maximum magnetic field B_0 [T]	0.91
Maximum parameter K_{max}	2.7

which they begin to fall off. Their values range typically between 0 and 0.45. Therefore, depending on the requested energy range, different undulator harmonics are used. By opening the undulator gap (decreasing its parameter K), the energy of a given harmonic is increased, until its intensity falls below the intensity of the next odd harmonic at the highest accessible $K = K_{max}$, corresponding to the minimum undulator gap. Then, the undulator is closed again and the new, higher harmonic is further used.

Raw undulator radiation exhibits rather low degree of coherence. Nevertheless, thanks to its high intensity and exceptional angular collimation, the coherence can be improved at the cost of intensity loss. The native spectral bandwidth of undulator harmonics, as in Eq. (2.2.3), determines the longitudinal coherence length. Yet, it can further be decreased by installing a monochromator downstream of the undulator, providing a much narrower spectral bandwidth, e.g. $1.3 \cdot 10^{-4}$ for the (111) reflection of a silicon double-crystal monochromator. The spatial coherence area, in turn, depends on the photon beam source size and the propagation distance from the undulator to the end-station, as discussed in section 1.1.4.2. Given the brilliance of an undulator $\mathcal{B}$, the respective coherent flux F_{coh} is expressed by [30]:

$$F_{coh} = \mathcal{B}\lambda^2 \frac{\Delta\lambda}{\lambda} \tag{2.2.6}$$

The number of spatially coherent photons decreases therefore with the second power of the photon energy. At 3rd-generation synchrotron storage rings, the absolute coherence area exhibits significant asymmetry due to the much larger horizontal beam emittance. Introducing slits right after the undulator allows to redefine the horizontal source size and hence increase the horizontal transverse coherence length.

As an example, an U32 undulator used at PETRA III synchrotron light source (Hamburg, Germany) can be considered [31, 32]. Tab. 2.1 shows its most important parameters. Using Eq. (2.2.2), the first-harmonic lowest energy of 2.4 keV can be calculated for $K = K_{max}$. At the electron beam energy of 6 GeV and the beam current of 100 mA, the first undulator harmonic delivers a photon flux of approximately 5×10^{17} photons s^{-1}mrad^{-2}(0.1% BW)$^{-1}$ [26]. Assuming a source size of about $140 \times 5\,\mu m^2$, the undulator brilliance would then equal 7.1×10^{20} photons s^{-1}mm^{-2}mrad^{-2} (0.1% BW)$^{-1}$. Finally, for the photon energy of 7.3 keV and the fractional bandwidth of $1.3 \cdot 10^{-4}$, the undulator can deliver a coherent flux of 2.6×10^{12} photons per second.

Chapter 3

Methods

Previous chapters introduced X-rays as electromagnetic waves, their free-space propagation and the theory of their interaction with matter. The chapter about X-ray generation summarised X-ray sources available to date, outlining the characteristics of synchrotron radiation storage rings. The presented theoretical background provides a solid foundation necessary for understanding the X-ray microscopy techniques used in this thesis.

The following sections will introduce the concepts of two imaging methods: ptychography and X-ray fluorescence. Section 3.1 will present a principle of ptychographic imaging in synchrotron applications, iterative phase retrieval, and further possibility of extending the technique to quantitative computed tomography. Subsequently, section 3.2 will give an overview of the application of energy-dispersive X-ray fluorescence in elemental mapping at sub-micrometre spatial resolutions. The chapter combines information published in the literature with representative own experimental demonstrations, being a proprietary contribution to this thesis.

3.1 Ptychographic coherent diffractive imaging

Contemporary synchrotron sources provide highly intense and coherent X-ray beams promoting a variety of challenging experimental techniques. In 1990s first third-generation synchrotron storage rings came to operation being an important milestone for scanning X-ray microscopy. Accompanied with advances in X-ray optics fabrication and high-precision instrumentation, scanning X-ray microscopy techniques were established as multifunctional probes of extended specimens. Compared with electron microscopy, they could access much larger sample volumes thanks to the high penetration power of X-rays, at spatial resolutions beyond conventional visible light microscopes. Their resolving power was though limited by the size of the focal spot which translated to long measurement times and higher dose imparted to the specimen.

In the early 2000s, first demonstrations of coherent diffraction X-ray microscopy were shown. The method exploited the significant increase in brilliance and the coherent fraction of synchrotron X-ray beams, providing a phase shift contrast of weakly scattering samples at a diffraction- and wavelength-limited spatial resolution. Yet, its applicability was vastly limited to isolated and small specimens and it lacked robustness in the associated phase retrieval procedures.

In the 1970s, the concept of a new scanning microscopy method based on coherent electron diffraction, called ptychography [1, 2], was proposed. Availability of even more intense and coherent X-ray beams, offered by low-emittance synchrotron sources, and sufficient computational resources allowed ptychography to emerge in the late 2000s as

a promising X-ray imaging technique. It robustly combined the features of the scanning X-ray microscopy and the coherent diffractive imaging, overcoming in the same time their most pronounced limitations. It opened a possibility of quantitative and robust imaging of extended specimens (large fields of view) at diffraction- and dose-limited spatial resolutions, surpassing the X-ray optics fabrication limits.

3.1.1 Experimental realisation

Far-field X-ray ptychography utilises a highly spatially coherent and monochromatic X-ray beam. Fig. 3.1.1 illustrates the basic principle of a conventional ptychographic experiment. Fully or partially coherent X-ray radiation is focussed by a set of optical elements to a localised yet not fully focussed spot. The sample is raster-scanned across such an illumination (probe) perpendicularly to the beam direction. Ptychography requires the neighbouring illuminated areas to overlap at least 60% [6]. The scattered radiation is propagated to an area pixel detector in the far-field regime. In contrast to conventional microscopes, ptychography does not use any objective lens between the sample and the detector. Instead, a coherent diffraction pattern is recorded at every point of the scan. To ensure successful image reconstruction, all diffraction patterns must be sufficiently oversampled. The conventional approach adopted from coherent diffraction imaging experiments uses the Nyquist sampling criterion which requires the smallest features in the diffraction patterns (called speckles) to be sampled by at least two detector pixels. As the speckle size is proportional to a ratio between the propagation distance z and the size of the illuminating probe D_{probe}, one can define a dimensionless quantity referred to as the oversampling ratio σ, as follows:

$$\sigma_{x,y} = \frac{\lambda z}{D_{\text{probe}} \Delta x_2} \tag{3.1.1}$$

where λ is the wavelength of the X-ray beam and Δx_2 is the detector pixel size. The oversampling ratio must then be equal or greater than 2 in each of the x, y directions to ensure the sufficient sampling in the Fourier space. Despite an existent evidence that ptychography allows to relax this criterion [33, 34], it is still advised to use the conventional CDI-approach in challenging experimental applications.

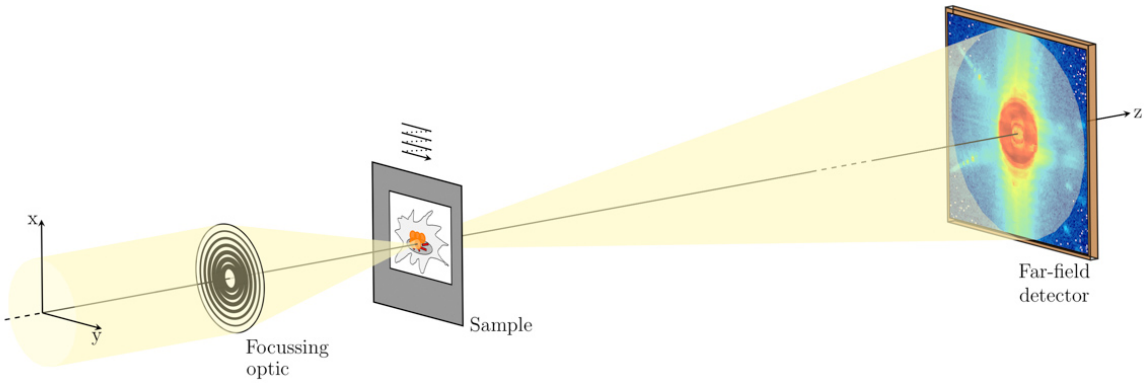

Fig. 3.1.1: Basic principle of ptychographic imaging. A coherent portion of X-ray beam, focussed by a set of X-ray optical elements, is used to form a localised illumination (probe). The sample is scanned across the confined beam keeping a substantial overlap between the adjacent scan points. The resulting coherent diffraction patterns are recorded by an area pixel detector in the far-field regime.

A complete ptychographic dataset consists of a series of diffraction patterns and an array of corresponding x/y positions of the sample with respect to the illuminating probe. To decode the image of the sample, the complete dataset is used by an iterative Fourier-transform-based reconstruction algorithm to obtain a quantitative optical density image of the measured specimen.

3.1.2 Iterative phase retrieval

The name *ptychography* derives from the Greek $\pi\tau\upsilon\xi$ that means *to fold* and was coined in the 1970s in the field of transmission electron-diffraction microscopy [1]. It referred to the folding and interference between Bragg peaks of a crystal illuminated with a finite and coherent illumination. Acquisition of the resulting diffraction patterns at two different sample positions would allow to resolve the ambiguity in the phase problem between the correct solution and its complex conjugate. The concept was further extended to non-periodic objects and scanning transmission electron-diffraction microscopy [35] utilising the Wigner-distribution deconvolution technique as an analytic solution [36]. Its first implementation with visible light [37] was followed by successful applications in scanning transmission electron microscopy [38] and soft X-ray scanning transmission microscopy [39]. Albeit promising, this non-iterative method did not result in a breakthrough that would lead to routine applications. Hence, in such form, ptychography did not advance beyond the proof-of-concept demonstrations due to both experimental and analytical obstacles.

Only in the early 2000s, thanks to rapidly growing computational power and implementation of the fast Fourier transform algorithm [40], a new category of phase retrieval algorithms has emerged. Iteratively alternating between the direct and the Fourier space, they would use the oversampled diffraction data to retrieve a unique set of the object phases [41]. Particularly successful was the application of the iterative phase retrieval in the field of lensless diffraction-based X-ray microscopy, which resulted in several impressive demonstrations, like the imaging of a freeze-dried yeast cell [42], lead nanocrystals [43], and a pyramid-like test object [44]. Yet, the underlying principal limitations prevailed over those promising results. To reach an unambiguous solution, the iterative phase retrieval needed *a priori* knowledge of the object support, narrowing down the scope of applications to isolated specimens. Moreover, the algorithm featured slow convergence (typically thousands of iterations) and was still prone to stagnation with a superposition of the true solution and its complex-conjugate twin image.

After more than a 30-year-long 'dark age', a combination of ptychography with the iterative phase retrieval was proposed in the mid 2000s [45]. Referred to as the ptychographic iterative engine (PIE), it exploited the redundant information from the overlapping illuminated sample areas at different relative positions of the sample with respect to the probe. Such an approach resolved the twin-image ambiguity and offered robust convergence. Fig. 3.1.2 shows a sketch of the most basic ptychography algorithm. It iterates over the diffraction patterns (here labelled from 1 to 6) originating from the different scan points (grey arrow loop) in order to reconstruct the complex-valued object transmission function $O(\mathbf{r})$. At each jth scan point (orange disk), the algorithm constructs a corresponding complex-valued exit wave $\psi_j(\mathbf{r})$, being a multiplication of the known illumination function (probe), $P(\mathbf{r}-\mathbf{r}_j)$, and the object function $O(\mathbf{r})$ at the respective scan position $\mathbf{r}_j$:

$$\psi_j(\mathbf{r}) = P(\mathbf{r}-\mathbf{r}_j)O(\mathbf{r}) \tag{3.1.2}$$

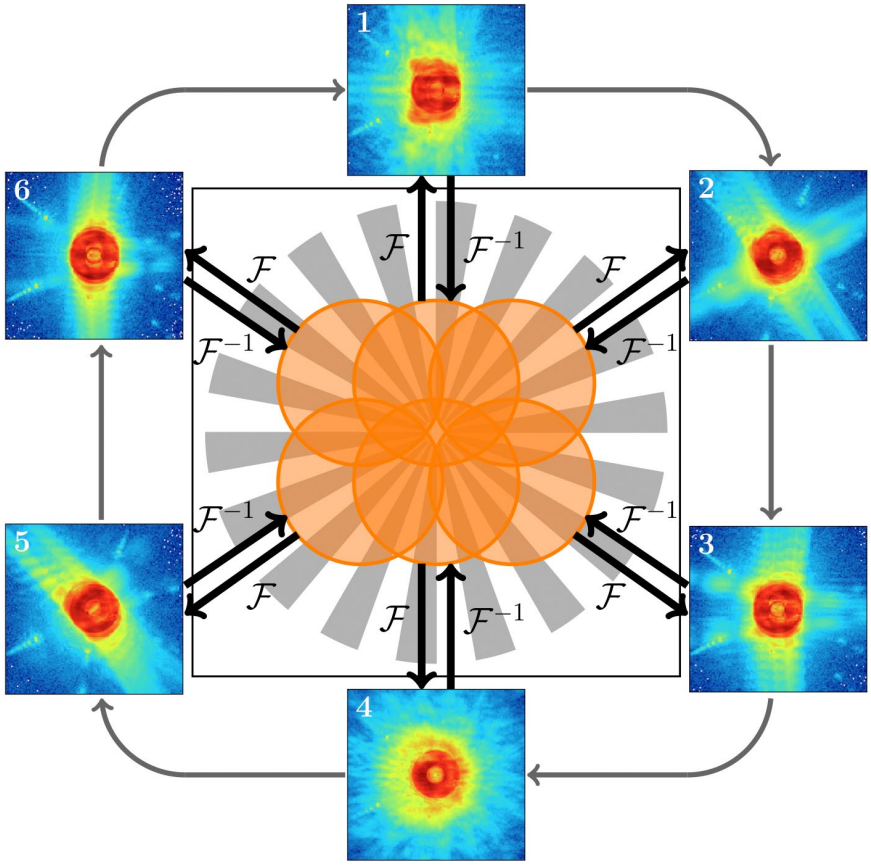

Fig. 3.1.2: A schematic representation of the most basic ptychographic iterative phase retrieval algorithm. The algorithm iterates over a set of diffraction patterns (labelled from 1 to 6), as indicated by the grey-arrow loop. At each scan point (denoted with an orange disk), a multiplication of the illumination function (probe) and the object transmission function constructs the corresponding exit wave, which is propagated to the Fourier space ($\mathcal{F}$ denotes a forward Fourier transform). In the Fourier space, the current diffraction intensities are substituted with the measured ones, retaining the phases. The back-propagated ($\mathcal{F}^{-1}$) corrected exit wave is then used to update the object function within the illumination region. The algorithm continues then with the next scan point until all points are processed.

The resulting current guess of the exit wave is then propagated using the Fraunhofer approximation based on a forward Fourier transform $\mathcal{F}$, as discussed in section 1.1.3.1. In the Fourier space, the guessed diffraction intensities are replaced by the measured ones $I_j(\mathbf{q})$ (black arrows), while the phases are kept intact:

$$\tilde{\psi}_j(\mathbf{q}) = \sqrt{I_j(\mathbf{q})}\,\underbrace{\frac{\mathcal{F}[\psi_j(\mathbf{r})]}{|\mathcal{F}[\psi_j(\mathbf{r})]|}}_{\text{phase}} \tag{3.1.3}$$

where $\mathbf{q}$ represents the reciprocal space coordinate. The result is back-propagated ($\mathcal{F}^{-1}$) and constitutes a corrected exit wave, which is then used to update the object transmission function in the given illumination area. The algorithm advances then to the next scan position until all of them are processed which closes one iteration. The folding and, hence, interference of the diffraction orders from the overlapping illuminated regions result in a high degree of redundancy enabling fast convergence. The algorithm iterates until it

converges on a satisfactory solution. Within the Fraunhofer approximation, the reciprocal space coordinate $\mathbf{q}$ is related to the real space coordinate $\mathbf{r}$, $\mathbf{q} = \frac{2\pi}{\lambda z}\mathbf{r}$ (section 1.1.3.1). This allows to derive the resulting real-space pixel size of the ptychographic reconstruction Δx_1:

$$\Delta x_1 = \frac{\lambda z}{N \Delta x_2} \tag{3.1.4}$$

assuming that a crop area of $N \times N$ detector pixels is used in the reconstruction.

In the presented form, the ptychographic iterative engine allowed to solve for the sample amplitude and phase images, provided that the illuminating probe was precisely known, which significantly hindered widespread applications of the method. The final breakthrough came with the publication of the generalised approach permitting simultaneous reconstruction of both the complex-valued probe and the object transmission function [46, 3]. It used the concept of a two-constraint difference map based on the idea of PIE. In this way, ptychographic reconstruction could start from a rough initial guess of the unknown illuminating probe and a typically plain or random initial guess of the object transmission function.

Nowadays, several of such ptychographic algorithms, permitting the concurrent probe and object retrieval, are in use, including: the extended Ptychographic Iterative Engine (ePIE) [5], a conjugate-gradient-based method [4], and a maximum-likelihood optimisation refinement [47]. In this thesis, all ptychographic reconstructions were obtained using an implementation of the difference-map ptychographic algorithm, with some of them (tomographic projections) being further optimised by the maximum-likelihood refinement.

3.1.2.1 Difference map algorithm

Ptychographic phase retrieval, allowing for a simultaneous reconstruction of the complex-valued probe and object functions, can be realised by the difference map approach with two constraint sets. For all $j = 1, \ldots, N$ scan points, the corresponding exit waves $\psi_j(\mathbf{r})$ (also called the views) are formulated as a product of the object function $O(\mathbf{r})$ and the common probe function $P(\mathbf{r})$ in the plane of the sample, shifted to the scan position $\mathbf{r}_j$, as in Eq. (3.1.2). This is referred to as **the overlap constraint**, which imposes that the object is reconstructed as one consistent complex-valued function. All the views are then propagated to the Fourier space and must orderly fulfil the second constraint. It is known as **the Fourier constraint**, which enforces the measured intensities $I_j(\mathbf{q})$ to be consistent with the reconstruction for all scan points, i.e.:

$$I_j(\mathbf{q}) = |\mathcal{F}[\psi_j(\mathbf{r})]|^2 \equiv |\tilde{\psi_j}(\mathbf{q})|^2 \tag{3.1.5}$$

In the Fourier domain, the amplitudes of the propagated views are replaced by the square root of the measured intensities, keeping the phases unchanged, as shown in Eq. (3.1.3). The corrected views are then back-propagated to the real space:

$$\Psi_j(\mathbf{r}) = \mathcal{F}^{-1}[\tilde{\psi_j}(\mathbf{q})] \tag{3.1.6}$$

and used in the coupled set of equations to update the current estimates of the object transmission function:

$$O^{n+1}(\mathbf{r}) = \frac{\sum_j P_j^*(\mathbf{r} - \mathbf{r}_j)\Psi_j(\mathbf{r})}{\sum_j |P_j(\mathbf{r} - \mathbf{r}_j)|^2} \tag{3.1.7}$$

and the illuminating probe:

$$P^{n+1}(\mathbf{r}) = \frac{\sum_j O_j^*(\mathbf{r}+\mathbf{r}_j)\Psi_j(\mathbf{r}+\mathbf{r}_j)}{\sum_j |O_j(\mathbf{r}+\mathbf{r}_j)|^2} \tag{3.1.8}$$

which serve as initial guesses for the following $(n+1)$th iteration. * denotes here the complex conjugation. As this problem cannot be analytically solved, the algorithm is applied iteratively for typically 50-100 cycles. The vital question though remains whether the obtained final amplitudes and phases are indeed unique. This issue is inherent to iterative algorithms in general, however, it has been empirically shown that the ptychographic difference-map algorithm, amongst the others, becomes unstable when the sets of constraints are incompatible. To obtain a more statistically valid and hence unique solution, it is customary to average over many variations of the object and probe estimates from the final iterations. At that stage, changes in further updates are namely only a result of noise or other experimental uncertainties.

3.1.2.2 Maximum likelihood refinement

Ptychographic imaging relies on acquisition of high-quality intensity distributions of the coherent scattering propagated into the far-field, being a couple-metre distance in the case of hard X-rays. The probabilistic nature of the measurement and unavoidable experimental imperfections contribute with noise that affects the scattered wavefront before reaching the detector. Standard iterative algorithms do not tackle this problem, which hinders the convergence and questions the reconstruction uniqueness. Averaging over multiple solution estimates from the final iterations increases the statistical significance of the reconstruction, at the cost of resolution loss. Alternatively, an additional refinement step, based on likelihood maximisation, can be implemented, choosing the statistical model that most appropriately reflects the measurement conditions.

In ptychography, the reconstruction searches for the pair $(P(\mathbf{r}), O(\mathbf{r}))$ that satisfies the Fourier constraint (Eq. (3.1.5)). Even in the experimentally perfect measurement (the best scenario), the counting statistics contribute to the measured noise, which give a Poisson distribution. In such a case, the probability p of measuring $n_j(\mathbf{q})$ photons, given $P(\mathbf{r})$ and $O(\mathbf{r})$, is:

$$p(n_j(\mathbf{q}) \mid P(\mathbf{r}), O(\mathbf{r})) = \frac{[I_j(\mathbf{q})]^{n_j(\mathbf{q})}}{n_j(\mathbf{q})!}\mathrm{e}^{-I_j(\mathbf{q})} \tag{3.1.9}$$

Subsequently, it is possible to construct an associated negative log-likelihood function $\mathcal{L}$ given the observed data $n_j(\mathbf{q})$:

$$\begin{aligned}\mathcal{L} &= -\log \prod_j \prod_{\mathbf{q}} p(n_j(\mathbf{q}) \mid P(\mathbf{r}), O(\mathbf{r})) \\ &= -\sum_j \sum_{\mathbf{q}} w_j(\mathbf{q}) \left\{ n_j(\mathbf{q}) \log I_j(\mathbf{q}) - I_j(\mathbf{q}) - \log\left[n_j(\mathbf{q})!\right] \right\}\end{aligned} \tag{3.1.10}$$

where $w_j(\mathbf{q})$ is a binary mask function ensuring that only intensities from the valid pixels are taken into account. Ptychographic reconstruction or refinement aims at maximising the likelihood, that corresponds to minimisation of the aforementioned negative log-likelihood function. It therefore requires the calculation of its gradients for any

$(P(\mathbf{r}), O(\mathbf{r}))$. The respective derivatives read as follows:

$$g_{O(\mathbf{r})} = \frac{\partial \mathcal{L}}{\partial O(\mathbf{r})} = \sum_j P(\mathbf{r} - \mathbf{r}_j)\chi_j^*(\mathbf{r}) \tag{3.1.11}$$

$$g_{P(\mathbf{r})} = \frac{\partial \mathcal{L}}{\partial P(\mathbf{r})} = \sum_j O(\mathbf{r} + \mathbf{r}_j)\chi_j^*(\mathbf{r} + \mathbf{r}_j) \tag{3.1.12}$$

where $\chi_j^*(\mathbf{r})$ is an auxiliary function which has the simplest form in the Fourier space, namely:

$$\begin{aligned} \tilde{\chi_j}(\mathbf{q}) &= \frac{\partial \mathcal{L}}{\partial I_j(\mathbf{q})}\tilde{\psi_j}(\mathbf{q}) \\ &= w_j(\mathbf{q})\left(1 - \frac{n_j(\mathbf{q})}{I_j(\mathbf{q})}\right) \end{aligned} \tag{3.1.13}$$

In the presence of additional sources of noise, it is more appropriate to select a Gaussian distribution as the likelihood function, where its σ parameter denotes the spatially dependent measurement uncertainties. The further discussion and implementation details are extensively discussed in [47]. Given the appropriate physical and noise models, the maximum-likelihood optimisation refinement allows for an efficient extraction of all the available information from measured diffraction data. The decrease in reconstruction noise visibly improves image quality and its spatial resolution, being particularly useful in low-dose and ultra-fast imaging schemes, when short exposure times result in sparse intensity distributions.

3.1.2.3 Generalisation to partially coherent illuminations

An important prerequisite for the ptychographic reconstruction approaches presented so far has been a fully spatially and longitudinally coherent illumination. Any relaxation of this condition would result in smearing of the diffraction speckles and hence deterioration of reconstructed image quality and its spatial resolution. On the other hand, taking advantage of an increased incident photon flux would allow for faster data acquisition and hence would improve the experimental throughput. Alternatively, it could help achieving even higher spatial resolutions, as for majority of specimens the dose required for imaging at resolution d is inversely proportional to the resolution's fourth power, $1/d^4$ [48].

A generalised framework of the mixed-state ptychographic reconstruction has therefore been developed to account for any experimental scenarios leading to blurry diffraction data [49]. The state mixtures of an imaging system can be categorised into three groups: (1) fluctuations of the incident, probing radiation representing the concept of partial coherence [50, 51], (2) mixed states (modes) within the investigated object, such as a vibrating sample [52] or the spins of an Ising model [49], and (3) a detector point-spread function [53]. The algorithm represents the blurred diffraction data as a sum of diffraction intensities over multiple mutually incoherent illumination modes and/or multiple modes of the object transmission function. If the object is in its pure state, such a sum is a spectral decomposition equivalent to the mode expansion of the mutual coherence function $\Gamma(\mathbf{r}_1, \mathbf{r}_2, \tau)$, as discussed in section 1.1.4. A partially coherent illumination can therefore be represented in terms of its mutual optical intensity $J(\mathbf{r}_1, \mathbf{r}_2)$ as a linear combination of an orthonormal set of N probe modes $P_k(\mathbf{r})$, as follows:

$$J(\mathbf{r}_1, \mathbf{r}_2) \equiv \Gamma(\mathbf{r}_1, \mathbf{r}_2, \tau = 0) = \sum_{k=1}^{N} \eta_k P_k(\mathbf{r}_1) P_k^*(\mathbf{r}_2) \tag{3.1.14}$$

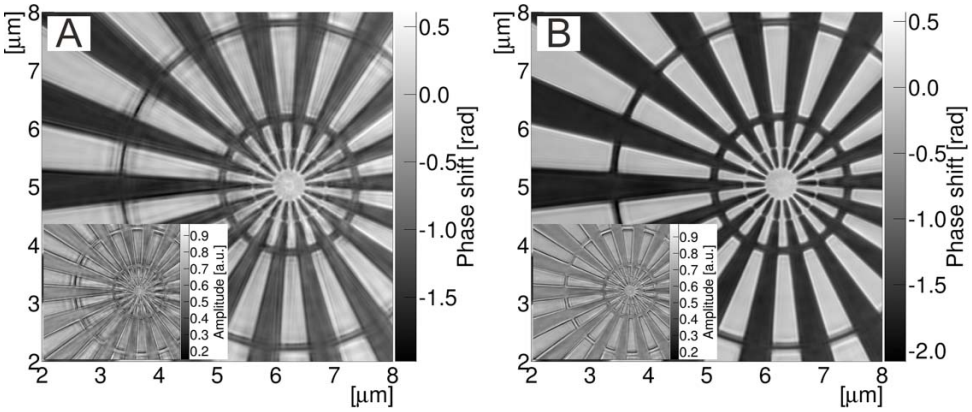

Fig. 3.1.3: Ptychographic scan of a Siemens star test object using a partially coherent illumination. (A) shows the single-mode reconstruction using a conventional difference-map algorithm. The image is considerably affected by decoherence artefacts. The reconstruction quality visibly improves assuming three probe modes (B). Proprietary results, published and reproduced from [50].

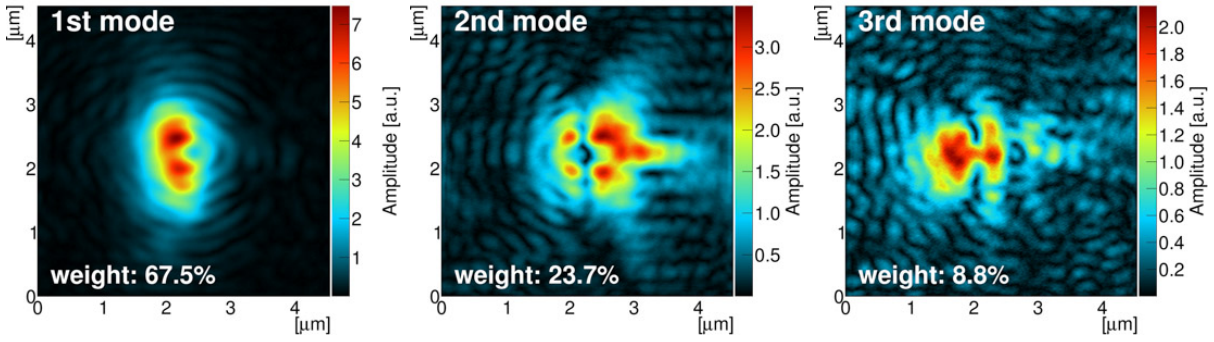

Fig. 3.1.4: Amplitudes of the three orthogonalised probe modes from the reconstruction in Fig. 3.1.3B. The fractions of the total probe intensity for each of the modes are indicated by the corresponding weight values. Proprietary results, published in [50].

where η_k is an intensity fraction of the kth probe mode, $k = 1, \ldots, N$. All the probe modes are themselves fully coherent, yet, mutually incoherent. The multimodal modification of the Fourier constraint takes the following form:

$$\tilde{\psi}_j^k(\mathbf{q}) = \sqrt{I_j(\mathbf{q})} \frac{\mathcal{F}[\psi_j^k(\mathbf{r})]}{\sqrt{\sum_{k=1}^{N} |\mathcal{F}[\psi_j^k(\mathbf{r})]|^2}} \tag{3.1.15}$$

where $I_j(\mathbf{q})$ is the jth measured diffraction pattern. Explicit implementations of the multimodal parametrisation of the object and probe update functions can be found in [49] for all three most frequently used ptychographic algorithms (the difference map, the extended PIE and the maximum-likelihood refinement).

As an exemplary experimental demonstration, based on own results published in [50], a ptychographic scan of a nano-fabricated Siemens star test structure was recorded with a partially coherent illumination. Fig. 3.1.3A shows the ptychographic phase and amplitude (inset) obtained with a conventional single-mode difference-map algorithm. Clearly visible artefacts stemming from insufficient spatial coherence deteriorate the image quality. Reconstructing the same dataset using an implementation of the multimodal difference-map algorithm with 3 probe modes significantly improves the phase and amplitude images (Fig. 3.1.3B). The raw probe reconstructions are in general a linear combination of the

actual probe modes that constitute an orthonormal base. Here, the Gram-Schmidt orthogonalisation method was applied to obtain the orthogonalised modes (Appendix A), whose corresponding amplitudes are shown in Fig. 3.1.4. Such an orthogonalised base can then be used to retrieve the intensity fractions η_k of each probe mode, indicated as *weights* in the figures. The first probe mode dominates, with the intensities of the remaining modes decaying, which is consistent with the Gaussian Schell model of the partially coherent sources [20].

3.1.3 Ptychographic X-ray Computed Tomography

The 2010s have begun with another important milestone for ptychographic imaging. One of the key advantages of X-rays is their weak interaction with matter and therefore a long penetration depth, permitting in many cases non-destructive 3D investigations of entire specimens. Given the promising results of 2D ptychographic imaging, necessary advances in instrumentation and further algorithmic developments were addressed to enable experimental realisation of the ptychographic X-ray computed tomography (PXCT). Conceptually, such an upgrade required implementation of a sample rotation stage in a standard 2D ptychographic setup, as shown in Fig. 3.1.5. The setup would then allow to rotate the specimen around the tilt axis, perpendicular to the direction of the incident X-ray beam, and record a standard 2D ptychographic projection. A tomographic dataset would consist of a series of 2D projections acquired over a known range of tilt angles (usually 180°).

The first successful implementation of PXCT was demonstrated in quantitative volumetric imaging of a piece of the mouse femur bone at a nanoscale spatial resolution [54]. Since then a huge effort has been made to improve the performance and the workflow of the method in order to make it available to a broader community of users. Currently, several instruments capable of performing PXCT are in operation worldwide, including: OMNY [55] and flOMNY [56] at cSAXS beamline (SLS, Switzerland), Bionanoprobe [57] (APS, USA), PtyNAMi [58] at P06 beamline (PETRA III, Germany), I13 beamline [59]

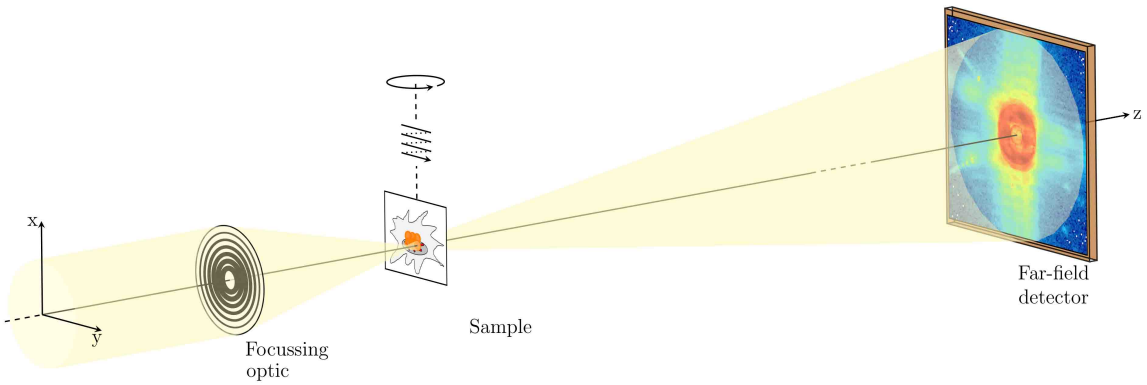

Fig. 3.1.5: Basic principle of ptychographic X-ray computed tomography. The sample is positioned on a highly precise mechanical stage that permits 2D scanning across a localised and highly coherent illumination and rotation around the rotation axis perpendicular to the X-ray beam direction. A series of standard 2D ptychographic scans is recorded at for range of known tilt angles, usually spanning equally over a range of 180°. The coherent diffraction patterns, recorded by an area pixel detector in the far-field regime, are used by a ptychographic iterative engine to reconstruct independently 2D phase and amplitude projections that are then used as input to a fully quantitative tomographic reconstruction.

(Diamond, UK), with more under construction.

Mechanical challenges in ptychographic nanotomography concern realisation of a highly precise rotation scanning sample stage featuring long-term stability and, preferably, a cryogenic sample environment to reduce the effect of radiation damage caused by repetitive acquisition of tens to hundreds of tomographic projections. Despite its challenging implementation, ptychographic tomography has become a versatile 3D imaging method allowing for high-resolution, quantitative investigations of both radiation-resistant samples and weakly-absorbing biological tissues and cells. Its outstanding resolving power down to an isotropic resolution of 16 nm was demonstrated in tomographic imaging of a tantalum-coated nano-porous silica glass [60]. Such high spatial resolutions and an excellent phase sensitivity have been exploited in 3D non-destructive imaging of integrated circuits [61], such as a 22-nm-technology Intel processor, revealing fine physical structure details down to single transistors and their interconnects. On the other hand, the multi-keV PXCT has also proven particularly successful in low-dose imaging of biological structures, utilising phase contrast that dominates over practically negligible absorption in this photon energy range. The method has been applied in imaging of frozen-hydrated single cells [62] and extended tissue volumes [63] as well as in quantification of mineral distributions in human dentine [64].

The most common approach to analysis of ptychographic tomography data consists nowadays of the following steps [65]: (1) independent ptychographic reconstruction of 2D projections yielding corresponding amplitude and phase images, (2) phase-unwrapping and removal of the constant and linear phase offsets (necessary for alignment), (3) multi-stage alignment of the projections to correct for positioning inaccuracies (centre-of-mass alinement, vertical-mass-distribution-invariance alignment [65], efficient subpixel registration [66], iterative tomographic consistency alignment [67]), (4) quantitative tomographic reconstruction from the both amplitude and phase modalities, (5) post-processing of the phase and attenuation volumes (optical or electron density contrasts with a possibility of calibration to the mass density distribution). The following sections will refer to these steps, introducing the principles of computed tomography, discussing briefly alignment routines relevant to this thesis and quantitative density contrast offered by ptychographic tomography.

3.1.3.1 Concepts of computed tomography

Synchrotron implementations of computed tomography (CT), unlike X-ray tube-based laboratory sources, utilise parallel beams. In computed tomography, 2D projection images consist of signals emerging from the individual, two-dimensional object slices, perpendicular to the rotation axis. In the case of a parallel-beam CT, these signals are decoupled from one another and hence the problem can be simplified to two-dimensional functions.

Let us then consider a tomographic experiment from a single object slice $f(x, y)$, as shown in Fig. 3.1.6A. The reference frame (x, y) is associated with the object and is coplanar with the laboratory reference system (t, s), with s axis denoting the beam direction. The two coordinate systems are rotated with respect to each other by an angle θ and, therefore, their relation can be expressed by the following rotation-matrix transformation:

$$\begin{pmatrix} x \\ y \end{pmatrix} = \begin{pmatrix} \cos\theta & -\sin\theta \\ \sin\theta & \cos\theta \end{pmatrix} \begin{pmatrix} t \\ s \end{pmatrix} \tag{3.1.16}$$

For the given angle θ, all line integrals of the slice taken along the s direction constitute a projection $P_\theta(t)$, which is recorded by an intensity pixel detector. Mathematically, it

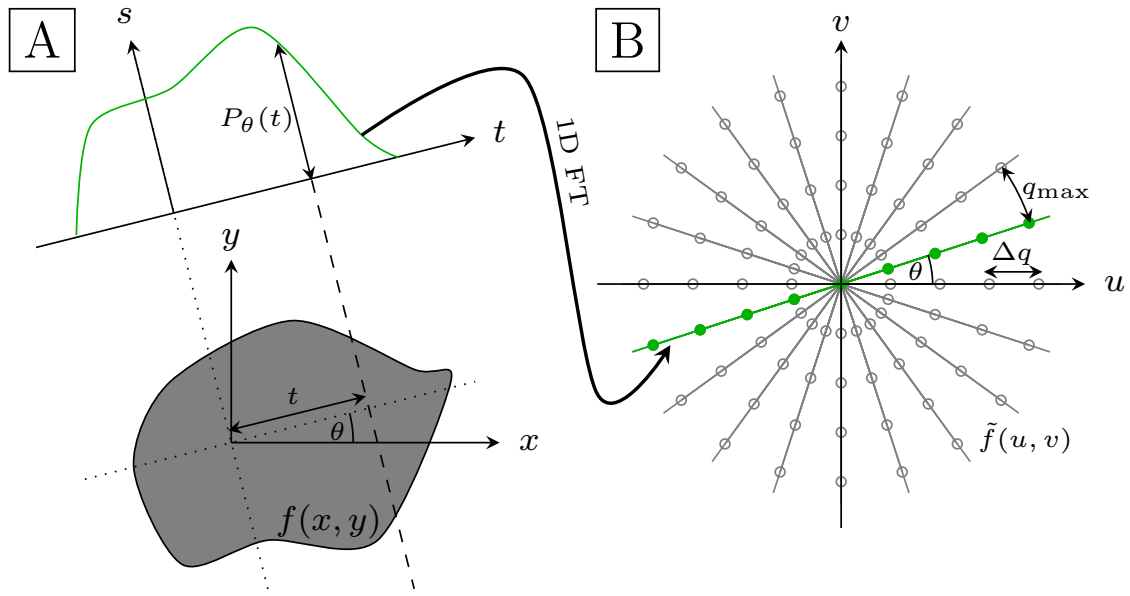

Fig. 3.1.6: Demonstration of the Radon transform (A) and the Fourier slice theorem (B).

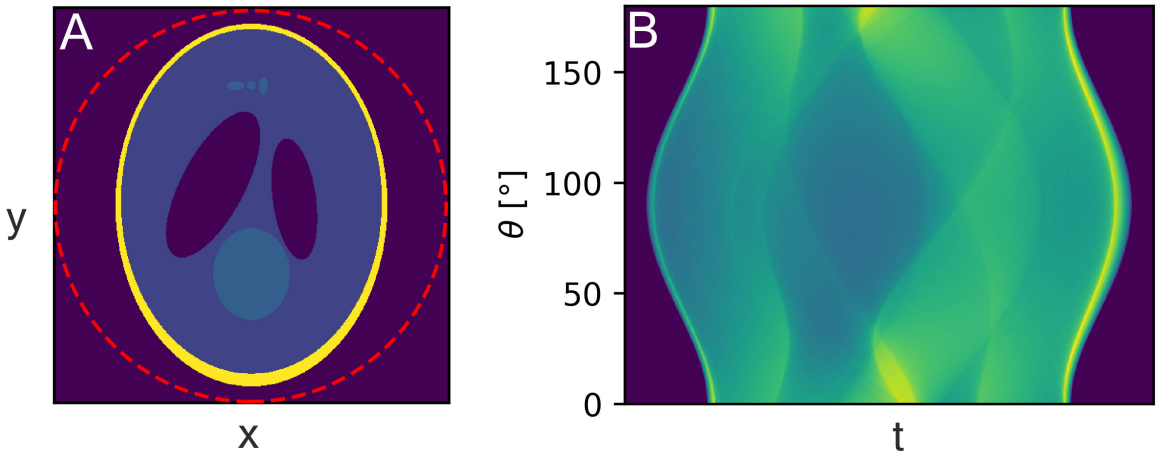

Fig. 3.1.7: A simulated phantom image representing one slice (A) and its sinogram (B), consisting of 360 projections and computed over an angular range of 180°. The centre of rotation was positioned in the centre of the red dashed circle.

can be expressed using the Radon transform [68] of the function $f(x, y)$, namely:

$$P_\theta(t) = \mathcal{R}_\theta[f(x,y)] = \iint_{-\infty}^{+\infty} f(x,y)\delta(x\cos\theta + y\sin\theta - t)\,\mathrm{d}x\mathrm{d}y \tag{3.1.17}$$

where $x\cos\theta + y\sin\theta = t$ is a parametrisation of the projection line that is used as the argument of a Dirac distribution δ. As an example, Fig. 3.1.7A shows a simulated phantom object slice and its Radon transform (Fig. 3.1.7B), comprising 360 projections (1D) over an angular range of 180°. It is also referred to as the sinogram, due to the sinusoidal paths, to which the off-centre object features of different density get projected upon rotation by a half-full angle.

In practice though, the detector measures a set of projections over a given range of tilt angles, that requires an inverse transformation to retrieve the image of the object slice. The Radon transform is closely related to the Fourier transform. Let us denote a 2D

Fourier transform $\tilde{f}(u,v)$ of the object slice $f(x,y)$:

$$\tilde{f}(u,v) = \iint_{-\infty}^{+\infty} f(x,y)\mathrm{e}^{-\mathrm{i}(xu+yv)}\,\mathrm{d}x\mathrm{d}y \tag{3.1.18}$$

and a 1D Fourier transform $\tilde{P}_\theta(\omega)$ of the slice projection $P_\theta(t)$ at the angle θ:

$$\tilde{P}_\theta(\omega) = \int_{-\infty}^{+\infty} P_\theta(t)\mathrm{e}^{-\mathrm{i}\omega t}\,\mathrm{d}t \tag{3.1.19}$$

According to the Fourier slice theorem (Fig. 3.1.6B), a line in the 2D Fourier transform of the object slice, $\tilde{f}(u,v)$, taken at an angle θ with respect to the u axis and passing through the origin (denoted in green), is equivalent to the 1D Fourier transform of the corresponding slice projection, $\tilde{P}_\theta(\omega)$, i.e.:

$$\tilde{P}_\theta(\omega) = \tilde{f}(\omega\cos\theta, \omega\sin\theta) \tag{3.1.20}$$

In this way, a real-space tomographic projection becomes a slice of the object Fourier space. Acquisition of a sufficient number of angular projection fills the object Fourier space, from which the object slice $f(x,y)$ can then be retrieved by means of an inverse 2D Fourier transform. As the spacing between the radial slices in the Fourier space increases at higher spatial frequencies, it is important to ensure sufficient sampling to avoid deterioration of high-resolution features. Therefore, the maximum spatial frequency $q_{\max}$ must not exceed the size of the reciprocal-space pixel Δq (Fig. 3.1.6B). Given N_{pix} pixels in each slice of the object Fourier space and N_{proj} equally spaced angular projections, the circumference of the outermost sampling circle can be expressed in two ways, leading to the following approximation:

$$\pi\Delta q N_{\mathrm{pix}} \approx 2N_{\mathrm{proj}}q_{\max} \tag{3.1.21}$$

which, combined with the sampling criterion, $q_{\max} \leq \Delta q$, yields

$$N_{\mathrm{proj}} \geq \frac{\pi}{2}N_{\mathrm{pix}} \tag{3.1.22}$$

Equivalently, the minimum number of angular projections necessary to sufficiently sample an object of the largest lateral extent a equals:

$$N_{\mathrm{proj}} \geq \frac{\pi}{2}\frac{a}{\Delta x_1} \tag{3.1.23}$$

where Δx_1 the real-space pixel size of a corresponding 2D projection, being effectively the tomogram voxel size, provided that N_{proj} are spaced equally over an angular range of 180°.

3.1.3.2 Tomography from the derivative of wrapped phase

The task of a tomographic reconstruction algorithm is to find the inverse transformation of the object Fourier space, $\tilde{f}(u,v)$, to obtain the real-space object slice, $\tilde{f}(x,y)$. This can be realised by the following inverse 2D Fourier transform:

$$f(x,y) = \iint_{-\infty}^{+\infty} \tilde{f}(u,v)\mathrm{e}^{\mathrm{i}(xu+yv)}\,\mathrm{d}u\mathrm{d}v \tag{3.1.24}$$

As shown in the previous section, the object Fourier space $\tilde{f}(u,v)$ is effectively filled using polar reciprocal space coordinates (ω,θ), thereby, the above inverse transformation must be rewritten, using $(u,v)=(\omega\cos\theta,\omega\sin\theta)$ for $\omega\in(-\infty,\infty)$ and $\theta\in[0,\pi)$, as follows:

$$\begin{aligned} f(x,y) &= \int_0^{\pi}\int_{-\infty}^{+\infty}\tilde{f}(\omega\cos\theta,\omega\sin\theta)\mathrm{e}^{\mathrm{i}(x\omega\cos\theta+y\omega\sin\theta)}|\omega|\,\mathrm{d}\omega\mathrm{d}\theta \\ &= \int_0^{\pi}\int_{-\infty}^{+\infty}\tilde{P}_\theta(\omega)\mathrm{e}^{\mathrm{i}\omega t}\underbrace{|\omega|}_{\text{reciprocal space filter}}\mathrm{d}\omega\mathrm{d}\theta \end{aligned} \tag{3.1.25}$$

where, in the second line, the Fourier slice theorem and the parametrisation equation for t were used. Eq. (3.1.25) provides the base for the filtered back-projection (FBP) algorithm, one of the most frequently used approaches to tomographic reconstructions. It can be rewritten into the following operator form:

$$f(x,y)=\int_0^{\pi}\mathcal{F}_\omega^{-1}\{|\omega|\mathcal{F}_t[P_\theta(t)]\}\,\mathrm{d}\theta \tag{3.1.26}$$

The FBP algorithm executes the subsequent steps:

(1) measures the object projections $P_\theta(t)$,
(2) obtains the corresponding Fourier-space slices by means of the 1D Fourier transform, $\tilde{P}_\theta(\omega)=\mathcal{F}_t[P_\theta(t)]$,
(3) performs reciprocal space filtering $\tilde{h}(\omega)\tilde{P}_\theta(\omega)$, where $\tilde{h}(\omega)=|\omega|$ is the so-called *Ram-Lak* filter and belongs to a selection of frequency-domain filters $\tilde{h}(\omega)$ utilised in tomographic reconstructions,
(4) takes the respective inverse Fourier transforms of the reciprocal-space-filtered Fourier slices, $\mathcal{F}_\omega^{-1}\{|\omega|\mathcal{F}_t[P_\theta(t)]\}$,
(5) back-projects the inverse Fourier transforms of the filtered Fourier slices for all angles θ across the real-space object slice image, performing the outer integration in Eq. (3.1.26).

Such a reconstruction algorithm could be readily used to process an angular series of ptychographic projections. However, it is quite likely that in individual phase projections, the maximum reconstructed phase shift will exceed 2π rad due to substantial optical thickness of the measured specimen, leading to the so-called phase wrapping. This means, that since all the reconstructed phases are confined to a range of $[-\pi,\pi)$ rad, the affected phase projections would exhibit strong phase jumps, as the phase shift reaches beyond 2π rad. Using wrapped-phase projections as input to the above implementation of the FBP algorithm results in strong artefacts, while phase-unwrapping may not always be feasible [65]. Yet, another important Fourier transform theorem permits tomographic reconstruction directly from the derivative of the phase projection. The theorem states, that:

$$\mathcal{F}_t\left[\frac{\partial P_\theta(t)}{\partial t}\right]=2\pi\mathrm{i}\omega\;\mathcal{F}_t[P_\theta(t)] \tag{3.1.27}$$

Therefore, by modifying the reciprocal-space filter in Eq. (3.1.26), the filtered back-projection from the derivative of phase-wrapped projections can be redefined, as follows:

$$f(x,y)=\int_0^{\pi}\mathcal{F}_\omega^{-1}\left\{\frac{|\omega|}{2\pi\mathrm{i}\omega}\mathcal{F}_t\left[\frac{\partial}{\partial t}P_\theta(t)\right]\right\}\,\mathrm{d}\theta \tag{3.1.28}$$

Differentiation of the wrapped phase conveniently removes any wrapping discontinuities, provided that the relative phase difference between the neighbouring pixels is still less than π rad. Such an approach was already used in X-ray differential phase contrast tomography [69] and beam deflection tomography [70] and has also enabled robust reconstructions of ptychographic tomography data.

3.1.3.3 Alignment approaches

Finite mechanical precision of tomographic experimental setups has its inevitable consequences in long-term drifts and inaccuracies in specimen centering on the rotation axis. This results in misalignment of 2D projections, which is reflected in an impaired sinogram, affecting gravely the quality of tomographic reconstruction. To mitigate this problem, an additional step prior to the tomographic reconstruction is needed to correct for the misalignment of recorded data. Typically, projection alignment involves first a coarse correction on length-scales greater than aimed resolution, which is then followed by the fine alignment. Below, three alignment approaches, relevant to this thesis and reported in literature, are briefly summarised. Note, that they are applied to unwrapped, so-called well-behaved, projection areas, i.e. containing no phase residua.

Horizontal centre-of-mass alignment Involves computation of a centre of mass within the selected well-behaved projection area [65]. This approach requires the horizontal projection size to exceed the largest horizontal extent of the measured sample, i.e. all projections must contain empty regions on both sides of the specimen. In the case of phase-contrast imaging, mass is understood as the integral of the projected phase. For every angular projection, a normalised sum of phase shift values weighted with their horizontal coordinates is computed. The result is then used to shift the respective projection to the appointed, common centre position.

Vertical-mass-distribution-invariance alignment It is a robust, iterative algorithm aiming at minimisation of vertical fluctuations in the mass of the sample and is used when the entire vertical span of the sample cannot be measured [65]. Theoretically, the vertical mass distribution should be invariant for all angular projections which is the basic argument of this alignment approach. For every angular projection, its vertical mass distribution $M_\theta(y)$ can be computed by integrating the phase along x direction. Further, constant and linear Legendre polynomials are removed from $M_\theta(y)$ using a least-squares fit, making it more sensitive to small sample fluctuations that facilitates a robust alignment. The iterative routine alternates between vertical and horizontal (center-of-mass) alignment steps, to converge on an improved solution.

Tomographic consistency alignment It is an iterative sinogram-based horizontal alignment technique, used in a "refinement" step or in the case of interior tomography, when the sample extends beyond the horizontal projection size [67]. Tomographic consistency states that by applying the inverse Radon transform by filtered back-projection (FBP), followed by a Radon transform, the original sinograms can be retrieved only if they are consistent with the object's 3D representation, which is not the case for misaligned projections. The alignment routine starts from utilising FBP to compute a given tomographic slice. Subsequently, a Radon transform algorithm is used to generate a synthetic sinogram from this slice. The synthetic sinogram is then used to refine the positions of the original projections, minimising their mutual mean squared error. The whole process is repeated iteratively, starting from low-resolution sinograms (e.g. decreased fivefold) towards the final resolution for better robustness.

3.1.3.4 Quantitativeness of ptychographic tomography

Ptychographic iterative reconstruction algorithms find a solution to the phase problem, yielding the complex-valued transmission function of the investigated object, providing

both amplitude and phase contrast [71]. In the hard X-ray regime, the phase modality bears most of the information, hence its importance in quantitative imaging. All individual ptychographic 2D phase-shift projections quantify the phase of retardation of the incident wave field, as it passes though the specimen, and serve as input to a tomographic reconstruction. Tomographic reconstruction algorithms, such as FBP, retain the quantitativeness, yielding phase shift slices $f(\mathbf{r}) = \phi(\mathbf{r})$. The 3D phase-shift distribution can then be directly recalculated into a map of refractive index decrement $\delta(\mathbf{r})$, informing on how much the real part of the refractive index deviates from unity:

$$\phi(\mathbf{r}) = -\frac{2\pi}{\lambda}\int_0^{\Delta}\delta(\mathbf{r})\,\mathrm{d}z = -\frac{2\pi\Delta}{\lambda}\delta(\mathbf{r}) \tag{3.1.29}$$

where Δ is a voxel size, λ is the wavelength of the incident X-ray beam, and z is propagation direction. Away from the absorption edges, the following formula allows to further obtain directly a 3D electron density map:

$$n_e(\mathbf{r}) = \frac{2\pi}{\lambda r_0}\delta(\mathbf{r}) \tag{3.1.30}$$

where r_0 is the classical electron radius. This is a strong advantage of phase X-ray tomography to render volumetric electron density distributions of investigated specimens. Further calibration to mass density requires *a priori* knowledge of the chemical composition of the measured sample. Based on the ratio between the molar mass A and the total electron number Z in a molecule comprising the sample, an accurate 3D map of mass density, $\rho_{\mathrm{m}}(\mathbf{r})$, can be derived:

$$\rho_{\mathrm{m}}(\mathbf{r}) = \frac{n_e(\mathbf{r})}{N_A}\frac{A}{Z} \tag{3.1.31}$$

where N_A is the Avogadro constant. Interestingly enough, the ratio A/Z is close to $2\,\mathrm{g\,mol^{-1}}$ for the most of light atoms, except for hydrogen, for which A/Z equals $1\,\mathrm{g\,mol^{-1}}$. Provided that the object consists of material phases not strongly varying in mass densities, mass density contrast in ptychographic tomography obtained using one global calibration ratio A/Z (corresponding to the most dominant density phase) remains accurate.

3.2 Energy-dispersive X-ray fluorescence mapping

One of the most prominent features of X-rays is their elemental specificity, meaning that under certain conditions the probing X-ray beam is able to make the sample emit detectable signals being a unique fingerprint of the sample-constituting elements (see section 1.2.3). The phenomenon is known as X-ray fluorescence emission and is a routine X-ray microscopy imaging method allowing for qualitative and quantitative determination of elemental distributions down to the ppm concentration level.

In the majority of synchrotron-based X-ray microscopy applications, X-ray fluorescence (XRF) is used to obtain spatially-resolved distribution maps of elements in a specimen. In the case of 2D-mapping, as shown in Fig. 3.2.1, the sample is raster-scanned across a tightly focussed beam. It is namely the beam size which ultimately limits the spatial resolution, provided that it is equal or greater than the scanning step size. If the energy of the incident X-rays exceeds the binding energy thresholds of atoms constituting the sample, the atoms will fluoresce emitting isotropically characteristic radiation. At each point of the scan, the resulting XRF spectrum is acquired by an energy-dispersive XRF detector. At the synchrotron with horizontally polarised X-rays, the detector should be positioned in the horizontal plane at 90° with respect to the incident beam to minimise

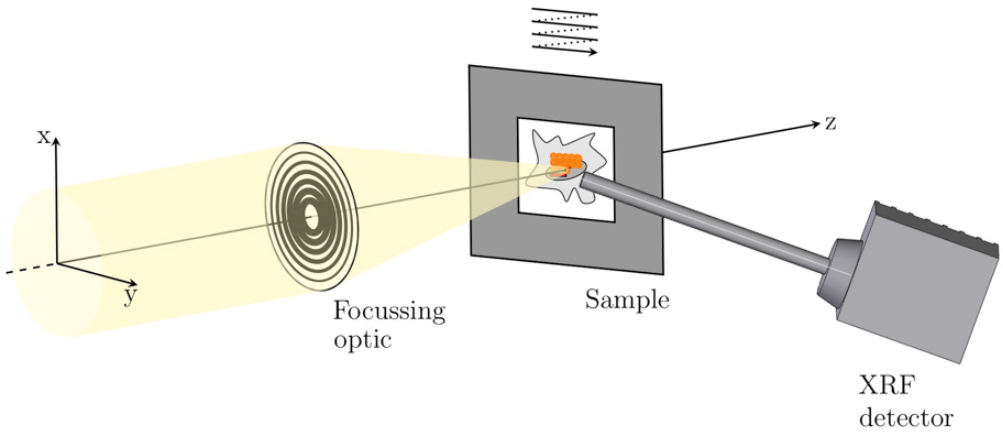

Fig. 3.2.1: Schematic view of an X-ray fluorescence 2D mapping experiment. A focussing optic is used to confine the X-ray beam into a small footprint, whose size determines the maximum achievable spatial resolution. The sample is raster-scanned across such an illumination. Typically, it is also tilted by an angle of 45° to facilitate XRF detection. At every scan point, the emitted characteristic radiation is recorded by an energy-dispersive silicon drift detector. The detector is usually positioned perpendicularly to the incoming beam in the horizontal plane to minimise scattering background.

background scattering. Additionally, flat specimens are usually tilted by 45° with respect to the incident beam towards the detector to facilitate X-ray fluorescence detection. X-ray fluorescence tomography requires, in turn, acquisition of a series of such 2D maps for an angular range of 180°, provided the symmetric XRF detection to address self-absorption of the fluorescence signal within the sample.

3.2.1 XRF detection system

Detection of X-ray fluorescence is typically realised by an energy-dispersive silicon drift detector (SDD) that allows to determine the energy of a detected photon in the range from 100 eV to several tens of keV, at a typical energy resolution of 120 eV. It uses a silicon active area in which an incident X-ray fluorescence photon is absorbed, generating a number of electron-hole pairs that depends on the incident photon energy. This proportionality between the charge and the energy deposited by the incident photon is the key to enable measurement of spectra. The high bias voltage makes the electrons drift towards a small anode as a charge pulse. A preamplifier is then used as a current integrator to convert the charge collected at the anode to a voltage signal, that retains the proportionality to the energy deposit. The magnitude of the voltage step pulse caused by every detection event allows to determine the energy of the incident photon.

The resulting weak voltage pulses must subsequently be amplified for further processing, which takes place in the main amplifier. This process involves also suppression of random fluctuations in the signal produced by thermal noise and is referred to as the pulse shaping. The optimum noise suppression is achieved by shaping the pulses to be wide in time, allowing thereby to obtain the best total energy resolution. This time interval required to process a pulse, so-called peaking or shaping time, determines effectively the difference between consecutive pulse shapes and may result in undesirable effects in high count-rate applications. As the count rate increases, two events may occur within

a time less than the peaking time of the amplifier. Consequently, the charge signals become indistinguishable, which results in an erroneous *pileup* energy signal. Depending on the degree of pulse overlap, the effect creates the pileup continuum, spanning the energy range between a given full energy peak and twice its energy, contributing to an effective background. Additionally, the pileup continuum features discrete peaks at its upper end, called sum peaks, which represent the exact coincidence in time of two mono-energetic signals, that causes their summation. To aid this effect, a pileup rejector system is usually implemented within the main amplifier, that utilises appropriate electronic logic to discriminate the overlapping pulses, which would otherwise result in ambiguous energy signals. Even in a high count-rate performance, this leads to an effective elimination of the pileup continuum and to a substantial reduction of the sum peaks. Yet, it becomes apparent, that the overall operation of the main amplifier, including the pulse shaping and the pileup rejection, imposes a system dead-time. During this time the system does not accept any new input, which – if substantial – may impair quantitative analysis. Therefore, certain empirical dead-time corrections should be applied to ensure reliability of measured data. In addition, several measures can be taken to prevent the substantial dead-time, e.g. attenuation of the incident X-ray beam, inserting collimation apertures in front of the detector's nosepiece, or retracting the detector. The dead-time should in general stay below 20-30%.

The final component of the pulse processing is a multichannel analyser (MCA), which sorts the output pulses from the main amplifier, according to variation in their amplitudes. It splits the range of the detected pulse amplitudes into discrete increments and, subsequently, counts and stores the number of pulses that fall within a given increment. As the MCA retains the spectral quantitativeness of the voltage signal, the amplitude increments are effectively energy *bins*, referred to as channels. Every peak of a mono-energetic line (its FWHM) should preferably be covered by at least 5 of such channels. Transformation of the pulse amplitude distribution into a digital form is realised by an analog-to-digital converter (ADC). The ADC offers flexibility of choice of the digital offset and conversion gain, that assign, respectively, zero to a particular channel and an energy increment per channel (usually around 10 eV/channel), given the known energy range of an entire spectrum. An associated ADC-conversion time adds to the overall processing dead-time. The resulting array of counts per channel is stored in the MCA memory and can be transferred in a respective file format to an external location.

3.2.2 Evaluation of XRF spectra

Interpretation of an X-ray spectrum requires correct identification and understanding of all phenomena which contribute to its final shape. Below, descriptions of the most important contributions are provided.

Characteristic lines X-ray fluorescence radiation is emitted in a form of narrow spectral lines, characteristic for a given transition in an investigated element. Such a line features a Lorentzian distribution, which upon the convolution with the nearly Gaussian detector response function, results in the so-called Voight profile, usually observed in the measured spectra. Yet, as the detector energy resolution is typically one order of magnitude greater than the natural characteristic line width (Lorentz width), a Gaussian function serves also as an acceptable first-order approximation of the line profile. Finally, as introduced in section 1.2.3, the measured emission spectrum of a given element is a superposition of many transitions. Therefore, all possible satellite lines must be taken into consideration in the analysis.

Background In X-ray fluorescence induced by synchrotron radiation, the background derives primarily from coherent and incoherent scattering of the incident X-ray beam by the sample. An incomplete charge collection of these scattering events from the detector active volume results in a continuum background extending over lower energies in the spectrum. It has a rather complex shape, dependent on the initial spectral profile of the exciting radiation, as well as on the sample composition.

Pileup and sum peaks With the pileup effects being almost completely suppressed in modern digital pulse-processors, only true sum peaks are typically observed in an X-ray spectrum. They originate from summation of two mono-energetic signals, which coincide in time due to very high count rates. Sum peaks are therefore expected when several peaks at lower energy dominate the spectrum. Their position in the spectrum and count rate result from addition of the respective parameters of the two parent-pulses.

Escape peaks Characteristic radiation impinging on the active silicon area of the detector makes the silicon atoms fluoresce, which consequently diminishes the energy of the incident characteristic X-rays by the energy of *escaping* silicon K photons. The resulting lower-energy peaks, referred to as the escape peaks, are hence expected 1.74 keV (Si K_α) below the original parent-peak. Very often, positions of certain escape peaks interfere with positions of the other lower-energy characteristic lines, e.g. Ti K_α at 4.51 keV and the Fe K_α escape peak at 4.65 keV.

Other contributions Apart from being responsible for most of the background, scattering of the incident excitation radiation can additionally be observed in form of two peaks. The first – the coherent scatter peak – occurs at a position of the excitation energy and its width appears similar to a normal fluorescence line. The second – the incoherent (Compton) scatter peak – is in turn shifted towards the lower energies, according to the Compton-effect formula, as in Eq. (1.2.22). Moreover, it features a broader structure, stemming from a wider angular distribution of the incoherent scattering, and hence is rather difficult to model. Another very pronounced spectrum artefact is associated with measurements performed in air, which result in strong characteristic Ar K_α and K_β lines at 2.957 keV and 3.191 keV, respectively. Their elimination is realised by enclosing the specimen and the detector with vacuum, which additionally facilitates detection of low-energy characteristic lines from light elements, that would otherwise be substantially attenuated and scattered by air.

As a proprietary example, Fig. 3.2.2 shows a raw cumulative XRF spectrum obtained during mapping of a thin iron film deposited on a silicon-nitride membrane, used in quantitative XRF analysis in this thesis. The energy of the incident X-ray beam was 7.35 keV, inducing X-ray fluorescence from all atoms up to iron. Inspection of observed characteristic lines permits identification of detectable elements (Si, S, and Fe). As the measurement was performed in air, the strong argon K lines can be observed. Due to substantial count rate of Ar and Fe peaks, above the overlapping scatter peaks, a series of sum-peaks occurs. This part of the spectrum is normally excluded from further analysis.

3.2.3 Processing methods of XRF spectra

A number of mathematical techniques exist to pre-process X-ray fluorescence spectra. This involves, for example, filtering methods allowing for noise reduction and spectra

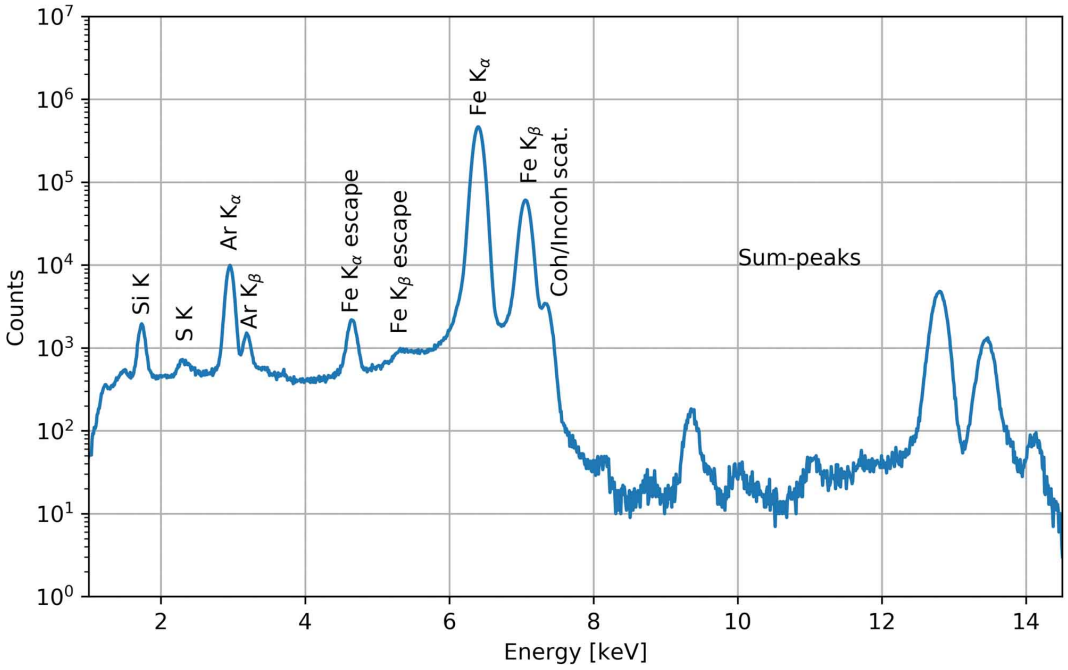

Fig. 3.2.2: A raw X-ray fluorescence cumulative spectrum from an in-air scan of a thin iron film deposited on a silicon-nitride membrane at an excitation energy of 7.35 keV. The spectrum allows for identification of several characteristic lines over the continuum background, with associated escape and sum peaks.

smoothing, which help in inspection of noisy spectra and are incorporated in most of automatic peak search routines. Having pre-characterised the measured spectra, the aim of further analysis is to obtain the number of counts under the characteristic X-ray lines (net peak area) corrected for the background. The net peak area is namely proportional to the concentration of the analyte and, hence, is the basis of quantitative analysis. Probably the most routine approach involves the least-squares fitting algorithm with a prior estimation of the background model. Here, these two steps of XRF spectra processing are discussed: the background estimation via peak stripping and the non-linear least-squares fitting [72].

Background modelling

In general, there are two ways to deal with the continuum background: (1) the background can be estimated and then subtracted from the experimental data before further evaluation of the peaks, or (2) the background can be fitted with an analytical function, which serves as an additional input to the least-squares fitting algorithm and is simultaneously estimated with the spectrum peaks. The method used in this thesis belongs to the first group and is referred to as the peak stripping. It removes rapidly varying signals in a spectrum by comparing the channel content y_i with the contents of its neighbours. More specifically, in an iterative procedure the content of an ith channel is compared against the average m_i of two channels at a distance w away from i, that is:

$$m_i = \frac{y_{i-w} + y_{i+w}}{2} \tag{3.2.1}$$

If the channel content y_i is above the average m_i, it is replaced by the average. Repeating the entire procedure over many iterations makes the peak be gradually *stripped away*.

As the method is very sensitive to local fluctuations in the background due to counting statistics, additional spectrum smoothing prior to the stripping is a compulsory step.

Least-squares fitting

Least-squares fitting method is based on the assumption that the measured spectrum of an unknown sample is a linear combination of spectra of pure elements constituting the specimen. This assumption holds well for background-corrected characteristic lines. It therefore implies, that the content $Y(i)$ of the ith channel can be expressed in terms of the channel contents $y_j(i)$ of m spectrum constituents ($j = 1, \ldots, m$), as follows:

$$Y(i) = \sum_{j=1}^{m} a_j y_j(i) \tag{3.2.2}$$

where a_j are the coefficients determining the contribution of the constituent spectra to the unknown spectrum, used in the subsequent quantitative analysis. The values of a_j coefficients can be obtained by means of multiple linear least-squares fitting. With respect to the coefficients a_j, the method minimises χ^2, given by the following formula:

$$\chi^2 = \sum_i \frac{1}{\sigma_i^2}(Y_i - Y(i, a_j))^2 \tag{3.2.3}$$

where Y_i is the ith channel content and σ_i is the associated uncertainty of the unknown spectrum, while the summation is performed over a given fitting region.

To motivate the need for using the least-square fitting, let us consider the first-order approximation of a single peak profile given by a Gaussian distribution, as follows:

$$P(A, \sigma, x_0) = \frac{A}{\sigma_{\text{ch}}\sqrt{2\pi}} \exp\left[-\frac{(x_i - x_0)^2}{2\sigma_{\text{ch}}^2}\right] \tag{3.2.4}$$

where A denotes the peak area in counts and is a linear parameter, while σ_{ch} is the Gaussian peak width and x_0 is the peak maximum location, both of them expressed in channel number and being non-linear parameters. Therefore, in order to find optimum values for the two latter parameters, a non-linear least-squares fitting procedure must be applied. However, processing a spectrum consisting of many characteristic lines would require to use at least one of such function for each peak, which would dramatically increase number of parameters to optimise (3 parameters per peak). Such an approach would therefore hardly lead to finding the global minimum. Instead, the fitting function can be rewritten to enable fitting of all spectral lines simultaneously. In the peak search step, the elements, that the sample consists of, are identified. Based on this knowledge and tabulated emission lines, all characteristic lines which constitute the spectrum can be predicted. Assuming the following channel-to-energy calibration equation:

$$E(i) = E_0 + \mathcal{G} \cdot i \tag{3.2.5}$$

where E_0 is the photon energy of the 0-th channel and $\mathcal{G}$ is the spectrum gain (in eV/channel), the fitting function can be written in terms of energy, as follows:

$$\mathcal{P}(i, E_j) = \frac{\mathcal{G}}{\sigma_{\text{E}}\sqrt{2\pi}} \exp\left[-\frac{[E(i) - E_j]^2}{2\sigma_{\text{E}}^2}\right] \tag{3.2.6}$$

where E_j denotes the energy of the jth characteristic line and σ_{E} the peak width, given by:

$$\sigma_{\text{E}}^2 = \left(\frac{\mathcal{N}}{2.3548}\right)^2 + 3.85 \cdot F_{\text{Fano}} \cdot E_j \tag{3.2.7}$$

In the last equation, $\mathcal{N}$ is the electronic noise contribution to the peak width (typically 80-100 eV FWHM), F_{Fano} is the Fano factor (for silicon: ~ 0.014)[3.1], and 3.85 is the energy of an electron-hole pair creation in silicon. Subsequently, a response function for the fitted spectrum, consisting of m lines, can be constructed, as follows:

$$Y(i) = \sum_{j=1}^{m} A_j \mathcal{P}(i, E_j) \tag{3.2.8}$$

where $\mathcal{P}$ represents the Gaussian profiles of the all m characteristic lines and A_j their peak areas. The above equation can directly be compared with Eq. (3.2.2), which is an input to the minimisation algorithm.

In conclusion, the task of the non-linear least-squares fit algorithm is to optimise: E_0, $\mathcal{G}$, $\mathcal{N}$, and F_{Fano} for the entire fitting region as well as the peak area parameters A_j. Eqs. (3.2.5) and (3.2.6) can then be used to retrieve the actual positions and widths of all characteristic lines in the spectrum. As a result of this approach, a non-linear fitting of 10 peaks requires now only 14 parameters, instead of 30. Finally, it is important to mention, that in general there exists no direct solution to a case of least-squares fitting, where at least one of the parameters is non-linear. The nonlinear least-squares fitting attempts to find the minimum of a function in an m-dimensional space, such as generally defined in Eq. (3.2.3). The nature of this process is iterative, that requires initial values to start the search. Further details regarding XRF spectra fitting are extensively discussed in [72].

3.2.4 Quantitative XRF analysis

Background-corrected and fitted X-ray fluorescence spectra serve as a basis for further quantitative analysis, in which a direct relationship between the intensity of a given characteristic line and the concentration of the corresponding element is exploited. However, before such conversion, the effect of sample (mass) thickness on X-ray emission must be considered. In general, there are two thresholds: (1) the linear thickness m_{thin} of a specimen below which the absorption effect vanishes, and (2) the linear thickness m_{thick} above which the incident excitation radiation is either fully absorbed in the sample or backscattered from it. These thresholds allow to distinguish three classes of specimens depending on their linear thickness: (1) thin samples, $m < m_{\text{thin}}$, for which the intensity loss of characteristic lines due to attenuation by the sample material is neglegible; (2) intermediate thickness samples, $m_{\text{thin}} \leq m < m_{\text{thick}}$; and (3) infinitely thick samples, $m \geq m_{\text{thick}}$, for which, above the saturation sample thickness m_{thick}, no further increase of characteristic radiation intensity is observed. This issue should be addressed preferably at the stage of sample preparation, when all effects related to attenuation of the incident X-rays (so-called scatter mass thickness) by the specimen and any subsequent self-absorption of the characteristic radiation lines within the specimen must be carefully considered.

In the case of thin samples, the concentration of the constituent elements is approximately a linear function of the intensity of the corresponding characteristic line. It is reflected in the following equation:

$$I_i = M_i C_i \tag{3.2.9}$$

where C_i is the concentration of the analyte i, I_i is the intensity the respective XRF line, and M_i is the sensitivity calibration constant, expressed in counts per concentration

[3.1] Fano factor measures the dispersion of a probability distribution of a Fano noise, which arises whenever energy is converted to an electric charge, e.g. in silicon drift detectors. The Fano noise results from the energy loss in a collision, which is not wholly statistical. The Fano factor is material specific.

unit. This method involves therefore an additional measurement of a series of standards of known composition under the same experimental conditions, in order to find the sensitivity calibration constants for all elements present in the unknown specimen.

More specifically, the expression in Eq. (3.2.9) can be formulated in terms of experiment-related quantities [72]. Given the mass per unit area (areal mass) m_i of the analyte i, the intensity of the corresponding fluorescent radiation can be described by:

$$I_i(E_i) = \mathcal{G}\ \varepsilon(E_i)\ \sigma_i(E_0) I_0(E_0)\ \beta(E_0, E_i)\ m_i \tag{3.2.10}$$

where $\mathcal{G}$ is the geometry factor determined experimentally, $\varepsilon(E_i)$ is the detector efficiency for detecting a fluorescent photon of the energy E_i, $\sigma_i(E_0)$ is proportional to the total photoelectric mass absorption coefficient of the analyte i at the energy E_0 and the fluorescence yield of the given characteristic line, and $I_0(E_0)$ is the incident beam intensity. Additionally, for the intermediate thick samples, the absorption correction coefficient β is necessary, given by the following formula:

$$\beta_i = \frac{1 - \mathrm{e}^{-[\mu(E_0)\csc\Psi_{\mathrm{in}} + \mu(E_i)\csc\Psi_{\mathrm{out}}]m_i}}{[\mu(E_0)\csc\Psi_{\mathrm{in}} + \mu(E_i)\csc\Psi_{\mathrm{out}}]m_i} \tag{3.2.11}$$

where μ is the energy-dependent mass absorption coefficient, and Ψ_{in} and Ψ_{out} are the effective incidence and takeoff angles, respectively.

In quantitative analysis of XRF spectra it is important to be aware of all phenomena which affect the simple linear proportionality, as in Eq. (3.2.9), between the intensity of a given spectral line and the concentration of the associated element. Their collective sum is referred to as the total matrix effect, where matrix is understood as all elements present in a sample except the analyte element. As already mentioned, absorption of the incoming primary X-rays and the resulting characteristic radiation by the matrix is a first contribution to the total matrix effect, which compromises the aforementioned proportionality. Moreover, if the matrix consists of elements whose own characteristic lines (if co-emitted) can make the atoms of the measured analyte fluoresce, it will result in the enhancement of its spectral line. It is known as so-called secondary fluorescence, which significantly impairs the intensity-concentration proportionality. Total matrix-effect can be compensated for using empirical or mathematical methods [72] or avoided by using thin specimens.

Chapter 4

Evolution of the correlative X-ray microscopy experiments

All experiments reported in this thesis were performed at beamline P11 at PETRA III synchrotron light source situated on the premises of the Deutsches Elektronen-Synchrotron in Hamburg, Germany. PETRA III is a third-generation storage ring in operation since 2009. Before, it had been used as a booster ring in high energy particle physics. As a result, it features a uniquely large circumference of 2.3 km, which makes is ideally suited for generation of highly brilliant hard X-rays. PETRA III operates at an electron beam energy of 6 GeV and a beam current of 100 mA in the top-up mode, maintaining the decay of the photon beam flux within 1%. Its ultra-low electron beam emittance, horizontally down to 1 nm rad, makes it particularly suitable for coherence applications. PETRA III provides three experimental halls, which accommodate 15 independent end-stations in the main *Max-von-Laue* hall, with further 6 in two newer *Ada-Yonath* and *Paul-P.-Ewald* halls in operation since 2016, and 4 more beamlines in the planning or construction phase.

Beamline P11 is located in the Max-von-Laue experimental hall and is dedicated to state-of-the-art and high-resolution structural investigations of biological specimens on complementary length scales, by means of X-ray crystallography and multimodal X-ray microscopy. Fig. 4.1 shows a schematic layout of P11. X-rays are generated by a 2-m-long U32 undulator situated in a high-β section of the PETRA III storage ring. It results in

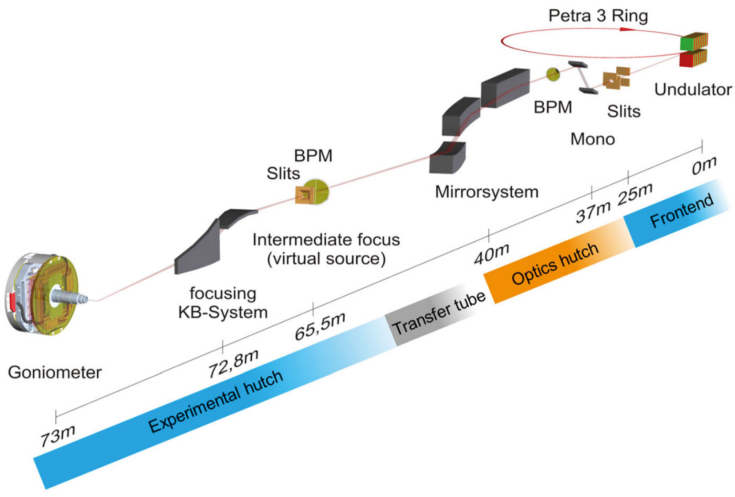

Fig. 4.1: Schematic layout of beamline P11 at PETRA III synchrotron light source. Reproduced from [73].

a source size of $141.5 \times 4.9\,\mu m^2$ (h×v, RMS) and a divergence of $7.1\,\mu rad \times 2.1\,\mu rad$ (h×v, RMS) [74]. The beamline front-end comprises a set of horizontal and vertical power slits. Further downstream, the beam enters the optics hutch, where it is monochromatised by a double crystal silicon monochromator actively cooled with liquid nitrogen. The monochromatic fraction of the beam is further reflected and (de)focussed by a set of two horizontally deflecting Kirkpatrick-Baez (KB) mirrors and one vertically deflecting KB mirror. Their first task is to achieve enough horizontal separation from the neighbouring beamline (P12). Furthermore, as all mirrors can be actively bent concavely, i.e. focussed, such an optical configuration allows to generate a secondary source at a distance of 65.5 m, which is a typical setting in crystallography experiments. The horizontally deflecting mirrors can be also bent convexly, resulting in beam defocussing, exploited in the first phase of the X-ray microscopy experiments. Long-term stability of the X-ray beam is achieved at P11 with a beam-position closed-loop feedback system. Using two beam position monitors – first 2 m downstream of the monochromator and second at the position of the secondary source – the beam position is constantly monitored and stabilised with the grazing angle of the second horizontally deflecting KB mirror and the pitch of the second monochromator crystal. Further measurement stability is ensured by an 8-meter-long granite block, being a key feature of the experimental hutch and serving as a vibration-damping support for both end-stations.

The first end-station developed at P11 was the macromolecular crystallography, available in user operation since 2013 [73]. In mid-2012, first proof-of-concept experiments with scanning transmission X-ray microscopy took place [75], denoting begin of the development of a scanning X-ray microscope at P11 [76]. The ultimate goal of this project was set to provide an in-vacuum *bio-imaging* instrument with a cryogenic sample cooling environment. The setup was supposed to be optimised for photon energies between 7 keV to 10 keV and able to exploit phase and elemental contrasts of biological matter by means of two scanning probe imaging methods: X-ray ptychography and X-ray fluorescence mapping. This ambitious aim has required reaching several milestones in order to test and gradually upgrade the in-house designed instrumentation, as well as to gain necessary experience in sample preparation, data acquisition, and evaluation.

Mutual coexistence of both the crystallography and the bio-imaging end-stations in the P11 experimental hutch (EH) has imposed certain order, according to the design of the beamline optics and requirements of both experiments. Two in-vacuum chambers accommodating: (1) the secondary source (with auxiliary beam slits and attenuation filters) at the beginning of the EH, and (2) the second KB-mirror system at the rear of the EH, occupied in total around 2.5 m of the beamline granite block. The remaining space of about 5.5 m between the chambers was dedicated to the bio-imaging experiment. To ensure the maximum propagation distance between the sample and the detector necessary for ptychography, the X-ray microscope was positioned at 1.5 m downstream of the secondary source, i.e. 67 m away from the source. In a default configuration (flat KB mirrors in the optics hutch), it resulted in the theoretical transverse coherence lengths spanning an area of $14.6 \times 421.3\,\mu m^2$ (h×v) at a photon energy of 6.4 keV at the position of the microscope.

In the first phase, the focus of the bio-imaging project was to establish X-ray ptychography at beamline P11 and evaluate the resolving power of the prototypical scanning microscope in 2D imaging of radiation-resistant, strongly-scattering test structures. In such an arrangement ptychography was reported to yield spatial resolutions down to 10 nm in the hard X-ray regime [77, 78]. Not only did it require to meet stringent requirements of stability and precision of sample positioning, but also to optimise the coherent flux and the spatially coherent area of X-rays delivered to the experimental hutch of beamline

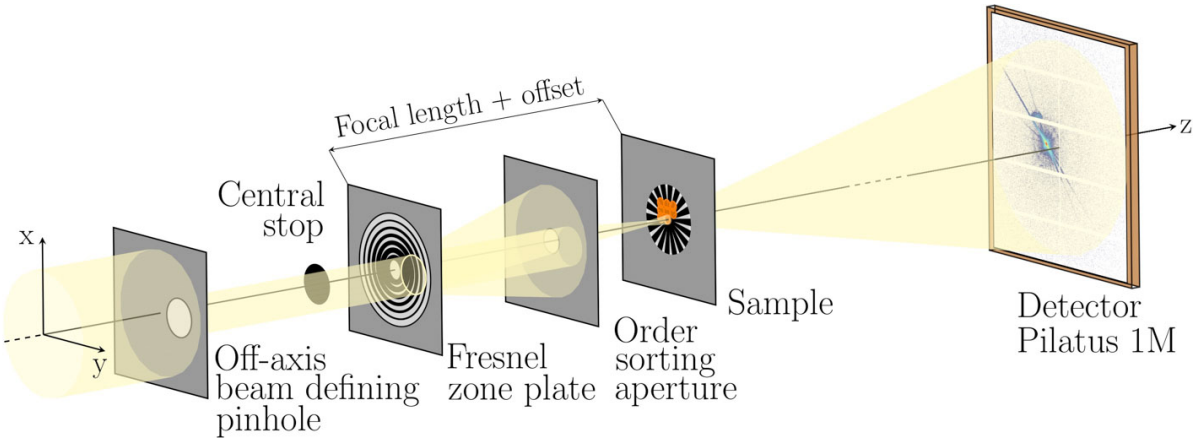

Fig. 4.2: Scheme of the prototypical experimental setup for ptychographic imaging in 2D at beamline P11 using an off-axis illuminated Fresnel zone plate and a single photon counting Pilatus pixel detector for recording coherent diffraction patterns. Reproduced from an own publication in [50].

P11. The latter was addressed by exploiting highly flexible X-ray optics of P11 in the opposite manner to the standard *focussing* settings for crystallography experiments. As mentioned in the beamline description, both horizontally deflecting KB mirrors could be defocussed causing demagnification of the source. In this way, the horizontal spatial coherence could heuristically be improved even by the factor of 2. Fig. 4.2 shows a schematic of the first experimental setup used for ptychographic imaging in 2D at P11. As a compromise between focussing efficiency in the energy range of the microscope operation, robust alignment, and spatial restrictions, Fresnel zone plates (FZP) [21] were chosen as a focussing optic[4.1] Their use required implementation of an order sorting aperture (OSA) downstream of the lens, to select the most efficient first-order focus, and a central stop upstream of the lens, to block the direct beam that would otherwise leak through the OSA. Yet, with a typical FZP diameter of 100 µm, the available spatial coherence area could still only partially match the zone plate's aperture. Therefore, upstream of the lens a beam defining aperture was installed to select only fully coherent X-rays. Such an off-axis illumination resulted in a proportional decrease of the numerical aperture of the lens which, though, was not considered a limitation, as spatial resolutions offered by ptychography would not depend on the focal spot size any longer. The first experimental setup used a conservative circular off-axis beam defining pinhole, whose diameter was to match the shorter, i.e. horizontal, transverse coherence length. The microscope consisted of piezomotorised x/y stages for positioning of the optical elements and the specimen. All these efforts resulted in first successful ptychographic experiments in late 2013 and early 2014, which focussed on comparing the quality of ptychographic reconstructions from measurements recorded at different degrees of spatial coherence. By means of the multimodal reconstruction algorithm (section 3.1.2.3), intensity fractions of the respective coherent probe modes were obtained, which allowed to verify the capacity of P11 for coherent diffractive imaging experiments. Finally, under the best conditions of spatial coherence, the resolving power of the scanning microscope was demonstrated down to 10 nm in imaging of a highly scattering test structure. Detailed discussion and further experimental parameters can be found in [50].

[4.1] A Fresnel zone plate is a diffractive X-ray optical element, whose first-order focal length f depends on the incident radiation wavelength λ, the lens diameter D, and its outermost zone width Δr, i.e. $f = D\Delta r/\lambda$.

The second phase of the project began in 2015, after a 14-month-long shutdown of PETRA III dedicated to construction of two extension experimental halls. It was targeted at exploiting the scanning nature of ptychography which allows for a simultaneous acquisition of nanoscale X-ray fluorescence (XRF). The main objective was therefore a necessary upgrade and stepwise optimisation of the experimental setup to enable concurrent measurement of both coherent diffraction patterns and X-ray fluorescence spectra. A pilot experiment took place in November 2015, using a standard 2D ptychography scanner complemented with an SDD X-ray fluorescence detector (Vortex-EM). Due to a right angle between the sample and the incident beam, the XRF detector had to be installed in a slightly back-scattering geometry to facilitate detection of fluorescent radiation emitted by the specimen. In this exploratory experiment, a part of an electroplated aperiodic and dual-tone test structure was scanned at a photon energy of 8.5 keV, acquiring simultaneously both ptychographic and XRF datasets. The sample was deposited on a silicon-nitride membrane and consisted of electroplated golden fossil-diatom-like structures overlaid with overplated nickel particles. Fig. 4.3A shows its SEM image with the exact scan area denoted in red. The reconstructed ptychographic phase image of this area is shown in Fig. 4.3B. Significant penetration power of X-rays allowed to see beyond the nickel particle of a rather undefined shape to reveal much sharper golden structures. The scan was performed with a 340-nm probe, whose reconstructed amplitude distribution is shown in Fig. 4.3C. Simultaneously to ptychographic imaging, XRF spectra were recorded which allowed to obtain the Ni K-line map of the scanned area, as shown in Fig. 4.3D. The shape of the nickel particle coincided with the one obtained from ptychography. This particular measurement was recorded with an exposure time of 1 s per scan point and a step-scan approach, meaning that the sample motors would accelerate, move between the neighbouring illuminated areas, and stop for the diffraction and fluorescence data to be acquired. Despite the positioning accuracy, such scanning approach generated substantial time overhead. For that version of the experimental setup it meant that decreasing the exposure time below 200 ms per scan point would not result in an acquisition rate faster than 5 Hz. The scanned area rates of only up to $0.026\,\mu m^2\,s^{-1}$ could be achieved with a sub-micron beam size. To improve the measurement throughput, more time efficient scanning schemes had to be implemented, as well as the XRF detector position had to be optimised to maximise the solid angle of XRF detection.

4.1 Concurrent ptychography and XRF in 2D

With advances in instrumentation, the limitations encountered in the pilot experiment could fortunately be addressed. Characteristics of ultralow-emittance synchrotron storage rings, such as PETRA III, have namely triggered substantial development in fast scanning approaches, permitting an efficient use of the augmented X-ray flux. One of the possible solutions was then to abandon the precise, yet slow, step-scanning and replace it with the continuous-motion scanning scheme, known already from the conventional scanning nano-probe microscopy. In this approach the specimen was moved at a constant speed across the focussed X-ray beam, while externally-triggered detectors would acquire data at a requested frame-rate, that eventually defined the spatial step size of a scan. Adaptation of the continuous-motion scanning in ptychography [79, 80, 81] was facilitated by the mixed-state reconstruction algorithm [49], which allowed to treat the smearing in diffraction data, resulting from the motion blur, as decoherence along the fast-scan axis. This ability of reconstructing still sharp images from somewhat obscure

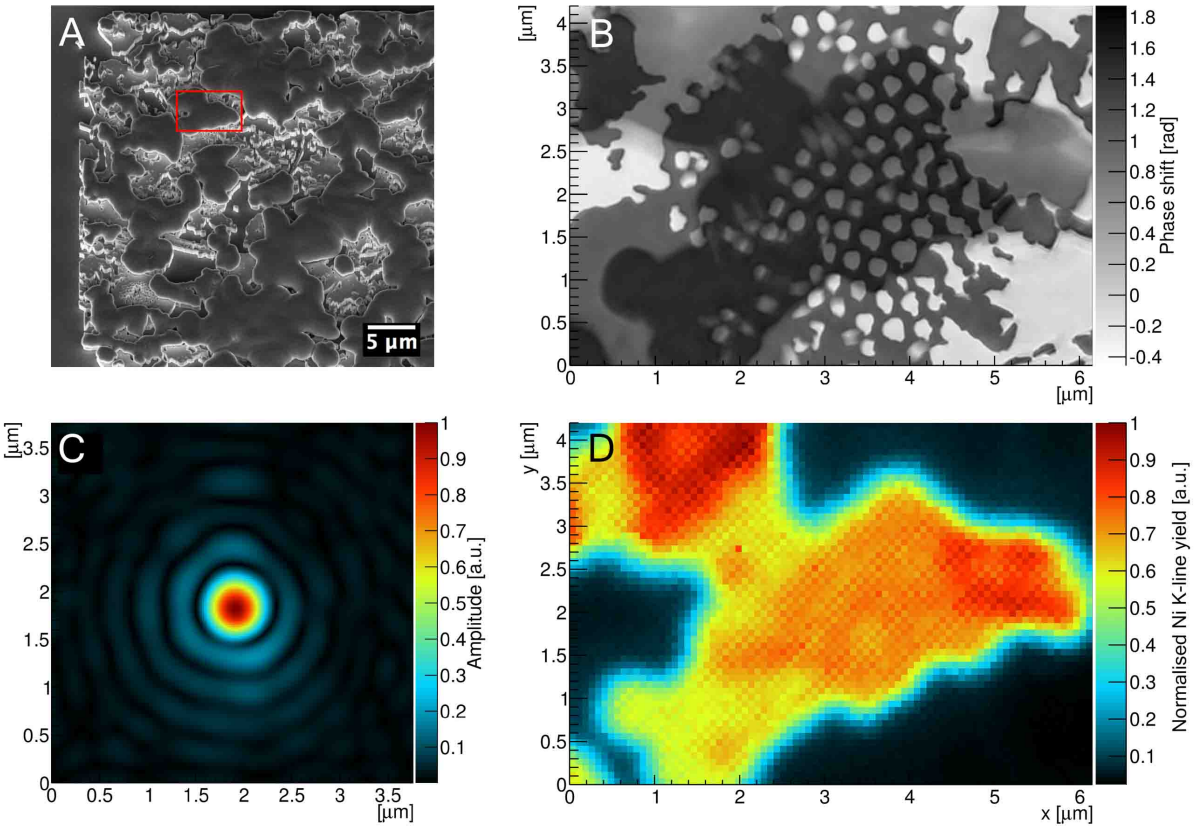

Fig. 4.3: First concurrent ptychographic and X-ray fluorescence (XRF) imaging of an aperiodic dual-tone test structure at an energy of 8.5 keV at beamline P11. (A) shows a scanning-electron micrograph of the sample consisting of overplated nickel particles superimposed on sharper electroplated golden structures. The red rectangle denotes the actual scan area. (B) shows the ptychographic phase image of the selected region revealing both overlaid nickel and gold structures, obtained using 200 iterations of the difference-map algorithm. The scan was recorded using a step-scan carriage-return trajectory and a symmetric 340-nm probe whose amplitude reconstruction is shown in (C). Simultaneously to coherent diffraction, XRF spectra were acquired, yielding the Ni K-line map (D). The shape of the nickel particle is in agreement with results obtained by ptychography.

Tab. 4.1: Evolution of the simultaneous 2D ptychography and X-ray fluorescence experimental setup.

Parameter	**Pilot**	**Commissioning**		**Application**
	Nov. 2015	**Jun. 2016**	**Nov. 2016**	**Jun./Aug. 2017**
Front-end slits	open			
Optics hutch mirrors	both horizontal: convex (defocussing), vertical: flat			
Beam defining aperture	circular pinhole		laster-cut slits	piezomotorised slits
Incident flux measurement	NA			silicon photodiode thickness: 25 µm
Fresnel zone plate Δr	60 nm	30 nm		
OSA holder	aluminium alloy			silicon
Sample mount	cylindrical	kinematic, ThorLabs		
Sample–incident beam angle	90°	75°		
Scanning mode	step-scan	carriage-return fly-scan		
Triggering	software	hardware, PiLC		
Flight tube	evacuated			He-flushed
Detector (ptychography)	Pilatus 6M	Eiger 1M	Pilatus 1M	Pilatus 1M/300k

fly-scan diffraction patterns has certainly rendered a prospect of the considerable decrease of measurement time overhead, leading to an efficient mapping of significantly larger areas. Yet, the so-far proposed piezo scanning units have offered an effective scan area of around $100 \times 100\,\mu m^2$ with an interferometric control of motor positions [82, 83, 84, 85, 86]. While it was sufficient for imaging of single cells and confined tissue volumes, scanning larger areas was still prone to artefacts induced by a coarse positioning system [87]. In order to overcome these limitations, the aim of the next stages of the bio-imaging project was to develop a flexure-based piezomotorised stage, allowing for high-throughput and seamless measurements within an area of $4 \times 4\,mm^2$, using continuous-motion scanning. Tab. 4.1 summarises evolution of certain key aspects of the multimodal scanning microscope at P11 from the pilot phase in late 2015, throughout the commissioning phase in 2016, till the application phase in 2017. In the following, the two latter phases will be discussed.

4.1.1 Commissioning phase

Year 2016 was dedicated to commissioning and first measurements using an upgraded setup for simultaneous continuous-motion-scan ptychographic and X-ray fluorescence imaging. The first experiment took place at beamline P11 in June 2016. Fig. 4.1.1A shows a schematic layout of the scanning microscope. Coherent fraction of X-ray beam was still selected with a conservative circular off-axis beam defining pinhole (BDP), followed by a central stop (CS) to block the direct beam. First-order focus of a partially illuminated Fresnel zone plate (FZP) was selected by an order sorting aperture (OSA). The specimen was placed in the vicinity of the back-focal plane and tilted by 15° to normal incidence to facilitate detection of XRF signal. Using an inhouse-developed x/y scanner, the sample was raster-scanned across the beam. The far-field diffraction patterns were recorded by a single photon counting detector Eiger 1M[4.2] (pixel size: 75 µm) positioned downstream

[4.2] kindly lent by Dectris Ltd., Switzerland, `https://www.dectris.com`

of the sample at a distance of 2.6 m. Along the propagation distance, an evacuated flight-tube was installed to suppress absorption and scattering of X-rays in air. Simultaneously, at each scan point, an XRF spectrum was acquired using an XRF silicon drift detector, Vortex-EM, with a total active area of 50 mm^2.

Fig. 4.1.1B shows the actual realisation of the scanning microscope revealing its mechanical design details. The incident X-rays were coming in from the right side, through a Kapton window at the exit of the evacuated flight-tube. The first two elements in the beam, i.e. the BDP (1) and the CS (2), were attached to two x/y piezo-motor stages. Third element in the beam path were the FZPs used for nano-focussing of the X-rays. The FZPs were deposited on a silicon-nitride membrane which was glued to the downstream end of an aluminium tube. The tube was inserted into a solid support (3) and then fixed with two screws from the top. The position of the FZPs along the beam could be manually adjusted to a given FZP focal length (here approx. 35 mm). As the FZP focal length is proportional to the photon energy, further fine-tuning of the X-ray beam footprint on the sample was realised by slightly changing the energy of the incident X-rays. Unlike in the pilot experiment, the upgraded setup utilised lenses with a higher numerical aperture (outermost zone width: 30 nm) to let the diffracted cone diverge more, spreading the intensity signal over a larger detector area and avoiding, thereby, saturation of pixels due to the count-rate limit. Fig. 4.1.1C provides a magnified view of the setup in the sample area.

The FZPs were followed by an OSA manufactured from platinum, which was placed approximately 2 mm upstream of the sample. The OSA was glued to an aluminium-alloy support (alloy EN AW-7075: Mn 0.3 Mg 2.1-2.9). The aluminium support was attached to an x/y piezomotor stage (4) using a magnetic coupling.

The specimens were prepared on silicon-nitride membranes. For the measurements these membranes were glued to a sample kinematic base plate, Thor Labs KBT1X1T (7), also shown in Fig. 4.1.1D. Such a base plate was magnetically mounted on the sample scanner (6). Main element of the sample scanning unit was a 2D piezomotor-driven flexure stage. The flexure was manufactured from titanium alloy Ti-6Al-4V with electrical discharge machining (EDM). It was capable of scanning a $4\times4\,mm^2$ field of view. The two scanning axes were each equipped with linear encoders and operated in closed loop. For an independent positioning reference the scanner was further complemented with two interferometric sensors. For this, the sample scanner was equipped with two perpendicular mirrors which reflected signals of the interferometer lasers. During the measurements, the positions obtained from the incremental encoders were observed to be affected by intrinsic distortions on a micrometer level compared to the interferometer signals.

Both the OSA piezo-motor stage (4) and the sample scanning unit (6) were fixed at a 15° angle with respect to the normal incidence to optimise the signal acquired with the Vortex-EM XRF detector (5). A tilt of the entire scanner unit ensured a constant position of the sample-beam interaction point along the beam direction and hence the same beam size over the entire scan range. The aluminium OSA-support was in turn positioned perpendicularly to the incident beam to avoid any beam clipping (see Fig. 4.1.1C).

The entire setup was mounted onto XYZ stepper motor translational Kohzu stages (not shown here) allowing to align the X-ray microscope with respect to the X-ray beam. Alignment of the microscope required a CCD camera positioned within a short distance behind the sample scanner. The alignment procedure was performed in the following order: (i) alignment of the FZP with the XYZ stepper-motor tower, (ii) alignment of the BDP, the CS, and the OSA with respect to the FZP, (iii) inserting and aligning a test sample, (iv) optimising the distance between the sample and the XRF detector.

As mentioned at the beginning, one of the key features of this setup was to minimise

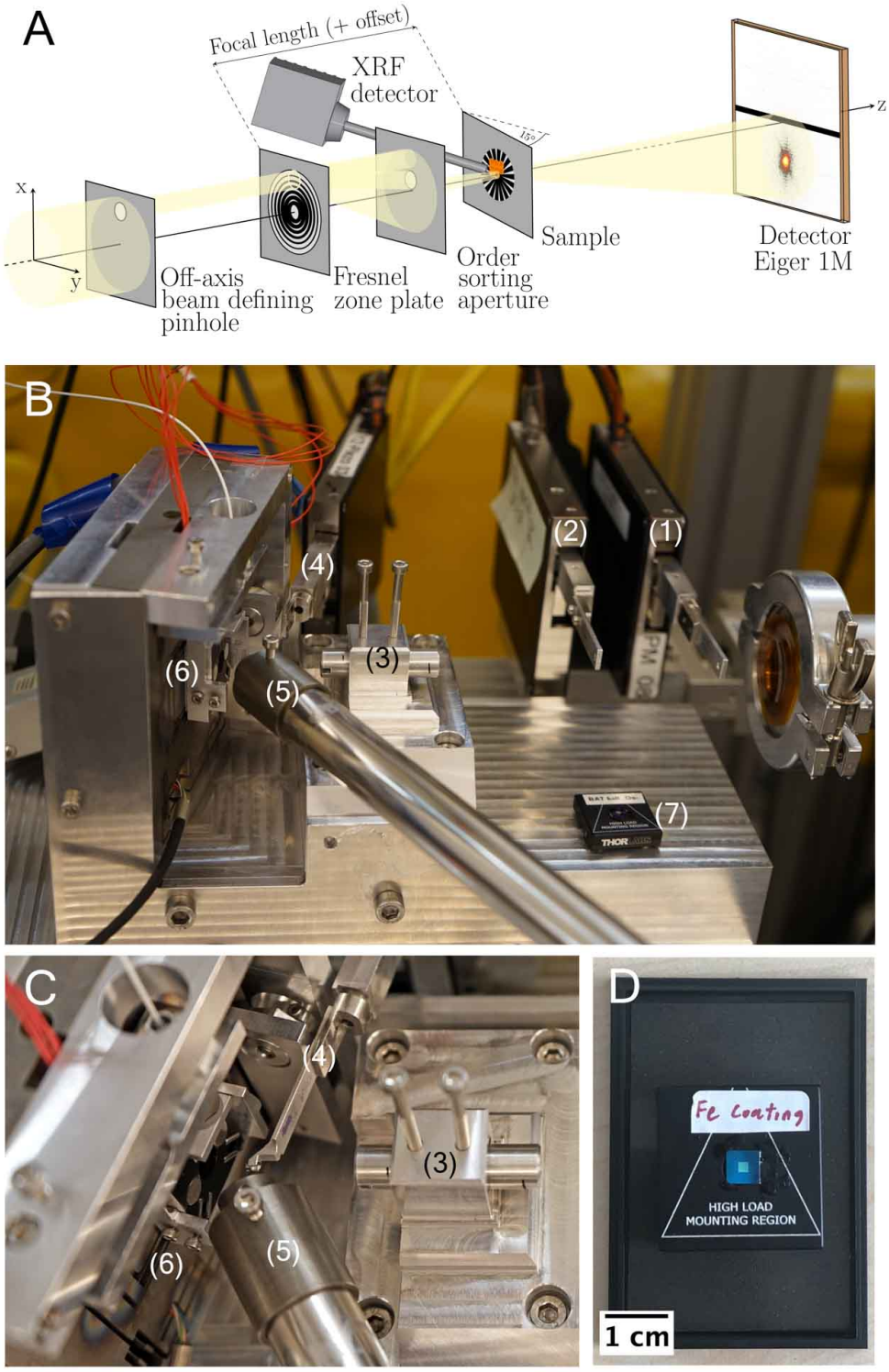

Fig. 4.1.1: Experimental setup for simultaneous ptychographic and X-ray fluorescence imaging in 2D at beamline P11 during the commissioning phase in 2016. (A) shows a schematic layout denoting an off-axis illuminated Fresnel zone plate (FZP), (B) presents the actual realisation indicating the following components: (1) beam defining pinhole, (2) central stop, (3) unmotorised, fixed support for FZPs attached to the downstream end of an aluminium tube, (4) order sorting aperture, (5) silicon drift detector Vortex-EM, (6) flexure-based scanning unit, and (7) sample kinematic base plate. (C) shows a closer view of the sample area and (D) a silicon-nitride membrane with the specimen, attached to the ThorLabs kinematic base plate, on a magnetic bottom surface of the sample transfer box (transparent cover removed for clarity).

the measurement time overhead with the continuous-motion scanning. Here, the fly-scan was realised using the Raspberry Pi Logic Controller (PiLC), a multifunctional and customisable FPGA-based module for fast signal processing developed by the Experiment Control group at DESY Photon Science. The PiLC TTL output was used to send a 5 V standard trigger signal to synchronously acquire data with two detectors and to collect motor encoder and interferometer positions at the same frame rate. The carriage-return continuous-motion scanning was implemented in the following manner: the sample was set at a position a few micrometers before the starting position. The offset allowed the horizontal motor to accelerate to the desired continuous-scanning speed. The starting horizontal position was fed into the PiLC, which would start sending the triggers only once the horizontal motor had reached that position. From that point on, the device would emit a given number of triggers at a specified frequency. The trigger signal length and period were decoupled and could be set up according to the specifications of the detectors. The motor would continue driving a few micrometers beyond the ending position so that its deceleration would not affect the data recorded at the end of the line. Afterwards, the motor would advance to the next line at a maximum design speed to reduce the time overhead. At the end of each scan line, the motor position data were retrieved from the PiLC buffer and flushed into an HDF5 metadata file together with XRF spectra and relevant beamline status parameters.

The first experiment in June 2016 was performed using a scanning script with a graphical user interface and featuring only an implementation of the aforementioned carriage-return continuous-motion scanning routine. Fly-scan performance of the setup was first tested in imaging of silicified and unstained macrophage cells deposited on a silicon-nitride membrane. Silicification of the cultured cells was meant to transform their complex cellular structure into a stable biocomposite silica frustules [88]. Such an approach allowed to enhance the imaging contrast of otherwise weakly-interacting biological matter and generate quasi-biological test samples with arbitrary arrangement of structures at various length scales. Fig. 4.1.2A shows the ptychographic phase image of a representative silicified macrophage, acquired with 50-nm step size at a frame rate of 20 Hz with a symmetric 180-nm probe (FWHM). As the image consisted of around 180 000 diffraction patterns, every second diffraction pattern was taken to create two complementary sub-datasets, which were then reconstructed independently. The resulting images were subsequently used to evaluate the resolving power of the microscope using Fourier ring correlation (FRC) method [89]. Fig. 4.1.2B shows the FRC curve with the respective resolution threshold lines. As two correlated images originated from the same measurement, the intersection of the FRC curve with the 1/2-bit threshold line determines the adequate half-period resolution limit, i.e. 53 nm. Further experimental parameters are provided in Tab. C.1 (Appendix C).

Simultaneous acquisition of both ptychographic and X-ray fluorescence datasets in the continuous-motion-scan mode was tested in imaging of a thin brown adipose tissue section labelled with 30-nm superparamagnetic iron-oxide nanosomes (SPIOs) [90, 91, 92]. The SPIOs were multifunctional nanoparticle probes designed for medical imaging to facilitate selective targeting of atherosclerotic plaques. By binding to certain target molecules, the nanoparticles could serve as a new medical diagnosis tool. Fig. 4.1.2C shows the reconstructed ptychographic phase (in greyscale) overlaid with the normalised Fe K-line distribution map (in red-scale). The measurement was performed with a 100-nm step size at a frame rate of 5 Hz and with a symmetric 200-nm probe (FWHM). The scan speed was vastly limited by a rather low level of detectable XRF signal. Detailed experimental parameters are provided in Tab. C.1 (Appendix C). Resolution of the iron map was evaluated using its radially-averaged power spectral density (PSD), as shown in Fig. 4.1.2D.

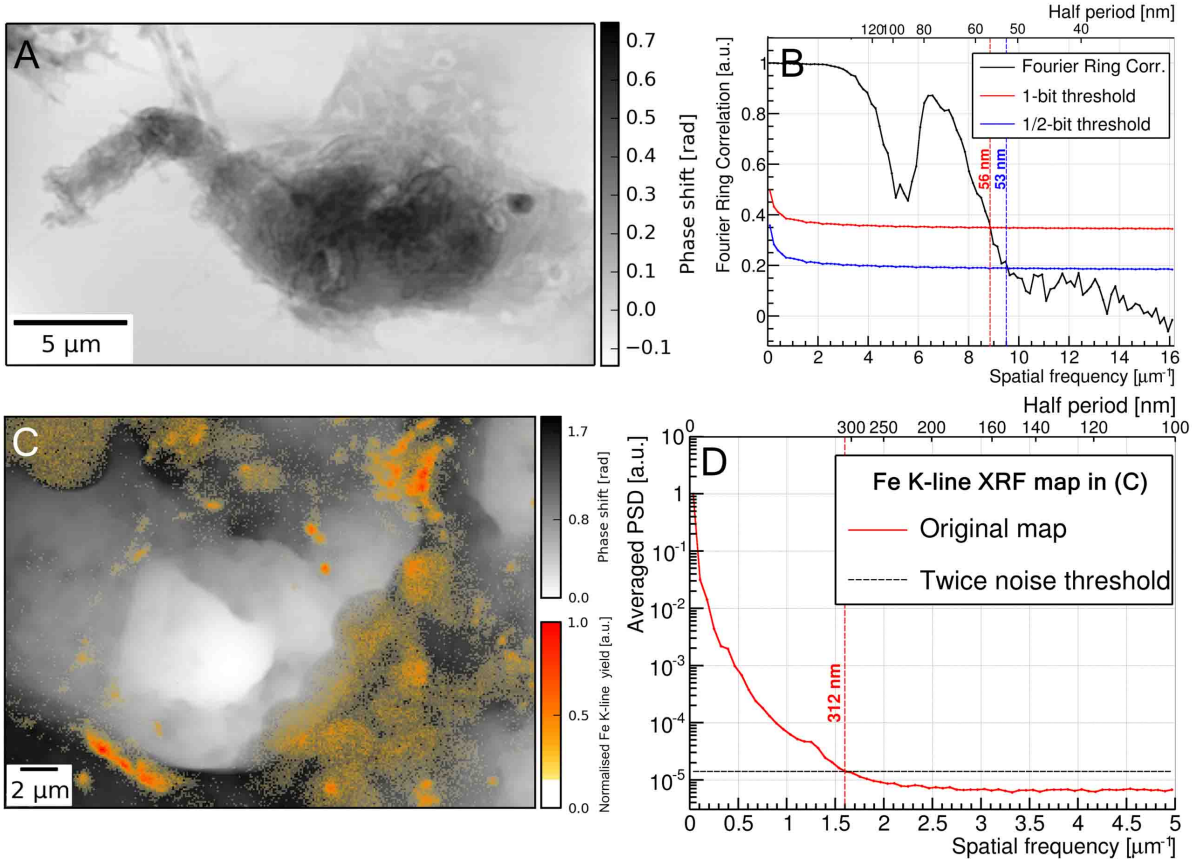

Fig. 4.1.2: Preliminary experiments using the 2D X-ray microscope at beamline P11 in a continuous-motion-scan mode. (A) shows the ptychographic phase image of a silicified and unstained macrophage at a spatial resolution of 53 nm, as indicated by the intersection of the Fourier ring correlation curve and the 1/2-bit threshold line in (B). (C) shows iron K-line XRF map (in red-scale) superimposed on the reconstructed ptychographic phase (in greyscale) of a thin brown adipose tissue section labelled with superparamagnetic iron-oxide nanosomes. In (D), the spatial resolution of the Fe map equals 312 nm and was determined by an intersection between its radially-averaged power spectral density (PSD) and the threshold line denoting twice the noise level. Both ptychographic reconstructions were obtained by the difference-map algorithm with a single probe mode, using 100 iterations in (A) and 150 iterations in (C).

Its intersection with the threshold line, denoting twice the noise level [93], determines the spatial resolution limit of 312 nm, which corresponds well with the probe size (200 nm) enlarged by the fly-scan step size (100 nm).

Both preliminary measurements allowed to test the full operation of the scanner and evaluate its resolving power capabilities in both imaging modalities. The given implementation of continuous-motions scanning increased the scanned area rate up to about $0.043\,\mu m^2\,s^{-1}$ at an overall time overhead of 15%. The measurement throughput with simultaneous XRF mapping could further be improved by exploiting the entire spatial coherence area of the incident beam.

In November 2016, the second commissioning experiment took place, introducing a few modifications to the setup used in June (for a summary, see Tab. 4.1). The incident photon flux was increased by substituting the circular beam defining pinhole with laser-cut slits. Manufactured from tantalum in three rectangular shapes (h×v): $30\times50\,\mu m^2$, $30\times80\,\mu m^2$, and $30\times100\,\mu m^2$, the slits accounted for an asymmetric spatial coherence area (wider vertically than horizontally). Additionally, as this time a Pilatus 1M detector (pixel size: 172 µm) was used to record coherent diffraction patterns, the sample-to-detector distance was increased to 4.5 m, to avoid pixel saturation due to the count-rate limit. Finally, the GUI-based scanning script was optimised and replaced by two command-line scripts for step- and fly-scanning, respectively. In this way, many consecutive scans could be batched in a single shell script. Exploiting the key feature of the 2D scanning stage, i.e. ±2-mm scanning ranges in both directions, several targets (e.g. biological cells) within an entire silicon-nitride membrane could first be preselected without any secondary coarse positioning and then batch-scanned using the programmable scripts. This allowed for an efficient use of e.g. night shifts, without need of any direct scientific supervision.

In this form, the experimental setup was mature enough to explore potential biological applications possible within the established collaborations. Moreover, the measurements allowed to test sample preparation protocols and the pipeline of correlative imaging consisting of: (1) visible-light microscopy and fluorescence imaging in the auxiliary laboratory of beamline P11, (2) X-ray microscopy at P11, and (3) post-beamtime scanning electron microscopy of selected areas at DESY NanoLab[4.3].

Such an approach was applied in imaging of a monolayer of cultured macrophage cells infected with *Shigella*. The bacteria were genetically modified with a green-fluorescent protein, making them emit bright green light when exposed to visible light. Cells were stained with osmium tetroxide to enhance contrast in X-ray imaging. Fig. 4.1.3A shows a visible-light micrograph of the silicon-nitride membrane's corner with a monolayer of infected macrophages. The differential interference contrast image in greyscale was overlaid with the green fluorescence signal, indicating locations of many *Shigella* bacteria. In the inset the preselected cell is shown, denoted with a red rectangle in the overview image. Fig. 4.1.3B shows the subsequently obtained ptychographic phase reconstruction of the preselected macrophage. Black arrows indicate anticipated two groups of bacteria, whose location correlates well with the low-resolution visible-light image in Fig. 4.1.3A. Detailed experimental parameters are provided in Tab. C.1 (Appendix C). As an *a posteriori* measurement, Fig. 4.1.3C presents the scanning-electron micrograph of the same cell's surface. Amongst the cell membrane ruffles none of bacteria was observed, suggesting their internalisation within the cytosol.

Full operation of the scanning X-ray microscope was verified in preliminary measure-

[4.3] access to instruments and services available at DESY NanoLab can be granted upon an application in the PETRA III proposal system and is available for external users.

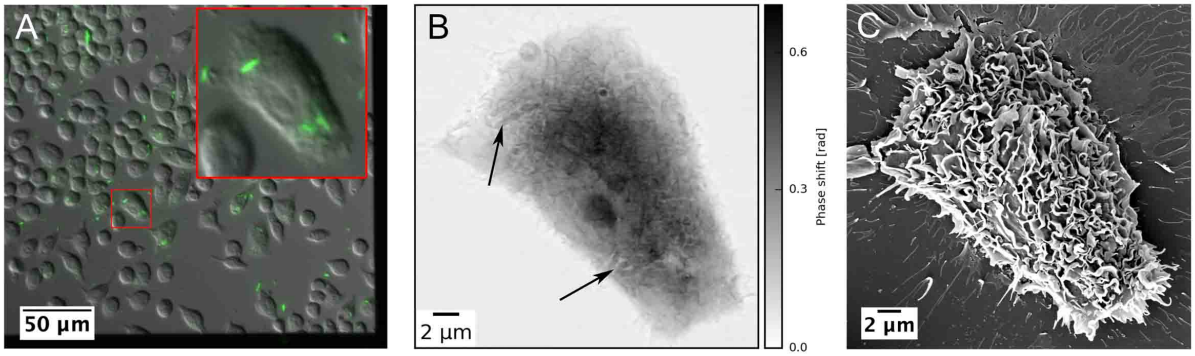

Fig. 4.1.3: Correlative imaging of *Shigella*-infected macrophage cells. (A) shows the differential-interference-contrast image (in greyscale) of a silicon-nitride membrane's corner with macrophage cells, overlaid with the green-fluorescence signal from tagged bacteria (in green). A magnified view of the preselected cell (red rectangle) is presented in the inset. (B) shows the X-ray ptychographic phase image of the cell, acquired at an energy of 7.35 keV, with black arrows indicating two bacteria groups. The ptychographic reconstruction was obtained by 200 iterations of the difference-map algorithm with a single probe mode. (C) shows the cell's surface image obtained by scanning electron microscopy. Absence of bacteria suggests their internalisation within the cytosol.

ments of macrophage cells treated iron-oxide nanocontainers. Following the aforementioned correlative approach, in this case both the ptychographic phase images and the simultaneously obtained iron X-ray fluorescence maps of preselected cells were correlated with their SEM images. An example of such a measurement is shown in Fig. D.1 in Appendix D. The iron map revealed several agglomerates of iron-oxide nanocontainers. The ptychographic phase reconstruction provided in turn a high-resolution projected morphology of the cell which allowed to contextualise occurrence of the agglomerates within the cell. Finally, the SEM image of the cell's surface revealed which of the agglomerates were internalised in the cell, that was a valuable contribution of this preliminary study. Thanks to the batch-scanning capability, many cells were scanned, allowing to observe that a substantial fraction of cells would not adhere well to the membrane, taking a highly spherical shape. This resulted in very few features visible in 2D ptychographic projections, indicating need of improving the sample preparation protocol. Last but not least, the acquired XRF maps sometimes exhibited artefacts due to sudden changes in intensity of the incident beam, that could not be entirely mitigated by the beam-position feedback system of P11.

In both experimental demonstrations, the scanner operated in a continuous-motion-scan mode, yielding scanned area rates of about $0.057\,\mu m^2\,s^{-1}$ with an overall scanning time overhead up to 14%. An astigmatic probe with a size of $200 \times 300\,nm^2$ was used.

4.1.2 Application phase

Both commissioning experiments in 2016 allowed to test the multimodal 2D scanning microscope at beamline P11, indicating its strengths and pointing out recommended improvements. In 2017, final modifications of the setup were implemented resulting in a mature instrument. This marked the beginning of the application phase, which consisted of two successful experiments dedicated to two different biomedical cases, discussed thoroughly in chapter 5. In this section, the final design of the setup is described.

The final version of the in-air 2D scanning microscope allowed for quantitative cor-

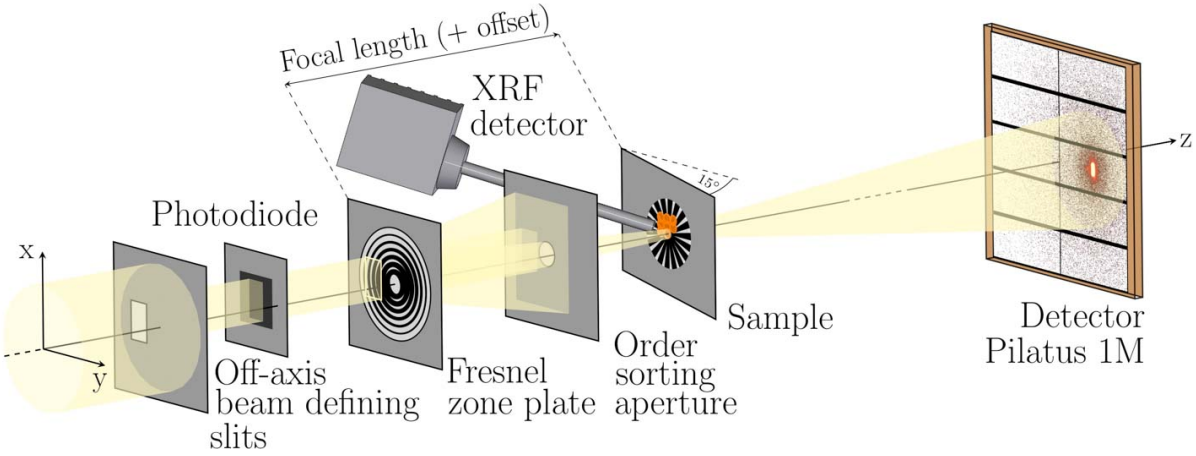

Fig. 4.1.4: Scheme of the experimental setup for simultaneous ptychographic and X-ray fluorescence imaging in 2D at beamline P11 in the application phase in 2017. The setup used a silicon photodiode for incoming flux measurement, an off-axis illuminated Fresnel zone plate, a silicon drift detector for X-ray fluorescence acquisition, and a single photon counting Pilatus pixel detector for recording coherent diffraction patterns.

relative studies of first-row transition metals in major and minor concentrations in the context of biological structure, by means of simultaneous ptychographic and X-ray fluorescence imaging. Fig. 4.1.4 shows a conceptual layout of the microscope. As introduced in the second experiment of the commissioning phase, the coherent fraction of the beam was selected with off-axis and, preferably tuneable, beam defining slits. Further downstream, a thin photodiode would monitor and measure the intensity of the incident beam, enabling normalisation of the recorded XRF maps. Central stops turned out to be redundant due to the off-axis illumination and were removed from the setup. Arrangement of the remaining optical elements remained unchanged. To increase safety of experiments at negligible decrease of diffraction data quality, the flight-tube between the sample and the far-field detector was not evacuated anymore, but flushed with helium.

Mechanical design of the final version of the 2D microscope retained most of the important elements from the commissioning phase, introducing though some improvements. Fig. 4.1.5 shows rendered views of the final mechanical design, with the X-ray beam denoted in red. All mechanical components are labelled and explained for completeness in the caption of Fig. 4.1.5. Here, only changes with respect to the previous version are discussed. As shown in Fig. 4.1.5A, tuneable beam defining slits, selecting a coherent portion of the incident X-ray beam, were realised by a slit system (2) consisting of 4 independent tantalum blades controlled by piezo motors. The corresponding control software allowed for adjusting the slits centre position and horizontal and vertical slit widths. Second element in the beam was a 25-µm-thick silicon diode attached to a piezo motor stage (3), which was used to constantly monitor and record the flux of the incident X-ray beam. Further upgrade concerned the support of the order sorting aperture (OSA), as can be seen in a magnified view of the setup in the sample area provided in Fig. 4.1.5B. The new OSA-support was manufactured from silicon (7, denoted in green). Using silicon as material for the OSA-support ensured no parasitic X-ray fluorescence background in the energy range of first-row transition metals, that would otherwise be caused by impurities in aluminium-alloy holders in close proximity of the sample used in previous experiments. The silicon support was directly attached to the aluminium arm (8) of an x/y piezomotor stage (9), without any magnetic coupling to avoid any long-term drifts. This x/y piezomotor stage was further mounted onto a stepper-motor Z translation stage for positioning of

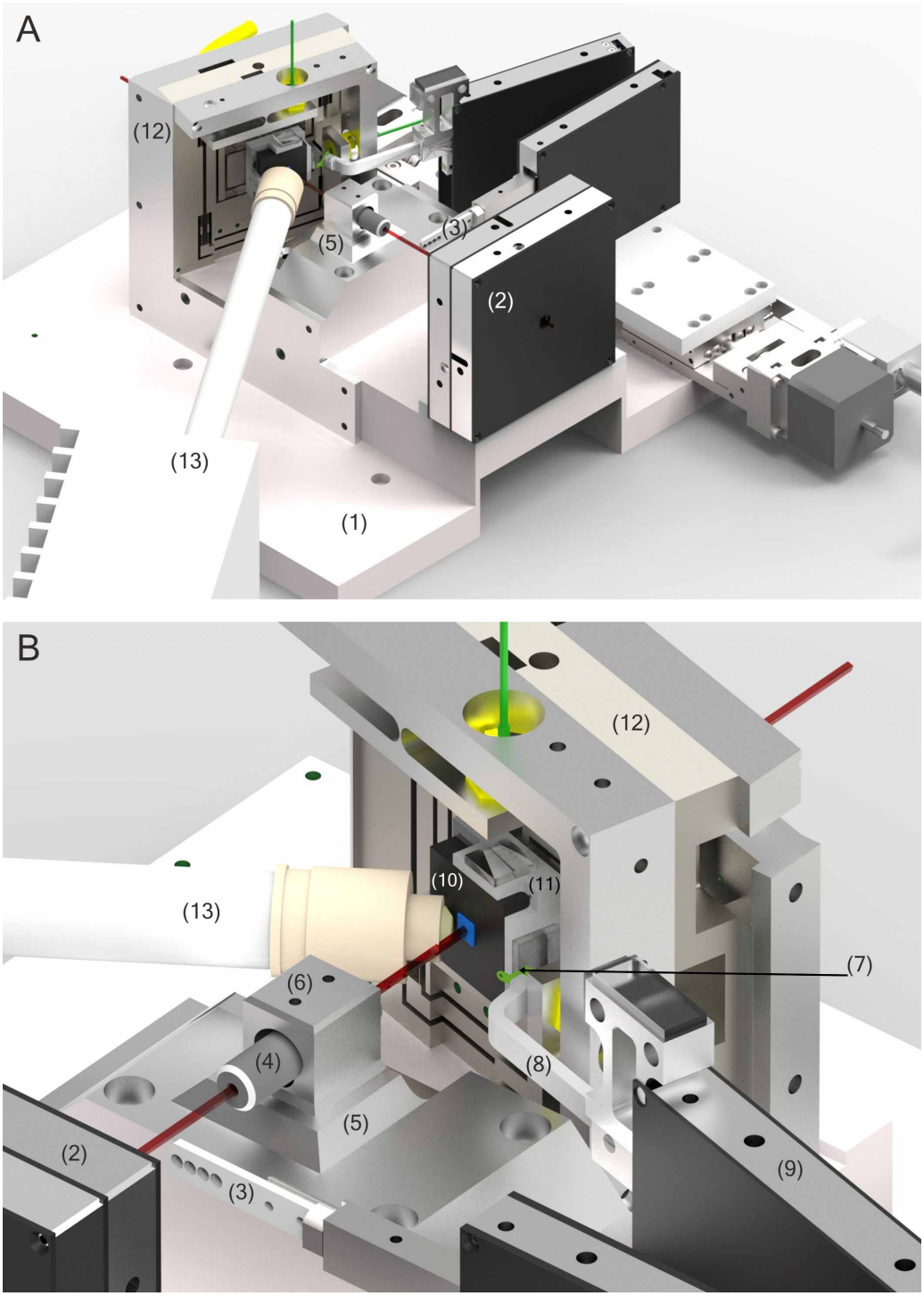

Fig. 4.1.5: High-throughput scanning X-ray microscope (A) using a flexure-based scanner with a total travelling range of $4\times4\,\mathrm{mm}^2$ (h×v) and an interferometric position control. (B) provides a closer view of the sample area. The X-ray beam was denoted in red. The setup components are: (1) aluminium-alloy base plate, (2) 4-blade slit system, (3) piezomotorised holder for the silicon diode, (4) Fresnel zone plate (FZP) tube, (5) FZP support, (6) two screws fixing the position of the FZP tube, (7) silicon support for an order sorting aperture (OSA), (8) piezomotorised arm, (9) OSA piezo motor, (10) sample kinematic base plate with a Si_3N_4 membrane carrying the specimen denoted in blue, (11) sample scanner, (12) flexure-based scanning unit, (13) silicon drift detector Vortex-EM. Two interferometer heads were denoted in yellow, whose signal was reflected by two perpendicular mirrors attached to the sample scanner.

the OSA along the beam.

The scanner retained its key feature of a $4 \times 4\,\mathrm{mm}^2$ scan range without any secondary coarse positioning. Motion control was realised with GALIL DMC4080 Controllers. Attocube FPS3010 interferometers provided an independent positioning reference for both perpendicular axes. The heads of the sensors are denoted in yellow in Fig. 4.1.5.

The implementation of the continuous-motion scanning was modified to include an incident beam intensity measured by the Si diode. The diode was read out by the PiLC alongside with the motor encoder and the interferometer signals at the same frame rate. Like in the previous version, the data from the PiLC buffer and the corresponding XRF spectra were flushed into an HDF5 metadata file at the end of each scan line. The file was common for one scan and included relevant beamline and scan status parameters (see Appendix E), facilitating robust documentation of measurements. The file structure was compatible with the file format accepted by PyMca X-ray Fluorescence Toolkit [94], used for batch-fitting of XRF spectra in this thesis.

Finally, real-time data processing of many intermediate, often sparser sampled, scans was realised with an application called PtyksP11, being a proprietary contribution of the author of this thesis. PtyksP11 is a graphical-user-interface C++ program, using the cross-platform Qt GUI toolkit [95], and has been developed since mid-2015, gaining more and more new features over the course of reported experiments. Its major functionality is an online analysis of the scanning X-ray microscopy datasets, by providing an image of the scanned area in four contrast: transmission, differential phase contrast in x and y, and dark field. The second functionality is a preview of XRF maps and the respective cumulative spectrum, with a possibility of region-of-interest selection. PtyksP11 has been fully integrated with the structure of the aforementioned metadata file. With a single click it imports relevant scan parameters, allowing for a robust setup. Having processed an overview scan, the program allows to interactively select the sub-region for the next scan (in the absolute coordinate system of the scanner), to define the new scan parameters, and subsequently to generate the corresponding configuration file for the command-line scanning script. More details about PtyksP11 can be found in Appendix F.

4.2 Multimodal 3D microscope

Having completed the first milestone with an in-air high-throughput 2D scanning X-ray microscope, the bio-imaging project advanced to the second stage in late 2017, aimed at providing the capability of tomographic measurements. An inherent bulkiness of the 2D scanner could hardly allow for a direct combination with a rotation stage. The upgrade required therefore a major conceptual change in the sample scanner design, permitting free movement in all $x/y/z$ directions and rotation around the axis perpendicular to the incident beam.

The change in instrumentation has come together with a fundamental modification in settings of beamline P11 source and optics for the bio-imaging experiments. So far, the horizontally deflecting mirrors in the P11 optics hutch were defocussed to increase the horizontal transverse coherence length. This allowed to deliver X-ray beam of a spatial coherence area of $40 \times 60\,\mu\mathrm{m}^2$ at a photon energy of 7.3 keV to the bio-imaging end-station. Such an arrangement resulted, therefore, in an off-axis and partial illumination of the used Fresnel zone plate. The resulting probe had an astigmatic shape and asymmetric side-lobes, affecting the resolution of X-ray fluorescence maps. Moreover, diffraction patterns recorded with an off-axis illuminated zone plate would often feature relatively intense spots near the patterns' centre. This artefact originated most probably from higher half-

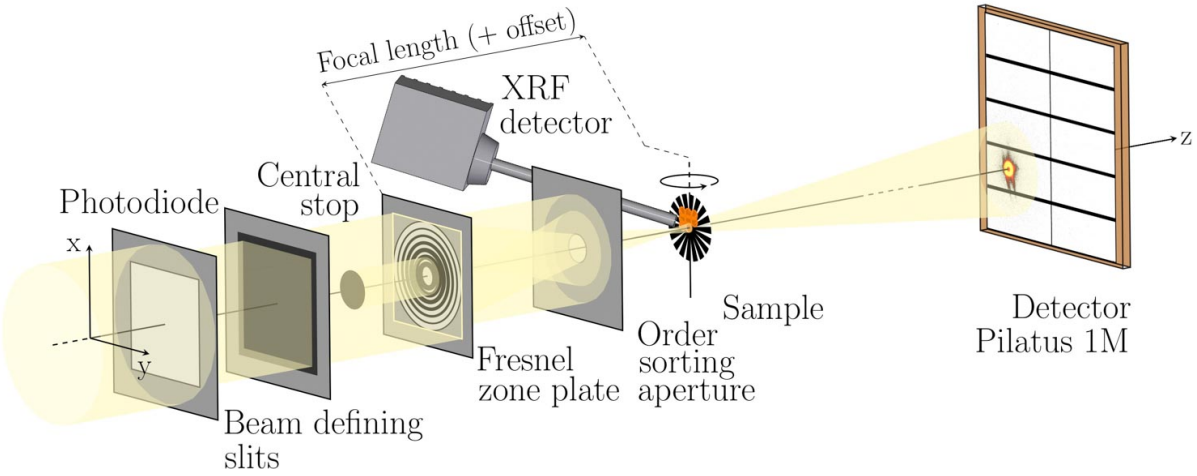

Fig. 4.2.1: Scheme of the experimental setup for simultaneous ptychographic and X-ray fluorescence imaging in 3D at beamline P11 using a silicon photodiode for incoming flux measurement, a fully illuminated Fresnel zone plate, a silicon drift detector for X-ray fluorescence acquisition, and a single photon counting Pilatus pixel detector for recording coherent diffraction patterns.

order foci of the used line-doubled zone plates [96], leaking at very shallow angles through the order sorting aperture. Further peculiarity of the off-axis illumination was the fact, that the diffracted radiation cone, that exited the zone plate, would diverge away from the optical axis. A change of the probe size, by adjusting the photon energy, would result in a different interaction point between the beam and the sample in the xy plane. This would be especially disadvantageous in the tomography setup, where the sample was to be motorised in the direction of the optical axis (z) and changes of the probe size would occur more often. The ideal solution would be the diffracted beam propagating along the optical axis, that could only be realised with a fully illuminated focussing optic. To allow this, alternative beamline settings were found to generate enough spatial coherence area at the bio-imaging end-station. It involved redefining the horizontal source size with the horizontal power slits in the beamline P11 front-end, 25 m downstream of the undulator (see Fig. 4.1). The horizontal slits would be closed to an opening of ca. 30 µm. The coherent flux area would then be further heuristically optimised with the KB mirrors in the optics hutch in both directions (slightly focussed), based on ptychographic reconstructions of test structures. Such an approach allowed to illuminate fully a 150-µm-diameter zone plate, that would make the diffracted radiation propagate further on-axis and produce a diffraction-limited focal spot, utilising the nominal numerical aperture of the lens.

Fig. 4.2.1 shows a conceptual representation of the scanning X-ray microscope permitting acquisition of both ptychographic and X-ray fluorescence tomography datasets. Following the new beamline settings, the opening of the beam defining slits (BDS) would isolate the coherent fraction of the incident X-ray beam to illuminate fully the Fresnel zone plate (FZP). The incident photon flux was measured by a thin photodiode. The direct beam was blocked by a central stop (CS) upstream of the FZP, while the first-order focus was selected by an order sorting aperture downstream of the lens. The specimen was positioned on an $x/y/z$ motorised rotation stage. Next to the sample, a silicon drift detector recorded XRF spectra, while, simultaneously, coherent diffraction patterns were acquired by a far-field single photon counting detector. Along the propagation distance between the sample and the far-field detector, a helium-flushed flight-tube was installed.

Mechanical design of the new 3D scanning X-ray microscope is shown in a rendered

overview in Fig. 4.2.2. The setup was positioned on the beamline granite support on a motorised breadboard (1), which allowed to align the instrument horizontally in the X-ray beam (denoted in red). Vertical alignment was realised with a piezomotorised tripod (2) attached to the base plate (3) of the setup. The tripod legs allowed to adjust the height, and the pitch and yaw tilt angles of the adjustable microscope platform (4).

Similarly to the 2D scanner, the 4-blade slit system was used as the beam defining slits (not shown here), being the first element in the beam. The second element was a 10-µm-thick transmission photodiode (5), Alibava AS04-105A, for measurement of the incident photon flux, positioned on a horizontal pneumatic arm. The third element in the beam were central stops deposited on a silicon-nitride membrane, which was attached to a x/y piezomotor stage (6). All these three elements were at fixed positions along the beam and installed on the reference base plate.

Fig. 4.2.3A provides a magnified view of the setup in the sample area. The fourth element in the beam were the Fresnel zone plates, attached to an end of a threaded brass tube (not visible), which, like in the 2D setup, was inserted to the FZP support (7) and fixed with two screws. The first version of the setup in June 2018 featured a higher-numerical-aperture lens (outermost zone width: 60 nm), to avoid saturation of Pilatus 1M detector pixels. In November 2018, the setup was complemented with an on-axis visible-light microscope (8), positioned between the FZP and the order sorting aperture (9). The on-axis microscope remained permanently in the beam, thanks to a 500-µm-diameter hole drilled in its centre. The hole allowed the diffracted beam to pass undisturbed, while the microscope would constantly provide a magnified view of the sample. Its dimensions and working distance required a change in the FZP numerical aperture (outermost zone width: 90 nm), which would provide a focal length of about 80 mm at 7.3 keV, while keeping the FZP diameter unchanged (150 µm). This change in focussing optics has also triggered a need for a smaller-pixel far-field detector, able to process an increased photon fluence rate. As a comparison, Fig. 4.2.3B shows a photograph of the sample area of the setup, with a retracted XRF detector (10) for clarity. The on-axis microscope was followed by the order sorting apertures, in two diameters: 10 and 20 µm, manufactured from a single piece of platinum (9). They were glued to an aluminium arm (11), which was attached to an x/y piezomotor stage perpendicularly to the normal incidence. The OSA position along the beam could be adjusted with a Z stepper motor stage (12). Specimens were prepared either on silicon-nitride membranes or milled with a focussed-ion beam to form a cylindrical shape suitable for tomographic imaging. Dedicated sample holders were developed for both flat and rotationally-symmetric specimens. In Fig. 4.2.3B, a brass sample holder with a 0.2-mm-thick etched tungsten pin is shown (13), on top of which a cylindrically-shaped sample was attached. The sample holder was inserted into an in-house developed magnetic mount (14) and secured with a little screw.

The sample scanner consisted of a rotation stage attached to the fixed base plate, a 2-mm-range coarse vertical stepper/piezo motor, that were coupled with translational sample stage (15) through the hole in the adjustable microscope platform (4). Movement in the horizontal plane xz was realised with a 2D long-range flexure, motorised first with a pair of piezo motors in June 2018, which were later substituted with voice-coil motors in November 2018. Operating at speeds of up to several millimetres per second, the voice-coil motors have set a completely new standard in total measurement times, dramatically increasing the scan area mapped in unit time. Fine movement of the sample in vertical direction was accomplished with a 120-µm-range Physik Instrumente piezostack (16), P-621ZCD, on top of which a highly polished stainless-steel reference cylinder (17) was installed. The reference cylinder severed as a reflective surface for two perpendicular interferometric sensors (18,19), that were an independent positioning reference of the

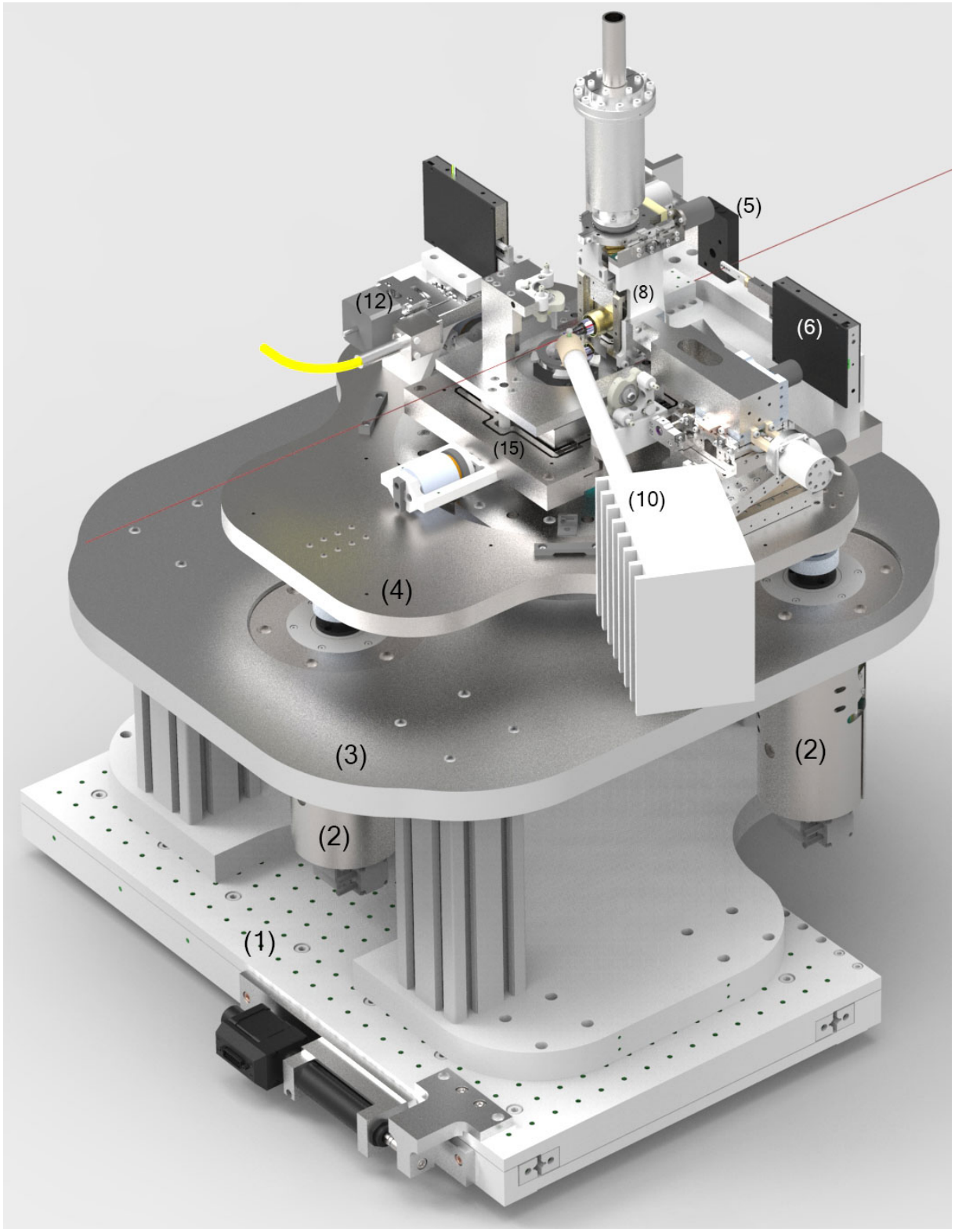

Fig. 4.2.2: A rendered overview of the ultrafast 3D scanning X-ray microscope. The X-ray beam was denoted in red. The setup components visible in this view are: (1) motorised breadboard, (2) piezomotorised tripod (third leg not visible here), (3) fixed base plate, (4) adjustable microscope platform, (5) thin silicon photodiode, (6) central stop piezo motor stage, (8) on-axis microscope, (10) silicon drift detector Vortex-EM, (12) order sorting aperture Z-stepper motor, (15) flexure-based xz sample scanner.

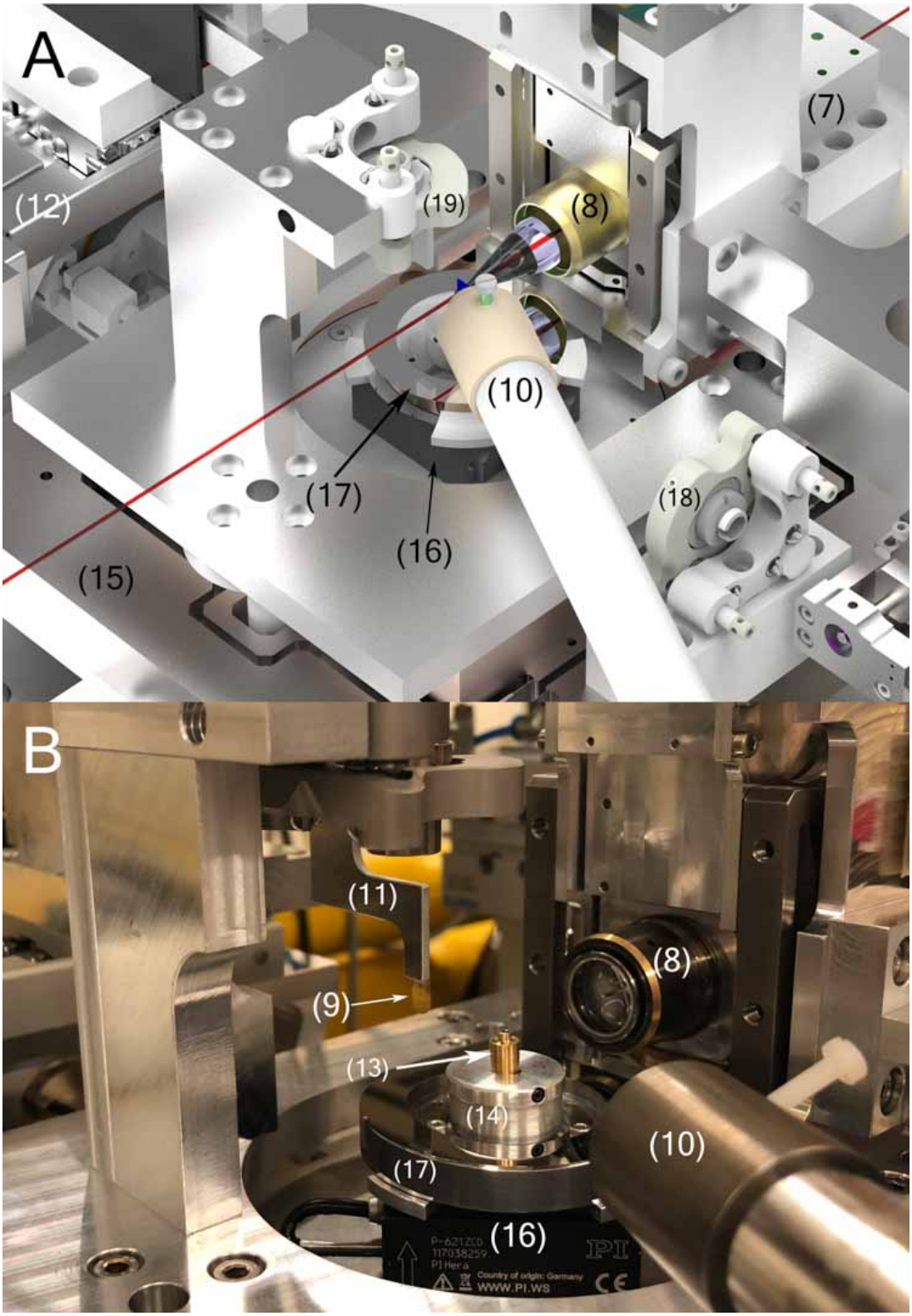

Fig. 4.2.3: Magnified view of the ultrafast 3D scanning X-ray microscope in the sample area. (A) shows a rendered view. (B) shows a photograph with the retracted X-ray fluorescence detector for clarity. The setup components visible in these views are: (7) Fresnel zone plate support, (8) on-axis microscope, (9) platinum order sorting aperture (OSA), (10) silicon drift detector Vortex-EM, (11) aluminium arm for OSA, (12) OSA Z-stepper motor, (13) brass sample holder, (14) magnetic sample mount, (15) flexure-based xz sample scanner, (16) short-range vertical piezostack, (17) reference cylinder, (18,19) supports for laser interferometer sensors.

Tab. 4.2: Evolution of the ultrafast ptychographic tomography experimental setup until the end of 2018.

Parameter	**Jun. 2018**	**Nov. 2018**
Front-end slits	closed horizontally to 30 µm	
Optics hutch mirrors	horizontal, vertical: slightly focussed	
Beam defining aperture	piezomotorised slits	
Incident flux measurement	Alibava transmission silicon photodiode AS04-105A, thickness: 10 µm	
Fresnel zone plate Δr	60 nm	90 nm
OSA holder	silicon	
On-axis microscope	NA	Olympus SLMPLN20X x/y/z/yaw/pitch stage
Sample mount	kinematic, inhouse	
Sample XZ stage	piezo motors	voice-coil motors
Reference cylinder	stainless steel, 1.4404	
Sample–incident beam angle	±90°	
Scanning mode	carriage-return fly-scan	
Triggering	hardware, PiLC	
Flight tube	He-flushed	
Detector (ptychography)	Pilatus 1M	Eiger 500k

sample. The middle hole of the reference cylinder was occupied by a permanent magnet and a V-groove to kinematically attach and align the sample mount. Due to space restrictions, the SDD Vortex-EM detector was installed at an angle of 115° from the incident beam. Along a 4.4-m propagation distance between the sample and the far-field detector, a helium-flushed flight-tube was installed. The implementation of the continuous-motion carriage-return scanning, utilising the PiLC Trigger generator, remained unchanged as developed for the 2D scanning microscope. Tab. 4.2 provides a tabulated summary of the most important characteristics of the 3D scanning X-ray microscope and several design upgrades in the commissioning phase in 2018. This period consisted of two successful experiments within the scope of a long-term proposal at beamline P11, aimed at establishing the instrument for multimodal 3D scanning X-ray microscopy of biological specimens as one of the beamline's end-stations.

The focus of the preliminary experiment in June 2018 was to test the new experimental setup and demonstrate feasibility of tomographic measurements with a biological sample on a flat substrate. To accomplish this, a monolayer of cultured macrophages infected with tuberculosis and treated with iron-oxide nanocontainers was prepared. The cells were grown on a silicon-nitride membrane, osmium-stained and air-dried.

Following the established procedure of cell preselection, as described in subsection 4.1.1, a representative macrophage infected with tuberculosis and treated with iron-oxide nanocontainers was preselected using visible-light microscopy. The fluorescence image confirmed the presence of at least one *Mycobacterium tuberculosis* (*M.tb.*) in the cell. Another important criterion at the preselection was, that the cell would also be located in the middle of the silicon-nitride membrane to facilitate centering on the rotation axis.

As a first step, a pair of parallactic images of the cell was acquired at angles ±7.5° with respect to the incident beam of an energy of 7.375 keV. The corresponding ptychographic

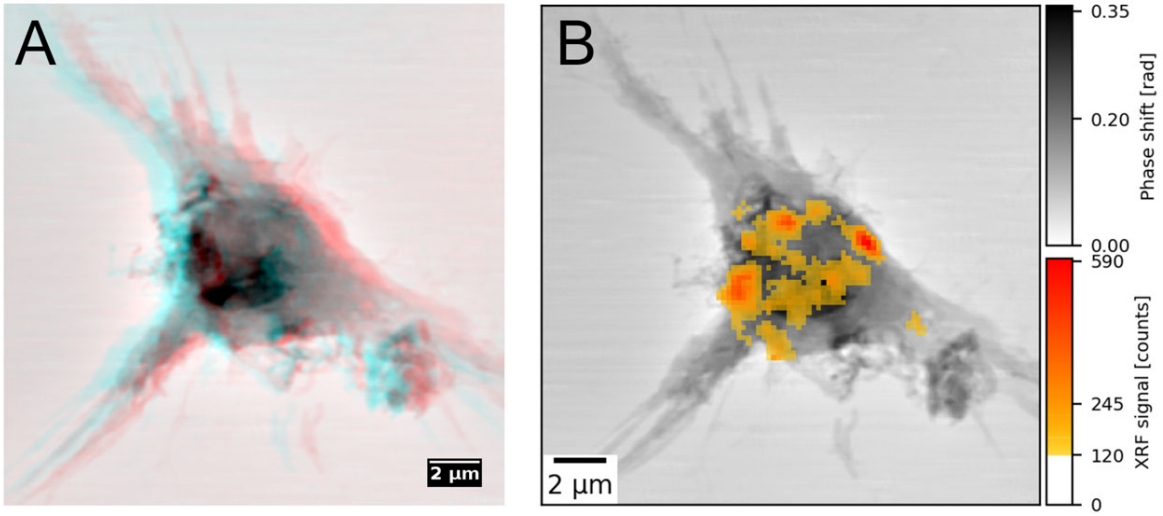

Fig. 4.2.4: Simultaneous ptychographic and X-ray fluorescence imaging of a tuberculosis-infected macrophage treated with iron-oxide nanocontainers measured at 7.375 keV with the first version of the 3D scanning microscope in June 2018. (A) shows a stereoscopic image of the cell whose red and cyan channels originate from two ptychographic phase images recorded at ±7.5° with respect to the incident beam. (B) shows one of the projected views overlaid with the iron X-ray fluorescence distribution map, which demonstrates the presence of agglomerates of iron-oxide nanocontainers. Each of the two parallactic projections imparted a dose of 3.35 MGy on the cell, including a time overhead of 13%. Ptychographic reconstructions were obtained by the difference-map algorithm with a single probe mode, using 100 iterations in (A) and 150 iterations in (B). Ptychographic reconstructions were obtained by 200 iterations of the difference-map algorithm, followed by 50 iterations of the maximum-likelihood refinement, and using a single probe mode.

phase reconstructions were converted into the red and cyan channels to yield a composite stereoscopic image shown in Fig. 4.2.4A. Simultaneously to ptychographic imaging, the iron X-ray fluorescence map of the cell was recorded. Fig. 4.2.4B shows the Fe distribution map (in red-scale) superimposed on the corresponding ptychographic phase image (in greyscale) of the macrophage. The Fe map revealed agglomerates of iron-oxide nanocontainers on top or inside the cell. The scan was acquired at a fly-scan speed of $2\,\mu m\,s^{-1}$ and a frame rate of 10 Hz, using a probe size of 0.5 µm. This resulted in a scanned area rate of $0.353\,\mu m^2\,s^{-1}$, which takes into account an overall scanning time overhead of 13%.

As a second step, a proof-of-concept missing-wedge ptychographic tomography was performed on the preselected cell. Since that version of the setup did not have the on-axis microscope yet, the cell was centred in the rotation centre using a rather faint absorption image provided in real time by a CCD camera positioned in a short distance downstream of the sample. The tomographic dataset consisted of three sub-datasets, each comprising 31 projections over an angular range of ±30° (angular step: 2°). The sub-tomograms were shifted with respect to each other by an angular step of 0.67° to allow for combining them all in a single equally sampled tomogram. To reduce the overall time of the measurement, the probe was defocussed to a size of 1.2 µm, permitting larger step sizes. This resulted in a scanned area rate of $1.17\,\mu m^2\,s^{-1}$, i.e. four times greater than in the previous stereoscopic scans, while retaining a similar time overhead of 15%. Detailed experimental parameters are provided in Tab. C.3 (Appendix C). Fig. 4.2.5A shows the reconstructed ptychographic phase of a representative 2D projection. Red arrow denotes the location of

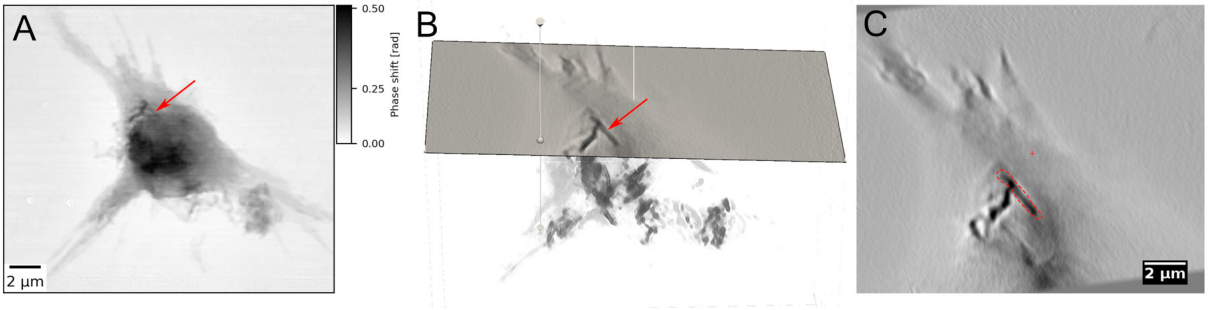

Fig. 4.2.5: Missing-wedge ptychographic tomography of a tuberculosis-infected macrophage cell at a photon energy of 7.375 keV. The tomographic dataset consists of 31 projections recorded over an angular range of ±30° (angular step: 2°). (A) shows an exemplary ptychographic phase 2D projection. Ptychographic reconstructions were obtained by 200 iterations of the difference-map algorithm, followed by 50 iterations of the maximum-likelihood refinement, and using a single probe mode. (B) provides a rendered overview of the reconstructed volume. The substantial missing wedge in the tilt angles resulted in a highly anisotropic resolution in 3D. The isolated slice shows the plane (at 47° from the vertical axis), in which one *Mycobacterium tuberculosis* can be observed. Red arrows in (A) and (B) denote the position of the bacterium. In (C) the slice with the bacterium, surrounded with a red, dashed line, is shown.

a *M.tb.* bacteria, hardly visible in the projected view. Subsequently, all projections from three sub-datasets were merged. Inspection of the final dataset revealed though a substantial radiation damage occurring on a scale of even up to 250 nm. The dose imparted by each 31-projection sub-dataset was equal to 43.6 MGy. The dose calculation method in ptychographic experiments is described in Appendix G. Therefore, for a preliminary tomographic reconstruction, only the first sub-dataset was chosen, which resulted in a very sparse angular sampling. The tomographic reconstruction was performed with the IMOD software package [97]. Although the tomogram did not reveal any particular sub-cellular structures apart from the macrophage-specific filopodia and cellular membrane ruffles, it allowed to isolate the anticipated *M.tb.* bacterium in the upper part of the cell. Fig. 4.2.5B provides a low-resolution rendered overview of the cell, obtained with the *tomviz* software package [98]. The substantial missing wedge resulted in a strongly anisotropic resolution in 3D. Therefore, orthoslices in xz and yz planes contain hardly any meaningful details. Nevertheless, it was possible to identify a slice at 47° angle with respect to the vertical axis, as visualised in Fig. 4.2.5B, which is in plane with the bacterium (indicated with a red arrow). Fig. 4.2.5C shows the actual slice, where the bacterium was denoted with a red, dashed loop.

Despite the radiation damage, the reported preliminary tomographic measurements present the potential of the 3D scanning microscope in biological applications, in which it is preferential to prepare the specimens on a flat surface, as it is routinely done in cryo-electron microscopy. While mechanically already feasible, performing similar high-quality scans with the presented 3D scanner requires a cryogenic sample cooling. The acceptable doses in sub-100-nm X-ray imaging of frozen-hydrated biological specimens are reported to be even of the order of $10^8 - 10^9$ Gy [99, 100]. This upgrade is anticipated after the successful commissioning of the room-temperature in-air setup.

Concerning the design, the measurements in June 2018 allowed to test mechanical performance of the 3D setup and identify potential weak points. The latter were addressed until the next experiment in November 2018 (Tab. 4.2). Instead of aligning specimens

with a CCD camera and X-ray absorption contrast, resulting in additional irradiation, an on-axis microscope was installed between the Fresnel zone plate and the order sorting aperture. The xz piezo motors of the sample scanner were replaced with a pair of voice-coil motors, yielding one order of magnitude higher scanned area rates at all probe sizes. Finally, a smaller-pixel detector (Eiger 500k) allowed for a substantial increase of the used probes up to 4.6 µm. In this way, the instrument has turned into a versatile 3D scanning X-ray microscope, able to perform in two modes: (1) simultaneous ptychographic and X-ray fluorescence tomography with a focussed beam (≤ 0.5 µm) and (2) ultrafast and low-dose ptychographic tomography with several-micrometer-large probes. Experimental demonstrations of the setup capabilities in ptychographic tomography from November 2018 are further discussed in chapter 6, while the evolution of all bio-imaging setups at beamline P11 is once again shortly summarised in Conclusion and outlook. Also there, future prospects for further development of the instrument are discussed.

Chapter 5

High-throughput multimodal X-ray imaging of biological specimens

Metal ions play an important role in the vital functions of living organisms. They are present in various biological systems in a vast range of concentrations as structural, electrolyte (minor), and trace elements. From being major tissue components (e.g. Ca in bones) to constituents of essential biological molecules (e.g. Fe in hemoglobin), metals take part in the majority of extra- and intracellular processes. In particular, first-row transition metals (Mn, Fe, Cu, Ni, Zn) - despite their minute concentrations - are involved in sub-cellular processes. Moreover, their abnormal accumulation in human brain was correlated with mechanisms leading to neurodegeneration diseases such as Parkinson's and Alzheimer's [101, 102, 103]. Metal compounds have also been utilised as novel drug delivery systems by addressing metabolic properties of bacterial agents [104, 105] or as more efficient medical imaging markers tracking tissue of interest [90, 92, 91].

In all aforementioned cases, studies of metal contributions require knowledge of their quantitative spatial distributions with respect to the sub-cellular structure. Electron-probe Energy-Dispersive Spectroscopy offers elemental mapping at nanometer-range spatial resolutions and high excitation efficiency in the low-Z-element range. Yet, it is vastly limited by short penetration depth, Bremsstrahlung background from the electron source, reducing peak-to-background ratio, and invasive sample preparation requirements [106]. On the contrary, recent developments in hard X-ray microscopy at modern synchrotron radiation sources have opened new paths of non-destructive and diverse probing of biological specimens. With advances in hard X-ray nanofocussing, nanoscale X-ray fluorescence (XRF) can provide a unique elemental contrast at below 100-nm spatial resolutions and remarkable excitation efficiency of elements in trace concentrations. Yet, interpretation of XRF data may become challenging due to missing information on morphology of a measured biological specimen. Enhanced coherence properties and higher photon fluxes of third-generation synchrotrons have promoted phase contrast hard X-ray imaging techniques for the investigation of weakly absorbing biological structures. Combination of propagation-based full-field phase contrast imaging and X-ray fluorescence mapping was used in quantitative elemental analysis of single cells [107] and extended tissue sections [108]. The method of scanning Zernike phase contrast was implemented along with XRF to qualitatively correlate the occurrence of low-Z elements with sub-cellular organelles [109].

In the advent of diffraction-limited synchrotron light sources [110], ptychography was consolidated with nanoscale XRF in concurrent imaging of a freshwater diatom [111]. Both techniques were further extended by in-vacuum cryogenic sample cooling, providing simultaneously qualitative distributions of light elements within a cell and its morphology

at remarkable sensitivity and sub-50-nm spatial resolution [112]. Further developments involved the implementation of a continuous-motion scanning scheme [79, 80, 81, 113] and a sample rotation which enabled simultaneous acquisition of a tomographic dataset in both modalities with reduced time overhead [100]. Yet, these demonstrated solutions have until now featured an accessible field of view limited to the imaging of single cells. Recently, quantitative correlative 2D imaging of five entire nematodes has been demonstrated using a 2.5-µm beam (FWHM) and typical X-ray fluorescence microscopy scan parameters for scanning areas of up to 0.1 mm^2 at an energy of 10 keV, though with a resolution of 280 nm in ptychography [114].

However, reaching higher spatial resolutions in both modalities has so far been restrained by insufficiently coherent flux at higher photon energies. As a result, the concurrent ptychographic and nanoscale X-ray fluorescence imaging has practically allowed only for low-Z-element mapping in single specimens with X-ray excitation energies limited to 5.2 keV. This limitation has until now stemmed from relatively high emittance values of synchrotron sources that kept the spatially coherent fraction of X-ray beam below 0.1% at high photon energies (>10 keV). New low-emittance storage rings, such as PETRA III or NSLS-II, and recently emerging diffraction-limited synchrotron sources (MAX IV) allow to overcome this limitation, providing up to 2 orders of magnitude improvement in the degree of spatial coherence [110]. Hence, this latest generation of synchrotron sources brings advances in quantity, enabling the increase of experimental throughput and statistical relevance, as well as in quality, such as enhancement in signal-to-noise ratio and spatial resolution [115].

Within the scope of this thesis, the multimodal concept of simultaneous ptychography and nanoscale X-ray fluorescence has been optimised for quantitative probing of statistically-relevant population of biological specimens at higher X-ray energies. A detailed description of the experimental setup evolution is provided in chapter 4, with a focus on the final realisation of the 2D scanning stage in section 4.1.2. The following two sections demonstrate the application of this method in correlative imaging of macrophages treated with Fe_2O_3 nanocontainers, that target antibiotic drugs to intracellular *Mycobacterium tuberculosis* (section 5.1), and in a study of perilacunar bone matrix mineralisation (section 5.2).

5.1 Efficient drug delivery

Innovative nano-medical approaches for drug delivery aim at enhancing local and reducing peripheral drug concentrations. Iron-oxide nanocarriers [104] represent a novel tool for a targeted delivery of the anti-tuberculosis antibiotics to infected macrophages. Tuberculosis (TB) is one of the most important bacterial infections worldwide causing high mortality and morbidity. The causative agent, *Mycobacterium tuberculosis*, is a facultative intracellular pathogen which can survive and grow in phagosomes upon phagocytosis by macrophages [116, 117]. These host cells, otherwise well equipped to kill bacterial invaders, serve as niches for mycobacteria. More importantly, the membrane-enclosed phagosome and the lipid-rich cell wall of the mycobacteria pose a significant challenge for an efficient drug delivery as they hinder antibiotics entering the bacteria. Hollow Fe_2O_3 nanocontainers loaded with antibiotics, which can target anti-TB drugs to intracellular mycobacteria, are a potential solution to this inherent problem of the TB treatment. The nanocontainers are actively internalised into macrophages and release antibiotics in close proximity to the mycobacteria. This happens upon slow metabolic dissolution of the Fe_2O_3 wall, exploiting the mycobacteria's need for iron.

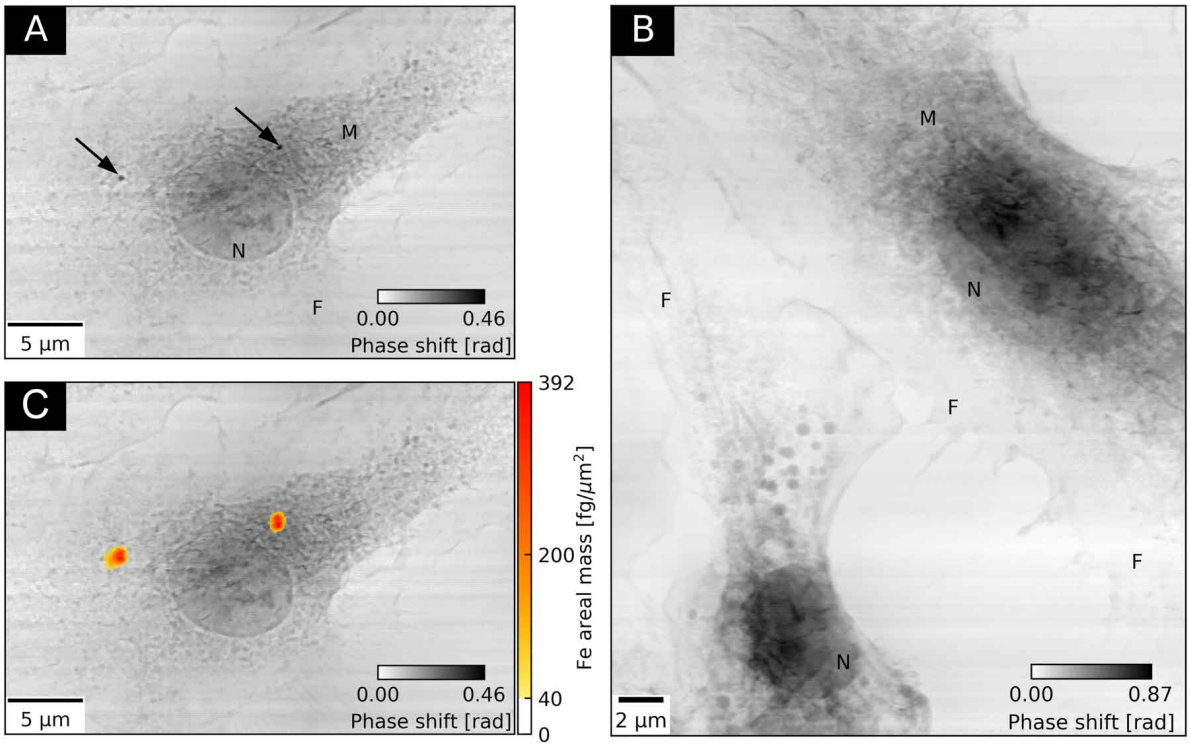

Fig. 5.1.1: Multimodal imaging of two groups of macrophage cells at a photon energy of 7.35 keV. (A) presents the reconstructed ptychographic phase of a macrophage treated with Fe_2O_3 nanocontainers targeting *Mycobacterium tuberculosis*. Black arrows indicate the internalisation of two agglomerates of nanocontainers in the cell. (B) shows the ptychographic phase of two untreated control cells. Both images allow for identification of cellular nuclei (N), membrane ruffles (M) and filopodia (F). (C) presents Fe areal mass map obtained simultaneously by means of XRF superimposed on the ptychographic phase of the representative nanocontainer-treated macrophage.

As a first application, the uptake of iron-oxide nanocontainers in macrophages has been studied by correlating iron X-ray fluorescence mapping with respect to the subcellular structure obtained by simultaneous ptychographic imaging at a photon energy of 7.35 keV. Both the nanocontainer-treated and the control-group cells were prepared on silicon-nitride membranes, stained with osmium-tetroxide, and air-dried. The detailed sample preparation protocol is provided in Appendix B.1. Prior to X-ray measurements, visible-light micrographs of all membranes were acquired, based on which the candidate cells were preselected. Subsequently, in the case of iron-oxide nanocontainer-treated macrophages, overview X-ray microscopy scans of 200×200-µm^2 areas, which included those cells, were recorded to concurrently obtain low-resolution iron and conventional scanning-transmission-X-ray-microscopy (STXM) maps, as shown in Fig. F.1 in Appendix F. Based on the presence of iron signal correlated with the STXM images, the cells of interest were identified for subsequent nanoscale mapping with simultaneous ptychography and X-ray fluorescence.

5.1.1 Results

Figs. 5.1.1A and 5.1.1B show ptychographic phase images of macrophage cells. The quantitative grayscale contrast denotes a relative phase shift which is proportional to the pro-

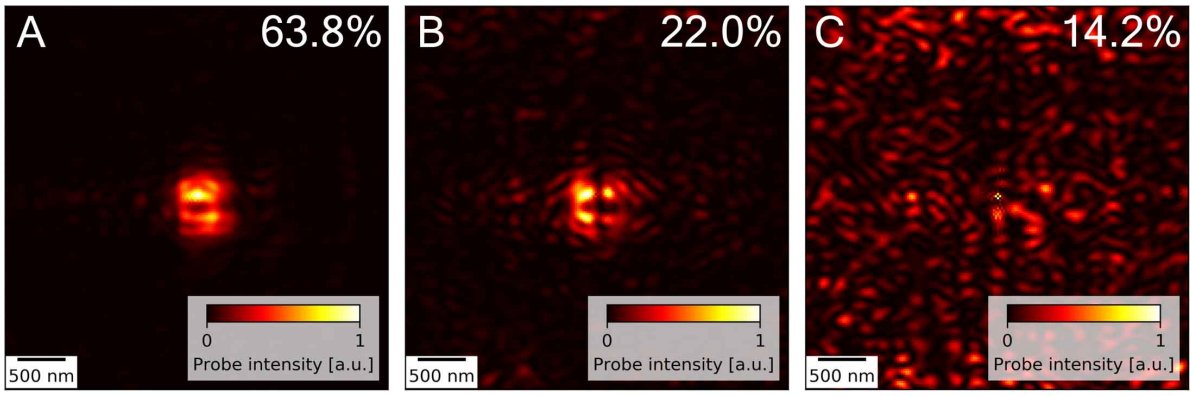

Fig. 5.1.2: Orthogonalised probe modes of the nanocontainer-treated macrophage scan in Fig. 5.1.1A. (A), (B), and (C) indicate the first, second, and third mode, respectively. The fractions of the total incident photon flux of 5.4×10^8 photon s^{-1} are indicated in the upper-right image corners. The probe size was assessed to equal $400 \times 600\,nm^2$ (h×v).

jected electron density of a cell. In Fig. 5.1.1A, a representative macrophage treated with Fe_2O_3 nanocontainers is shown. The image allows to identify basic cellular structures like the nucleus (N), cell membrane ruffles (M), and macrophage-specific filopodia (F). The two high density spots, indicated with black arrows, are two nanocontainer agglomerates internalised within the cytosol. For comparison, Fig. 5.1.1B shows the cytoplasm of two untreated control cells. Ptychographic datasets were reconstructed with 200 iterations of the difference map algorithm [3] and three orthogonal probe modes [49]. For the scan in Fig. 5.1.1A, the intensity distributions of the reconstructed, orthogonalised probe modes are shown in Fig. 5.1.2. Numbers in the upper-right corners indicate the intensity fractions of the total incident photon flux of 5.4×10^8 photon s^{-1}, carried by the respective illumination modes. The scans were recorded at a horizontal fly-scan speed of $0.83\,\mu m\,s^{-1}$ and a scan step size of 125 nm in both directions. Further increase of the probe modes number did not yield any qualitative improvement of the reconstructed images. The overall probe size was estimated to $400 \times 600\,nm^2$ (h×v). Another challenge in the analysis was long-term source instability, which compromised the quality of some ptychographic reconstructions, resulting in pronounced non-linear background phase offsets. In the case of single cells, empty image areas were used to obtain phase profiles for a global background correction. Alternatively, a representative affected scan (Fig. 5.1.1B) was split into 14 overlapping sub-scans (20% overlap along the slow scan axis), each updating the common object, but having independent probes. Each subscan consisted of 5000 diffraction patterns, equivalent to about 12 min of data acquisition. This approach diminished substantially the non-linear phase background.

Simultaneously to ptychographic imaging, Fe spatial distribution maps were obtained by means of X-ray fluorescence measurements. Detailed experimental parameters are provided in Tab. C.2 (Appendix C). A 470-nm-thick iron film deposited with electron-beam evaporation on a Si_3N_4 membrane was used for calibrating the Fe K-line XRF yield to Fe areal mass. The quantification steps were described in detail in the following section. XRF spectra were batch-fitted using PyMca X-ray Fluorescence Toolkit [94].

Fig. 5.1.1C shows the Fe areal mass distribution map superimposed on the ptychographic phase of the nanocontainer-treated macrophage. Two distinct iron spots coincide well with the positions of the nanocontainer agglomerates obtained by ptychography. They reach maximum Fe areal mass values of 392(18) fg μm^{-2} (left) and 351(17) fg μm^{-2} (right). The difference in the size of the agglomerates obtained by both imaging techniques

stems from the inherently superior spatial resolution offered by ptychography.

5.1.1.1 Quantification of iron signal

In this section, it is described how iron areal mass maps were obtained from the raw iron distributions. As already mentioned, an iron film of a thickness of 470(2) nm, deposited with electron-beam evaporation on a Si_3N_4 membrane, was used for the quantification of an iron mass per unit area. Repeated X-ray transmission measurements revealed the film density to be about 21% less than the tabulated bulk density. It may be a result of a different arrangement of Fe atoms in the deposited film than in a crystalline structure. The product of the film's thickness and mass density yielded an areal deposition mass of 2.827(17) µg mm^{-2}, which was then used for the areal mass calibration of the Fe maps.

Between the consecutive scan batches of the cells, five 6×6-µm^2 Fe maps of the calibration standard were independently measured, ensuring the same experimental conditions and scan parameters as for the cell scans. All Fe maps of the cells and the calibration standard were first normalised by the flux of the incoming X-ray beam (Si diode data) correcting for intensity fluctuations. Histograms of Fe counts from 5 independently measured Fe maps of the calibration standard were fitted with a Gaussian distribution and averaged, yielding a mean of 3516(31) counts per resolution area. Combined with the areal mass of the calibration standard, a calibration coefficient of 0.8041(86) ng mm^{-2}count^{-1} was derived and applied to all Fe maps measured under the same experimental conditions.

The quantitative Fe maps were further used to determine the integrated Fe mass, the area of every nanocontainer agglomerate, and the number of nanocontainers per agglomerate. These parameters were calculated from all pixels within the agglomerate, whose signal was greater than around 40 ng mm^{-2} (50 counts). This threshold was chosen to exclude the background and the native cellular Fe levels.

The integrated Fe mass was calculated as a sum of the multiplications of Fe areal mass and the resolution area for every selected pixel, normalised by an overlap factor of 15.1. The resolution area (525 × 600 nm^2, h×v) was defined as the probe size (400 × 600 nm^2, h×v) augmented horizontally by the 125-nm step size due to continuous scanning. It was therefore much larger than an area of a single pixel, i.e. 125×125 nm^2. The overlap factor stemmed from the substantial oversampling of the Fe maps (necessary for ptychography), that would overestimate the integrated Fe mass. It was determined by simulating the intensity distribution within the entire scanned area, using the reconstructed probe profile and the relative sample-probe scan positions. 10 different areas of a size of the illuminating probe were isolated from such an intensity distribution. The total intensity accumulated within each of them was divided by the number of incident photons. Subsequently, 10 resulting values were averaged, yielding a mean overlap factor of 15.1. A similar approach was used in estimation of the absorbed dose, as described in Appendix G.

The area of a nanocontainer agglomerate was calculated from the total number of pixels per agglomerate. Its uncertainty was estimated by approximating the agglomerate's shape to a circle.

The following steps explain calculation of the nanocontainer number per agglomerate. The mass of a single nanocontainer of 1.13(36) × 10^{-17} g was obtained assuming a hollow Fe_2O_3 sphere model with an inner diameter of 10(1) nm and an outer diameter of 18(1) nm [104]. Dividing the nanocontainer mass by the mass of Fe_2O_3 molecule, a number of Fe_2O_3 molecules per nanocontainer of 50000(11000) was estimated. The integrated Fe mass of each agglomerate was recalculated into the number of Fe_2O_3 molecules using tabulated atomic masses. By dividing the latter by the number of Fe_2O_3 per nanocon-

Tab. 5.1: Quantitative analysis of two nanocontainer agglomerates internalised in the macrophage in Fig. 5.1.1C.

Parameter	Left agglomerate	Right agglomerate
Maximum Fe areal mass [fg µm^{-2}]	392(18)	351(17)
Integrated Fe mass [fg]	327(4)	411(5)
Area [µm^2]	1.4(5)	2.1(6)
Antibiotic load per agglomerate [pg]	0.52(5)	0.66(6)

tainer, the numbers of nanocontainers (NC) in each agglomerate were obtained. For example, the two nanocontainer agglomerates shown in Fig. 5.1.1C comprise 35300(7400) and 44400(9400) NC, for the left and the right agglomerate, respectively. The standard uncertainties of about 20% originate from uncertainties of the nanocontainer dimensions. Further, the integrated Fe masses and the areas of these agglomerates are provided in Tab. 5.1.

5.1.1.2 Statistical analysis

For more statistically-relevant results, under the same conditions a population of 14 cells was measured, in which 22 agglomerates of nanocontainers were identified. Ptychographic reconstructions overlaid with Fe distribution maps of 13 remaining cells are shown in Fig. 5.1.3. As described in the previous section, for each agglomerate its integrated Fe mass was calculated. Every nanocontainer comprises 43 wt% of Fe_2O_3 (sphere wall), 48 wt% of antibiotics, and 9 wt% of water [104]. By expressing the integrated Fe masses in terms of total Fe_2O_3 mass, the weight proportions were used to estimate the distribution of antibiotic load per agglomerate, as shown in Fig. 5.1.4A. For almost half of the investigated agglomerates this number does not exceed 0.7 pg antibiotic per agglomerate. It is also the case for the two agglomerates shown in Fig. 5.1.1C, whose estimated antibiotic loads are provided in Tab. 5.1.

Subsequently, for each agglomerate the corresponding area was calculated. Fig. 5.1.4B shows a correlation between the integrated Fe mass M and the area A of all nanocontainer agglomerates as derived from X-ray fluorescence maps. A monotonic growth of the agglomerate integrated Fe mass with its area can be observed. A linear test function was chosen to approximately model the observed relation. The implied average planar spread of agglomerates could potentially be related to the preparation method of the nanocontainer-treated macrophages on a flat substrate. A linear trend line was fitted according to the equation $M = \alpha(A - \beta)$ to account for the observed non-zero A-intercept. The linear parameter α of 0.293(15) pg µm^{-2} can be interpreted as a mean Fe areal mass of the entire set of agglomerates. It can also be converted into a mean number of nanocontainers (NC) per unit area of 31700(6800) NC per µm^2, based on the calculation steps provided in the previous section. The additive parameter β equals 0.45(22) µm^2 and can in turn be attributed to a systematic overestimate of the agglomerate areas due to the lower resolving power of XRF. This argument is also supported by visibly smaller agglomerate sizes in the ptychographic image.

5.1.2 Discussion

In this application, the method of concurrent ptychography and X-ray fluorescence allowed to visualise and quantify the uptake of Fe_2O_3 nanocontainers in a population of macrophages in the context of their sub-cellular organelles. Fe maps revealed the presence

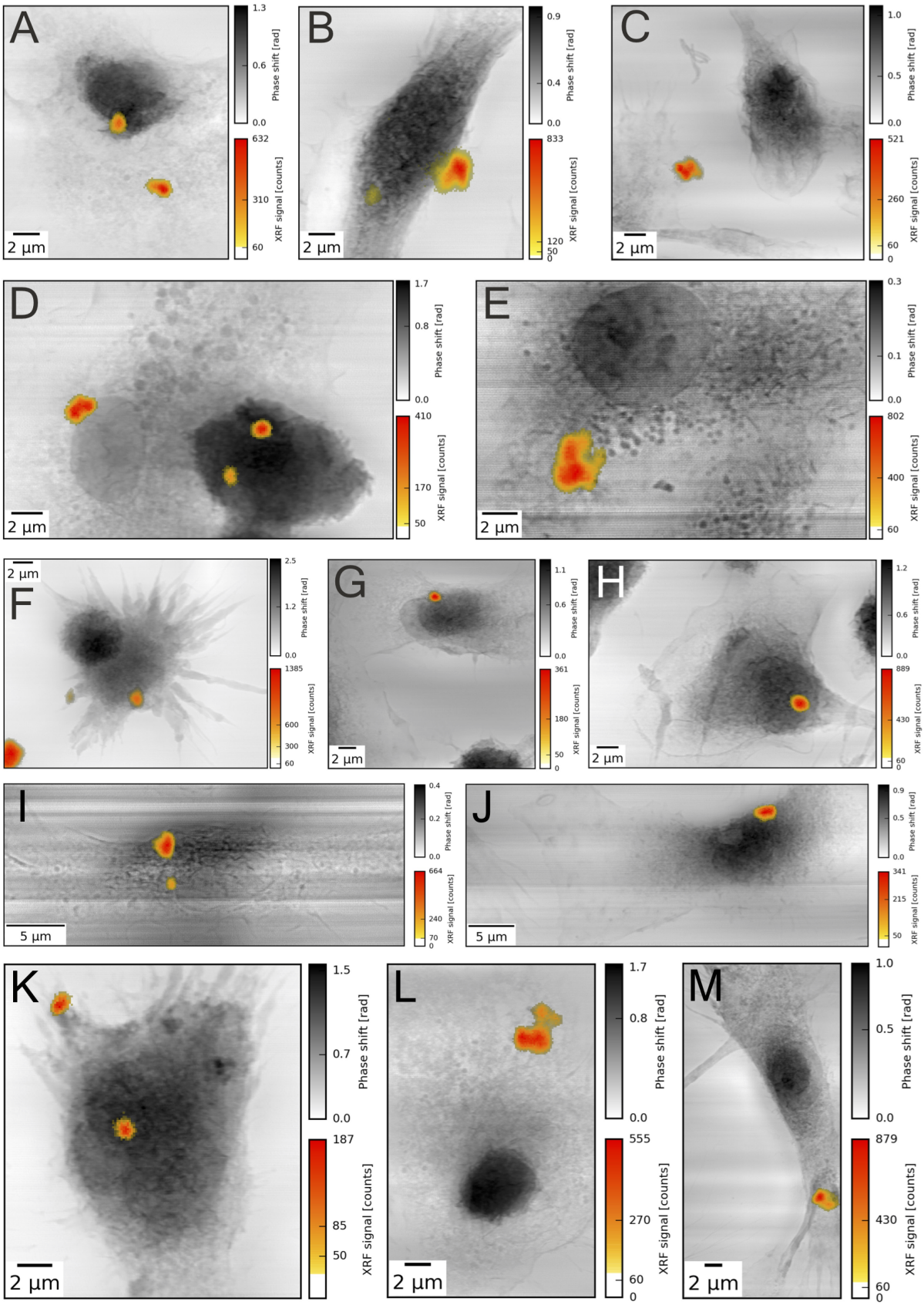

Fig. 5.1.3: Ptychographic phase reconstructions overlaid with iron distribution maps of 13 macrophages treated with Fe_2O_3 nanocontainers and measured under the same conditions. XRF signal scale denotes Fe K-line XRF yield.

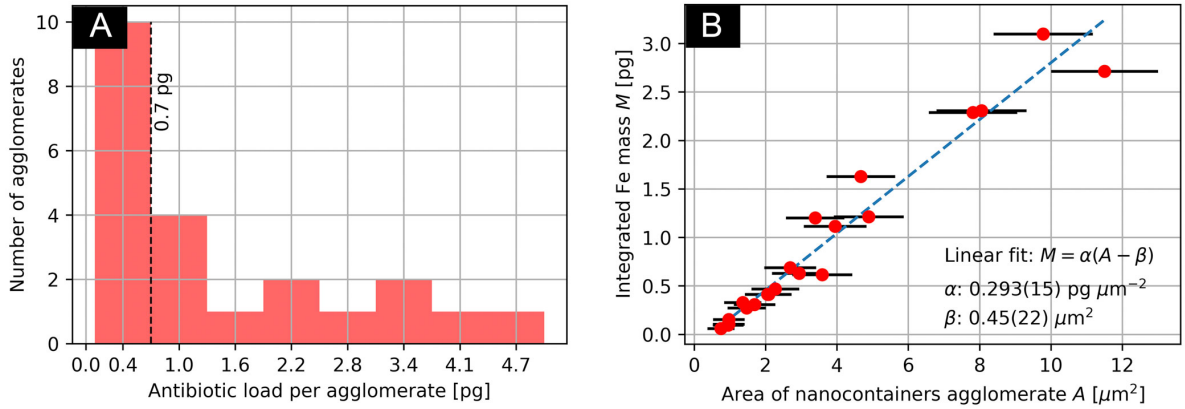

Fig. 5.1.4: Simultaneous ptychography and X-ray fluorescence (XRF) of macrophages treated with Fe_2O_3 nanocontainers targeting *Mycobacterium tuberculosis*. In 14 cells measured under the same conditions, 22 agglomerates of nanocontainers were found. For each of them, its integrated Fe mass and area were calculated. The integrated Fe masses were further recalculated into the corresponding antibiotic contents in the agglomerate, using weight proportions known from the previous study [104]. (A) shows histogram of the estimated antibiotic load per agglomerate. Antibiotic contents below 0.7 pg tend to dominate. (B) presents a linear relation between the integrated Fe masses of nanocontainer agglomerates and their areas.

of nanocontainer agglomerates while the simultaneously acquired ptychographic images complemented these with detailed cellular morphology views at sensitivity and spatial resolution unmatched by any other scanning X-ray microscopy technique. Further, the quantitative Fe areal mass maps of the nanocontainer-treated macrophages allowed to compute the distribution of antibiotic load per agglomerate. It can serve as a complementary assessment of the nanocontainer efficacy in tuberculosis infection treatment. The long penetration depth of hard X-rays allows to look beyond the sample surface and investigate the whole volume of the cell without a need of sectioning. Despite still missing depth information, the linear model of the relation between the integrated Fe mass and the area of the nanocontainer agglomerates yields an averaged number of nanocontainers per agglomerate unit area. Assuming a generic height of 1 µm, a mean concentration of 31700(6800) nanocontainers per agglomerate unit volume was found. The obtained value remains in good agreement with the previous study based on the statistical evaluation of transmission electron microscopy images [104].

5.2 Bone matrix mineralisation

Pathologies of the skeleton are among the most common morbidities worldwide. Age-related bone loss (osteoporosis) is supposed to increase in its clinical significance with the current demographic development. Its detrimental result are fragility fractures that remain difficult to treat. Bone quality is a result of the complexity of the bone micro- and nano-structure and the tissue remodelling process. The cellular network of the osteocytes in bone has emerged as key factor of bone remodelling executed by bone-resorbing osteoclasts and bone-forming osteoblasts. It has been demonstrated that the osteocytes govern a local volume of matrix surrounding the osteocyte lacunae (perilacunar matrix), which is actively turned over by the osteocytic activity [118, 119, 120]. Osteocytes acidify their

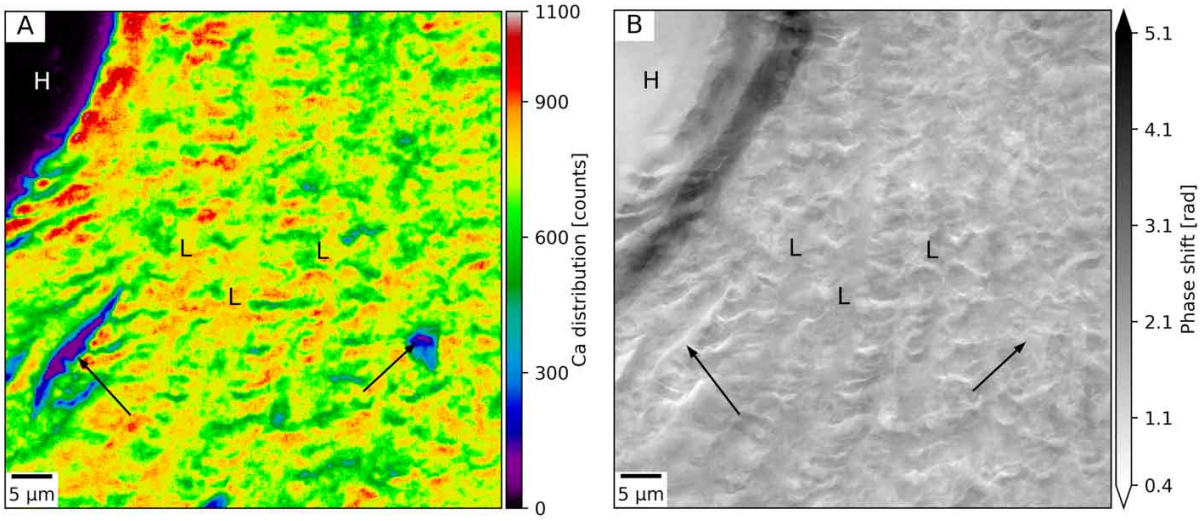

Fig. 5.2.1: Simultaneous ptychography and X-ray fluorescence (XRF) of a thin and unstained human bone section at 7.15 keV. (A) shows the Ca distribution as obtained by XRF mapping and (B) the ptychographic phase shift. Both (A,B) allow to identify a Haversian canal (H) and concentric lamellae (L). In (A), the Ca depletion areas (black arrows) indicate perilacunar matrices of two osteocyte lacunae, while the corresponding areas in (B) exhibit no change in phase shift, which is proportional to the projected density.

lacuno-canalicular volume to demineralise the local bone matrix [118]. This mechanism appears to serve as a response to an increased calcium demand, e.g. during lactation. Yet, mechanistic studies show that osteocytes utilise a far less acidic pH than osteoclasts to dissolve the bone mineral [121]. Therefore, the perilacunar matrix would need to be more susceptible to the demineralisation by means of a differential elemental or structural composition. Perilacunar matrix governed by osteocytes is hypothesised to be distinctively different from the remaining bone matrix. It is supposed to allow demineralisation by the osteocytic bone resorption and easier lacuna-shape adaptation in differential loading scenarios.

As a second application, concurrent X-ray fluorescence and ptychographic imaging was used to investigate human perilacunar matrix mineralisation by means of its spatially-resolved calcium concentration map. For this purpose, an unstained and resin-embedded thin human cortical bone section was prepared on a silicon-nitride membrane. Detailed sample preparation protocol is provided in Appendix B.2.

5.2.1 Results

Based on the visible-light image of the entire section, a $70 \times 70\,\mu m^2$ area of the cortical bone matrix in the proximity of a Haversian canal was preselected. It was subsequently scanned with a nano-focussed X-ray beam at a photon energy of 7.15 keV. Detailed experimental parameters are provided in Tab. C.2 (Appendix C). Fig. 5.2.1 shows the Ca map (A) and the ptychographic phase (B) of the selected bone region. It is possible to identify a fragment of the resin-filled Haversian canal (H), concentric lamellae rings (L), and two osteocyte lacunae (black arrows). The surrounding bone matrix was partially affected by typical cutting artefacts during sample preparation causing ruptures without any embedding medium.

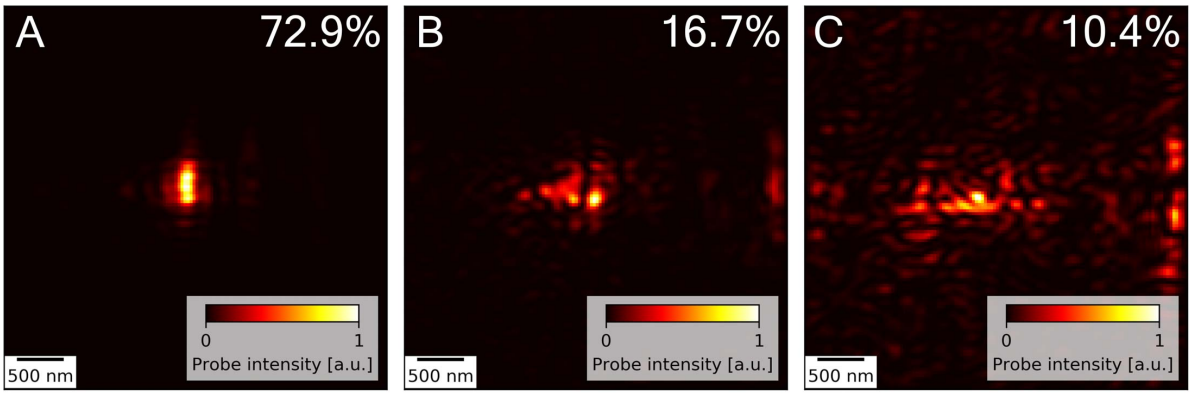

Fig. 5.2.2: Orthogonalised probe modes of the human cortical bone section in Fig. 5.2.1B. (A), (B), and (C) indicate the first, second, and third mode, respectively. The fractions of the total incident photon flux of 3.75×10^8 photon s^{-1} are indicated in the upper-right image corners. The probe size was assessed to equal $200 \times 400\,nm^2$ (h×v).

The raw Ca map in Fig. 5.2.1A was obtained using the spectra batch-fitting in the PyMca X-ray Fluorescence Toolkit [94]. The map was further refined with the interferometer positions to eliminate the distortions observed in the motor encoder positions. It was realised with `scipy.interpolate.griddata` routine from the SciPy Python library.

The ptychographic dataset was reconstructed using 100 iterations of the difference map algorithm and three orthogonal probe modes. Further increase of the probe modes number did not result in any qualitative improvement of the reconstructed object image. Fig. 5.2.2 shows the intensity distributions of the reconstructed, orthogonalised probe modes, with the respective intensity fractions in the upper-right corners of the sub-figures. The overall probe size was estimated to $200 \times 400\,nm^2$ (h×v). The scan was acquired with an incident photon flux of 3.75×10^8 photon s^{-1} at a horizontal fly-scan speed of $2\,\mu m\,s^{-1}$. It consisted of 326×326 scan points with a scan step size of 200 nm, equal in both directions. This resulted in a rather sparse linear overlap in the horizontal direction, causing artefacts in the ptychographic image due to the grid-scan pathology [122].

5.2.1.1 Spatial resolution analysis

While spatial resolutions of X-ray fluorescence mapping are inherently limited by the size of the X-ray beam footprint on the sample, the use of spatially coherent illumination and iterative phase retrieval instead of an objective lens makes ptychography surpass that limit. The X-ray fluorescence and ptychographic images of the human bone matrix shown in Fig. 5.2.1 are both rich in structural details and can be used to evaluate spatial resolution limits of both imaging techniques. For this purpose, two distinct Fourier-transform-based methods – suitable for each measurement – were employed.

The resolution of the X-ray fluorescence calcium map (Fig. 5.2.1A) was derived from its power spectrum. An edge-softening Tukey window function was applied to the image. Subsequently, the power of its discrete Fourier transform was calculated. The obtained two-dimensional power spectral density was then averaged vertically and horizontally to account, respectively, for different horizontal and vertical illumination sizes. Fig. 5.2.3A shows two directionally averaged PSD curves whose intersections with the lines denoting twice the noise level [93] correspond to the half-period resolution limits of: 418 nm in

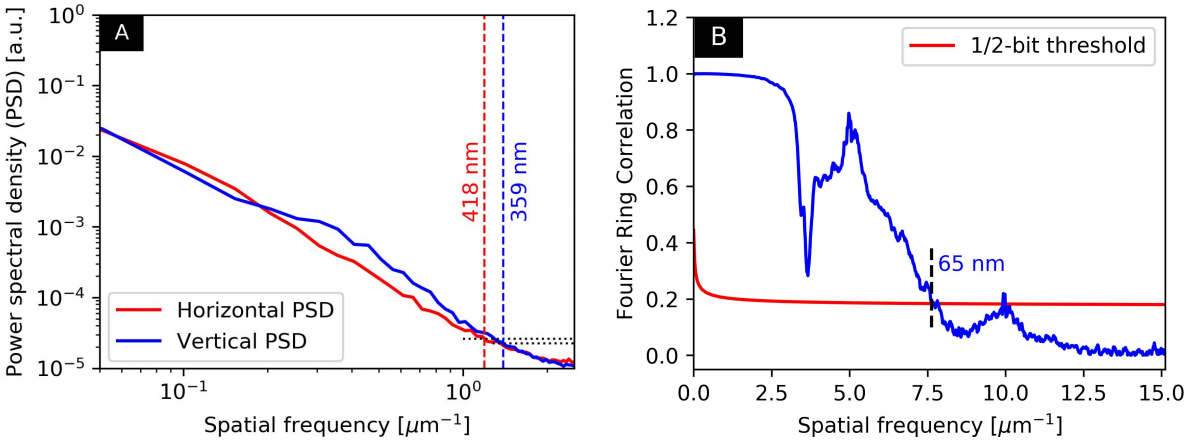

Fig. 5.2.3: Spatial resolutions of the human bone section measurements in Fig. 5.2.1. (A) presents horizontally- and vertically-averaged power spectral densities (PSD) of the raw Ca K-line map. The cross-sections of the PSD curves and twice the noise floor denotes half-period spatial resolutions of 418 nm×359 nm (h×v), respectively. Spatial resolution of the ptychographic phase image was evaluated by Fourier Ring Correlation (B) between reconstructions of two sub-datasets being complementary halves of the whole set of diffraction patterns. The reconstructions involved position refinement to break the raster-scan periodicity, resulting in grid-pathology artefacts. The cross-section of the FRC curve and the 1/2-bit threshold criterion provides a conservative spatial resolution estimation of 65 nm.

the horizontal direction and 359 nm in the vertical direction. The obtained values remain in very good agreement with the probe size obtained by ptychographic reconstruction (200 nm×400 nm, h×v) broadened horizontally by the 200-nm step of the continuous scanning.

The spatial resolution of the bone matrix ptychographic reconstruction in Fig. 5.2.1B was estimated with the Fourier ring correlation (FRC) method [89]. FRC requires typically two independently acquired images. In the absence of a repeated measurement, phase reconstructions from two complementary sub-datasets can be correlated, providing a more conservative resolution estimation [112]. Here, the sub-datasets were created according to the following pattern: (1) for even scan lines: even-numbered diffraction patterns, for odd scan lines: odd-numbered diffraction patterns; (2) for even scan lines: odd-numbered diffraction patterns, for odd scan lines: even-numbered diffraction patterns. Both sub-datasets were reconstructed using 100 iterations of the difference map algorithm and 3 probe modes. Additionally, refinement of the scan positions was enabled to break the raster-scan periodicity, resulting in step-scan-related grid-scan pathology artefacts. Solid blue line in Fig. 5.2.3B denotes the FRC between the two ptychographic sub-datasets. Its intersection with the 1/2-bit threshold line provides a spatial resolution limit of 65 nm.

5.2.1.2 Ptychography-enhanced calcium distribution

The raw Ca map in Fig. 5.2.1A is intrinsically affected by the projected density and thickness of the specimen called the mass-thickness effect. In the absence of calibration standards, the quantitative phase contrast image acquired simultaneously with the elemental map allows for a robust correction of this distortion, free of any scanning artefacts. Therefore, the lower halves of Figs. 5.2.1A and 5.2.1B were selected for further correction

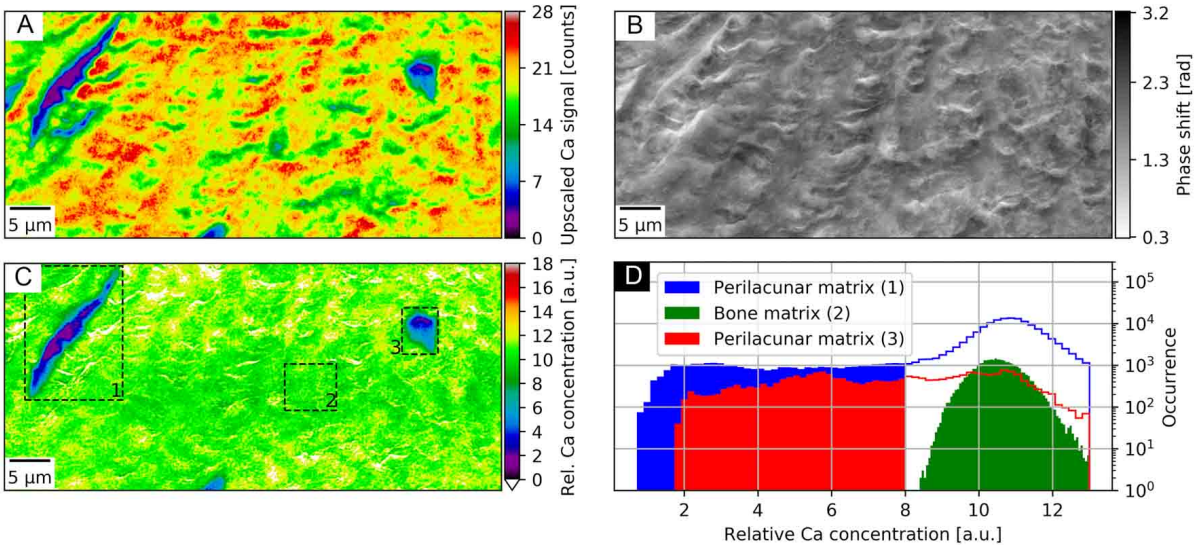

Fig. 5.2.4: Spatial distribution of relative Ca concentration of a human bone section using simultaneous ptychography and X-ray fluorescence (XRF) at 7.15 keV. (A) shows the lower half of the Ca map in Fig. 5.2.1A, upscaled bilinearly to the pixel size of the ptychographic reconstruction. (B) shows the corresponding ptychographic phase image. The Ca map in (A) was then divided by the regularised ptychographic phase (B). (C) presents the mass-thickness-corrected Ca map corresponding to the relative Ca concentration. Sample preparation artefacts were masked in white. (D) shows histograms of relative Ca concentrations values of three bone matrix areas as marked with dashed rectangles in (C). It compares relative Ca concentrations between two regions enclosing the identified perilacunar matrices (1, 3) and a representative region of the bone matrix (2). Face-filled in blue and red histogram values correspond to actual areas of the perilacunar matrices and span over visibly lower range of relative Ca concentrations than the values from the bone matrix (in green).

of the mass-thickness effect, as described in [108]. Since a background-corrected area under the Ca K-line peak is proportional to Ca areal mass and a ptychographic phase shift is proportional to the projected mass per unit area of the sample, the ratio of the two represents a relative Ca concentration map. The bilinearly upscaled Ca map (Fig. 5.2.4A) and the ptychographic phase (Fig. 5.2.4B) were aligned using subpixel image registration [66]. The upscaled Ca map was then divided by the ptychographic phase shift augmented by a regularisation phase offset of 0.1 rad to avoid division by zero. Fig. 5.2.4C shows the mass-thickness-corrected Ca map which corresponds to the relative Ca concentration. In the rupture areas stemming from cutting artefacts, the operation resulted in artificially elevated relative Ca concentrations. They originate from the difference in spatial resolution and sensitivity between XRF and ptychographic measurement. These areas were masked in white and excluded from the analysis. The obtained relative Ca concentration map (Fig. 5.2.4C) was used to compare the Ca content around two osteocyte lacunae with respect to the surrounding bone matrix. For this purpose, the relative Ca concentration values of the two perilacunar matrix regions (denoted as 1 and 3 in Fig. 5.2.4C) and a representative bone matrix area (2) were compared in the histogram in Fig. 5.2.4D. In the case of regions (1) and (3), the face-filled histogram regions represent the actual areas of the perilacunar matrices. The histogram shows depletion of Ca in the two regions around the osteocyte lacunae with respect to the remaining bone matrix area.

5.2.2 Discussion

In the second application, simultaneous ptychography and XRF were utilised to map the Ca concentration in human cortical bone tissue. The human bone consists to a large extent of a form of hydroxyapatite making Ca the major structural element of the bone. Although both imaging modalities allow for a general structure identification, XRF analysis benefits here from the simultaneously obtained ptychographic phase which removes the mass-thickness effect. The concurrent acquisition frees both measurements from any relative image distortions. The resulting relative Ca concentration map presents a much more uniform Ca distribution than the raw Ca map. The same effect had also been observed in similar previous studies of single cells [107] and neuronal tissue [108]. Within single micrometers around the osteocyte lacunae the Ca content visibly decreases. The comparison with concentrations in the remaining bone matrix further indicates a locally lower degree of mineralisation in the perilacunar matrix [123]. Yet, a statistically-relevant population of lacunae must be investigated to address the previous studies reporting a systematically higher mass densities of the perilacunar matrix [124, 125]. As an additional improvement, a local increase of the spatial resolution of Ca maps could diminish the artefacts from division by the ptychographic phase. Such higher resolutions could, for example, be realised by utilising multilayer Laue lenses as a probe-forming focussing optic, able to focus efficiently X-ray beam into a sub-10-nm focus [126].

5.3 Conclusion

The work presented in this chapter demonstrates the semiquantitative, structural investigation of elemental distributions in two biological systems at the nanoscale. It allows for high-throughput and seamless measurements of many targets with a long-range scanning unit and a highly coherent and intense X-ray beam. Finally, it extends on-the-fly ptychography and X-ray fluorescence to the multimodal imaging of a statistically-relevant number of samples at higher photon energies, while using sub-µm-sized beams. The method provides two complementary and unique contrast mechanisms. It demonstrates its potential in studying anti-tuberculosis drug delivery to macrophages, allowing for correlative measurements of the largest population of specimens to date. Further, the work shows that the method is very well suited to investigate the mineralisation of human bone matrix. It is therefore an important step towards concurrent studies of first-row transition metals distributions and the morphology of biological tissues by means of scanning X-ray microscopy.

An inherent limitation of the proposed imaging method is the lack of depth information which hinders unambiguous interpretation of superimposed features in 2D projections, especially in the case of thicker cells. Moreover, in the case of nanocontainer-treated macrophages only a complementary imaging method currently allows to distinguish whether the nanocontainer agglomerates are certainly internalised inside the cells (Appendix D). The solution is to combine both ptychography and X-ray fluorescence with computed tomography which would provide quantitative elemental and electron density contrasts of the reconstructed volume. Such an upgrade must also involve more efficient XRF detection, that will enable shorter exposure times at no loss in signal-to-noise ratio. It would also lower the dose imparted on the specimen per 2D projection, which in both reported experiments ranged from 6.85 to 8.65 MGy (Tab. C.2, Appendix C). Despite no observed radiation damage, these values approach the maximum tolerable doses for room-temperature imaging of chemically fixed samples at sub-100-nm spatial

resolutions [127, 128]. Therefore, extending this imaging method to tomography requires implementation of a cryogenic sample cooling to reduce the radiation damage at the nanoscale level. Despite the first proof-of-principle demonstrations [100, 129], new concepts are sought to improve the robustness of such a 3D elemental and structural mapping and make it reach the limit imposed by the available coherent flux.

Chapter 6

Ultrafast X-ray ptychographic tomography

The upgrade of the 3D scanning X-ray microscope in November 2018, as described in section 4.2, has been intended to bring the method of ptychographic X-ray computed tomography (PXCT) another, substantial step closer to reaching the measurement throughput that enables routine and statistically-relevant experiments. Combined with flexibility of the beamline P11, it resulted in a versatile experimental setup, featuring two operation modes: (1) ultrafast ptychographic tomography with several-micrometer-large beam sizes and (2) simultaneous ptychographic and X-ray fluorescence tomography with a submicrometer nano-probe. This chapter provides experimental demonstrations of both operation modes in ptychographic imaging of a nano-porous test structure and a piece of iron-rich radular tooth of a chiton (a marine mollusk).

The first operation mode, namely the ultrafast PXCT, was proven with a tomographic measurement of a silica nano-porous glass with a mean pore size of 140 nm. A glass bead had first been coated with a thin film of Ta_2O_5, using atomic layer deposition. As a result, Ta_2O_5 penetrated only within the outer, few-µm-thick layer of the glass bead, covering the surface of its pores with a film of an average thickness of 37 nm [60, 115]. Subsequently, using a focussed ion beam, a 20-µm-diameter pillar was extracted from the glass bead's surface inwards and attached to a tungsten pin on a sample holder. Such a cylindrically-shaped sample served as an optimal test structure for testing the imaging capabilities of the 3D scanning microscope. It provided namely dual-density-contrast features at two distinct length scales. Moreover, their curved interfaces and random orientations helped to avoid reflections of the incident X-ray beam, that would result in artefacts in tomographic reconstruction.

The fast acquisition of a PXCT dataset was realised with a 4.6-µm probe at a photon energy of 7.24 keV (Fig. 6.1A). Across such a micrometer-sized beam, the sample was continuously raster-scanned at a speed of $40\,\mu m\,s^{-1}$. The coherent diffraction patterns were recorded 4.4 m downstream of the specimen with an Eiger 500k detector[6.1], at a frame rate of 1 kHz. Detailed experimental parameters are provided in Tab. C.3 (Appendix C). Ptychographic reconstruction of the 2D projections consisted of 80 iterations of the difference-map algorithm, followed by 50 iterations of the maximum-likelihood refinement. A single probe mode was used. Fig. 6.1B shows a representative 2D ptychographic phase projection of the porous glass pillar. On its top, a protective layer of carbon can be seen, which was deposited to protect the upper structures from the focussed ion

[6.1] kindly lent by Dectris Ltd., Switzerland, `https://www.dectris.com`

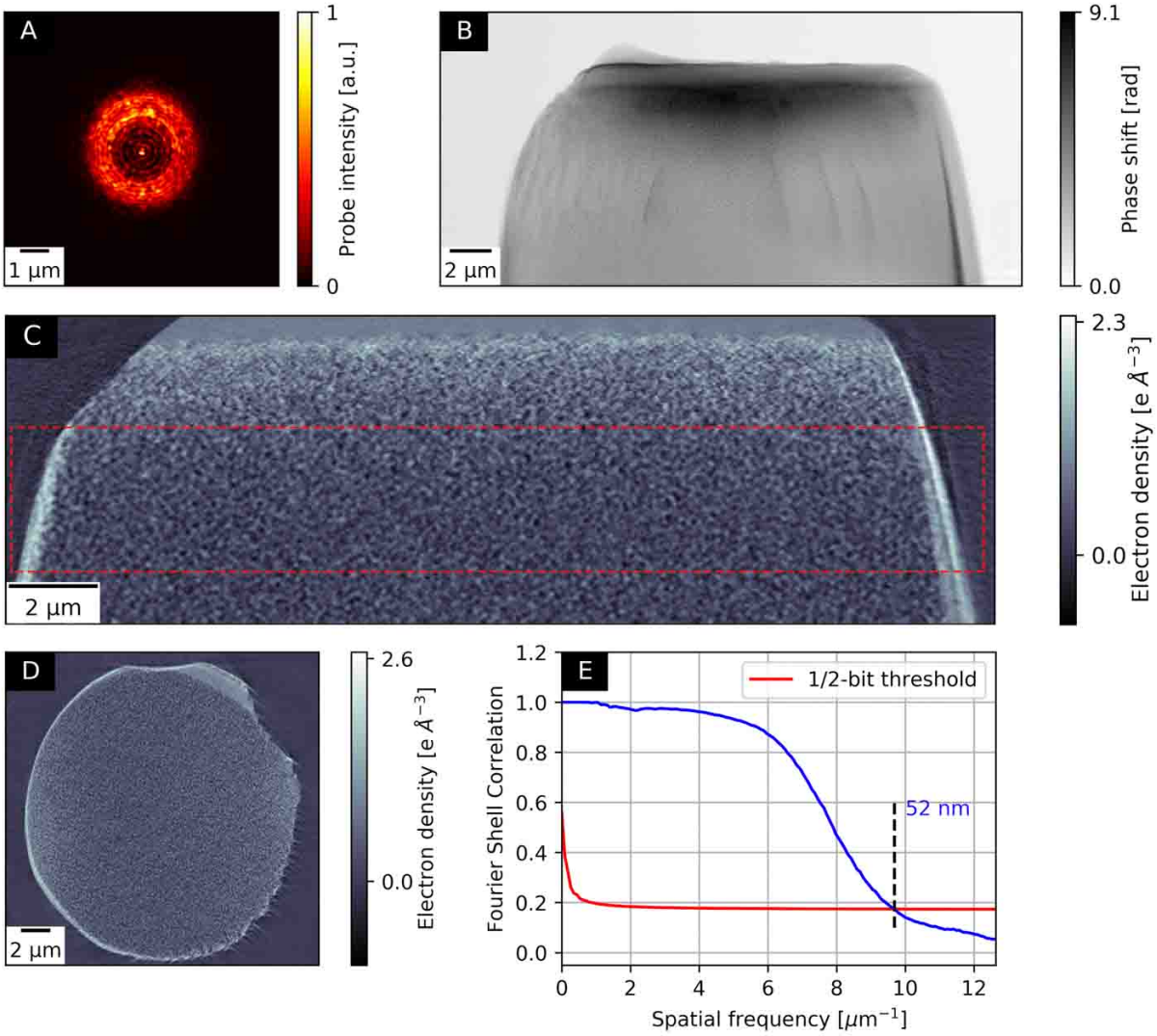

Fig. 6.1: Ultrafast ptychographic tomography at 7.24 keV of a piece of silica nano-porous glass coated from the top with Ta_2O_5 (average layer thickness: 40 nm). The average pore size was equal to 140 nm. (A) shows an intensity distribution of the 4.6 µm probe function. (B) shows a representative cropped ptychographic phase projection (unwrapped). (C) and (D) show xy and xz orthoslices of the reconstructed volume, respectively. Artefacts in (D) stem from distortions in a fraction of the 2D projections, caused by a loss of the interferometer signal. Yet, the slices allow to resolve the pores of the glass. (E) shows the Fourier shell correlation curve calculated for the sub-volume indicated in (C) with a dashed red rectangle. It intersects the 1/2-bit threshold at the isotropic spatial resolution limit of 52 nm. The resolution may be locally worsened by the aforementioned artefacts. The voxel size equaled 39 nm.

beam. Already in the projected view, a low-contrast grain structure indicates presence of the pores within the pillar. The phase image was unwrapped, using the `numpy.unwrap` routine from the NumPy Python library, and corrected for linear phase offsets. The view was cropped out of a larger scan area of $45 \times 15\,\mu m^2$ (h×v), which was the actual size of all projections in the tomographic dataset. In this way, each projection had horizontally enough empty space on both sides of the pillar as well as above it, to facilitate the alignment. The somewhat larger horizontal scan range accounted also for up to ±6-µm offsets in centering of the specimen. An average acquisition time per projection was equal to 32 s and included rotation and associated translative positioning of the sample. A substantial time overhead of 88% indicates further need of optimisation of the scanning script to account for one order of magnitude greater scanning speeds offered by the voice-coil motors.

The tomographic dataset consisted of 720 projections, acquired over a full angular range of 180° with a step of 0.25° within 6.5 h. This resulted in a Nyquist resolution limit of 43 nm in the horizontal plane for the upper part of the pillar. Due to a temporary loss of the signal from the horizontal interferometer, 6.5% ptychographic projections had to be reconstructed using the corresponding encoder position values. This induced distortions on a sub-µm level with respect to the projections, for which no signal loss had occurred.

The reconstructed ptychographic projections were first pre-aligned horizontally using the horizontal centre of mass and cropped to a view, as shown in Fig. 6.1B. The first step of the fine alignment utilised the efficient subpixel registration [66]. Vertically, the dataset alignment was further refined with the vertical-mass-fluctuation technique, while horizontally, the tomographic consistency alignment was used, as briefly described in section 3.1.3.3. The two latter steps were realised with the Matlab-based code for tomographic dataset processing, developed by the Coherent X-ray Scattering group, Swiss Light Source, at the Paul Scherrer Institut, Switzerland. The aligned projections were then reconstructed using the filtered back projection algorithm from unwrapped-phase projections, being also a part of the aforementioned implementation. Figs. 6.1C and 6.1D show central orthoslices in the planes xy and xz, respectively. Using Eqs. (3.1.29) and (3.1.30), the phase tomogram was calibrated to an electron density distribution. The voxel size was equal to 39 nm. Distortions in individual projections limited the accuracy in alignment and, hence, introduced artefacts in the resulting tomographic reconstruction, as visible e.g. in the xz slice in Fig. 6.1D. Quality of the obtained tomogram did not allow to resolve the high-resolution Ta_2O_5 film, whose presence, though, is indicated by an increasing average electron density towards the top of the pillar. Nevertheless, the slices allowed to resolve the 140-nm pores. The middle part of the reconstructed volume (as denoted in Fig. 6.1C) was used to estimate the 3D spatial resolution with Fourier shell correlation (FSC) [89]. Fig. 6.1E shows the FSC curve which intersects the 1/2-bit threshold at a half-period resolution limit of 52 nm. The obtained value is in agreement with the observed features, yet, should be treated with caution. Close to the pillar's surface the artefacts may namely prevail and worsen locally the actual resolution. The total dose deposited in the sample upon the measurement of 720 projections was equal to 0.14×10^9 Gy (see Appendix G).

The second operation mode of the new scanning 3D X-ray microscope was dedicated to simultaneous acquisition of ptychographic tomography and nanoscale X-ray fluorescence in 3D, using a highly focussed beam. To evaluate performance of the X-ray microscope in 2D ptychographic imaging, a $30 \times 30\,\mu m^2$ area of the same dual-tone irregular test structure, as measured in November 2015 (Fig. 4.3), was scanned using a 0.5-µm probe at a photon energy of 7.44 keV. While keeping the fly-scan speed unchanged at $40\,\mu m\,s^{-1}$, the sampling was adjusted by reducing the frame rate to 400 Hz and the vertical step

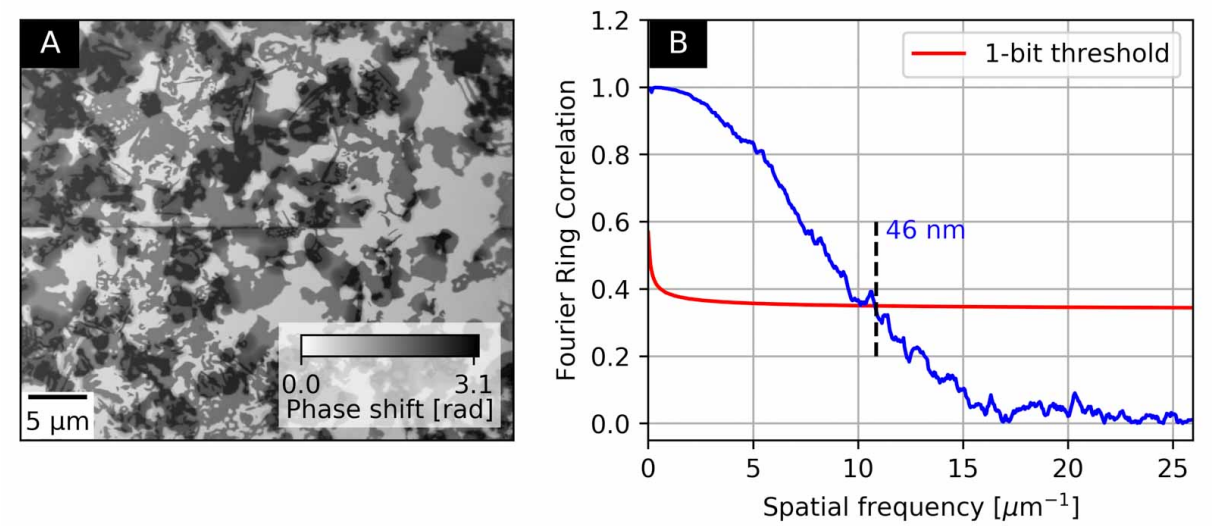

Fig. 6.2: Resolving power of the new 3D scanning X-ray microscope in 2D ptychography. (A) shows the ptychographic phase image of a dual-tone irregular test structure. The scan was performed at an energy of 7.44 keV with a probe size of 0.5 µm. The central scan area was measured independently again and the common ranges of both phase reconstructions were used to determine spatial resolution limit with Fourier ring correlation (FRC). (B) shows the corresponding FRC curve intersecting the more conservative 1-bit threshold line at a half-period resolution limit of 46 nm.

size to 200 nm. This resulted in a scanned area rate of 4.43 µm^2 s^{-1}, being two orders of magnitude greater than in the measurement performed 3 years earlier which had used the step-scan approach. Fig. 6.2A shows the reconstructed ptychographic phase of the test object. The central 15×15 µm^2 area was then scanned again. This allowed to select common views for both measurements and use them to evaluate the 2D spatial resolution with Fourier ring correlation (FRC). Fig. 6.2B shows the resulting FRC curve. As the measurements were acquired independently, a more conservative 1-bit threshold line could be used. The point where it intersects the FRC curve determines the half-period spatial resolution limit at 46 nm. The resolution could possibly be improved by increasing the frame rate of diffraction pattern acquisition, to reduce the motion blur.

Such settings of the X-ray microscope were used in the subsequent ptychographic tomography measurement of a piece of the iron-rich chiton's radular tooth. Due to high iron concentrations, the maximum count rate of the available digital pulse processor, used in X-ray fluorescence detection, has severely limited the quality and sensitivity of the recorded spectra. In turn, the results obtained from ptychographic tomography demonstrate fully the potential of the X-ray microscope and are discussed in detail in the following section.

6.1 Chiton's radular tooth ptychographic tomography

Chitons are marine mollusks with a considerable fossil record reaching half a billion years. They typically reside in the coastal areas, where they graze for algae on the oceanic rocks. Chitons are flattened and elongated mollusks, protected dorsally by a shell. With their broad and powerful foot, they can easily adhere to a rocky surface of their habitat.

Similarly to other mollusks, chitons have a radula, consisting of a belt of highly mineralised teeth, whose exact composition and morphology depend on a given chiton species. Amongst them, *Criptochiton stelleri* – the largest known species of chiton (up to a length of 33 cm) – possesses radular teeth of particular mechanical and architectural properties. The chiton teeth are constantly secreted in the rear part of the radula and advance along the radula belt towards its front, as their maturation progresses. A mature radular tooth consists of mineralised cap with three cusps, flexibly attached to the radula base. The cap is elongated laterally (0.7 mm wide and 0.2 mm thick) and features a biphasic structure, consisting of a hydrated iron-phosphate core region and a ferromagnetic iron-oxide (magnetite) outer veneer. Thanks to this spatially distinct organic and inorganic phases and an anisotropic crystal nucleation and growth, the chiton radular teeth have extraordinary mechanical properties. Characterised by hardness and stiffness larger than human enamel or calcium-carbonate-based mollusk shells [130], they effectively inhibit any crack propagation and are highly abrasion resistant. The radular teeth are therefore an interesting biomineral, whose principles could be utilised in the fabrication of synthetic composites.

Structural properties of the teeth of *Criptochiton stelleri*, were investigated with transmission and scanning electron microscopy of thin teeth cross-sections, including electron-induced energy-dispersive spectroscopy, as well as with micro-beam X-ray transmission and X-ray powder diffraction [130]. Within the scope of this thesis, a piece of *Criptochiton stelleri* chiton's tooth has been studied using quantitative ptychographic X-ray computing tomography at sub-100-nm spatial resolutions.

Fig. 6.1.1A shows an electron micrograph of the chiton's radular tooth, from which a thin pillar was milled out from the tooth's surface inwards, using a focussed ion beam. The region of extraction was denoted with a red rectangle. The ptychographic phase projection of the entire sample is shown in Fig. 6.1.1B. The pillar was about 50 µm tall, with its top denoting the tooth's surface level. Its maximal lateral width equaled 8 µm. While the upper half of the pillar exhibited a uniform projected density distribution, the lower half contained several cracks and density variation, the deeper it reached into the tooth's core. The scan was acquired with a 0.5 µm×0.8 µm probe of a fairly astigmatic intensity distribution, as shown in Fig. 6.1.1C. Having pre-characterised the piece of the chiton's tooth, its lower part was selected (dashed red rectangle in Fig. 6.1.1B) for further volumetric investigations, using nanoscale ptychographic X-ray tomography.

The tomographic dataset comprised 180 equally spaced projections over an angular range of 180°. Acquisition of each 30×25-µm^2 2D projection took 184 s, at a continuous scan speed of 40 µm s^{-1} and a frame rate of 400 Hz. The use of a smaller probe required a denser sampling, resulting in an increased time overhead due to a greater number of scan lines (125). Detailed experimental parameters are provided in Tab. C.3 (Appendix C). Each ptychographic projection dataset was first horizontally cropped to a field of view of 22×25 µm^2, based on a coarse horizontal centre-of-mass alignment, using the corresponding lower-resolution scanning X-ray transmission images. This eliminated an excess of the empty space on both sides of the pillar, which would otherwise result in a substantial non-linear background in ptychographic phase reconstructions. The cropped ptychographic datasets were then reconstructed with 80 iterations of the difference map algorithm, followed by 50 iterations of the maximum-likelihood refinement.

The set of projections was first pre-aligned horizontally, using a self-developed approach based on a sinogram of the modulus of the unwrapped-phase gradient. Neither horizontal centre-of-mass alignment nor efficient sub-pixel registration would namely give satisfactory results. Fig. 6.1.2A shows a raw wrapped phase sinogram, obtained from the middle horizontal lines of all 180 projections. The phase sinogram was then line-wise unwrapped and corrected for the linear and constant phase offsets, as shown in

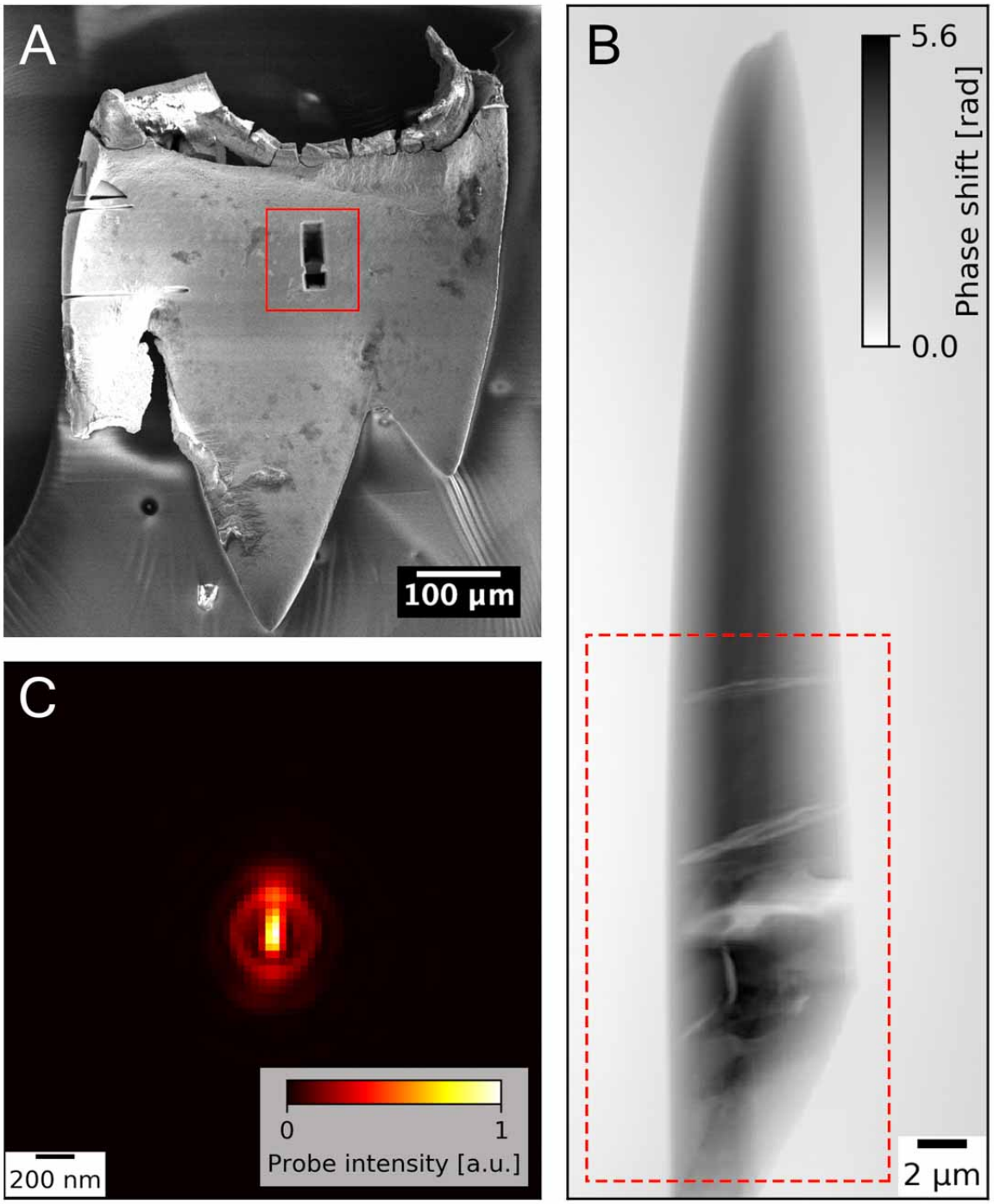

Fig. 6.1.1: Ptychographic imaging of a piece of the *Criptochiton stelleri* radular tooth at a photon energy of 7.44 keV. (A) shows an electron-micrograph of the entire tooth, exhibiting its three cusps. The red rectangle denotes the region, from which a thin pillar was extracted from the tooth's surface 50 µm inwards, using a focussed ion beam. (B) shows the ptychographic phase projection of the entire sample. Its upper part, corresponding to the region close to the tooth's surface, features a uniform projected density distribution. The lower part features cracks and structural details and, hence, it was selected for the subsequent tomographic imaging. (C) shows an intensity distribution of the X-ray beam, scanning the sample. The probe has an astigmatic profile of 0.5 µm×0.8 µm (h×v).

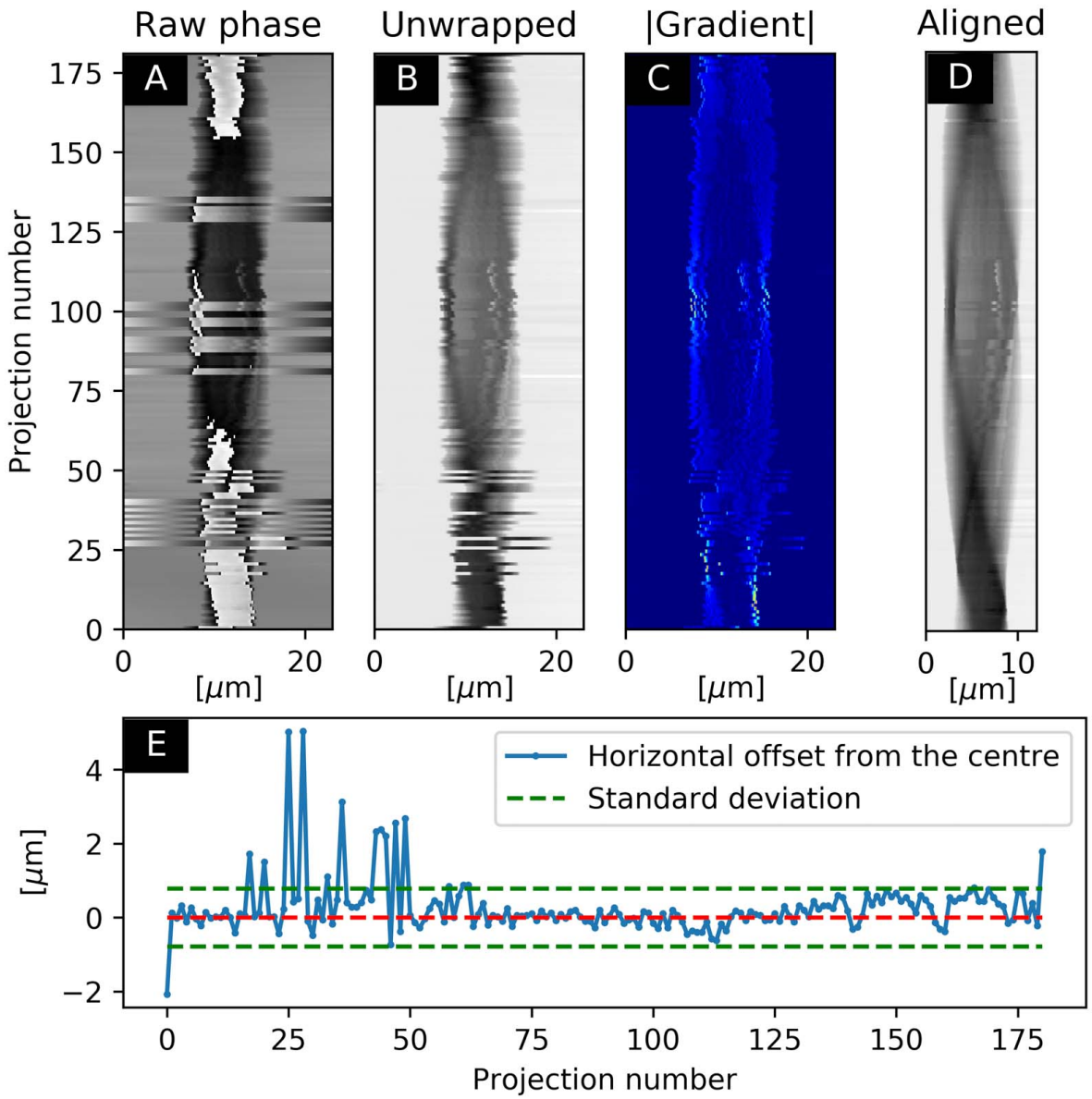

Fig. 6.1.2: Horizontal pre-alignment of the 2D ptychographic phase projections based on the absolute gradient values of the unwrapped phase sinogram. (A) shows a raw phase sinogram constructed from a horizontal line taken from the middle of the vertical range of every 2D projection. (B) shows an unwrapped sinogram corrected for linear and constant phase offsets. (C) shows a sinogram where phase profile for every projection was replaced by the modulus of its gradient. A |gradient| lower threshold value was chosen to identify the two coordinates, at which both edges of the pillar start. The average of the two positions defined a new centre specific to a given projection. The set of new centres was used to shift the sinogram lines accordingly. (D) shows the aligned phase sinogram, which was cropped to a common horizontal range. The plot of the horizontal offsets from the initial centre is shown for all projections in (E). While the most extreme offsets span a range of 7 µm, 90% of all projections remains within a standard deviation of 0.781 µm (two dashed green lines).

Fig. 6.1.2B. Subsequently, gradients of the each sinogram's line were calculated, using the `numpy.gradient` routine. Their absolute values, |gradient|, were plotted in Fig. 6.1.2C, as an edge-sensitive mask of the sample. As a next step, the lowest threshold value of the |gradient| was selected to indicate the begin of the edge slope on both sides of the specimen. For every projection in the sinogram, respective first horizontal position from the left side and the right side of the pillar were found, for which its modulus of the phase gradient was greater than the threshold value. The two positions were then averaged to yield the new centre coordinate, to which the corresponding projection was shifted. The whole sinogram was then horizontally cropped to find a common horizontal range for all projections. The aligned and cropped phase sinogram is shown in Fig. 6.1.2D. Its global consistency has been significantly improved. Further detail artefacts originate from a still missing vertical alignment. Finally, Fig. 6.1.2E shows the plot of how much offset the new centre coordinates were from the initial projection centre, as a function of the projection number. Despite the maximum relative offset of about 7 µm observed between isolated views in the first 30 projections, the offsets of 90% projections fall within the range defined by the standard deviation of ± 0.78 µm.

Such a prealigned tomographic dataset was further aligned vertically by minimising the mass fluctuations along this direction in the phase projections. The iterative alignment was applied to a 12-µm middle vertical range of the sample, avoiding areas with phase residua. The procedure was repeated several times for the same vertical range, while varying the high-pass filter applied to the vertical-mass-fluctuation curves. In this way, all outlying projections could be aligned. Subsequently, the horizontal alignment was refined with the tomographic consistency method. In the course of all alignment steps, it turned out to be impossible to centre correctly 3 out of 180 projections (at 159°, 164°, and 174°). As they were non-neighbouring, these views were then excluded from the tomographic reconstruction.

The aligned tomographic dataset was subsequently reconstructed with a filtered back projection algorithm, using unwrapped phase projections. Fig. 6.1.3 shows representative orthoslices in xy (A), yz (B), and xz (C). Similarly to the nano-porous glass tomogram, the phase tomogram was calibrated to an electron density distribution. The volume allows to identify structural elements like cracks on micro- and nanoscale and several material phases of various electron density. The voxel size was equal to 38 nm. Mild artefacts in the proximity of the diagonal cut in the lower right side of the slice in Fig. 6.1.3A originate from inevitable X-ray reflections from the fairly flat cut surface at glazing tilt angles. This effect was often combined with strong phase residua (vortices) induced by a sub-100-nm high-density layer of gallium, deposited during cutting the pillar off by the focussed ion beam. More slices of the volume along all three planes are provided in Appendix H. The total dose imparted on the piece of chiton's radular tooth was estimated to equal 1.4×10^9 Gy. The middle part of the reconstructed volume, as denoted with a dashed red rectangle in Fig. 6.1.3A, was selected for resolution estimation using Fourier shell correlation (FSC). Fig. 6.1.3D shows the resulting FSC curve, whose intersection with the 1/2-bit threshold represents the half-period limit of the isotropic 3D spatial resolution down to 65 nm.

As discussed in section 3.1.3.4, quantitative electron density contrast of the volume reconstructions obtained by ptychographic tomography can further be recalculated into the mass density distribution, given an approximately known chemical composition of the sample. As chiton radular teeth are rich in iron-oxide, the molecular parameters of magnetite were utilised to re-calibrate the volume contrast, using Eq. (3.1.31). A respective coefficient of $A/Z = 2.105$ was used. Fig. 6.1.4A shows an exemplary orthoslice in the mass density colour-scale contrast. The view allows to observe a distinct decrease in mass

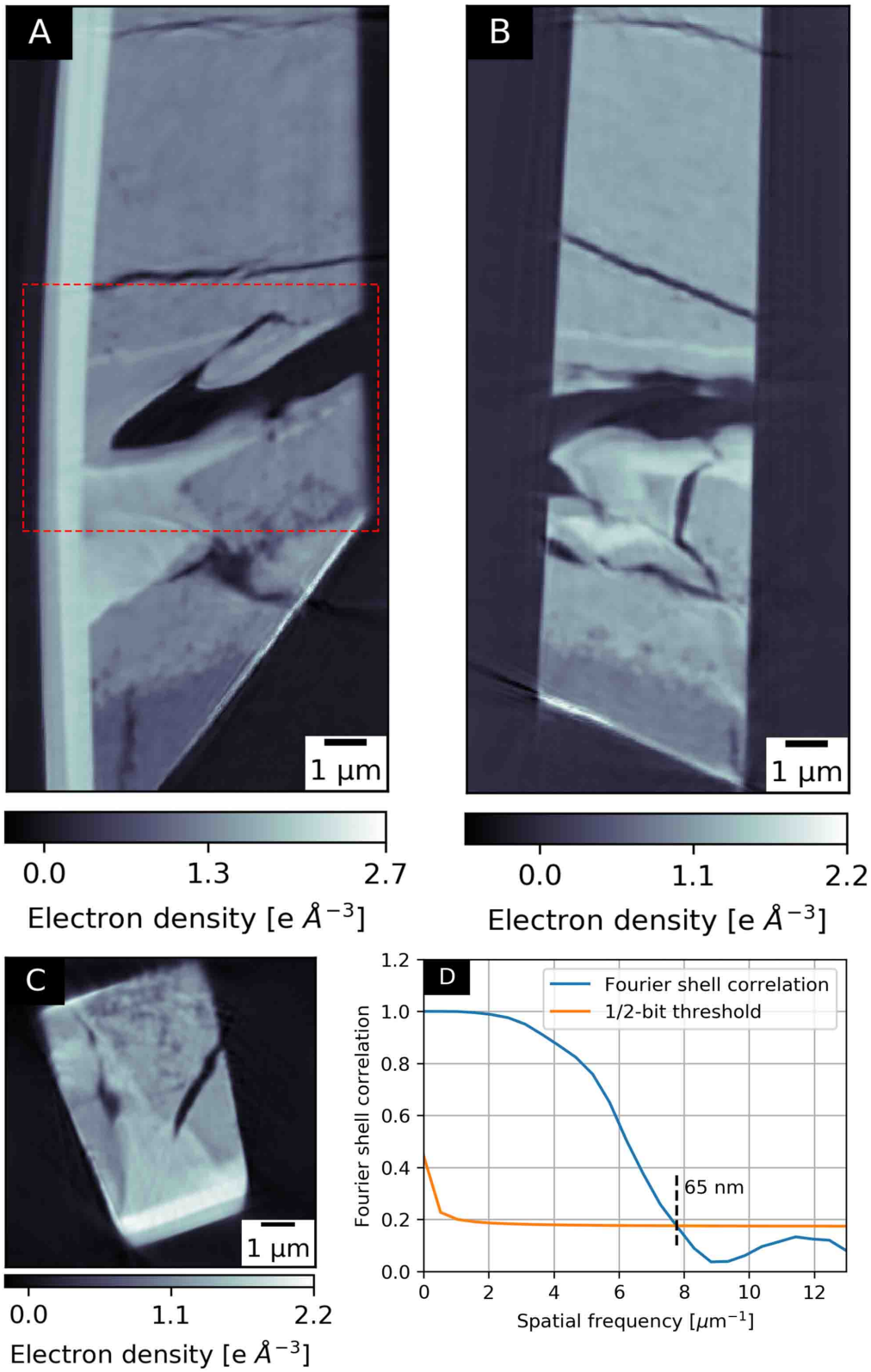

Fig. 6.1.3: Ptychographic tomography of a piece of the *Criptochiton stelleri* radular tooth at a photon energy of 7.44 keV. (A) and (B) show representative orthoslices of the reconstructed volume parallel to the rotation axis, in the planes yz and xy, respectively. (C) shows a representative orthoslice perpendicular to the rotation axis (xz plane), taken at one-third of the volume height. The part of the reconstructed volume enclosed with a dashed red rectangle in (A) was used to estimate the isotropic spatial resolution. (D) shows the corresponding Fourier shell correlation curve calculated for this region, which intersects the 1/2-bit threshold line at a spatial resolution limit of 65 nm. The voxel size was 38 nm.

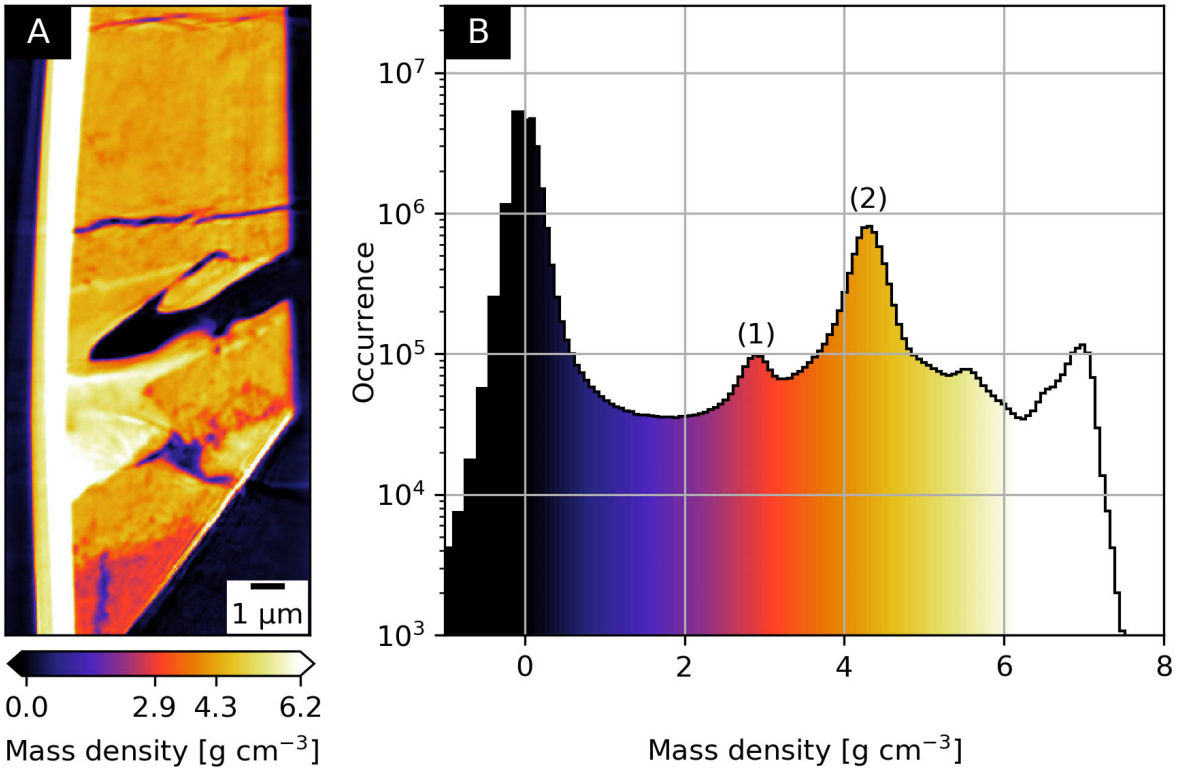

Fig. 6.1.4: Quantitative 3D mass-density map of a piece of the *Criptochiton stelleri* radular tooth obtained by ptychographic tomography. (A) shows a representative orthoslice recalibrated into the mass-density contrast. Visual inspections allows to identify the least-dense material phase in the lower part of the pillar (in red), followed upwards by a denser, dominant one (in orange). On the left side of the pillar, a highly-dense vertical layer is observed, which is a sample-preparation artefact. (B) shows a histogram of mass-density values from all voxels of the tomogram. The leftmost peak indicates the empty air region around the sample. The peak (1) at 2.9 g cm^{-3} denotes the hydrated iron phosphate, which is the main constituent of the organic core of the tooth. The peak (2) at 4.3 g cm^{-3} corresponds to the highly-mineralised magnetite outer shell of the tooth. The two rightmost peaks correspond to the gallium and platinum-carbide deposits from the focussed-ion-beam milling. Their mass densities are underestimated due to the different molar-mass-to-atomic-number ratios.

density in the lower part of the pillar (in red), above which a denser matter dominates (in orange). Additionally, a sub-micrometer-thick, vertical stripe can be seen on the left hand side, in bright yellow. Fig. 6.1.4B shows a histogram of mass-density values of all voxels in the tomogram. It allows to isolate four mass density fractions, apart from the leftmost peak at $0\,\mathrm{g\,cm^{-3}}$, corresponding to the empty air area around the pillar. The peak (1) at $2.9\,\mathrm{g\,cm^{-3}}$ represents the lighter, organic core of the radular tooth, consisting of hydrated iron phosphate. The mass density obtained from quantitative ptychographic tomography is in very good agreement with the tabulated value of $2.87\,\mathrm{g\,cm^{-3}}$ [131]. The following peak, (2), denotes a denser material phase of the iron tooth, i.e. the iron-oxide outer veneer. The obtained mass density of approximately $4.3\,\mathrm{g\,cm^{-3}}$ is somewhat lower than the tabulated bulk density of magnetite ($5.15\,\mathrm{g\,cm^{-3}}$ [132]). Two further peaks correspond to the materials, whose presence cannot be explained for this particular species of chiton. They turned out to be a rather strong residual deposits of platinum carbide and gallium from the focussed ion beam writing and milling, that also partly penetrated to the empty compartments within the sample.

6.2 Conclusion

The work presented in this chapter has opened a new category of bio-imaging experiments at beamline P11. Despite certain mechanical challenges, the upgraded scanning 3D X-ray microscope allowed for two preliminary demonstrations of volumetric imaging by means of ptychographic X-ray computed tomography. The setup could be operated in two complementary modes: (1) ultrafast and low-dose ptychographic tomography and (2) prototypical simultaneous ptychographic and X-ray fluorescence tomography, by utilising probe sizes between 0.5 µm to 4.6 µm. Tab. 6.1 provides a detailed comparison between the two operation modes.

Ultrafast ptychographic X-ray tomography was demonstrated in 3D mapping of a nanoporous glass. The combination of a large probe with a high frame-rate detector allowed to fully utilise the fast-scanning capacity offered by the voice-coil motors. The reconstructed volume, albeit affected by distortion artefacts in a small fraction of the projections, permitted visualisation of the 140-nm pores of the glass at an isotropic spatial resolution down to 52 nm. The relatively high dose can be compared with the previous study by Holler, *et al.* [60]. In their research, namely, a dose of 1.2×10^{10} Gy imparted on a similar specimen (also 720 projections) allowed to obtain an isotropic resolution of 16 nm. As the dose in imaging scales with the inverse fourth power of the resolution [48], the dose used in the experiment reported in this thesis should have allowed for reaching 49-nm spatial resolutions. The spatial resolution obtained by the FSC would therefore indicate an almost dose-restrained resolution limit. This should be though taken with caution in the context of the artefacts, resulting from the distortions observed in a small fraction of the 2D projections. Elimination of these distortions in future experiments will certainly enable even more efficient use of the incident photon fluence.

In the second experimental application, a ptychographic tomogram of a pillar extracted from an iron-rich chiton's radular tooth was obtained. The measurement was realised with a one order of magnitude smaller probe, while retaining the same fly-scan speed. This exploited therefore potential settings for a future simultaneous acquisition of nanoscale X-ray fluorescence in 3D. The isotropic resolution of the tomogram was ultimately restrained down to around 70 nm by the Nyquist resolution limit (angular sampling) and the fly-scan-induced motion blur. The quantitative analysis of the tomographic reconstruction allowed to identify two sample-relevant mass densities corresponding to two

Tab. 6.1: Versatile 3D scanning X-ray microscope at beamline P11.

Parameter	**Ultrafast ptychographic tomography**	**Ptychography and XRF**
Energy	Slightly above Fe K absorption edge (7.112 keV)	
Probe size	4.6 µm	0.5 µm
Fly-scan speed	$40\,\mu m\,s^{-1}$	
Acquisition rate	1 kHz	0.4 kHz
Scanned area rate[6.2]	$39.2\,\mu m^2\,s^{-1}$	$6.1\,\mu m^2\,s^{-1}$
Resolution elements/s [6.3]	up to $100\,kpixel\,s^{-1}$	up to $16\,kpixel\,s^{-1}$
Expected dose/projection (biological cell)	0.43×10^5 Gy	2.46×10^5 Gy

expected elements of the radular teeth structure: the iron-phosphate core and the magnetite outer veneer. A 50-µm-tall pillar extracted from the concave side of the tooth inwards was therefore long enough to penetrate thought the highly-mineralised magnetite shell. The magnetite mass density obtained by ptychographic tomography is lower than the tabulated bulk value, which can be explained by the presence of organic elements, as reported in [130], as well as the nano-cracks, resulting in a less dense structure.

Both specimens used in the reported experiments were highly radiation-resistant. Imaging of more radiation-sensitive samples would require a currently unavailable cryogenic sample environment. As an outlook towards future measurements of biological samples, the parameters of both experiments were used to estimate expected doses that, in both cases, would be deposited onto a biological cell. Tab. 6.1 provides the two dose values, as per projection. From the previous study by Diaz, *et al.* [62], it is known that a dose of 3.6×10^5 Gy distributed over 288 ptychographic projections allowed to obtain a tomogram of frozen-hydrated cells at 180 nm spatial resolution. With the doses feasible with the scanning 3D X-ray microscope at beamline P11, at least a 2.5-fold increase in resolution can be expected in the anticipated ptychographic tomography experiment of cryo-cooled biological samples.

[6.2] includes a total measurement overhead of around 90% (November 2018)
[6.3] assuming a detector with 75-µm pixels and a propagation distance of 4.4 m

Conclusion and outlook

Scanning X-ray microscopy at modern synchrotron radiation facilities offers several complementary contrast mechanisms allowing for spatially-resolved investigations of complex specimens. A particularly demanding specimen group comprises biological tissues and cells, whose irradiation sensitivity sets a stringent requirement for highly efficient use of every X-ray photon they interact with. By using high-quality coherent X-ray beams, ptychography enables dose-limited and quantitative phase-contrast imaging of weakly-absorbing sub-cellular structures in 2D and 3D at sub-100-nm spatial resolutions. At the cost of discarding around 99% of the incident, yet incoherent, photon flux, ptychography surpasses limitations of the conventional scanning-probe microscopy, restrained by the size of the beam footprint on the sample. While several contrast mechanisms, like differential phase contrast or dark field have successfully been replaced by ptychography at a great increase in sensitivity and resolution, efficient use of the incident X-ray photons must also include the complementary element-sensitive imaging contrast. It is obtained by acquisition of the X-ray fluorescence signal, being a unique fingerprint of elements constituting the specimen. Fluorescent photons are intrinsically emitted by those elements whose absorption edges fall below the excitation energy. Unlike in ptychography, spatial resolutions in X-ray fluorescence are beam-size-limited, while reaching the trace-metal concentration level has typically been realised with much higher incident photon fluxes than required for ptychography. These apparently contradictory characteristics make the combination of ptychography and X-ray fluorescence a challenging endeavour and the efforts spent to develop such a multimodal X-ray microscope should not be taken for granted. With the ever-growing potence of contemporary synchrotron-light sources, several pioneering experiments of concurrent ptychographic and X-ray fluorescence imaging of single specimens have lately been demonstrated worldwide. Alongside with the recent findings, the aim of this PhD thesis was to demonstrate the feasibility and explore opportunities of the method of combined ptychography and X-ray fluorescence in multimodal imaging of biological specimens at photon energies permitting mapping of first-row transition metals. The project exploited the excellent coherent properties of X-ray beams at beamline P11 of the low-emittance PETRA III synchrotron light source at DESY, Germany. Furthermore, in order to increase the significance of this combined structural and elemental mapping to the biomedical community, necessary technological aspects regarding the so-far low throughput of this method have been addressed. Advances in instrumentation were validated with experimental demonstrations concentrated on several biological cases.

The first stage of this PhD thesis was dedicated to establishing the concurrent ptychographic and X-ray fluorescence imaging in 2D at beamline P11. Implementation of the continuous-motion scanning significantly accelerated the measurements, whereas the resulting motion blur in diffraction data was alleviated with the mixed-state difference-map ptychographic reconstruction algorithm. The long-range scanning unit allowed for artefact-less serial mapping of many targets at nanometer precision, distributed over an area up to $4 \times 4\,\mu m^2$. With the mature 2D X-ray microscope, the correlative X-ray imag-

ing methods were applied in quantitative investigations of two vital biological examples.

The first application concerned the multimodal imaging of macrophages treated with iron-oxide nanocontainers, used for efficient delivery of anti-tuberculosis drugs to infected cells. Ptychographic images visualised a number of sub-cellular details and enabled an unambiguous interpretation of the simultaneously recorded iron X-ray fluorescence maps. The iron distributions revealed clusters of nanocontainers within the macrophages. Using a custom-designed reference sample, the iron maps were carefully calibrated to the projected areal mass density with values between tens to hundreds $\mathrm{fg\,\mu m^{-2}}$ per resolution area. Installing a thin silicon photodiode to monitor and measure the incident photon flux proved essential to ensure consistent experimental conditions for all measured datasets. The quantitative iron maps allowed to determine the distribution of the antibiotic load in the nanocontainer-agglomerates under investigation. Through this biomedical application, the method of simultaneous ptychography and quantitative X-ray fluorescence has been applied, in this thesis, to the largest population of specimens to date. Such an approach allowed for a statistical analysis, so much demanded in biomedical research.

In the second application, the local degree of mineralisation in human cortical bone tissue was studied, using simultaneous ptychography and calcium X-ray fluorescence mapping. Both the ptychographic phase image and the Ca map of a thin bone section allowed for identification of structural elements on the micro- and nanoscale, including two osteocyte lacunae. Since the ptychographic phase is proportional to the projected mass density of the tissue, it was used to remove the mass-thickness effect from the Ca distribution map. This operation was demonstrated for the first time, in this thesis, for the concurrently obtained structural and elemental maps of a biological specimen. Thanks to the simultaneous acquisition of both modalities, the mass-thickness-removed Ca distribution was free of any distortions. The only artefacts were the ruptures in bone tissue, which were an inevitable consequence of thin-section cutting. The resulting relative Ca concentration map exhibited the notably lower Ca content proximal to the osteocyte lacunae with respect to the surrounding bone matrix. This observation was correlated with the anticipated, distinctively different characteristics of the perilacunar bone matrix and requires further study on a statistically-relevant population of lacunae.

Both experimental applications show how correlative scanning X-ray microscopy can contribute to interdisciplinary biomedical research. The so-far implemented advances in instrumentation have enabled efficient scanning of many samples deposited on a flat substrate, which is a generally preferred preparation method in cellular biology.

The second stage of this PhD thesis was focussed on transferring the experience gained in the 2D imaging experiments to quantitative 3D X-ray microscopy, using ptychographic X-ray computed tomography. This was realised with a new X-ray microscope, designed for 3D correlative measurements of biological specimens at incident photon energies up to 10 keV. The preliminary missing-wedge tomography of a tuberculosis-infected macrophage demonstrated potential of the method by allowing to isolate a *Mycobacterium tuberculosis* within the cell, otherwise hardly visible in single 2D projections. The subcellular structural details were though beyond the resolving power, which was impaired by a highly anisotropic angular sampling and a substantial radiation damage, resulting from room-temperature measurements. The most important outcome of this stage of the PhD project were the subsequent ptychographic tomography experiments of a piece of nano-porous glass and quantitative volumetric imaging of a chiton's radular tooth. Both applications demonstrated the versatility of the new 3D scanning X-ray microscope, operated in air at a fly-scan speed of $40\,\mathrm{\mu m\,s^{-1}}$ with flexible beam sizes ranging from several micrometers down to a few hundreds of nanometers.

In the first experiment, a 4.6-µm beam was used to image a nano-porous glass sample,

which highlighted an outstanding capability of the microscope to perform ultrafast ptychographic tomography. With the scanned area rates reaching $39.2\,\mu m^2\,s^{-1}$, it has been the fastest on-the-fly ptychographic tomography reported to date. The reconstructed volume allowed for identification of 140-nm pores at an isotropic spatial resolution of 52 nm.

In the second experiment, the use of a 0.5-µm beam enabled 3D mapping of a piece of the marine mollusk tooth, using ptychographic tomography with simultaneous acquisition of X-ray fluorescence. Being itself a highly-iron-rich biomineral of extraordinary stiffness and hardness, the chiton's radular tooth was sufficiently irradiation-resistant and consisted of two mass-density phases. Reconstruction of the iron XRF projections turned out to be challenging due to the count-rate limit of the detector's digital pulse processor. On the other hand, ptychographic tomography yielded a volumetric representation of the electron density distribution of the specimen at a Nyquist-sampling-limited isotropic spatial resolution of 65 nm. Recalibration into the mass density contrast allowed for identification of two expected structural elements of the chiton's tooth: the iron-phosphate core and the outer iron-oxide veneer. Temporary limitations of the method currently originate from (1) occasional sample positioning failures caused by so-far insufficiently strong reflection of the horizontal interferometer signal from the curved surface of the reference cylinder, and (2) too slow X-ray fluorescence counting.

Both the 2D scanning unit and the upgraded 3D X-ray microscope have allowed for a series of successful experimental demonstrations of in-air on-the-fly simultaneous ptychographic and X-ray fluorescence imaging in biological applications. There are three major areas, in which their performance can further be improved.

Both instruments would vastly benefit from an enhanced X-ray fluorescence detection. A dedicated, multi-element SDD detector, featuring much larger active area would collect fluorescent photons from a respectively larger solid angle, facilitating trace-element mapping at least cost of the acquisition rate. On the other hand, a new digital pulse processor, able to process higher count-rate signals, would allow to record high quality XRF tomographic projections. Another substantial improvement of both the X-ray fluorescence spectra and the coherent diffraction is reduction of the scatter noise by enclosing the entire beam path in vacuum. This includes the X-ray optics and the sample scanner, together with the active area of the XRF detector, as well as elimination of the air gap between the end of the flight-tube and the far-field ptychography detector. This will finally eliminate the air-derived K line of argon in the XRF spectra and enable efficient detection of low-Z, life-relevant elements, whose characteristic lines have so far been significantly absorbed in air.

The second improvement relates to the quality of ptychographic reconstructions from sparsely sampled fly-scans, for which a nano-focussed beam was used. The raster-grid pathology artefacts, observed also by others [122], originate from an intrinsic symmetry of the line scan trajectory. In future experiments, the spiral continuous scan path should be implemented to break the scan pattern periodicity and considerably alleviate the raster-grid artefacts [133].

The ultimate limitation of the method, especially in tomographic imaging of soft biological tissue and cells, is the radiation damage. Therefore, the third improvement concerns extending the upper limit of accepted doses towards the GGy range, by complementing the sample scanner with cryogenic sample cooling.

All aforementioned improvements have been included in the further development strategy of the 3D scanning microscope and are foreseen to be implemented in the nearest future.

Tab. 7.1: Expected parameters of the 3D scanning X-ray microscope at beamline P11 in the simultaneous 3D ptychography and X-ray fluorescence operation mode.

Parameter	**Ultimate PETRA III**	**PETRA IV**
Energy	Slightly above Fe K absorption edge (7.112 keV)	
Probe size	0.1 µm	
Fly-scan speed	$20\,\mu m\,s^{-1}$	$200\,\mu m\,s^{-1}$ (10x)
Acquisition rate	0.4 kHz	4 kHz
Scanned area rate[7.1]	$1.1\,\mu m^2\,s^{-1}$	$11\,\mu m^2\,s^{-1}$
Expected dose/projection (biological cell)	2.46×10^6 Gy	2.46×10^7 Gy (10x)
Expected spatial resolution (cryo-cooled biological cell)[7.2]	27 nm	15 nm
180 projections, $10\times10\,\mu m^2$	5 h	27 min

Recent years have brought a new milestone to the research with synchrotron radiation, thanks to first emerging fourth-generation storage rings. The first facility to upgrade successfully has been MAX IV in Lund, Sweden [29]. It is to be followed by the SIRIUS synchrotron in Campinas, Brazil, and ESRF in Grenoble, France, currently under construction. Many other facilities, such as APS in Chicago or Spring-8 in Japan, are preparing their upgrade plans, including PETRA III in Hamburg, Germany.

Simultaneous ptychographic and XRF imaging should indeed find its major application at diffraction-limited synchrotron light sources. The 3D scanning X-ray microscope, optimised and used in this thesis, has been designed to take full advantage of the ultimately coherent photon flux of the new-generation synchrotron facilities. Tab. 7.1 compares its expected performance between the ultimate operation at PETRA III and the predicted operation at PETRA IV diffraction-limited source [134]. The parameter values have been extrapolated from the most recent experiments reported in this thesis. At PETRA III, simultaneous structural and elemental mapping, in the moderately hard X-ray regime and with a 0.1-µm nano-focussed beam, could allow for acquisition of a tomogram of a $10\times10\,\mu m^2$ object within 5 h. However, from the most recent experiments it is known that reaching trace-metal sensitivity in the concurrent XRF mapping would require around 50-fold increase of the incident photon flux. While a factor of 5 could be gained with a dedicated multi-element XRF detector, collecting the fluorescent photons from the maximal solid angle, the method will still be limited by the available coherent flux at PETRA III. The planned upgrade to an ultralow-emittance synchrotron light source, PETRA IV, is anticipated to deliver diffraction-limited X-ray beams up to 10 keV, resulting in 100-fold increase in the available coherent flux. As shown in the second column in Tab. 7.1, these two additional orders of magnitude of the incident coherent photons could: (1) finally enable mapping of elements in trace concentrations, while still maintaining the total dose within the acceptable limits, and (2) allow for 10 times faster scanning, thanks to the outstanding characteristics of the voice-coil motors in the sample scanner. An ultimately coherent flux will therefore favour hybrid measurement schemes, such as concurrent ptychography and XRF, facilitating high-throughput volumetric characterisation of a statistically-relevant population of samples.

[7.1] includes a total measurement overhead of 10%

[7.2] based on the previous study by Diaz, *et al.* [62], where a dose of 3.6×10^5 Gy distributed over 288 ptychographic projections allowed to obtain a tomogram of frozen-hydrated cells at 180 nm spatial resolution.

Tab. 7.2: Expected parameters of the 3D scanning X-ray microscope at beamline P11 in the ultrafast ptychographic tomography operation mode.

Parameter	**Ultimate PETRA III**	**PETRA IV**
Energy	Slightly above Fe K absorption edge (7.112 keV)	
Probe size	4.6 µm	
Fly-scan speed	80 µm s^{-1}	400 µm s^{-1} (5x)
Acquisition rate	2 kHz	10 kHz
Scanned area rate[7.3]	66 µm^2 s^{-1}	330 µm^2 s^{-1}
Expected dose/projection (biological cell)	0.21×10^5 Gy	0.42×10^6 Gy (20x)
Expected spatial resolution (cryo-cooled biological cell)[7.4]	88 nm	42 nm
720 projections, 50×30 µm^2	4.5 h	54 min

Similarly, Tab. 7.2 shows the gain in experimental performance between the ultrafast ptychographic tomography experiments conducted ultimately at PETRA III and the anticipated operation at PETRA IV. By comparing the doses used in other ptychographic tomography experiments in biological applications conducted worldwide, the ultimate measurements at PETRA III could still be realised with twice higher fly-scan speeds, resulting in further reduction of the total acquisition time. With the PETRA IV, the 100-fold increase in the coherent flux could be split between an additional dose, yielding potentially higher-resolution tomograms, and another order of magnitude decrease in measurement times. It should be noted that the continuous acquisition rates greater than 2 kHz are beyond the capabilities of currently available pixelated detectors, used for capturing coherent diffraction patterns. The proposed values were chosen to ensure a motion blur of up to 40 nm. In case the detector technology does not keep up, a beam chopper could be used to form X-ray pulses of desired duration, while avoiding unnecessary sample irradiation.

Following the concept of pulsed X-ray beam, novel compact X-ray sources – producing fully coherent and attosecond-long X-ray pulses – offer ideal experimental conditions for snapshot ptychographic tomography with simultaneous X-ray fluorescence mapping. One of such compact sources, based on inverse Compton scattering, is developed within the AXSIS project at the Center for Free Electron Laser Science at DESY in Hamburg, Germany [135]. It is designed to generate up to 10^8 spatially coherent photons per pulse at 1 kHz repetition rate, providing enough photon flux for XRF mapping of first-row transition metals, alongside with electron-density distribution obtained by ptychography. Moreover, the ultrashort pulses will enable acquisition of snapshot diffraction patterns with essentially no motion blur. At such a pulsed source, quality of the on-the-fly ptychography should reach the one known from step-scan experiments, at all benefit of the continuous-motion scanning. While reducing the measurement overhead, the fly-scanning will no longer reduce the contrast of diffraction data, removing the need of more sophisticated and computationally exhaustive ptychographic reconstruction algorithms.

In the context of such significant advances in instrumentation and X-ray sources, a question for far-reaching goals for X-ray ptychography in biological applications arises

[7.3] includes a total measurement overhead of 10%

[7.4] based on the previous study by Diaz, *et al.* [62], where a dose of 3.6×10^5 Gy distributed over 288 ptychographic projections allowed to obtain a tomogram of frozen-hydrated cells at 180 nm spatial resolution.

and whether pursuing them may make the technique face any conceptual limits.

The first challenge for X-ray ptychography would be to provide capabilities for imaging of frozen-hydrated specimens down to isotropic spatial resolutions of 10 nm, which is considered the limit imposed by radiation damage [48]. While 2D ptychography has already delivered a detailed view of an entire, hydrated eukaryotic cell at a sub-20-nm resolution [113], reaching resolving powers beyond 50 nm in ptychographic tomography for label-free organic matter is still considered a real challenge [100], mostly still due to instrumentation limitations and insufficiently coherent X-ray flux. Therefore, with highly brilliant X-ray beams anticipated at diffraction-limited synchrotron light sources, such as PETRA IV, the isotropic resolutions in ptychographic tomography could further be improved, given the positioning stability below 10 nm and ultra-low background in measured diffraction patterns. In this way, the method would be capable of resolving membranes of unsectioned and unstained hydrated cells, being of significant importance in cellular biology.

The second challenge for ptychographic X-ray tomography would be imaging of extremely large tissue volumes, allowing for high-resolution investigations of entire intact organs or small animal specimens. While very recently X-ray ptychography has been applied to 2D imaging of whole freeze-dried nematodes [114], volumetric studies of such organisms have so far been a domain of full-field imaging methods [136] at rather moderate isotropic resolutions (hundreds of nanometers). With a growing throughput, scan range, and precision of the scanning stages, ptychographic tomography could succeed in imaging of extremely thick specimens by incorporating recently developed multi-slice techniques [137, 138], allowing to surpass the depth-of-focus limitation. Conceptually, multi-keV phase-contrast 3D X-ray microscopy should be capable of imaging of 200-µm-thick frozen-hydrated specimens down to 10 nm spatial resolutions [139]. Yet, investigations of even thicker samples may come at rather significant cost of the resolving power, e.g. due to a challenge of obtaining amorphous ice over such organ-scale thicknesses.

At last, the author would like to emphasise importance of the synergy between the interdisciplinary natural sciences and cutting-edge technological development. While the former defines the goal to understanding the mysterious and fascinating frontiers of nature, it also inspires the latter to provide necessary advances in instrumentation to make the dream experiments happen. Ptychographic imaging, rapidly developing over the last decade, in all its variants has a strong potential of serving the biomedical research, complementing cryo-electron microscopy. With the upcoming, ultimately brilliant synchrotron radiation sources, accompanied with joint scientific, technological, and computational efforts, the multimodal scanning X-ray microscopy will enter a new era of becoming a routine method of choice in biomedical applications.

Appendix A

Orthogonalisation of probe modes

Let us consider k non-orthogonal probe modes $\{\pi_1, \pi_2, \ldots, \pi_k\}$, being a result of a multimodal ptychographic reconstruction. Each probe mode is a two-dimensional complex function, $\pi_k(x, y)$, defined in a discretised domain $0 \leq x, y \leq N-1$, where N is a number of pixels in each of the dimensions. Let us further define an inner product of two such probe modes, as follows:

$$\langle \pi_1 | \pi_2 \rangle = \sum_n \sum_m \pi_1(n, m) \cdot \pi_2^*(n, m) \tag{A.1}$$

where $0 \leq n, m \leq N-1$ and * denotes complex conjugation. The goal is to find a set of orthogonal probe modes $\{P_1, P_2, \ldots, P_k\}$, being the actual solution, and their orthonormal base $\{e_1, e_2, \ldots, e_k\}$, which allows to calculate intensity fractions of a respective orthogonal mode in the original modes. In this thesis, the Gram-Schmidt orthogonalisation method was implemented, according to the following:

$$\begin{aligned} P_1 &= \pi_1 \\ P_2 &= \pi_2 - \frac{\langle \pi_2 | P_1 \rangle}{\langle P_1 | P_1 \rangle} P_1 \\ &\vdots \\ P_k &= \pi_k - \sum_{j=1}^{k-1} \frac{\langle \pi_k | P_j \rangle}{\langle P_j | P_j \rangle} P_j \end{aligned} \tag{A.2}$$

Further, an orthonormal base can be constructed by performing normalisation of all orthogonal modes, as follows:

$$e_i = \frac{P_i}{\|P_i\|} \tag{A.3}$$

where $\|P_i\| = \sqrt{\langle P_i | P_i \rangle}$. The non-orthogonal probe modes $|\pi_i\rangle$, $i = 1, \ldots, k$, can be expressed as linear combinations of the orthonormal base vectors $|e_i\rangle$ and coefficients α_{ij}, as given by:

$$|\pi_i\rangle = \sum_{j=1}^{i} \alpha_{ij} |e_j\rangle \tag{A.4}$$

The intensity fraction η_i of the ith probe mode is a sum in quadrature of the intensity fractions of the ith mode in all original probe modes, normalised by the total probe

intensity, namely:

$$\eta_i = \frac{\sum_{j=i}^{k} \alpha_{ji}^2}{\sum_{l=1}^{k}\sum_{j=1}^{l} \alpha_{lj}^2} = \frac{\sum_{j=i}^{k} \langle e_i|\pi_j\rangle^2}{\sum_{l=1}^{k}\sum_{j=1}^{l} \langle e_j|\pi_l\rangle^2} \tag{A.5}$$

where $\alpha_{ij} = \langle e_j|\pi_i\rangle$. In this thesis, the above orthogonalisation method was implemented as a proprietary C++ program, for automatic processing of raw results from multimodal ptychographic reconstructions.

As an example, let us consider 3 raw probe modes $\{\pi_1, \pi_2, \pi_3\}$. Using Eqs. (A.2) and (A.3), their orthonormal base can be found, $\{e_1, e_2, e_3\}$. The raw probe modes can therefore be represented in the form of the following linear combinations:

$$\begin{aligned} |\pi_1\rangle &= \alpha_{11}|e_1\rangle \\ |\pi_2\rangle &= \alpha_{21}|e_1\rangle + \alpha_{22}|e_2\rangle \\ |\pi_3\rangle &= \alpha_{31}|e_1\rangle + \alpha_{32}|e_2\rangle + \alpha_{33}|e_3\rangle \end{aligned} \tag{A.6}$$

Subsequently, by applying Eq. (A.5), the formulae for intensity fractions of all three probe modes can be derived, as follows:

$$\begin{aligned} \eta_1 &= \frac{\alpha_{11}^2 + \alpha_{21}^2 + \alpha_{31}^2}{\alpha_{11}^2 + \alpha_{21}^2 + \alpha_{22}^2 + \alpha_{31}^2 + \alpha_{32}^2 + \alpha_{33}^2} \\ \eta_2 &= \frac{\alpha_{22}^2 + \alpha_{32}^2}{\alpha_{11}^2 + \alpha_{21}^2 + \alpha_{22}^2 + \alpha_{31}^2 + \alpha_{32}^2 + \alpha_{33}^2} \\ \eta_3 &= \frac{\alpha_{33}^2}{\alpha_{11}^2 + \alpha_{21}^2 + \alpha_{22}^2 + \alpha_{31}^2 + \alpha_{32}^2 + \alpha_{33}^2} \end{aligned} \tag{A.7}$$

Appendix B

Sample preparation

B.1 Macrophages

We used murine-bone-marrow-derived macrophages as host cells. Firstly, the macrophages were deposited on a Si_3N_4 membrane coated with poly-L-lysine to facilitate cell adhesion. Subsequently, the monolayers of macrophages were treated with Fe_2O_3 nanocontainers in DMEM containing 10% FCS for 2 h at 37 °C/ 7% CO_2 and fixed with 4% paraformaldehyde. Cells were visualised using a visible-light bright field imaging to identify the cells of interest for subsequent X-ray measurements. Afterwards, the cells were further fixed with 2.5% solution of glutaraldehyde in phosphate-buffered saline buffer. In order to stabilise the cells and enhance the imaging contrast, the inactivated macrophages were stained with OsO_4 and, finally, dried in air according to the following protocol:

1) 10 min phosphate-buffered saline (PBS)
2) 10 min 1% OsO_4 in PBS
3) dipping in water to remove bulk OsO_4
4) 10 min washing in water
5) ethanol (EtOH) gradient: 50/70/90/100/100% EtOH in water, 10 min each
6) freon 113 gradient: 50/80/100/100% freon 113 in EtOH, 10 min each
7) fresh freon 113, oven 40.5 °C, over night

B.2 Bones

Bone samples were obtained from the tibia plateau of a 19-year-old male individual (surgical waste material), based on written consent of the patient. The study was approved by the local ethics committee (Hamburg Chamber of Physicians, WF-020/17). The bone material was fixed with neutrally buffered formalin within one hour from material collection to permit best results for studying bone matrix quality and cellular biology, in combination. Once fixed, specimens were cut to a size of 1 cm^3 using a diamond-coated band saw (Exakt, Norderstedt, DE) to allow for embedding in polymethylmetacrylate (PMMA) after dehydration in ascending grades of alcohol. The PMMA blocks including the specimen were cut using a microtome (Leica, Wetzlar, DE) to produce 4-µm-thin consecutive sections. The thin bone sections were deposited on Si_3N_4 membranes and air-dried.

Appendix C

Parameters of experiments

Tab. C.1: Parameters of representative scans in the commissioning phase of the simultaneous ptychographic and X-ray fluorescence imaging in 2D at beamline P11.

Parameter	**Silicified macrophage cell** (Fig. 4.1.2A)	**NC-labelled tissue** (Fig. 4.1.2C)	**Shigella-infected macrophage** (Fig. 4.1.3B)
Front-end slits	horizontally, vertically: fully open		
Energy	7.35 keV	7.275 keV	7.35 keV
Optics hutch - KB mirrors			
Horiz. deflecting 1	Bender A: 375 µm, Bender B: 400 µm		
Horiz. deflecting 2	Bender A: 375 µm, Bender B: 400 µm		
Vert. deflecting	Bender A: 0 µm, Bender B: 0 µm		
Secondary source chamber			
Attenuating filter transmission	100%		
Beam defining aperture (off-axis)	circular pinhole diameter: 30 µm		$30\times80\,\mu m^2$ (h×v)
Fresnel zone plate			
diameter	150 µm		200 µm
outermost zone width Δr	30 nm		
focal length ($1st$ order)	26.7 mm	26.4 mm	35.6 mm
Order sorting aperture	10 µm		
Sample-to-detector distance	2.64 m		4.51 m
Detector	Eiger 1M		Pilatus 1M
format	1030 × 1065 pixels		981 × 1043 pixels
pixel size	$75 \times 75\,\mu m^2$		$172 \times 172\,\mu m^2$
Probe size (h×v)	180 nm×180 nm	200 nm×200 nm	200 nm×300 nm
Scan format (scan points)	601 × 301	301 × 301	351 × 351
Fly-scan speed	$0.88\,\mu m\,s^{-1}$	$0.5\,\mu m\,s^{-1}$	$0.8\,\mu m\,s^{-1}$
Scan step size	44 nm	100 nm	80 nm
Exposure time	50 ms	200 ms	100 ms
Acquisition rate	20 Hz	5 Hz	10 Hz
Incident photon flux [$ph\,s^{-1}$]	1.7×10^8	2.3×10^8	5.5×10^8
Overhead	15%		14%

Tab. C.2: Parameters of representative scans in the application phase of the simultaneous ptychographic and X-ray fluorescence imaging in 2D at beamline P11.

Parameter	**Macrophage cell with NC** (Fig. 5.1.1A,C)	**Macrophage cell control group** (Fig. 5.1.1B)	**Cortical bone section** (Fig. 5.2.1A,B)
Front-end slits	horizontally, vertically: fully open		
Energy	7.35 keV		7.15 keV
Optics hutch - KB mirrors			
Horiz. deflecting 1	Bender A/B: 375 µm/400 µm		
Horiz. deflecting 2	Bender A/B: 400 µm/400 µm		
Vert. deflecting	Bender A/B: 0 µm/0 µm		
Secondary source chamber			
Attenuating filter transmission	100%		60%
Beam defining slits (off-axis) (h×v)	$40 \times 60\ \mu m^2$		
Fresnel zone plate			
diameter	200 µm		
outermost zone width Δr	30 nm		
focal length (1*st* order)	35.6 mm		34.6 mm
Order sorting aperture	10 µm		
Sample-to-detector distance	4.2 m		
Detector	Pilatus 1M		Pilatus 300k
format	981 × 1043 pixels		487 × 619 pixels
pixel size	$172 \times 172\ \mu m^2$		$172 \times 172\ \mu m^2$
Probe size (h×v)	400 nm×600 nm		200 nm×400 nm
Scan format (scan points)	281 × 193	217 × 273	326 × 326
Fly-scan speed	$0.83\ \mu m\ s^{-1}$		$2\ \mu m\ s^{-1}$
Scan step size	125 nm		200 nm
Exposure time	150 ms		100 ms
Acquisition rate	6.67 Hz		10 Hz
Incident photon flux [photon s^{-1}]	5.4×10^8	2.4×10^8	3.7×10^8
Overhead	8.9%	10.7%	14%
Dose			
net	6.28 MGy	2.77 MGy	7.59 MGy
incl. overhead	6.84 MGy	3.06 MGy	8.65 MGy

Tab. C.3: Parameters of representative scans in the commissioning phase of the ptychographic X-ray tomography at beamline P11.

Parameter	**TB-infected macrophage cell** (Fig. 4.2.5)	**Nano-porous glass** (Fig. 6.1)	**Chiton's radular tooth** (Fig. 6.1.3)
Front-end slits	horizontal opening: 30 µm, vertically: fully open		
Energy	7.375 keV	7.24 keV	7.44 keV
Optics hutch - KB mirrors			
Horiz. deflecting 1	Bender A/B: 0 µm/0 µm		
Horiz. deflecting 2	Bender A/B: −400 µm/−400 µm		
Vert. deflecting	Bender A/B: 400 µm/400 µm		
Secondary source chamber			
Attenuating filter transmission	100%		
Beam defining slits (h×v)	200×200 µm^2		
Central stop	50 µm		
Fresnel zone plate			
diameter	150 µm		
outermost zone width Δr	60 nm	90 nm	
focal length (1*st* order)	53.5 mm	78.9 mm	81.0 mm
Order sorting aperture	20 µm		
Sample-to-detector distance	4.45 m	4.2 m	
Detector	Pilatus 1M	Eiger 500k	
format	981 × 1043 pixels	1030 × 514 pixels	
pixel size	172 × 172 µm^2	75 × 75 µm^2	
Probe size (h×v)	1.2 µm×1.2 µm	4.3 µm×4.6 µm	0.5 µm×0.8 µm
Scan format (scan points)	83 × 40	1125 × 15	300 × 125
Fly-scan speed	3.0 µm s^{-1}	40 µm s^{-1}	40 µm s^{-1}
Scan step size (h×v)	300 nm×300 nm	40 nm×1 µm	100 nm×200 nm
Exposure time (ptychography)	40 ms	0.9 ms	2 ms
Acquisition rate (exposure time for XRF)	10 Hz	1 kHz	400 Hz
Incident photon flux [photon s^{-1}]	9.8×10^8	1.53×10^9	1.8×10^9
Overhead	15%	88%	96%
Number of projections	31	720	180
Angular range	±30°	±90°	±90°
Angular step	0.67°	0.25°	1°
Dose/tomogram			
ptychography only	10.83 MGy	137 MGy	1.13 GGy
incl. acquisition rate (XRF)	37.9 MGy	152 MGy	1.41 GGy

Appendix D

Internalisation of nanocontainers in macrophages

In the absence of complete volumetric information, an additional verification of nanocontainers uptake is required. In a pilot study previous to the presented work, we used the scanning electron microscopy (SEM) to visualise the surface of the cell. We observed that the larger nanocontainer agglomerates were usually not internalised inside the cells and hence were visible in an SEM image. Fig. D.1A shows the ptychographic phase image of a representative macrophage treated with iron-oxide nanocontainers, while in Fig. D.1B the ptychographic image was overlaid with the Fe distribution map. The Fe map allows to identify 5 nanocontainer agglomerates. A subsequently recorded SEM image of the same cell in Fig. D.1C reveals that the largest agglomerate (dashed line) is located on the top of the cell. The remaining smaller agglomerates (solid line) are not visible and are hence supposed to be within the cytosol.

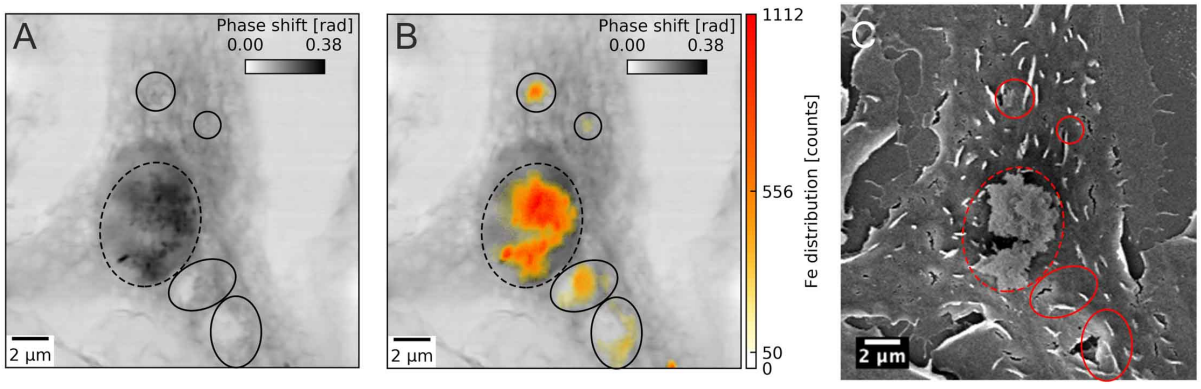

Fig. D.1: Verification of nanocontainer agglomerates internalisation by scanning electron microscopy (SEM) based on a previous work. (A) shows the ptychographic phase image of an exemplary macrophage treated with iron-oxide nanocontainers. (B) shows the iron distribution map superimposed on the ptychographic image. 5 nanocontainer agglomerates can be identified. (C) shows an SEM image of the surface of the same cell. The largest agglomerate can be observed on the top of the cell (dashed line) whereas the remaining smaller agglomerates were internalised inside the cell.

Appendix E

Scan metadata file

Tab. E.1: Structure of a unified HDF5 metadata file generated for every scan ($N_x \times N_y$ scan points).

Dataset address	**Description**	**Format**	**Type**
`/data/diode_flux`	Silicon transmission photodiode signal	$N_x \times N_y$	float
`/data/fluorescenceData`	X-ray fluorescence spectra	$N_x \times N_y \times 2048$	float
`/data/petraCurrent`	PETRA III beam current [mA]	N_y	float
`/data/x_enc`	Horizontal motor encoder positions [µm]	$N_x \times N_y$	float
`/data/y_enc`	Vertical motor encoder positions [µm]	$N_x \times N_y$	float
`/data/x_imf`	Horizontal interferometer sensor readout [µm]	$N_x \times N_y$	float
`/data/y_imf`	Vertical interferometer sensor readout [µm]	$N_x \times N_y$	float

Tab. E.2: List of attributes of the `/data/fluorescenceData` dataset with the relevant beamline and scan parameters.

Parameter token	**Parameter description**	**Unit**	**Type**
`mono_E`	Monochromator energy	keV	float
`HM1_bendA`	Horizontally deflecting mirror 1: bender A value	µm	float
`HM1_bendB`	Horizontally deflecting mirror 1: bender B value	µm	float
`HM2_bendA`	Horizontally deflecting mirror 2: bender A value	µm	float
`HM2_bendB`	Horizontally deflecting mirror 2: bender B value	µm	float
`VM_bendA`	Vertically deflecting mirror: bender A value	µm	float
`VM_bendB`	Vertically deflecting mirror: bender B value	µm	float
`filter_trans`	Filter transmission	$[0, 1]$	float
`if_slits_gapY`	Horizontal opening of the slits in the secondary source chamber	µm	`float`
`if_slits_gapZ`	Vertical opening of the slits in the secondary source chamber	µm	`float`
`if_slits_posY`	Horizontal position of the slits opening in the secondary source chamber	µm	`float`
`if_slits_posZ`	Vertical position of the slits opening in the secondary source chamber	µm	`float`
`ScanMode`	`step_scan` or `continuous_line`	NA	string
`centerX`	Horizontal position of the scan centre	µm	float
`centerY`	Vertical position of the scan centre	µm	float
`rangeX`	Horizontal range of the scan	µm	float
`rangeY`	Vertical range of the scan	µm	float
`startX`	Horizontal start position of the scan	µm	float
`startY`	Vertical start position of the scan	µm	float
`stepsizeX`	Horizontal step size of the scan	µm	float
`stepsizeY`	Vertical step size of the scan	µm	float
`stopX`	Horizontal stop position of the scan	µm	float
`stopY`	Vertical stop position of the scan	µm	float
`Nx`	Horizontal number of scan points	NA	int
`Ny`	Vertical number of scan points	NA	int
`scanVelocity`	Scan speed of the fast-axis motor (only in the `continuous_line` mode)	$\mu\mathrm{m\,s^{-1}}$	float
`rotationStage`	Tilt angle of the rotation stage	°	float
`exposureTime`	Exposure time	s	float
`exposureWindow`	Exposure window (frame rate) `exposureWindow` $\geq$ `exposureTime`	s	float
`sampleToDetectorDistance`	Propagation distance between the sample and the far-field detector	meter	float

Appendix F

PtyksP11

PtyksP11 is a standalone C++ application with a graphical user interface based on the cross-platform Qt GUI toolkit [95] and developed by the author of this thesis. It uses the `QCustomPlot` C++ Qt widget for plotting and data visualisation [140]. PtyksP11 has been developed and optimised on a Debian Linux distribution, which is a standard computing environment at beamline P11. Its main purpose is to provide a set of functionalities allowing for a real-time preliminary data processing and visualisation during the experiment. It has been particularly useful in setting up a series of 2D batch scans of different regions of interest, based on a low-resolution, large-field-of-view image. PtyksP11 utilises threads (`QThread`), which allow to send the calculations to the background, while retaining full control over the threads from the constantly active GUI (the GUI does not freeze during the calculations). Below the most important functionalities of the application are described.

Real-time STXM/DPC

Ptychographic reconstruction is usually a computationally heavy process and, in its default implementation, requires the entire scan to be already measured. Diffraction patterns are typically saved either in separate tiff or cbf files (Pilatus detectors) or accumulated from every scan line and flushed into a corresponding HDF5 file (Eiger detectors). To provide a preview of measurements in real time, the conventional method of scanning transmission X-ray microscopy (STXM) can be used. Fig. F.1A shows the STXM tab of the PtyksP11 application with an exemplary large-field-of-view scan of macrophage cells treated with iron-oxide nanocontainers. The left-side panel `Setup parameters` includes all necessary information about the scan. Browsing in the file structure allows to select the directory path and the scan name. Following the unified naming scheme of the scanning scripts, PtyksP11 searches for the respective metadata file, called `scan_name.h5`. Clicking the button `Load scan parameters` automatically imports first four parameters from the metadata file attributes and fills out the respective fields below. The meaning of the setup parameters is explained in Tab. F.1. The `Start` button begins the analysis. Knowing the naming scheme, the application waits for the anticipated diffraction patterns if the calculations are faster than the measurement. PtyksP11 processes the dataset providing four images in complementary contrasts: horizontal differential phase contrast (DPCx), vertical differential phase contrast (DPCy) [75], transmission (total summed intensity), and dark field (intensity summed outside of the dark field mask). The image panels are interactive, allowing to zoom in and out the field of view and the colourbar axes (mouse scroll) as well as drag the images (left mouse button). Further plotting options can be found in the top right panel (`Plotting options`), permitting to change the aspect ratio

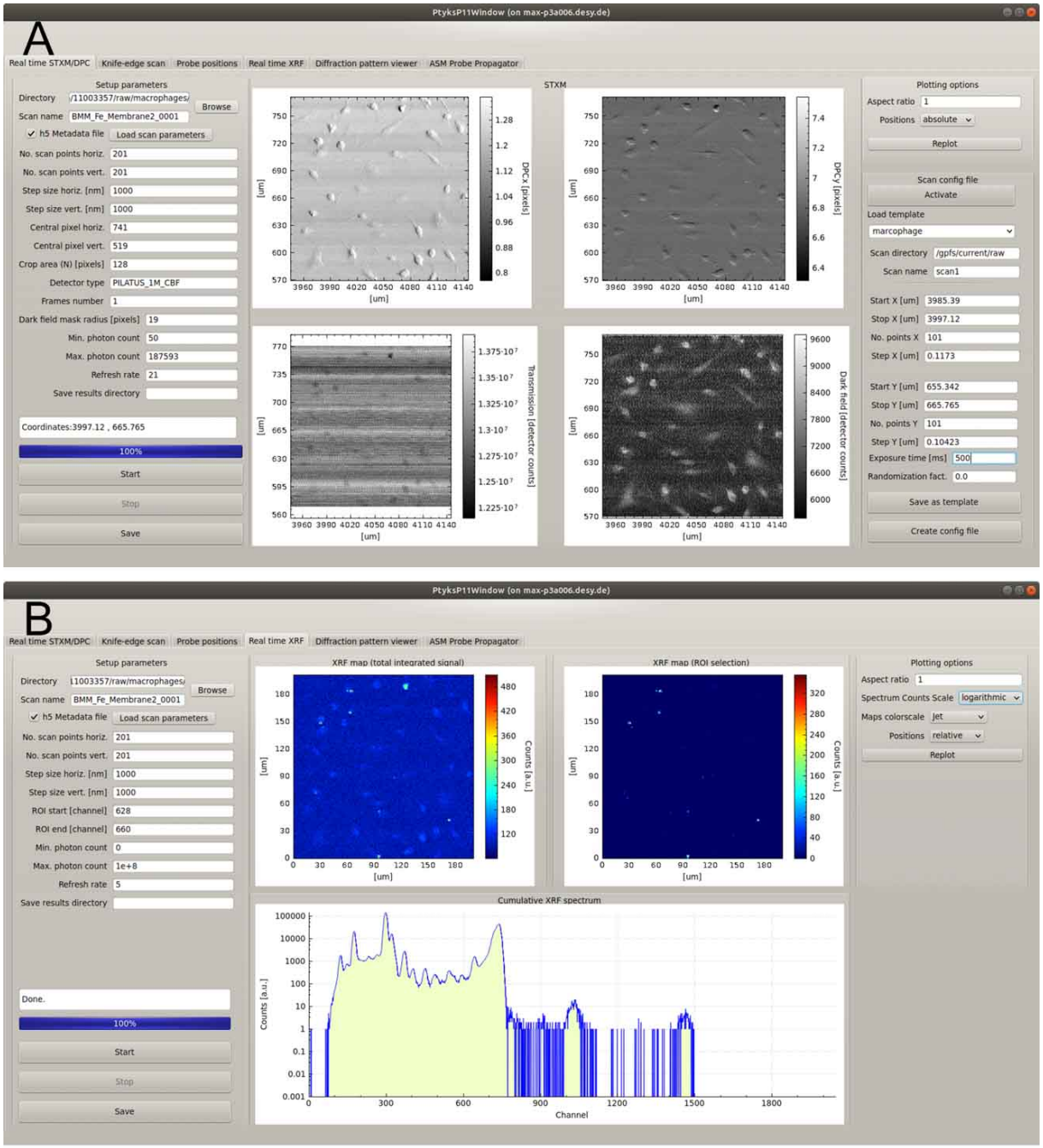

Fig. F.1: PtyksP11 C++ application with a graphical user interface based on the Qt GUI toolkit. (A) shows the STXM tab of the program allowing to process in real time the scanning X-ray microscopy data in a conventional way, providing four contrast mechanisms: horizontal differential phase contrast (DPCx), vertical differential phase contrast (DPCy), transmission (total summed intensity), and dark field (intensity summed outside the dark field mask). (B) shows the X-ray fluorescence panel for on-line visualisation of the XRF maps.

Tab. F.1: Setup parameters of the Real-time STXM/DPC tab of the PtyksP11 application.

Parameter	Description
`No. scan point horiz.`	Number of scan points in the horizontal direction
`No. scan point vert.`	Number of scan points in the vertical direction
`Step size horiz. [nm]`	Horizontal step size
`Step size vert. [nm]`	Vertical step size
`Central pixel horiz.`	Horizontal coordinate of the diffraction pattern centre
`Central pixel vert.`	Vertical coordinate of the diffraction pattern centre
`Crop area (N) [pixels]`	Square area of N×N pixels around the diffraction pattern centre selected for calculations
`Detector type`	Detector name and diffraction pattern file format (predefined implementations for: (cbf, tiff) Pilatus 300k, Pilatus 1M, Pilatus 2M, (h5, nxs) Eiger 500k, Eiger 1M, Lambda 750k, Jungfrau 500k)
`Frames number`	Number of diffraction patterns per file
`Dark field mask radius [pixels]`	Radius of a circular mask
`Min. photon count`	Maximum allowed photon count per pixel
`Max. photon count`	Minimum allowed photon count per pixel
`Refresh rate`	Number of scan points, whose multiple determines how often the image panels are updated
`Save results directory`	Directory path where the calculation results are saved as an HDF5 file

and toggle between the relative or the absolute scan positions. The absolute scan range is also retrieved from the scan metadata file. Moreover, the resulting 4 images can also be saved in an HDF5 file (`Save results directory`), by clicking the `Save` button in the lower left.

As mentioned in the main text (section 4.1.2), PtyksP11 facilitates a setup of several consecutive high-resolution scans, based on a large overview. It is realised with the bottom right panel in the Real-time STXM/DPC tab, called `Scan config file`. The panel is activated with the `Activate` button. This enables a custom feature of selecting the sub-regions of interest within the four images of the overview scan. In order to define a new scan of a rectangular area over a cell, two mouse clicks at the requested diagonal corners are necessary. The application retrieves the absolute positions of the points of the mouse clicks and fills out automatically the parameters `StartX/Y` and `StopX/Y` of the new scan. The start point is defined by a left mouse-click and the end point with the right mouse-click. Given the desired number of scan points, the program calculates the respective step sizes. Once finished, the form is used by the application to generate a configuration file (`Create config file`), which can immediately be used as an input file to the respective command-line scanning script.

Real-time XRF

The second important functionality of the PtyksP11 is dedicated to another, complementary X-ray microscopy modality utilised in the reported experiments, namely X-ray fluorescence. Fig. F.1B shows the respective XRF tab of the PtyksP11 application. The

`Setup parameters` panel resembles the corresponding panel in the STXM tab, with the same feature of importing the relevant scan parameters from the scan metadata file. By clicking the `Start` button, PtyksP11 reads in the recorded XRF spectra and plots: a cumulative XRF map in the upper left (the sum of all detector channel values per pixel), an XRF map of a given element in the upper right (based on the region-of-interest selection defined by the user in the setup panel), and a cumulative XRF spectrum. Similarly to the STXM tab, additional plotting options can be found on the right side.

PtyksP11 features several further options with some still under development, as indicated by the remaining application tabs in Fig. F.1.

Historically, the `Knife-edge scan` tab allowed for a robust processing of line scans recorded over a sharp and highly absorbing edge. The derivative of the resulting step profile for an independent assessment of the beam size.

The `Probe positions` tab provides diagnostics concerning the positions of the sample with respect to the incident beam. It plots a map of encoder and interferometer positions obtained from the scan metadata file.

Further, the `Diffraction pattern viewer` tab is responsible for visualisation of diffraction patterns from detectors, for which no viewing application is available, e.g. Jungfrau or Lambda detectors.

Finally, the last tab, `AMS Probe Propagator` takes a 2D complex probe function obtained by ptychographic reconstruction and propagates it within a defined distance along the optical axis. For this, it uses an angular-spectrum method (AMS) of X-ray field propagation, discussed in section 1.1.3.2. It allows to determine the distance from the focal spot or, e.g. by how much the sample must be moved along the optical axis to obtain a certain beam size. This feature is particularly useful in ptychographic tomography, and has so far been realised with external scripts. Its implementation in PtyksP11 is currently under development.

Appendix G

Radiation damage evaluation

In essentially any type of experiments with X-rays it is important to evaluate the degree to which interaction of this ionising radiation with a specimen may affect or even alter its structure. In this thesis, such analysis was done by calculating the surface dose D understood as energy deposited per unit mass [48], according to the following formula:

$$D = \frac{\mu}{\rho}\Phi_0 E N_{\mathrm{proj}} \tag{G.1}$$

where μ and ρ are the linear attenuation coefficient and the mass density of a specimen, respectively, Φ_0 is the incident photon fluence, i.e. the number of photons per unit area, E is the photon energy of the incident beam, and N_{proj} is the number of tomographic projections (if applicable).

In the ptychographic measurements reported in this thesis, the incident photon fluence was calculated from the transmitted intensity measured in the absence of specimen by a far-field single photon sensitive detector. As the detector is usually situated several meters downstream of the specimen, it is necessary to correct for any attenuation of X-rays between the sample position and the detector. This includes determining the total transmission T_{tot} of all air paths, Kapton windows, helium-flushed flight tube, and detector efficiency, as listed in Tab. G.1 for the experimental setup utilised in this thesis. Using the measured intensity in diffraction data, I_{diffr}, the incident photon intensity I_0 is given by:

$$I_0 = \frac{I_{\mathrm{diffr}}}{T_{\mathrm{tot}}} \tag{G.2}$$

To obtain the incident photon fluence, an effect of the overlap between neighbouring illuminated scan areas, inherent to ptychography, must be taken into account. Probably the most accurate approach is to *simulate* the scanning beam, using the probe function obtained by ptychographic reconstruction and the relative sample-probe x, y scan positions. The intensity distribution of the incident beam is then obtained by multiplying the normalised probe intensity distribution by the incident photon intensity I_0. From the scan positions, the scan area can be determined and used to construct an empty scan array (several times larger than the probe area). At every scan position, the incident intensity distribution is added to the respective fraction of the scan array, emulating exactly the multiple overlapping. Finally, the total intensity (number of photons) accumulated in the scan array is then divided by the scan area (e.g. in nm^2), to yield the incident photon fluence Φ_0.

Last but not least, the total dose D_{tot} should also include any additional dose resulting from the motion overhead, if the X-ray shutter has not been closed between exposures or centering, as follows:

$$D_{\mathrm{tot}} = D(1 + \Delta_{\mathrm{overh}}) \tag{G.3}$$

Tab. G.1: Elements of experimental setup contributing to attenuation of X-rays downstream of the specimen up to the surface of the far-field detector.

Order	**Material**	**Thickness**	**Transmission at 7.375 keV**
1.	air gap sample – flight tube	8 cm	0.8892
2.	flight-tube entrance window Kapton, $1.43\,\mathrm{g\,cm^{-3}}$	50 µm	0.9468
3.	helium at 1 bar and 295 K	435 cm	0.9840
4.	flight-tube exit window Kapton, $1.43\,\mathrm{g\,cm^{-3}}$	300 µm	0.7205
5.	air gap flight tube – detector	7 cm	0.9024
Total transmission			**0.5386**

Tab. G.2: Tabulated material parameters of three groups of specimen analysed in this thesis.

Material	**Energy**	$1/\mu$	ρ	**Source**
Macrophage cells, $H_{48.6}C_{32.9}N_{8.9}O_{8.9}S_{0.6}$	7.375 keV	704 µm	$1.35\,\mathrm{g\,cm^{-3}}$	[141]
Cortical bone	7.150 keV	$\mu/\rho = 72.30\,\mathrm{cm^2\,g^{-1}}$		[142]
Silica porous glass	7.240 keV	97.1 µm	$2.2\,\mathrm{g\,cm^{-3}}$	[28]
Magnetite, Fe_3O_4	7.440 keV	8.66 µm	$4.3\,\mathrm{g\,cm^{-3}}$	[28]

where Δ_{overh} denotes the measurement overhead in [%].

In this thesis, respective doses were evaluated for three groups of specimens: (1) macrophage cells, (2) cortical bone sections, and (3) a magnetite-rich piece of a chiton radula tooth. The mass density of the latter was taken from the mass-density volume obtained by ptychographic tomography and is lower than the bulk density of magnetite. Tab. G.2 summarises their material parameters at given photon energies.

Appendix H

Chiton's radular tooth tomographic slices

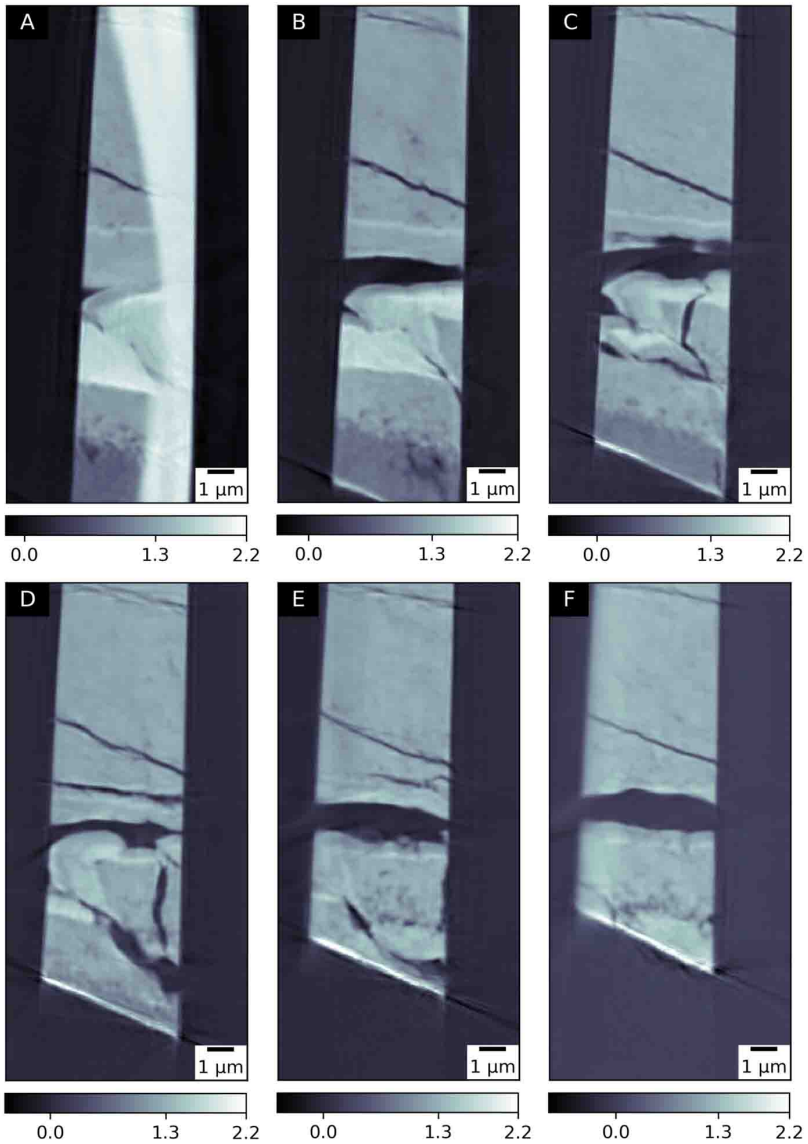

Fig. H.1: Tomographic XY orthoslices of a piece of the *Criptochiton stelleri* radular tooth. (A) begins at $Z_0 = 2.47\,\mu m$, (B-F) are at multiplications of $1.15\,\mu m$ from (A). Colorbars denote electron density in [e $Å^{-3}$].

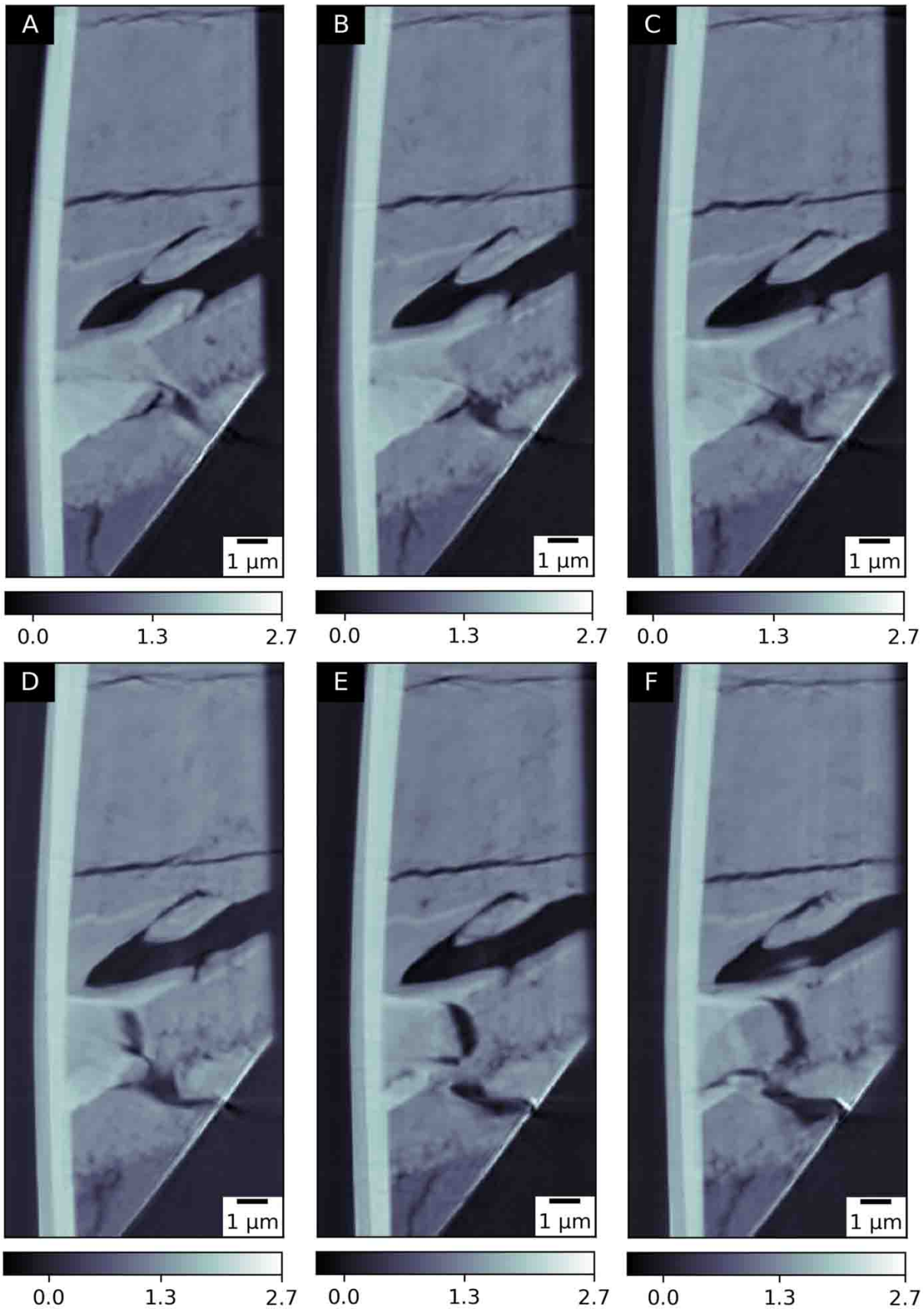

Fig. H.2: Tomographic YZ orthoslices of a piece of the *Criptochiton stelleri* radular tooth. (A) begins at $X_0 = 4.18\,\mu m$, (B-F) are at multiplications of $0.38\,\mu m$ from (A). Colorbars denote electron density in [e $Å^{-3}$].

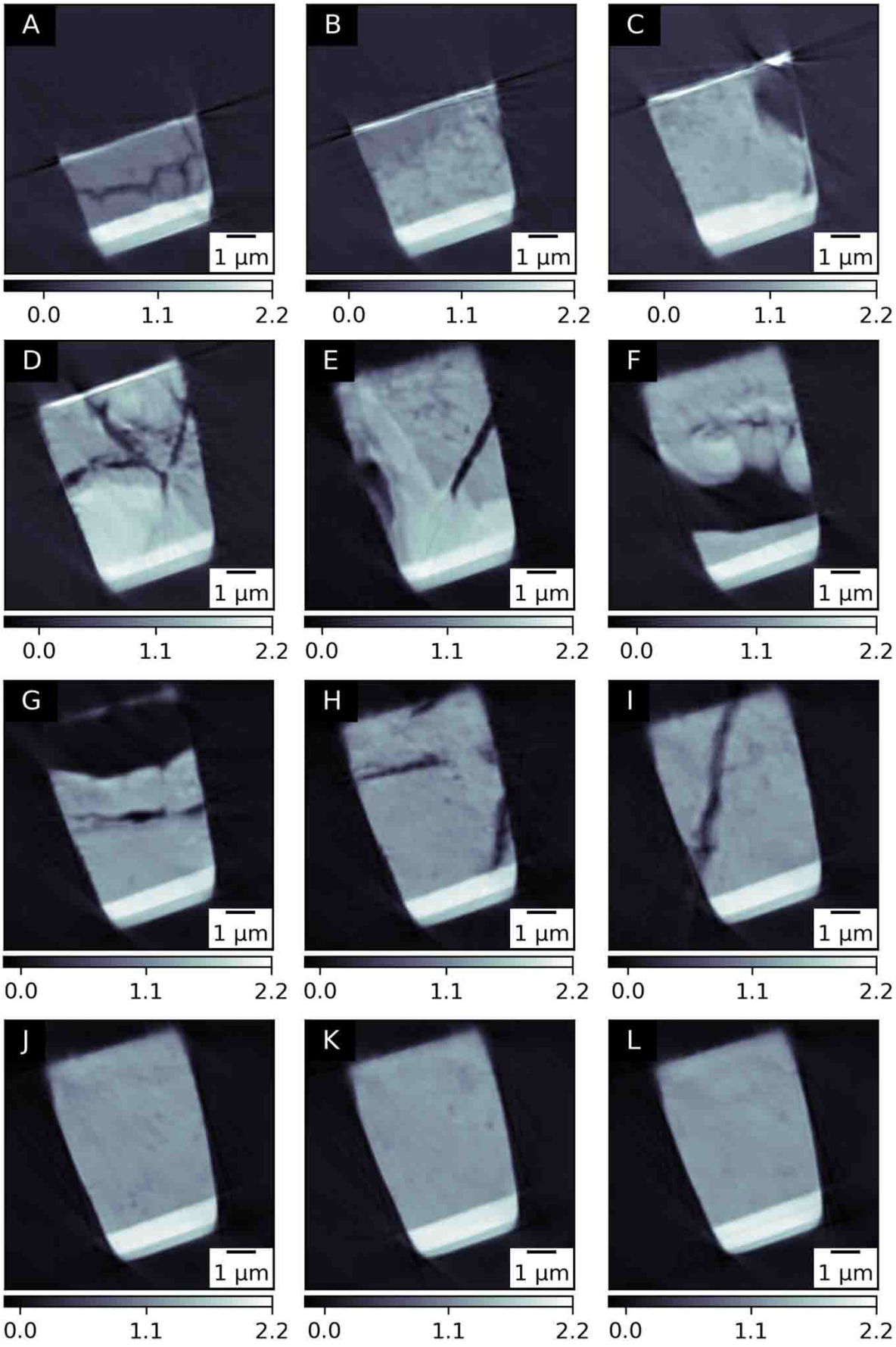

Fig. H.3: Tomographic XZ orthoslices of a piece of the *Criptochiton stelleri* radular tooth. (A) begins at $Y_0 = 1.52\,\mu m$, (B-L) are at multiplications of $1.52\,\mu m$ from (A). Colorbars denote electron density in [e $Å^{-3}$].

Acknowledgements

Over my PhD studies, I have had a chance to interact and work with many outstanding and motivating professionals, to whom I would like to express my sincere gratitude.

First, I would like to thank my PhD thesis supervisor, Dr. Alke Meents, for giving me the opportunity to pursue my PhD project within his group Biomedical Research with X-rays (FS-BMX). I thank Alke for many pioneering concepts and support during experiments at beamline P11 at PETRA III, for inspiring scientific discussions and a great dose of motivation and optimism. I thank my PhD thesis co-supervisor Prof. Dr. Henry Chapman for stimulating discussions and valuable comments to the thesis manuscript.

Further, I would like to express my thanks to all colleagues from the FS-BMX group for creating a pleasant work atmosphere. I thank Julia Lieske and Sebastian Günther for interesting discussions. I thank Vincent Hennicke and Pontus Fischer, who have been involved in the design and realisation of the scanning X-ray microscope. Further, I acknowledge Julian Sulikowski, Filip Guicking, Tim Packendorf, and Julian Bergtholdt for their support during X-ray imaging experiments. In particular, I would like to thank two former colleagues, both vastly involved in the bio-imaging project. I thank Martin Warmer for his professional help with sample preparation, genuine dedication, support at all experiments, and very interesting discussions on biological applications in X-ray microscopy. Further, I thank Istvan Mohacsi, with whom I performed many ptychographic experiments, for sharing with me his knowledge and experience in X-ray imaging and scientific computing. I also acknowledge Istvan as an author of the code for ptychographic reconstruction, which I utilised in my doctoral thesis.

I would like to thank the beamline P11 team for the yearlong cooperation, hosting and supporting our bio-imaging experiments. First, I thank Anja Burkhardt, the beamline scientist in charge of P11. Further, I thank Jan Meyer, Jakob Urbschat and Bernd Reime, who were frequently involved in the preparation of bio-imaging experiments at P11, contributing both to hardware and control software development. I also address my thanks to the beamline scientists: Eva Crossas, the former members: Saravanan Panneerselvam and Olga Lorbeer, as well as the recently joined Sofian Saouane and Johanna Hakanpää.

I acknowledge professional help and support of Andre Rothkirch and Tobias Spitzbart from the FS-EC group during our experiments at PETRA III.

My PhD project involved collaborations with several external groups, both on the method development as well as on the biological applications. Here, I would like to acknowledge them chronologically.

I thank the group of Christian David from Paul Scherrer Institut in Switzerland, for providing X-ray optics and professional expertise essential in the development of the scanning X-ray microscope at beamline P11. In particular, I would like to thank the postdoctoral scientists: Ismo Vartiainen and Felix Marschall for conducting several imaging experiments together with me.

Subsequently, I would like to thank the group of Marek Lankosz from the Faculty of Physics and Applied Computer Science at the AGH University of Science of Technology

in Kraków, Poland. I thank Marek Lankosz and Paweł Wróbel for their valuable contribution to optimising the method of nanoscale X-ray fluorescence in two proof-of-concept experiments.

I thank the group of Ulrich Schaible from the Research Center Borstel for a fruitful cooperation on tuberculosis infection and novel drug delivery based on iron-oxide nanocontainers loaded with antibiotics. I express my gratitude to Ulrich for providing us with cultured cells and for very interesting discussions on the obtained results. I acknowledge his group member, Jacqueline Eich, for sample preparation.

I thank the group of Michael Kolbe from the Center for Structural Systems Biology and Helmholtz Center for Infection Research for providing us with Shigella-infected cells for correlative X-ray imaging. I acknowledge Juana De Diego for sample preparation.

I would like to thank Katharina Jähn, from the group of Björn Busse at the University Medical Center Hamburg-Eppendorf, for an effective cooperation on the study of human bone matrix mineralisation. I thank Katharina for sharing her genuine excitement about science with me, for many interesting discussions and ideas, and providing us with prepared bone matrix sections.

Finally, I would like to thank Saša Bajt for giving me the opportunity to participate in imaging experiments with multilayer Laue lenses developed by her group. I thank Saša for giving us the opportunity to contribute to her project on chiton's radular teeth. I acknowledge Mauro Prasciolu for sample preparation.

Over three years of my doctoral studies, I have had an honour to be a scholarship holder of the Joachim Herz Foundation. I would like to express my most sincere gratitude to the Foundation for this generous financial support. Thanks to the scholarship grant, I could freely pursue my PhD project. I would also like to thank the project managers: Eva Ackermann, Julia Wernecke as well as Sophie-Dorothee Hoppenheit, for professional support and guidance during the programme.

I have pursued my PhD project in the framework of the PIER Helmholtz Graduate School, which is a graduate education programme at DESY in cooperation with Universität Hamburg. Participation in PIER allowed me to benefit from the rich portfolio of courses, workshops, and seminars, both to deepen my knowledge in the area of my PhD project as well as to broaden my horizons towards other research topics. I thank the PIER Team: Stefanie Tepass, Mirko Siemssen, Gabriele Keidel, Jennifer Vix, and their former colleague Maren Arnold-Vargen. I am utterly grateful to them for putting so much hearth into providing the best opportunities to PhD students, for all the help with sometimes-overwhelming German bureaucracy, annual organisation of the graduate weeks and PhD receptions in the exceptional Christmas atmosphere.

Beyond the academia, during my PhD studies I have met a group of fantastic and trustworthy people, whose generous support and dear friendship shall not be forgotten.

I would like to dearly thank Gabriele Keidel who, together with her late husband Roberto, hosted me at their home for the first 6 months of my PhD studies. I am thankful for their exceptional hospitality and creating a familiar atmosphere. I am very grateful for a possibility to practise my German in everyday situations and for their manifold useful tips on how to settle down in Hamburg.

Further, during my doctoral studies I have had finally the chance to return to music, which is my second passion. I would like to thank my dearest friends from the vocal ensemble *Polifonix* and all members of the choir at the Polish Catholic Mission in Hamburg.

Finally, I would like to thank my beloved Family for being a firm and solid point of reference, and having true faith in me. I thank you all for your support for my dream of becoming a scientist and being at my side in both the happy and the difficult moments of my doctoral studies.

Bibliography

[1] R. Hegerl and W. Hoppe, "Dynamische Theorie der Kristallstrukturanalyse durch Elektronenbeugung im inhomogenen Primärstrahlwellenfeld," *Berichte der Bunsengesellschaft für physikalische Chemie*, vol. 74, no. 11, pp. 1148–1154, 1970.

[2] F. Pfeiffer, "X-ray ptychography," *Nature Photonics*, vol. 12, pp. 9–17, Jan. 2018.

[3] P. Thibault, M. Dierolf, O. Bunk, A. Menzel, and F. Pfeiffer, "Probe retrieval in ptychographic coherent diffractive imaging," *Ultramicroscopy*, vol. 109, pp. 338–343, Mar. 2009.

[4] M. Guizar-Sicairos and J. R. Fienup, "Phase retrieval with transverse translation diversity: a nonlinear optimization approach," *Optics Express*, vol. 16, pp. 7264–7278, May 2008.

[5] A. M. Maiden and J. M. Rodenburg, "An improved ptychographical phase retrieval algorithm for diffractive imaging," *Ultramicroscopy*, vol. 109, pp. 1256–1262, Sept. 2009.

[6] O. Bunk, M. Dierolf, S. Kynde, I. Johnson, O. Marti, and F. Pfeiffer, "Influence of the overlap parameter on the convergence of the ptychographical iterative engine," *Ultramicroscopy*, vol. 108, pp. 481–487, Apr. 2008.

[7] A. M. Maiden, G. R. Morrison, B. Kaulich, A. Gianoncelli, and J. M. Rodenburg, "Soft X-ray spectromicroscopy using ptychography with randomly phased illumination," *Nature Communications*, vol. 4, p. 1669, Apr. 2013.

[8] R. Hoppe, J. Reinhardt, G. Hofmann, J. Patommel, J. D. Grunwaldt, C. D. Damsgaard, G. Wellenreuther, G. Falkenberg, and C. G. Schroer, "High-resolution chemical imaging of gold nanoparticles using hard x-ray ptychography," *Applied Physics Letters*, vol. 102, p. 203104, May 2013.

[9] D. A. Shapiro, Y.-S. Yu, T. Tyliszczak, J. Cabana, R. Celestre, W. Chao, K. Kaznatcheev, A. L. D. Kilcoyne, F. Maia, S. Marchesini, Y. S. Meng, T. Warwick, L. L. Yang, and H. A. Padmore, "Chemical composition mapping with nanometre resolution by soft X-ray microscopy," *Nature Photonics*, Sept. 2014.

[10] C. Donnelly, M. Guizar-Sicairos, V. Scagnoli, M. Holler, T. Huthwelker, A. Menzel, I. Vartiainen, E. Müller, E. Kirk, S. Gliga, J. Raabe, and L. J. Heyderman, "Element-Specific X-Ray Phase Tomography of 3D Structures at the Nanoscale," *Physical Review Letters*, vol. 114, p. 115501, Mar. 2015.

[11] C. Donnelly, V. Scagnoli, M. Guizar-Sicairos, M. Holler, F. Wilhelm, F. Guillou, A. Rogalev, C. Detlefs, A. Menzel, J. Raabe, and L. J. Heyderman, "High-resolution hard x-ray magnetic imaging with dichroic ptychography," *Physical Review B*, vol. 94, p. 064421, Aug. 2016.

[12] X. Shi, P. Fischer, V. Neu, D. Elefant, J. C. T. Lee, D. A. Shapiro, M. Farmand, T. Tyliszczak, H. W. Shiu, S. Marchesini, S. Roy, and S. D. Kevan, "Soft x-ray ptychography studies of nanoscale magnetic and structural correlations in thin $SmCo_5$ films," *Applied Physics Letters*, vol. 108, p. 094103, Mar. 2016.

[13] S. W. Hell, "Toward fluorescence nanoscopy," *Nature Biotechnology*, vol. 21, pp. 1347–1355, Nov. 2003.

[14] V. Lučić, A. Rigort, and W. Baumeister, "Cryo-electron tomography: The challenge of doing structural biology in situ," *The Journal of Cell Biology*, vol. 202, pp. 407–419, Aug. 2013.

[15] B. D. Engel, M. Schaffer, L. K. Cuellar, E. Villa, J. P. Elife, and W. Baumeister, "Native architecture of the Chlamydomonas chloroplast revealed by in situ cryo-electron tomography," *eLife*, no. 4, p. e04889, 2015.

[16] J. W. Goodman, *Introduction to Fourier Optics*, vol. 26 of *McGraw-Hill Physical and Quantum Electronics Series*. San Francisco, CA: McGraw-Hill, 1968.

[17] D. M. Paganin, "Coherent X-ray Optics." Oxford University Press, 2006.

[18] L. Mandel and E. Wolf, *Optical Coherence and Quantum Optics*. Cambridge: Cambridge Univ., 1995.

[19] A. A. Michelson and E. W. Morley, "On the Relative Motion of the Earth and the Luminiferous Ether," *Am. J. Sci.*, vol. 34, no. 203, pp. 333–345, 1887.

[20] J. W. Goodman, *Statistical Optics*. New York: Wiley-Interscience, 1985.

[21] J. Als-Nielsen and D. McMorrow, *Elements of Modern X-ray Physics; 2nd ed.* Hoboken, NJ: Wiley, 2011.

[22] M. A. Heald and J. B. Marion, "Classical Electromagnetic Radiation." Dover Publications, Inc., Mineola, New York, 2012.

[23] J. H. Hubbell, W. J. Veigele, E. A. Briggs, R. T. Brown, D. T. Cromer, and R. J. Howerton, "Atomic form factors, incoherent scattering functions, and photon scattering cross sections," *Journal of Physical and Chemical Reference Data*, vol. 4, pp. 471–538, Oct. 2009.

[24] O. Klein and Y. Nishina, "Über die Streuung von Strahlung durch freie Elektronen nach der neuen relativistischen Quantendynamik von Dirac," *Zeitschrift für Physik*, vol. 52, pp. 853–868, July 2013.

[25] C. T. Chantler, "Theoretical Form Factor, Attenuation, and Scattering Tabulation for Z=1–92 from E=1–10 eV to E=0.4–1.0 MeV," *Journal of Physical and Chemical Reference Data*, vol. 24, pp. 71–643, Oct. 2009.

[26] P. Willmott, *An Introduction to Synchrotron Radiation*. Wiley, 2011.

[27] A. C. Thompson and D. Vaughan, *X-ray Data Booklet*, Jan. 2001. Available at `http://xdb.lbl.gov`, retrieved on 8.05.2019.

[28] B. L. Henke, E. M. Gullikson, and J. C. Davis, "X-Ray Interactions: Photoabsorption, Scattering, Transmission, and Reflection at E = 50-30,000 eV, Z = 1-92," *Atomic data and nuclear data tables*, vol. 54, pp. 181–342, July 1993.

[29] M. Eriksson, J. F. van der Veen, and C. Quitmann, "Diffraction-limited storage rings – a window to the science of tomorrow," *Journal of Synchrotron Radiation*, vol. 21, pp. 837–842, Sept. 2014.

[30] F. van der Veen and F. Pfeiffer, "Coherent x-ray scattering," *Journal of Physics: Condensed Matter*, vol. 16, pp. 5003–5030, July 2004.

[31] M. Barthelmess, U. Englisch, J. Pflüger, A. Schöps, J. Skupin, and M. Tischner, "Status of the PETRA III insertion devices," *Proceedings of EPAC08*, 2008.

[32] J. Bahrdt, H. J. Baecker, W. Frentrup, A. G. Proc, M. Scheer, B. Schulz, U. Englisch, and M. Tischer, "Apple undulator for PETRA III," *Proceedings of EPAC08*, pp. 2219–2221, 2008.

[33] T. B. Edo, D. J. Batey, A. M. Maiden, C. Rau, and U. Wagner, "Sampling in x-ray ptychography," *Physical Review A*, 2013.

[34] D. J. Batey, T. B. Edo, C. Rau, U. Wagner, and Z. D. Pešić, "Reciprocal-space up-sampling from real-space oversampling in x-ray ptychography," *Physical Review A*, 2014.

[35] W. Hoppe, "Beugung im inhomogenen Primärstrahlwellenfeld. III. Amplituden- und Phasenbestimmung bei unperiodischen Objekten," *Acta Crystallographica Section A: Crystal Physics, Diffraction, Theoretical and General Crystallography*, vol. 25, pp. 508–514, July 1969.

[36] J. M. Rodenburg and R. H. T. Bates, "The Theory of Super-Resolution Electron Microscopy Via Wigner-Distribution Deconvolution," *Philosophical Transactions of the Royal Society of London. Series A: Physical and Engineering Sciences*, vol. 339, pp. 521–553, June 1992.

[37] B. C. McCallum and J. M. Rodenburg, "Two-dimensional demonstration of Wigner phase-retrieval microscopy in the STEM configuration," *Ultramicroscopy*, vol. 45, pp. 371–380, Nov. 1992.

[38] J. M. Rodenburg, B. C. McCallum, and P. D. Nellist, "Experimental tests on double-resolution coherent imaging via STEM," *Ultramicroscopy*, vol. 48, pp. 304–314, Mar. 1993.

[39] H. N. Chapman, "Phase-retrieval X-ray microscopy by Wigner-distribution deconvolution," *Ultramicroscopy*, vol. 66, pp. 153–172, Dec. 1996.

[40] J. W. Cooley and J. W. Tukey, "An Algorithm for the Machine Calculation of Complex Fourier Series," *Mathematics of Computation*, vol. 19, pp. 297–301, Apr. 1965.

[41] J. R. Fienup, "Phase retrieval algorithms: a comparison," *Applied Optics*, vol. 21, pp. 2758–2769, Aug. 1982.

[42] D. Shapiro, P. Thibault, T. Beetz, V. Elser, M. Howells, C. Jacobsen, J. Kirz, E. Lima, H. Miao, A. M. Neiman, and D. Sayre, "Biological imaging by soft x-ray diffraction microscopy.," *Proceedings of the National Academy of Sciences*, vol. 102, pp. 15343–15346, Oct. 2005.

[43] M. A. Pfeifer, G. J. Williams, I. A. Vartanyants, R. Harder, and I. K. Robinson, "Three-dimensional mapping of a deformation field inside a nanocrystal," *Nature*, vol. 442, pp. 63–66, July 2006.

[44] H. N. Chapman, A. Barty, S. Marchesini, A. Noy, S. P. Hau-Riege, C. Cui, M. R. Howells, R. Rosen, H. He, J. C. H. Spence, U. Weierstall, T. Beetz, C. Jacobsen, and D. Shapiro, "High-resolution ab initio three-dimensional x-ray diffraction microscopy," *Journal of the Optical Society of America A*, vol. 23, pp. 1179–1200, May 2006.

[45] J. M. Rodenburg and H. M. L. Faulkner, "A phase retrieval algorithm for shifting illumination," *Applied Physics Letters*, vol. 85, pp. 4795–4797, Nov. 2004.

[46] P. Thibault, M. Dierolf, A. Menzel, O. Bunk, C. David, and F. Pfeiffer, "High-resolution scanning x-ray diffraction microscopy.," *Science*, vol. 321, pp. 379–382, July 2008.

[47] P. Thibault and M. Guizar-Sicairos, "Maximum-likelihood refinement for coherent diffractive imaging," *New Journal of Physics*, vol. 14, p. 063004, June 2012.

[48] M. R. Howells, T. Beetz, H. N. Chapman, C. Cui, J. M. Holton, C. J. Jacobsen, J. Kirz, E. LIMA, S. Marchesini, H. Miao, D. Sayre, D. A. Shapiro, J. C. H. Spence, and D. Starodub, "An assessment of the resolution limitation due to radiation-damage in X-ray diffraction microscopy," *Journal of Electron Spectroscopy and Related Phenomena*, vol. 170, pp. 4–12, Mar. 2009.

[49] P. Thibault and A. Menzel, "Reconstructing state mixtures from diffraction measurements," *Nature*, vol. 494, pp. 68–71, Feb. 2013.

[50] K. Stachnik, I. Mohacsi, I. Vartiainen, N. Stuebe, J. Meyer, M. Warmer, C. David, and A. Meents, "Influence of finite spatial coherence on ptychographic reconstruction," *Applied Physics Letters*, vol. 107, p. 011105, July 2015.

[51] N. Burdet, K. Shimomura, M. Hirose, A. Suzuki, and Y. Takahashi, "Efficient use of coherent X-rays in ptychography: Towards high-resolution and high-throughput observation of weak-phase objects," *Applied Physics Letters*, vol. 108, p. 071103, Feb. 2016.

[52] J. N. Clark, X. Huang, R. J. Harder, and I. K. Robinson, "Dynamic Imaging Using Ptychography," *Physical Review Letters*, vol. 112, p. 113901, Mar. 2014.

[53] B. Enders, M. Dierolf, P. Cloetens, M. Stockmar, F. Pfeiffer, and P. Thibault, "Ptychography with broad-bandwidth radiation," *Applied Physics Letters*, vol. 104, p. 171104, Apr. 2014.

[54] M. Dierolf, A. Menzel, P. Thibault, P. Schneider, C. M. Kewish, R. Wepf, O. Bunk, and F. Pfeiffer, "Ptychographic X-ray computed tomography at the nanoscale," *Nature*, vol. 467, pp. 436–439, Sept. 2010.

[55] M. Holler, J. Raabe, A. Diaz, M. Guizar-Sicairos, R. Wepf, M. Odstrcil, F. R. Shaik, V. Panneels, A. Menzel, B. Sarafimov, S. Maag, X. Wang, V. Thominet, H. Walther, T. Lachat, M. Vitins, and O. Bunk, "OMNY—A tOMography Nano crYo stage," *Review of Scientific Instruments*, vol. 89, p. 043706, Apr. 2018.

[56] M. Holler, J. Raabe, A. Diaz, M. Guizar-Sicairos, E. H. R. Tsai, M. Odstrcil, A. Menzel, and O. Bunk, "High-resolution 3D scanning X-ray microscopes at the Swiss Light Source," *Microscopy and Microanalysis*, vol. 24, pp. 168–171, Aug. 2018.

[57] S. Chen, J. Deng, Y. Yuan, C. Flachenecker, R. Mak, B. Hornberger, Q. Jin, D. Shu, B. Lai, J. Maser, C. Roehrig, T. Paunesku, S. C. Gleber, D. J. Vine, L. Finney, J. VonOsinski, M. Bolbat, I. Spink, Z. Chen, J. Steele, D. Trapp, J. Irwin, M. Feser, E. Snyder, K. Brister, C. Jacobsen, G. Woloschak, and S. Vogt, "The Bionanoprobe: hard X-ray fluorescence nanoprobe with cryogenic capabilities," *Journal of Synchrotron Radiation*, vol. 21, pp. 66–75, Jan. 2014.

[58] C. G. Schroer, M. Seyrich, M. Kahnt, S. Botta, R. Döhrmann, G. Falkenberg, J. Garrevoet, M. Lyubomirskiy, M. Scholz, A. Schropp, and F. Wittwer, "PtyNAMi: ptychographic nano-analytical microscope at PETRA III: interferometrically tracking positions for 3D x-ray scanning microscopy using a ball-lens retroreflector," in *X-Ray Nanoimaging: Instruments and Methods III* (B. Lai and A. Somogyi, eds.), p. 103890E, International Society for Optics and Photonics, Sept. 2017.

[59] S. Sala, V. S. C. Kuppili, S. Chalkidis, D. J. Batey, X. Shi, C. Rau, and P. Thibault, "Multiscale X-ray imaging using ptychography," *Journal of Synchrotron Radiation*, vol. 25, pp. 1214–1221, July 2018.

[60] M. Holler, A. Diaz, M. Guizar-Sicairos, P. Karvinen, E. Färm, E. Härkönen, M. Ritala, A. Menzel, J. Raabe, and O. Bunk, "X-ray ptychographic computed tomography at 16 nm isotropic 3D resolution," *Scientific Reports*, vol. 4, p. 2758, Jan. 2014.

[61] M. Holler, M. Guizar-Sicairos, E. H. R. Tsai, R. Dinapoli, E. Müller, O. Bunk, J. Raabe, and G. Aeppli, "High-resolution non-destructive three-dimensional imaging of integrated circuits," *Nature*, vol. 543, pp. 402–406, Mar. 2017.

[62] A. Diaz, B. Malkova, M. Holler, M. Guizar-Sicairos, E. Lima, V. Panneels, G. Pigino, A. G. Bittermann, L. Wettstein, T. Tomizaki, O. Bunk, G. Schertler, T. Ishikawa, R. Wepf, and A. Menzel, "Three-dimensional mass density mapping of cellular ultrastructure by ptychographic X-ray nanotomography," *Journal of Structural Biology*, vol. 192, pp. 461–469, Dec. 2015.

[63] S. H. Shahmoradian, E. H. R. Tsai, A. Diaz, M. Guizar-Sicairos, J. Raabe, L. Spycher, M. Britschgi, A. Ruf, H. Stahlberg, and M. Holler, "Three-Dimensional Imaging of Biological Tissue by Cryo X-Ray Ptychography," *Scientific Reports*, vol. 7, p. 2480, July 2017.

[64] I. Zanette, B. Enders, M. Dierolf, P. Thibault, R. Gradl, A. Diaz, M. Guizar-Sicairos, A. Menzel, F. Pfeiffer, and P. Zaslansky, "Ptychographic X-ray nanotomography quantifies mineral distributions in human dentine," *Scientific Reports*, vol. 5, p. 9210, Mar. 2015.

[65] M. Guizar-Sicairos, A. Diaz, M. Holler, M. S. Lucas, A. Menzel, R. A. Wepf, and O. Bunk, "Phase tomography from x-ray coherent diffractive imaging projections," *Optics Express*, vol. 19, no. 22, p. 21345, 2011.

[66] M. Guizar-Sicairos, S. T. Thurman, and J. R. Fienup, "Efficient subpixel image registration algorithms," *Optics Letters*, vol. 33, no. 2, pp. 156–158, 2008.

[67] M. Guizar-Sicairos, J. J. Boon, K. Mader, A. Diaz, A. Menzel, and O. Bunk, "Quantitative interior x-ray nanotomography by a hybrid imaging technique," *Optica*, vol. 2, no. 3, p. 259, 2015.

[68] J. Radon, "Über die Bestimmung von Funktionen durch ihre Integralwerte längs gewisser Mannigfaltigkeiten," *Ber. Verh. Sächs. Akad. Wiss.*, pp. 262–277, Apr. 1917.

[69] F. Pfeiffer, C. Kottler, O. Bunk, and C. David, "Hard X-Ray Phase Tomography with Low-Brilliance Sources," *Physical Review Letters*, vol. 98, p. 108105, Mar. 2007.

[70] G. W. Faris and R. L. Byer, "Three-dimensional beam-deflection optical tomography of a supersonic jet," *Applied Optics*, vol. 27, pp. 5202–5212, Dec. 1988.

[71] A. Diaz, P. Trtik, M. Guizar-Sicairos, A. Menzel, P. Thibault, and O. Bunk, "Quantitative x-ray phase nanotomography," *Physical Review B*, vol. 85, p. 020104, Jan. 2012.

[72] R. Van Grieken and A. Markowicz, "Handbook of X-ray Spectrometry." Marcel Dekker, Inc., New York, 1993.

[73] A. Burkhardt, T. Pakendorf, B. Reime, J. Meyer, P. Fischer, N. Stübe, S. Panneerselvam, O. Lorbeer, K. Stachnik, M. Warmer, P. Rödig, D. Göries, and A. Meents, "Status of the crystallography beamlines at PETRA III," *The European Physical Journal Plus*, vol. 131, pp. 56–9, Mar. 2016.

[74] Machine parameters of PETRA III synchrotron light source at DESY in Hamburg, Germany, `http://photon-science.desy.de/facilities/petra_iii/machine/parameters/index_eng.html`, retrieved on 4.06.2019.

[75] K. Stachnik and A. Meents, "Scanning X-ray Microscopy with a Single Photon Counting 2D Detector," *Acta Physica Polonica A*, vol. 125, pp. 902–906, Mar. 2014.

[76] A. Meents, B. Reime, N. Stuebe, P. Fischer, M. Warmer, D. Goeries, J. Roever, J. Meyer, J. Fischer, A. Burkhardt, I. Vartiainen, P. Karvinen, and C. David, " Development of an in-vacuum x-ray microscope with cryogenic sample cooling for beamline P11 at PETRA III," *SPIE Optical Engineering + Applications*, vol. 8851, pp. 88510K–88510K–7, 2013.

[77] J. Vila-Comamala, A. Diaz, M. Guizar-Sicairos, A. Mantion, C. M. Kewish, A. Menzel, O. Bunk, and C. David, "Characterization of high-resolution diffractive X-ray optics by ptychographic coherent diffractive imaging," *Optics Express*, vol. 19, pp. 21333–21344, Oct. 2011.

[78] A. Schropp, R. Hoppe, J. Patommel, D. Samberg, F. Seiboth, S. Stephan, G. Wellenreuther, G. Falkenberg, and C. G. Schroer, "Hard x-ray scanning microscopy with coherent radiation: Beyond the resolution of conventional x-ray microscopes," *Applied Physics Letters*, vol. 100, no. 25, p. 253112, 2012.

[79] P. M. Pelz, M. Guizar-Sicairos, P. Thibault, I. Johnson, M. Holler, and A. Menzel, "On-the-fly scans for X-ray ptychography," *Applied Physics Letters*, vol. 105, p. 251101, Dec. 2014.

[80] J. N. Clark, X. Huang, R. J. Harder, and I. K. Robinson, "Continuous scanning mode for ptychography," *Optics Letters*, vol. 39, pp. 6066–6069, Oct. 2014.

[81] X. Huang, K. Lauer, J. N. Clark, W. Xu, E. Nazaretski, R. Harder, I. K. Robinson, and Y. S. Chu, "Fly-scan ptychography," *Scientific Reports*, vol. 5, p. 9074, Mar. 2015.

[82] B. Chen, B. Abbey, R. Dilanian, E. Balaur, G. van Riessen, M. Junker, C. Q. Tran, M. W. M. Jones, A. G. Peele, I. McNulty, D. J. Vine, C. T. Putkunz, H. M. Quiney, and K. A. Nugent, "Diffraction imaging: The limits of partial coherence," *Physical Review B*, vol. 86, p. 235401, Dec. 2012.

[83] M. Holler, J. Raabe, A. Diaz, M. Guizar-Sicairos, C. Quitmann, A. Menzel, and O. Bunk, "An instrument for 3D x-ray nano-imaging," *Review of Scientific Instruments*, vol. 83, p. 073703, July 2012.

[84] C. G. Schroer, P. Boye, J. M. Feldkamp, J. Patommel, D. Samberg, A. Schropp, A. Schwab, S. Stephan, G. Falkenberg, G. Wellenreuther, and N. Reimers, "Hard X-ray nanoprobe at beamline P06 at PETRA III," *Nuclear Instruments and Methods in Physics Research Section A: Accelerators, Spectrometers, Detectors and Associated Equipment*, vol. 616, pp. 93–97, May 2010.

[85] E. Nazaretski, H. Yan, K. Lauer, N. Bouet, X. Huang, W. Xu, J. Zhou, D. Shu, Y. Hwu, Y. S. Chu, and IUCr, "Design and performance of an X-ray scanning microscope at the Hard X-ray Nanoprobe beamline of NSLS-II," *Journal of Synchrotron Radiation*, vol. 24, pp. 1113–1119, Nov. 2017.

[86] R. Celestre, K. Nowrouzi, D. A. Shapiro, P. Denes, J. M. Joseph, A. Schmid, and H. A. Padmore, "Nanosurveyor 2: A Compact Instrument for Nano-Tomography at the Advanced Light Source," *Journal of Physics: Conference Series*, vol. 849, p. 012047, June 2017.

[87] M. Guizar-Sicairos, I. Johnson, A. Diaz, M. Holler, P. Karvinen, H.-C. Stadler, R. Dinapoli, O. Bunk, and A. Menzel, "High-throughput ptychography using Eiger-scanning X-ray nano-imaging of extended regions," *Optics Express*, vol. 22, no. 12, pp. 14859–14870, 2014.

[88] B. Kaehr, J. L. Townson, R. M. Kalinich, Y. H. Awad, B. S. Swartzentruber, D. R. Dunphy, and C. J. Brinker, "Cellular complexity captured in durable silica biocomposites.," *Proceedings of the National Academy of Sciences of the United States of America*, vol. 109, pp. 17336–17341, Oct. 2012.

[89] M. van Heel and M. Schatz, "Fourier shell correlation threshold criteria," *Journal of Structural Biology*, vol. 151, pp. 250–262, 2005.

[90] C. Jung, M. G. Kaul, O. T. Bruns, T. Du i, B. Freund, M. Heine, R. Reimer, A. Meents, S. C. Salmen, H. Weller, P. Nielsen, G. Adam, J. Heeren, and H. Ittrich, "Intraperitoneal Injection Improves the Uptake of Nanoparticle-Labeled High-Density Lipoprotein to Atherosclerotic Plaques Compared With Intravenous Injection: A Multimodal Imaging Study in ApoE Knockout Mice," *Circulation: Cardiovascular Imaging*, vol. 7, pp. 303–311, Mar. 2014.

[91] O. T. Bruns, H. Ittrich, K. Peldschus, M. G. Kaul, U. I. Tromsdorf, J. Lauterwasser, M. S. Nikolic, B. Mollwitz, M. Merkel, N. C. Bigall, S. Sapra, R. Reimer, H. Hohenberg, H. Weller, A. Eychmüller, G. Adam, U. Beisiegel, and J. Heeren, "Real-time magnetic resonance imaging and quantification of lipoprotein metabolism in vivo using nanocrystals," *Nature Nanotechnology*, vol. 4, pp. 193–201, Jan. 2009.

[92] A. Bartelt, O. T. Bruns, R. Reimer, H. Hohenberg, H. Ittrich, K. Peldschus, M. G. Kaul, U. I. Tromsdorf, H. Weller, C. Waurisch, A. Eychmüller, P. L. S. M. Gordts, F. Rinninger, K. Bruegelmann, B. Freund, P. Nielsen, M. Merkel, and J. Heeren, "Brown adipose tissue activity controls triglyceride clearance," *Nature Medicine*, vol. 17, pp. 200–205, Jan. 2011.

[93] P. Modregger, D. Lübbert, P. Schäfer, and R. Köhler, "Spatial resolution in Bragg-magnified X-ray images as determined by Fourier analysis," *Phys. Status Solidi A*, vol. 204, pp. 2746–2752, Aug. 2007.

[94] V. A. Solé, E. Papillon, M. Cotte, P. Walter, and J. Susini, "A multiplatform code for the analysis of energy-dispersive X-ray fluorescence spectra," *Spectrochimica Acta Part B: Atomic Spectroscopy*, vol. 62, pp. 63–68, Jan. 2007.

[95] Qt cross-platform Graphical User Interface toolkit, `https://www.qt.io`, retrieved on 6.06.2019.

[96] K. Jefimovs, J. Vila-Comamala, T. Pilvi, J. Raabe, M. Ritala, and C. David, "Zone-Doubling Technique to Produce Ultrahigh-Resolution X-Ray Optics," *Physical Review Letters*, vol. 99, p. 264801, Dec. 2007.

[97] J. R. Kremer, D. N. Mastronarde, and J. R. McIntosh, "Computer Visualization of Three-Dimensional Image Data Using IMOD," *Journal of Structural Biology*, vol. 116, pp. 71–76, Jan. 1996.

[98] B. D. A. Levin, Y. Jiang, E. Padgett, S. Waldon, C. Quammen, C. Harris, U. Ayachit, M. Hanwell, P. Ercius, D. A. Muller, and R. Hovden, "Tutorial on the Visualization of Volumetric Data Using *tomviz*," *Microscopy Today*, vol. 26, pp. 12–17, Jan. 2018.

[99] G. Schneider, "Cryo X-ray microscopy with high spatial resolution in amplitude and phase contrast," *Ultramicroscopy*, vol. 75, pp. 85–104, Nov. 1998.

[100] J. Deng, Y. H. Lo, M. Gallagher-Jones, S. Chen, A. Pryor, Q. Jin, Y. P. Hong, Y. S. G. Nashed, S. Vogt, J. Miao, and C. Jacobsen, "Correlative 3D x-ray fluorescence and ptychographic tomography of frozen-hydrated green algae," *Science Advances*, vol. 4, pp. eaau4548–701, Nov. 2018.

[101] K. J. Barnham and A. I. Bush, "Metals in Alzheimer's and Parkinson's Diseases," *Current Opinion in Chemical Biology*, vol. 12, pp. 222–228, Apr. 2008.

[102] G. Bjørklund, V. Stejskal, M. A. Urbina, M. Dadar, S. Chirumbolo, and J. Mutter, "Metals and Parkinson's Disease: Mechanisms and Biochemical Processes," *Current Medicinal Chemistry*, vol. 25, pp. 2198–2214, May 2018.

[103] J. A. Duce and A. I. Bush, "Biological metals and Alzheimer's disease: Implications for therapeutics and diagnostics," *Progress in Neurobiology*, vol. 92, pp. 1–18, Sept. 2010.

[104] P. Leidinger, J. Treptow, K. Hagens, J. Eich, N. Zehethofer, D. Schwudke, W. Oehlmann, H. Lünsdorf, O. Goldmann, U. E. Schaible, K. E. J. Dittmar, and C. Feldmann, "Isoniazid@Fe_2O_3Nanocontainers and Their Antibacterial Effect on Tuberculosis Mycobacteria," *Angewandte Chemie International Edition*, vol. 54, pp. 12597–12601, Aug. 2015.

[105] J. G. Heck, J. Napp, S. Simonato, J. Möllmer, M. Lange, H. M. Reichardt, R. Staudt, F. Alves, and C. Feldmann, "Multifunctional Phosphate-Based Inorganic–Organic Hybrid Nanoparticles," *Journal of the American Chemical Society*, vol. 137, pp. 7329–7336, June 2015.

[106] J. I. Goldstein, D. E. Newbury, J. R. Michael, N. W. M. Ritchie, J. H. J. Scott, and D. C. Joy, *Scanning Electron Microscopy and X-Ray Microanalysis*. Springer New York, 2017.

[107] E. Kosior, S. Bohic, H. Suhonen, R. Ortega, G. Devès, A. Carmona, F. Marchi, J. F. Guillet, and P. Cloetens, "Combined use of hard X-ray phase contrast imaging and X-ray fluorescence microscopy for sub-cellular metal quantification," *Journal of Structural Biology*, vol. 177, pp. 239–247, Feb. 2012.

[108] A. D. Surowka, M. Töpperwien, M. Bernhardt, J. D. Nicolas, M. Osterhoff, T. Salditt, D. Adamek, and M. Szczerbowska-Boruchowska, "Combined in-situ imaging of structural organization and elemental composition of substantia nigra neurons in the elderly," *Talanta*, vol. 161, pp. 368–376, Dec. 2016.

[109] C. Holzner, M. Feser, S. Vogt, B. Hornberger, S. B. Baines, and C. Jacobsen, "Zernike phase contrast in scanning microscopy with X-rays," *Nature Physics*, vol. 6, pp. 883–887, Nov. 2010.

[110] R. Hettel, "DLSR design and plans: an international overview," *Journal of Synchrotron Radiation*, vol. 21, pp. 843–855, Sept. 2014.

[111] D. J. Vine, D. Pelliccia, C. Holzner, S. B. Baines, A. Berry, I. McNulty, S. Vogt, A. G. Peele, and K. A. Nugent, "Simultaneous X-ray fluorescence and ptychographic microscopy of Cyclotella meneghiniana," *Optics Express*, vol. 20, no. 16, pp. 18287–18296, 2012.

[112] J. Deng, D. J. Vine, S. Chen, Y. S. G. Nashed, Q. Jin, N. W. Phillips, T. Peterka, R. Ross, S. Vogt, and C. J. Jacobsen, "Simultaneous cryo X-ray ptychographic and fluorescence microscopy of green algae," *Proceedings of the National Academy of Sciences*, vol. 112, pp. 2314–2319, Feb. 2015.

[113] J. Deng, D. J. Vine, S. Chen, Q. Jin, Y. S. G. Nashed, T. Peterka, S. Vogt, and C. Jacobsen, "X-ray ptychographic and fluorescence microscopy of frozen-hydrated cells using continuous scanning," *Scientific Reports*, vol. 7, p. 1642, Mar. 2017.

[114] M. W. M. Jones, N. W. Phillips, B. Abbey, D. J. Hare, G. A. van Riessen, D. J. Vine, M. D. de Jonge, and G. McColl, "Simultaneous nanostructure and chemical imaging of intact whole nematodes," *Chemical Communications*, vol. 55, pp. 1052–1055, Jan. 2019.

[115] P. Thibault, M. Guizar-Sicairos, and A. Menzel, "Coherent imaging at the diffraction limit," *Journal of Synchrotron Radiation*, vol. 21, pp. 1011–1018, Sept. 2014.

[116] G. Weiss and U. E. Schaible, "Macrophage defense mechanisms against intracellular bacteria," *Immunological Reviews*, vol. 264, pp. 182–203, Feb. 2015.

[117] B. E. Schneider, J. Behrends, K. Hagens, N. Harmel, J. A. Shayman, and U. E. Schaible, "Lysosomal phospholipase A 2: A novel player in host immunity to Mycobacterium tuberculosis," *European Journal of Immunology*, vol. 44, pp. 2394–2404, June 2014.

[118] K. Jähn, S. Kelkar, H. Zhao, Y. Xie, L. M. T. Lewis, V. Dusevich, S. L. Dallas, and L. F. Bonewald, "Osteocytes Acidify Their Microenvironment in Response to PTHrP In Vitro and in Lactating Mice In Vivo," *Journal of Bone and Mineral Research*, vol. 32, pp. 1761–1772, Aug. 2017.

[119] H. Qing, L. Ardeshirpour, P. D. Pajevic, V. Dusevich, K. Jähn, S. Kato, J. Wysolmerski, and L. F. Bonewald, "Demonstration of osteocytic perilacunar/canalicular remodeling in mice during lactation," *Journal of Bone and Mineral Research*, vol. 27, pp. 1018–1029, May 2012.

[120] B. Busse, H. A. Bale, E. A. Zimmermann, B. Panganiban, H. D. Barth, A. Carriero, E. Vettorazzi, J. Zustin, M. Hahn, J. W. Ager, K. Püschel, M. Amling, and R. O. Ritchie, "Vitamin D Deficiency Induces Early Signs of Aging in Human Bone, Increasing the Risk of Fracture," *Science Translational Medicine*, vol. 5, pp. 193ra88–193ra88, July 2013.

[121] H. Sano, J. Kikuta, M. Furuya, N. Kondo, N. Endo, and M. Ishii, "Intravital bone imaging by two-photon excitation microscopy to identify osteocytic osteolysis in vivo," *Bone*, vol. 74, pp. 134–139, May 2015.

[122] X. Huang, H. Yan, M. Ge, H. Öztürk, E. Nazaretski, I. K. Robinson, and Y. S. Chu, "Artifact mitigation of ptychography integrated with on-the-fly scanning probe microscopy," *Applied Physics Letters*, vol. 111, p. 023103, July 2017.

[123] D. P. Nicolella, J. Q. Feng, D. E. Moravits, A. R. Bonivitch, Y. Wang, V. Dusecich, W. Yao, N. Lane, and L. F. Bonewald, "Effects of nanomechanical bone tissue properties on bone tissue strain: implications for osteocyte mechanotransduction," *Journal of Musculoskeletal and Neuronal Interactions*, vol. 8, no. 4, pp. 330–331, 2008.

[124] M. Kerschnitzki, P. Kollmannsberger, M. Burghammer, G. N. Duda, R. Weinkamer, W. Wagermaier, and P. Fratzl, "Architecture of the osteocyte network correlates with bone material quality," *Journal of Bone and Mineral Research*, vol. 28, pp. 1837–1845, Aug. 2013.

[125] B. Hesse, P. Varga, M. Langer, A. Pacureanu, S. Schrof, N. Männicke, H. Suhonen, P. Maurer, P. Cloetens, F. Peyrin, and K. Raum, "Canalicular Network Morphology Is the Major Determinant of the Spatial Distribution of Mass Density in Human Bone Tissue: Evidence by Means of Synchrotron Radiation Phase-Contrast nano-CT," *Journal of Bone and Mineral Research*, vol. 30, pp. 346–356, Feb. 2015.

[126] S. Bajt, M. Prasciolu, H. Fleckenstein, M. Domaracký, H. N. Chapman, A. J. Morgan, O. Yefanov, M. Messerschmidt, Y. Du, K. T. Murray, V. Mariani, M. Kuhn, S. Aplin, K. Pande, P. Villanueva-Perez, K. Stachnik, J. P. Chen, A. Andrejczuk, A. Meents, A. Burkhardt, D. Pennicard, X. Huang, H. Yan, E. Nazaretski, Y. S.

Chu, and C. E. Hamm, "X-ray focusing with efficient high-NA multilayer Laue lenses," *Light: Science & Applications*, vol. 7, p. 17162, Mar. 2018.

[127] J. Maser, A. Osanna, Y. Wang, C. Jacobsen, J. Kirz, S. Spector, B. Winn, and D. Tennant, "Soft X-ray microscopy with a cryo scanning transmission X-ray microscope: I. Instrumentation, imaging and spectroscopy," *Journal of Microscopy*, vol. 197, pp. 68–79.

[128] S. Williams, X. Zhang, C. Jacobsen, J. Kirz, S. Lindaas, J. V. Hof, and S. S. Lamm, "Measurements of wet metaphase chromosomes in the scanning transmission X-ray microscope," *Journal of Microscopy*, vol. 170, pp. 155–165, May 1993.

[129] M. Kahnt, G. Falkenberg, J. Garrevoet, J. Hartmann, T. Krause, M. Niehle, M. Scholz, M. Seyrich, A. Trampert, A. Waag, H. H. Wehmann, F. Wittwer, H. Zhou, M. Hanke, and C. G. Schroer, "Simultaneous Hard X-ray Ptychographic Tomography and X-ray Fluorescence Tomography of Isolated Hollow Core-Shell GaN Rods," *Microscopy and Microanalysis*, vol. 24, pp. 32–33, Aug. 2018.

[130] J. C. Weaver, Q. Wang, A. Miserez, A. Tantuccio, R. Stromberg, K. N. Bozhilov, P. Maxwell, R. Nay, S. T. Heier, E. DiMasi, and D. Kisailus, "Analysis of an ultra hard magnetic biomineral in chiton radular teeth," *Materials Today*, vol. 13, pp. 42–52, Jan. 2010.

[131] PubChem is an open chemistry database at the National Institutes of Health (NIH), `https://pubchem.ncbi.nlm.nih.gov/compound/Ferric-phosphate`, retrieved on 10.06.2019.

[132] Mineralogy Database, `http://www.webmineral.com/data/Magnetite.shtml#.XP6pvy-B1R4`, retrieved on 10.06.2019.

[133] M. Odstrcil, M. Holler, and M. Guizar-Sicairos, "Arbitrary-path fly-scan ptychography," *Optics Express*, vol. 26, no. 10, p. 12585, 2018.

[134] C. G. Schroer, I. Agapov, W. Brefeld, R. Brinkmann, Y. C. Chae, H. C. Chao, M. Eriksson, J. Keil, X. Nuel Gavaldà, R. Röhlsberger, O. H. Seeck, M. Sprung, M. Tischer, R. Wanzenberg, and E. Weckert, "PETRA IV: the ultralow-emittance source project at DESY," *Journal of Synchrotron Radiation*, vol. 25, pp. 1277–1290, Sept. 2018.

[135] Attosecond X-ray Science: Imaging and Spectroscopy, project at Center for Free Electron Laser Science, Hamburg, funded by the European Research Council `https://axsis.desy.de`, retrieved on 24.06.2019.

[136] C. Olendrowitz, M. Bartels, M. Krenkel, A. Beerlink, R. Mokso, M. Sprung, and T. Salditt, "Phase-contrast x-ray imaging and tomography of the nematode Caenorhabditis elegans," *Physics in Medicine & Biology*, vol. 57, pp. 5309–5323, Aug. 2012.

[137] E. H. R. Tsai, I. Usov, A. Diaz, A. Menzel, and M. Guizar-Sicairos, "X-ray ptychography with extended depth of field," *Optics Express*, vol. 24, pp. 29089–29108, Dec. 2016.

[138] P. Li and A. Maiden, "Multi-slice ptychographic tomography," *Scientific Reports*, vol. 8, p. 2049, Feb. 2018.

[139] M. Du and C. Jacobsen, "Relative merits and limiting factors for x-ray and electron microscopy of thick, hydrated organic materials," *Ultramicroscopy*, vol. 184, pp. 293–309, Jan. 2018.

[140] `QCustomPlot` C++ Qt widget for plotting and data visualisation, `https://www.qcustomplot.com`, retrieved on 6.06.2019.

[141] R. A. London, M. D. Rosen, and J. E. Trebes, "Wavelength choice for soft x-ray laser holography of biological samples," *Applied Optics*, vol. 28, pp. 3397–3404, Aug. 1989.

[142] J. Hubbell and M. Seltzer, *Tables of X-ray Mass Attenuation Coefficients and Mass Energy-Absorption Coefficients*, 1995. Version 1.4, Report NISTIR-5632 (National Institute of Standards and Technology, 1995), Available at `https://dx.doi.org/10.18434/T4D01F`, retrieved on 24.05.2019.